Modelling of Turbulent Flow, Heat Transfer

and Solidification in A Twin-Roll Caster

by

Hideki Murakami

A thesis submitted to the Faculty of Graduate Studies and Research
in partial fulfilment of the requirement
for the Degree of Ph D

Department of Mining and Metallurgical Engineering
McGill University
Montreal, Canada
September 1993

ISBN 0-315-94694-6

PhD Thesis by Hideki Murakami

Long title:	Modelling of Turbulent Flow, Heat Transfer and Solidification in a Twin-Roll Caster
Short title:	Turbulent Flow, Heat Transfer and Solidification in a Twin-Roll Caster

To my wife Yoko

ABSTRACT

A computational modelling study has been undertaken for analysing the complex turbulent melt flow, involving convective and conductive heat transfer in the melt pool and the solidifying mushy-region within the wedge-shaped region of a vertical twin-roll stainless steel caster.

An essential feature of the model is the incorporation of the body-fitted curvilinear coordinate transformation method for correctly modelling the arbitrary shaped region of the caster in the presence of non-isothermal solidification. The model can also treat an obstacle such as a submerged nozzle within the domain. The dendritic columnar solidification of molten metal has been modelled through the implementation of the enthalpy-porosity technique. The transformed curvilinear momentum and energy transport equations were suitably non-dimensionalized and later solved for the physical variables, using a control-volume finite difference scheme. The pressure-velocity coupling of the momentum equations were resolved through a modification of the well-established SIMPLER algorithm.

In the absence of such previous studies for stainless steel, either mathematical or experimental, comparisons have been made of the present model with the experimental work carried out within Nippon Steel Corporation as well as with experimental studies of a similar system for a tin-lead alloy. Predictions based on the present model are in good agreement with experimental results.

Various parametric studies have been carried out for the important variables of the twin-roll casting system, and their effects on the turbulent velocity fields, temperature distributions within the melt, solidification profiles and the extent of the mushy region, have been predicted. The present results lead to many suggestions for the design of twin-roll casting systems.

RÉSUMÉ

Une étude de modélisation assistée par ordinateur a été entreprise portant sur l'analyse de la coulée en régime turbulent. Ce modèle tient compte des effets du transfert de chaleur par conduction et convection. Il peut de plus prendre en considération l'influence de la solidification du métal au niveau de la section conique d'un système vertical de coulée continue à deux cylindres en acier inoxydable, là où liquide et dendrites cohabitent.

Un caractère essentiel de ce modèle consiste en l'incorporation d'une méthode de transformation des coordonnées curvilignes d'un système de référence arbitraire pour modéliser une région de forme arbitraire d'un système de coulée en présence de solidification non-isotherme. Ce modèle peut aussi tenir compte, entre autres cas difficiles, d'un obstacle comme un orifice de coulée submergé. La solidification du métal en fusion par formation de dendrites à été modélisée en utilisant la technique dite "d'enthalpie-porosité". Les équations curvilignes transformées du transport de mouvement et d'énergie ont été reformulées de façon à être sans dimension, et résolues en utilisant une méthode de différence finie avec volume contrôlé. Le couplage de la vitesse et de la pression dans les équations de mouvement a été résolu par modification de l'algorithme bien connu SIMPLER.

En l'absence d'études antérieures (expérimentales ou de simulation) portant sur les aciers inoxydables, des comparaisons entre ce modèle et les travaux expérimentaux de Nippon Steel Corporation, ainsi qu'avec des expériences sur un système similaire d'alliage étain-plomb, ont été faites. Les prédictions basées sur le présent modèle sont en bon accord avec ces résultats expérimentaux.

Des études paramétriques ont été faites concernant les variables importantes liées au système de coulée avec rouleaux jumeaux verticaux. Leurs effets sur les champs de vitesse turbulente, les distributions de température dans le métal en fusion, les profils de solidification et la largeur de la zone liquide-solide, ont été prédits. Ces résultats sont utiles pour la mise au point des systèmes de coulée continue à rouleaux jumeaux.

ACKNOWLEDGEMENTS

The author is particularly indebted to Professor R.I.L.Guthrie and Professor M. Hasan for their detailed supervision, guidance and instruction during the whole of this research work.

Special thanks are also due to his good friends and various instructors in the Department of Mining and Metallurgical Engineering at McGill University: R.Sankaranarayanan for discussing and giving valuable suggestions about fundamental fluid dynamics, C.Jefferies and R.Aboutalebi for discussions concerning the mathematical model, L.Meissenheimer for her great help in preparing this thesis, Professor S.Yue for useful information regarding strip casting processes, Professor F.Mucciardi for the author's understanding of heat transfer phenomena, Professor J.E.Gruzleski for valuable suggestions about solidification processes, and Professor G.Carayannis for important computational techniques. G.Yamanoglu, F.Sebo, and M.Ikezawa have always encouraged and helped the author.

The author would like to acknowledge the influence of his instructors at Tokyo University: Professor T.Kobayashi for introducing numerical turbulent theories and Professor Y.Morinishi for introducing numerical techniques.

The author also wishes to thank good instructors in Nippon Steel Corporation: Dr S.Tanaka for giving him helpful information and suggestion about the twin drum caster, and Mr M.Tatsukawa, Mr. J.Hayashi, Dr Y.Ueshima, and T.Mizoguchi for discussion relating to heat transfer in the twin-roll casting process .

Finally, the author acknowledges the forbearance of his wife, Yoko.

TABLE OF CONTENTS

Abstract

Acknowledgements   Page

Table of Contents .... (1)

List of Figures .... (4)

List of Tables .... (9)

1. Introduction 1

    1.1 History of Twin Roll Caster 1

    1.2 Objectives 4

    1.3 Outline of Thesis 6

2. Literature Survey 9

    2.1 Twin Roll Caster 9

    2.2 Numerical Methods for Turbulence 15

    2.3 Body Fitted Coordinates 20

    2.4 Numerical Methods for Solidification 24

3. Twin Drum Caster 28

    3.1 General Characteristic of the Vertical Twin Drum Caster 28

    3.2 Experiments of Twin Drum Caster at N.S.C. 30

        3.2.1 Solidified Shell Thickness 30

        3.2.1 Surface Cracks 35

4. Mathematical Formulation of Problem 38

    4.1 Introduction 38

    4.2 Governing Equations 39

        4.2.1 General Form of Governing Equations 39

        4.2.2 Laminar Flow 41

4.2.3 Turbulent Flow 42
4 2.4 Non–Dimensionalization 44
4.3 Body Fitted Coordinates 45
4.3.1 Numerical Grid Generation 45
4.3.2 Transformation of Governing Equations 50
4.4 Modelling of Solidification 54
4.4.1 Latent Heat Formulation 54
4.4.2 Enthalpy–Porosity Technique 55
4.5 Boundary Conditions 58
4.5.1 Roll Surface 58
4.5.2 Symmetric Axis 61
4.5.3 Free Surface 62
4.5.5 Inlet & Outlet 62
4.6 Numerical Procedures 64
4.6.1 Discretization 64
4.6.2 Algorithm 67
4.6.3 Techniques for Convergence 70

5. Fluid Flow and Heat Transfer in a Wedge Shape Pool 71
5.1 Introduction 71
5.2 Closed System 73
5.2.1 Laminar Flow 73
5.2.2 Turbulent Flow 75
5.3 Inlet–Outlet System 85
5.4 Heat Transfer 89
5.4.1 Effects of Buoyancy Force 89
5.4.2 Effects of Turbulent Heat Transfer 90
5.4.3 Effects of Characteristic Length 91
5.5 Verification 99
5.6 Summary 107

6. Numerical Analysis of Fluid Flow, Heat Transfer and Solidification in Twin Roll Caster108

6.1 Introduction 108

6.2 Effects of Porosity Function Coefficient 109

6.3 Comparison with Experimental Data 114

6.4 Effects of Turbulent Prandtl Number 127

6.5 Effects of Superheat 133

6.6 Summary 137

7. Computational Studies of Transport Processes in A Twin Roll Stainless-Steel Caster 139

7.1 Introduction 139

7.2 Grid Selection and Effects 140

7.3 Effects of Gap Between Rolls 143

7.4 Effects of Superheat 144

7.5 Effects of Casting Speed 153

7.6 Effects of Nozzle Design 154

7.6.1 Inside Gap of Submerged Nozzle 154

7.6.2 Depth of Nozzle 155

7.6.3 Outside Thickness of Submerged Nozzle 156

7.6.4 Horizontally Impinging Flows 157

7.6.5 Height of Pool 158

7.7 Effects of Cooling Rate 159

7.8 Engineering Characteristics of Twin Roll Casters 160

7.10 Summary 179

8. Conclusions 181

Contributions to knowledge 182

Recommendations for future work 182

Nomenclature 184

Bibliography 186

LIST OF FIGURES

		page
Figure 1.1	Past, present,and future steel processing steps	2
Figure 1.2	Classification of casting	3
Figure 1.3	Bessemer's twin roll caster	5
Figure 2.1	Relation between solidification time and thickness of strip, columnar or equiaxed zone	13
Figure 2.2	Physical and transformed planes	22
Figure 3.1	3–D schematic diagram of twin roll caster	29
Figure 3.2	Twin Drum Caster (photograph)	31
Figure 3.3	Pilot plant apparatus of twin drum caster	33
Figure 3.4	Relation between casting speed and strip thickness	34
Figure 3.5	Transverse cross section around a longitudinal crack	36
Figure 3.6	Deviations in columnar zone thickness	37
Figure 4.1	Grid formation in the physical plane	48
Figure 4.2	Grid formation in the transformed plane	49
Figure 4.3	Schematic of columnar dendritic structure	56
Figure 4.4	Porosity function for momentum equation	59
Figure 4.5	Schematic of position	60
Figure 4.6	Relation between contact angle and liquid film thickness	63
Figure 4.7	Grid representation in the physical plane	65
Figure 4.8	Grid representation in the transformed plane	65
Figure 5.1	Grid structure on the physical domain	72
Figure 5.2	Non–dimensional velocity profile in the closed domain surrounded by walls	76
Figure 5.3	Relation between velocity and normal distance from roll (I)	77
Figure 5.4	Relation between velocity and normal distance from roll (II)	78
Figure 5.5	Non–dimensional velocity profile with free surface and symmetric axis	79
Figure 5.6	Non–dimensional velocity profile using turbulence model	80
Figure 5.7	Relation between velocity and distance normal from roll (III)	81

Figure 5.8	Relation between velocity and distance normal from roll (1V)	82
Figure 5.9	Profile of non-dimensional turbulent kinetic energy	83
Figure 5.10	Profile of non-dimensional turbulent energy dissipation	84
Figure 5.11	Non-dimensional velocity profile in the inlet-outlet system	86
Figure 5.12	Profile of turbulent kinetic energy in inlet-outlet system	87
Figure 5.13	Profile of rate of dissipation in inlet-outlet system	88
Figure 5.14	Non-dimensional velocity profile, $Re = 10^5$, $v_{in} = 0.5$	92
Figure 5.15	Non-dimensional velocity profile, $Re = 10^3$, $v_{in} = 0.5$	93
Figure 5.16	Temperature profile, θ_{in} 1.0, $\theta_{roll} = 0.0$	93
Figure 5.17	Computed without turbulent heat transfer	94
Figure 5.18	Local Nusselt number ($Re = 10^5$, $Ra = 10^8$, $Pr = 0.158$)	95
Figure 5.19	Non-dimensional velocity profile for two kinds of characteristic length	97
Figure 5.20	Isotherms for two kinds of characteristic length	98
Figure 5.21	Grid formation for the water model	101
Figure 5.22	Visualisation of flow by dye injection	102
Figure 5.23	Velocity profile of the water model	103
Figure 5.24	Concentration profile of dye (0.1 – 0.3 sec)	104
Figure 5.25	Concentration profile of dye (0.5 – 0.7 sec)	105
Figure 5.26	Comparison between computational and experimental results	106
Figure 6.1	Fluid flow and temperature profile ($C'' = 0$, $T_r = 150°C$)	115
Figure 6.2	Fluid flow and temperature profile ($C'' = 0.01$, $T_r = 150°C$)	115
Figure 6.3	Fluid flow and temperature profile ($C'' = 0.1$, $T_r = 150°C$)	116
Figure 6.4	Fluid flow and temperature profile ($C'' = 0.5$, $T_r = 150°C$)	116
Figure 6.5	Fluid flow and temperature profile ($C'' = 2.0$, $T_r = 150°C$)	117
Figure 6.6	Fluid flow and temperature profile ($C'' = 0$, $h_i = 4500/t^{0.547} W/m^2K$)	117
Figure 6.7	Fluid flow and temperature profile ($C'' = 0.01$, $h_i = 4500/t^{0.547} W/m^2K$)	118
Figure 6.8	Fluid flow and temperature profile ($C'' = 0.1$, $h_i = 4500/t^{0.547} W/m^2K$)	118
Figure 6.9	Fluid flow and temperature profile ($C'' = 0.5$, $h_i = 4500/t^{0.547} W/m^2K$)	119
Figure 6.10	Fluid flow and temperature profile ($C'' = 2.$, $h_i = 4500/t^{0.547} W/m^2K$)	119
Figure 6.11	Comparison of temperature profile	123

Figure 6.12	Comparison of temperature profile	124
Figure 6.13	Temperature at the centre line of mould	125
Figure 6.14	Relation between contact time and shell thickness	126
Figure 6.15	Comparison of temperature profiles for the effects of various turbulent Prandtl numbers ($C'' = 0.5$, $h_i = 4500/t^{0.547}$ W/m^2K)	129
Figure 6.16	Predicted temperatures at the centre line of the mould illustrating the effects of the turbulent Prandtl number ($C'' = 0.5$, $h_i = 4500/t^{0.547}$ W/m^2K)	130
Figure 6.17	Relationship between predicted contact time and shell thickness, as affected by turbulent Prandtl number ($C'' = 0.5$, $h_i = 4500/t^{0.547}$ W/m^2K)	131
Figure 6.18	Relation between predicted shell thickness and turbulent Prandtl number ($C'' = 0.5$, $h_i = 4500/t^{0.547}$ W/m^2K)	132
Figure 6.19	Comparison of predicted temperature profiles for various superheat	134
Figure 6.20	Temperature of centre line of mould illustrating effects of superheat ($C'' = 0.5$, $h_i = 4500/t^{0.547}$ W/m^2K, $Pr_t = 3.0$)	135
Figure 6.17	Relation between contact time and shell thickness for various superheats ($C'' = 0.5$, $h_i = 4500/t^{0.547}$ W/m^2K, $Pr_t = 3.0$)	136
Figure 7.1	Grid structure	145
Figure 7.2	Comparison of velocity profiles for various grid densities ($Re = 4.8 \times 10^5$, $Pr = 0.158$, $Ra = 3.3 \times 10^7$)	146
Figure 7.3	Comparison of turbulent energy profiles for the effects of grid density ($Re = 4.8 \times 10^5$, $Pr = 0.158$, $Ra = 3.3 \times 10^7$)	147
Figure 7.4	Comparison of temperature profiles for the effects of grid density ($Re = 4.8 \times 10^5$, $Pr = 0.158$, $Ra = 3.3 \times 10^7$)	148
Figure 7.5	Comparison of velocity profiles for various roll gaps (casting speed = 60 m/min, super–heat = 20 K)	149
Figure 7.6	Comparison of temperature profiles for various roll gaps (casting speed = 60 m/min, super–heat = 20 K)	150
Figure 7.7	Temperature profile of roll bite section for various roll gaps	151

Figure 7.8	Comparison of temperature profiles for various superheats (Dirichlet condition, casting speed = 60 m/min)	162
Figure 7.9	Comparison of temperature profiles for effect of super–heat (Neumann condition, casting speed = 60 m/min)	163
Figure 7.10	Temperature profile of the roll bite section for various superheats (Dirichlet condition)	164
Figure 7.11	Temperature profile of the roll bite section for effect of superheat (Neumann condition)	164
Figure 7.12	Comparison of velocity profiles for effect of casting speed (super–heat = 20 K, h_i =8000 W/m^2K)	165
Figure 7.13	Comparison of temperature profiles for effect of casting speed (super–heat = 20 K, h_i =8000 W/m^2K)	166
Figure 7.14	Relation between casting speed and shell thickness (super–heat = 20 K, h_i =8000 W/m^2K)	167
Figure 7.15	Comparison of velocity profiles for effect of inside thickness of submerged nozzle (casting speed = 60 m/min, super–heat = 20 K, h_i =8000 W/m^2K)	168
Figure 7.16	Comparison of temperature profiles for effect of inside thickness of submerged nozzle (casting speed = 60 m/min, super–heat = 20 K, h_i =8000 W/m^2K)	169
Figure 7.17	Comparison of velocity profiles for effect of depth of submerged nozzle (casting speed = 60 m/min, super–heat = 20 K, h_i =8000 W/m^2K)	170
Figure 7.18	Horizontal velocity profile of meniscus surface (casting speed = 60 m/min, super–heat = 20 K, h_i =8000 W/m^2K)	171
Figure 7.19	Comparison of temperature profiles for effect of depth of submerged nozzle (casting speed = 60 m/min, super–heat = 20 K, h_i =8000 W/m^2K)	172
Figure 7.20	Fluid flow and temperature profile (outside thickness = 174 $\rightarrow$ 221 mm, inside thickness = 15 mm, nozzle depth = 43 mm)	173

Figure 7.21	Fluid flow and temperature profile (outside thickness = 134 → 221 mm, inside thickness = 15 mm, nozzle depth = 101 mm)	173
Figure 7.22	Fluid flow and temperature profile (outside thickness = 134 → 221 mm, inside thickness = 80 mm, nozzle depth = 101 mm)	174
Figure 7.23	Fluid flow and temperature profile (outside thickness = 52 → 74 mm, inside thickness = 10 mm, nozzle depth = 63 mm)	174
Figure 7.24	Fluid flow and temperature profile (outside thickness = 174 → 221 mm, inside thickness = 19 mm, nozzle depth = 63 mm)	175
Figure 7.25	Temperature profile of roll bite section for effect of inlet system	176
Figure 7.26	Fluid flow and temperature profile at a low pool mould (outside thickness = 32 → 43 mm, inside thickness = 7 mm, nozzle depth = 49 mm)	175
Figure 7.27	Comparison of temperature profiles for various cooling rates (casting speed = 60 m/min, super-heat = 20 K)	177
Figure 7.28	Temperature profile of the roll bite section versus distance from the strip surface illustrating the effect of cooling rate	178

LIST OF TABLES

		page
Table 1	Semi-industrial twin roll casters in the world (steel)	8
Table 2	Heat transfer coefficients for twin roll casters	11
Table 3	Specifications of the twin drum caster	34
Table 4	Specifications of the water model	99
Table 5	Input data for computations (Sn-Pb)	109
Table 6	Conditions of calculations	120
Table 7	Input data for computations (stainless-steel)	140
Table 8	Comparison of temperature and CPU at three kinds of grid densities	143
Table 9	Number of iterations and CPU at three kinds of roll gaps	144
Table 10	Characteristics of the twin roll caster I	160
Table 11	Characteristics of the twin roll caster II	161

Chapter 1

INTRODUCTION

1.1 History of twin roll caster

Technical developments for shortening the production process for steel have continued for more than 100 years, chiefly, in order to reduce the production energy. It was done mainly by integrating functions and eliminating certain steps. One of the best examples is the shift from the ingot casting system to the continuous casting system, which integrated the casting and slabbing steps while eliminating ingot-making and roughing.

During the past two decades, the next trend in continuous casting, Near Net Shape Casting (NNSC), has been initiated in the U.S.A., Europe, Australia, and Japan. NNSC is a casting system which produces thin-slab or strip requiring less reduction of product thickness at the next step. The purposes of this process, therefore, is the reduction of rolling operations and capital costs, which result from partial or total elimination of the hot rolling process and from smaller caster. In addition, the rapid solidification associated with this method can improve the properties of plate products (Yoshida et al.,1986). Figures 1.1 and 1.2 show a process flow sheet for steel from raw material to cold rolled strip and a simplified clarification of casting systems by product thickness, respectively.

NNSC has attracted the steel industry's attention, and many researchers have been putting significant effort into its development. Worldwide activities in the development of NNSC in the steel industry have been reported, for instance, at International Conferences on Near Net Shape Casting (Y.Sahai et al. ed., 1988 and three Iron and Steel Society conferences (1990 - 1992)).

The twin roll casting system is one of the typical NNSC processes, particularly for strip or thin-strip casting. Twin roll casting systems are classified according to two types of

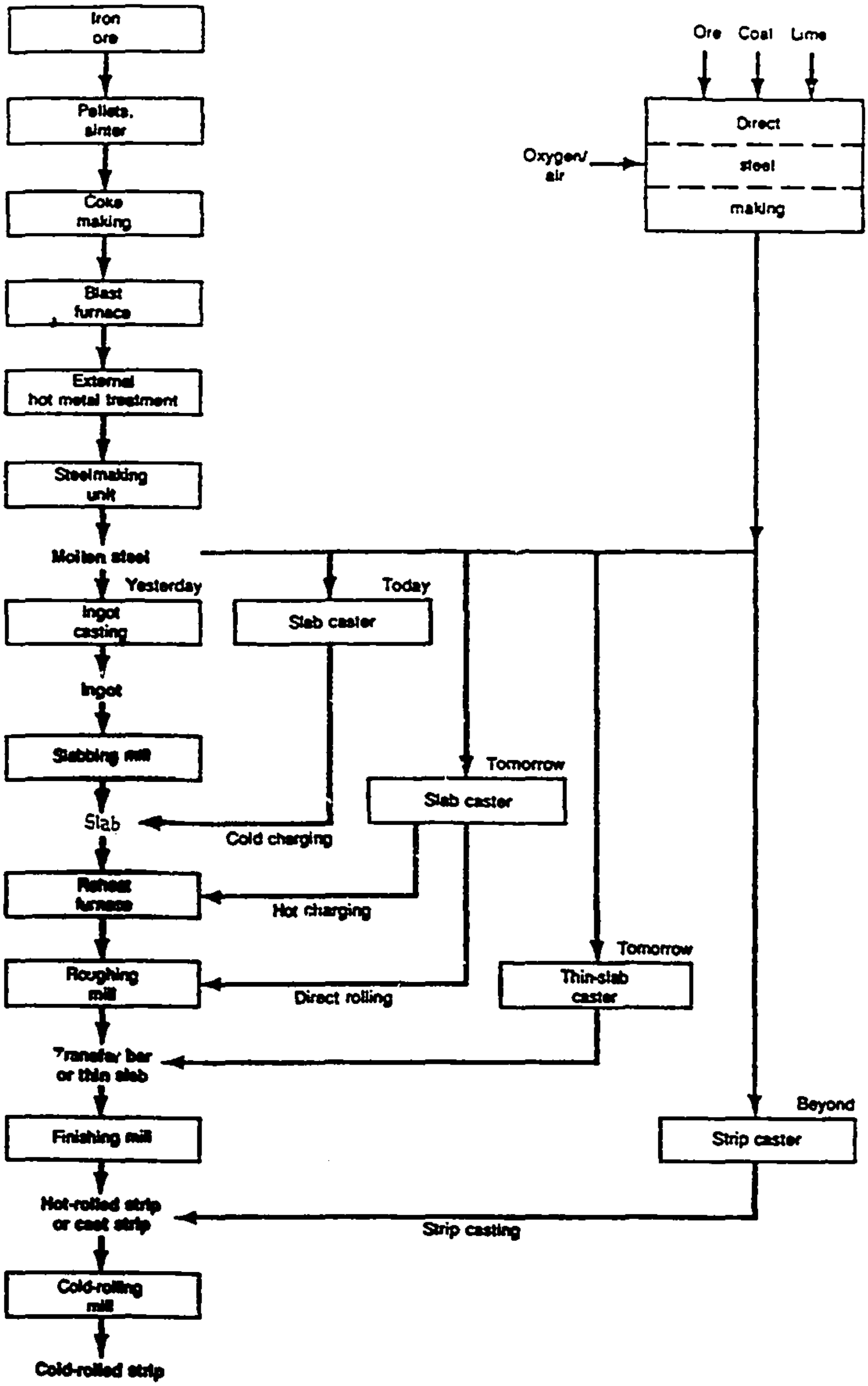

Figure 1.1 Past, present, and future steel processing steps

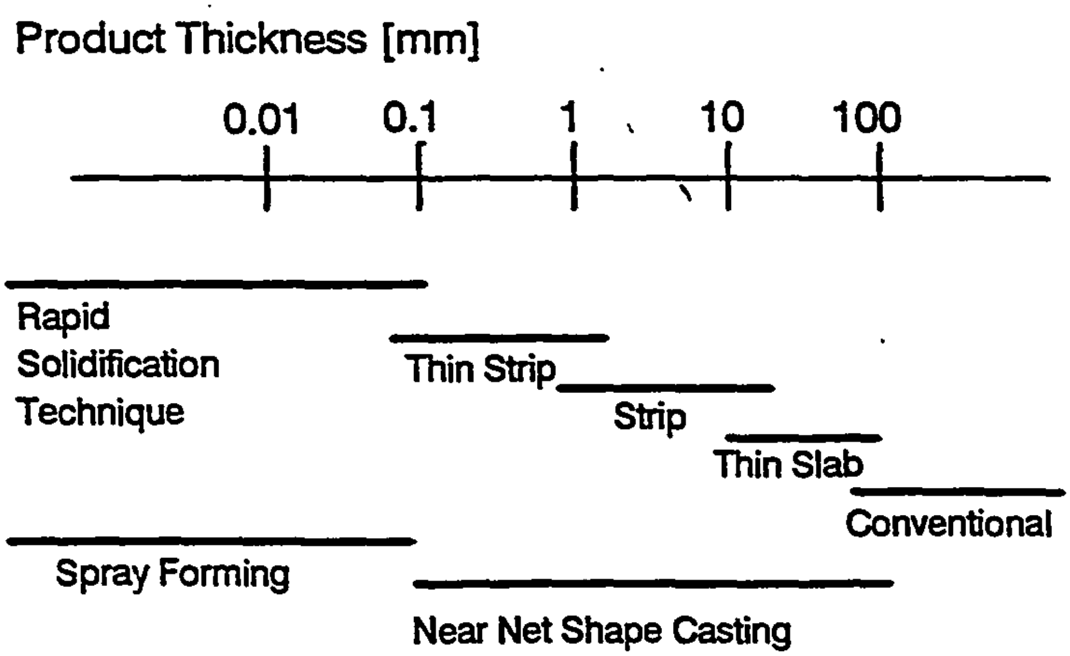

Figure 1.2 Classification of casting

combination of rolls, namely (a) equal diameter twin roll and (b) unequal diameter twin roll, or according to three pouring methods, (a) vertical (top or bottom) feeding, (b) inclined feeding (R.Kusakawa, 1985) and (c) pool feeding (N.Toyama et al, 1986). The concept of the twin roll casting was introduced in 1857 by Sir Henry Bessemer (H.Bessemer 1891) and is shown in Figure 1.3. As seen from the figure, Bessemer's original machine is a top feeding machine with equal diameter twin rolls, and this has been the dream of steelmaking engineers. Several researchers have found difficulty with his approach because the optimum product quality can be only achieved within a narrow range of specific conditions of thermo-mechanical casting parameters.

Today, intensive research effort is being undertaken around the world to develop an optimum design of equipment and operational conditions. The most popular experimental approach is to use a small hot model experiment ranging from 0.1 to 50 ton scale. Table 1 shows worldwide activities in the development of twin roll casting system for steel. Very few techniques developed to date, however, have been completely successful in full scale steel factory because of difficulties in maintaining the productivity and good quality of products.

Nippon Steel Corporation and Mitsubishi Heavy Industries Ltd. have been jointly developing the twin drum casting process since 1985 (Kasama et al, 1990). They have succeeded in operating a 10-ton scale, 800 mm wide casting for austenitic stainless steels of 18-8 base at Hikari Works, Nippon Steel Corp., November 1989. They have been continuing to study the economic feasibility of developing the process for industrialization, the stability of product quality and means for better cost performance.

1.2 Objectives

The twin roll casting process involves quite complicated control problems because of its poor stability with respect to heat and mass flow within the mould and the difficulty of controlling the kissing (nips) point of solidified shells on the rolls. If solidification, for example, is completed before the liquid reaches the minimum clearance point between the rolls, then deformation of the solid will occur if operating with fixed-gap. Therefore it is necessary in

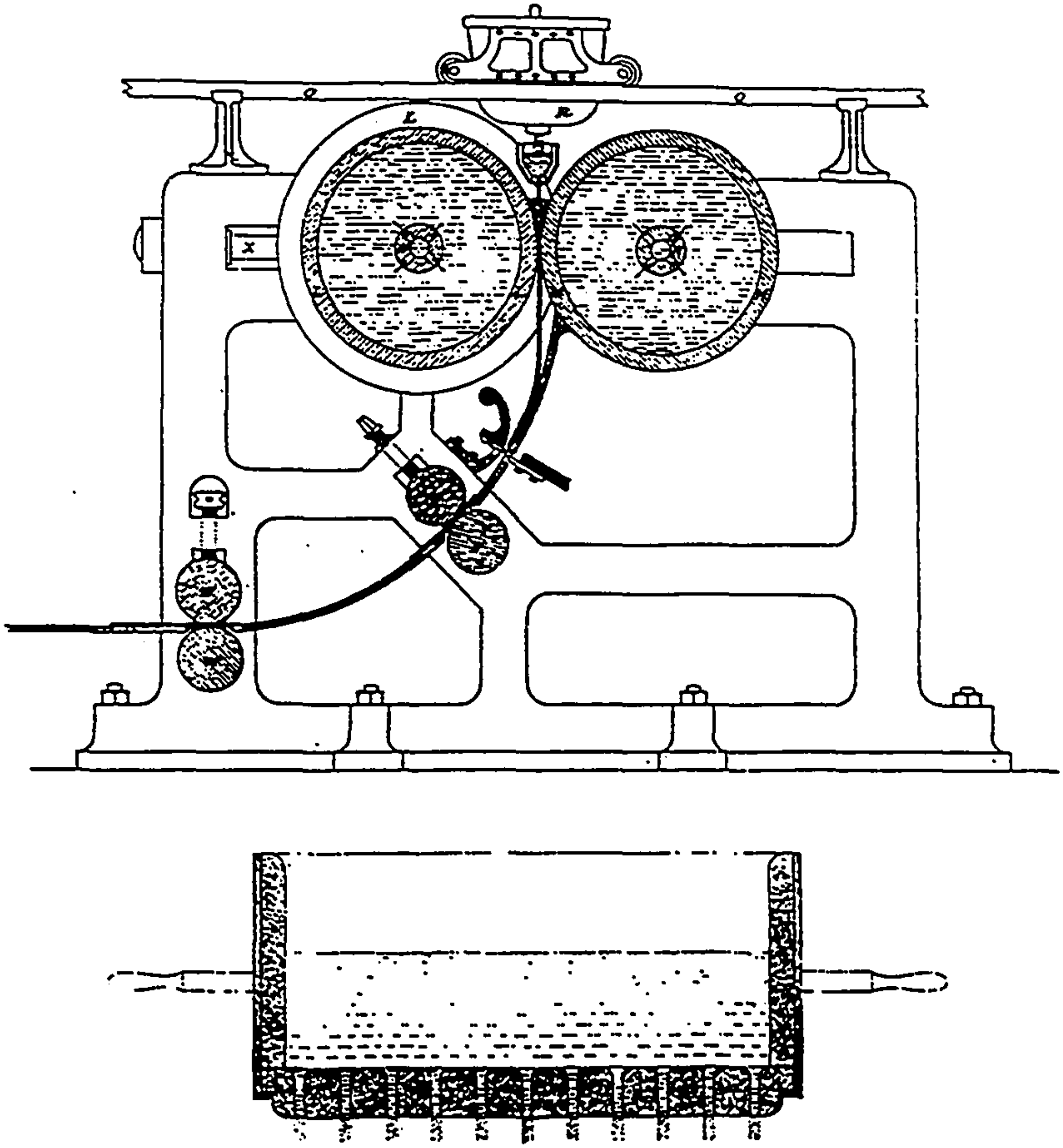

Figure 1.3 Bessemer's twin roll caster (1891)

designing optimum twin roll casting systems to develop efficient mathematical tools to elucidate the complicated flow and heat transfer mechanisms at work.

The aim of this research has been to develop a mathematical model and to simulate a vertical twin roll casting process. Such a model can provide a basic understanding of the interactions among mould design, metal properties, and operational variables. Obviously, such an understanding would be of great value for process optimization and to obtain desirable product qualities after due consideration of economic factors.

The specific objectives of the present research work are summarized as follows :

1. Development and verification of two-dimensional turbulent fluid flow and heat transfer model in an arbitrary shaped domain using a body fitted coordinate system.
2. Verification of the turbulent fluid flow model with water model experiments available for a twin roll caster.
3. Development of a computer code which models turbulent fluid flow and mushy region solidification heat transfer in vertical twin roll casting systems.
4. Verification of the solidification model with mathematical modelling or experimental solidification results for a twin roll caster.
5 Numerical investigation of the relationship of the molten metal pool and solidified shell thickness with operational parameters, specifically the feeding system and thin strip production rate, for a vertical twin roll caster.

1.3 Outline of Thesis

Chapter 2 reviews prior works which have appeared in the literature concerning twin roll casting systems including both mathematical and experimental studies. It also reviews previous work concerning mathematical treatments for arbitrary geometry, turbulence and solidification.

Chapter 3 describes a vertical twin roll caster, in particular, a semi-industrial scale twin drum caster presently in operation at Nippon Steel Corporation, Japan. It explains the important factors and engineering problems of the machine, and also presents a mathematical approach to tackle fluid flow and heat transfer in the wedge-shaped mould.

Chapter 4 formulates the two-dimensional vertical twin roll casting problem. It presents general governing turbulent transport equations and the solidification model. In addition, the body fitted coordinate technique, mathematical formulations and computational schemes are described in detail. A numerical procedure for solving the problem is developed here.

Chapter 5 presents numerical results in a wedge-shaped pool with a moving boundary. This chapter discusses the influence of inlet flow, turbulence and buoyancy force, and also validates the fluid flow model after comparing with experimental results of the water model of Nippon Steel Corp. (Suichi et al. ,1989).

Chapter 6 presents two-dimensional steady state results for flow, energy and solidification in a twin roll caster. This chapter investigates empirical parameters and operational factors and validates the modelling after comparing with Hojo's experimental results of the Sn-Pb alloy system (Hojo et al., 1987).

In Chapter 7, the important effects of various parameters of stainless steel are discussed, and for design of a twin roll casting system is suggested. This chapter also suggests suitable operational conditions for the twin roll casting processes.

Chapter 8 presents conclusions, contributions to knowledge, and recommendations for future work.

Table 1 Semi-industrial twin roll casters in the world

COUNTRY	COMPANY	THICKNESS	WIDTH	SCALE
Australia	BHP	1-3 mm	mm	10 t Model
Austria	Vöest-Alpine	0.5-8	250	Hot Model
Canada	Bessemer	5	200	230 kg Model
	IMRI	2	100	100 kg Model
China	Shanghi M.R.I	5		Hot Model
France	IRSID-CLECIM	1.5-5	800	0.3-8 t
Germany	Thyssen + IBM	5	150	100 kg Model
Italy	CSM	5-25	400-700	4-20 t + 300kg
Italy	Danielli			Hot Model
Korea(S)	POSCO + Davy	2.6	350	1 t Model
Japan	Hitachi	2.3	600	Prototype
Japan	Hitachi Zosen	6-7	60	350 kg Model
Japan	IHI	3	200	100 kg Model
Japan	Kobe Steel	3-40	75	150 kg Model
Japan	Kawasaki Steel	0.3-0.8	350	1500 kg Model
Japan	Nippon Yakin	2	300	300 kg Model
Japan	Nisshin Steel	0.8-2.3	300	120 kg Model
Japan	NKK	2-17	100	250 kg Model
Japan	NSC+Mitsubishi	1.6-5	800	10 t Model
Sweden	ASEA-R.School			20 kg Model
Switzerland	CONCAST	30-40	400	Hot Model
U.K.	British Steel C.	3	333	4 t + 250 kg
U.S.A.	BS/ARMCO/ INLAND	2		320 kg Model

LITERATURE SURVEY

2.1 Twin Roll Strip Casting

Sir Henry Bessemer obtained a patent (1865) for the first twin roll casting process that is shown in Figure (1.3). Bessemer produced thin sheet of 0.76 mm thickness and around 1m long using two 300 mm diameter chilled rolls with fixed gap. The major problem he had to overcome to make a thin strip was related to fluid flow distribution to the machine.

Since 1980, many researchers have began to investigate the twin roll casting system, mainly through experimental studies and simple mathematical heat transfer analyses. Many of these early investigators tried to obtain cooling rate data and correlations between solidified strip thickness and casting time or metal/mould contact time.

Kasama et al. (1986) tried to obtain a relation between the solidified shell thickness and solidification time in Pb–Sn alloy and 304 type stainless steel using a 100 kg scale twin roll caster. The specification was : 300 mm diameter rolls, 200 mm width, up to 30 m/min casting speed, less than 1 mm strip thickness. They reported that the solidification of thin strips cannot be obtained simply by assuming that it is proportional to the square root of solidification time (t). They suggested equation (2.1) from their heat transfer analysis for estimating strip thickness and have found good agreement with their experimental results.

$$d_s = \frac{k_s}{h_T}\left(1 + \frac{2h_T(T_L - T_{roll})}{\rho_s \lambda a k_s}\right)^{\frac{1}{2}} \tag{2.1}$$

$$a = \frac{1}{2} + \left(\frac{1}{4} + \frac{C_{ps}(T_L - T_{roll})}{3\lambda} \right)^{\frac{1}{2}} \tag{2.2}$$

They also measured the secondary dendrite arm spacing and estimated the average cooling rates and heat transfer coefficients (Kasama et al., 1987). Later Miyazawa et al. (1988) simplified the correlation between strip thickness and contact time with following simple functional relationship,

$$d_s \propto t^{0.56} \tag{2.3}$$

Kawakami et al. (1987) carried out a 250kg scale experimental study in carbon steel and 304 type stainless steel system and reported specific values for the apparent solidification coefficient. They also visualized fluid flow within the mould region using liquid paraffin.

Bethlehem Steel Corporation has undertaken a vertical twin roll casting process with Armco Inc., Weirton Steel and Inland Steel since late 1980's, and proposed the relation between heat transfer coefficient,h_T, the strip thickness,d_s, and contact time t. Equations (2.4) and (2.5), shown below, were obtained from an approximate analytical model on data published for twin roll casters (Hlinka et al., 1988, Burgo et al., 1990).

$$d_s = 0.146t^{0.628} \quad (\,0.01 < t\ [s] < 22\,) \qquad [inches] \tag{2.4}$$

$$h_s = \frac{352}{d_s^{0.547}} \qquad [Btu \bullet hr^{-1} ft^{-2} F^{-1}] \tag{2.5}$$

They are so derived an equation (eq.(2.6)) for an instantaneous interfacial heat transfer coefficient, h_{Ti}, and recommended its use for simple mathematical models.

$$h_{Ti} = \frac{109}{y_i^{0.547}} \qquad [Btu \bullet hr^{-1} ft^{-2} F^{-1}] \tag{2.6}$$

Nippon Steel Corp. has undertaken a 1 ton scale vertical twin roll casting program in 304 type stainless steel and correlated the solidification time, t (s), and strip thickness, d, based on their own physical model data (Figure 2.1). They reported the following relationship between the

the strip thickness and solidification time (Kasama et al., 1990).

$$d_s = 4.35t^{0.73} + 0.27 \qquad [mm] \qquad (2.7)$$

Table 2 summarizes approximate heat transfer coefficients for twin roll casters which various researchers have reported after fitting data to their mathematical models. Although the values have a wide range variation due to differences of machines, ways for measurement, and models, they are generally an order of magnitude larger than heat transfer coefficients for conventional casters.

Table 2 Heat Transfer Coefficients for Twin Roll Casters

reference & material	heat transfer coefficient	machine & thickness
Kasama et al. 1987 (SUS304)	12500 W/m^2K	NSC 100kg 0.5-2mm
Suichi et al. 1989 (SUS304)	7000+350/(t+0.03) W/m^2K	NSC 1600kg 0.5-5mm
Shinde et al. 1992 (SUS304)	6270 W/m^2K	NKK high-head
	25000 W/m^2K	NKK Low-head
	8360 W/m^2K	Sumitomo M.
Yamane et al. 1992	16700 W/m^2K	KSC Ni15Cr7Fe 0.5-0.7mm
	24300 W/m^2K	KSC SUS304 0.3-0.5mm
Hlinka et al. 1988 (Carbon-Steel)	13484 W/m^2K	BSCO 0.5-2mm
Takuda et al. 1990 (SUS304)	6700 W/m^2K	Kyoto Univ. 3 mm
Miyazawa & Szekely 1981 (Aluminium)	41800 W/m^2K	MIT 0.1 mm

Bagshaw et al.1988 (Al–1%Cu alloy)	34000 W/m^2K	Oxford Univ. 6.35 mm
Masounave et al. 1988 (Al–Cu, steel)	8500–10000 W/m^2K	IMRI 0.5–2 mm
Sanai & Inoue 1989 (40Pb40Bi12Sn8Cd)	7524 W/m^2K	Kyoto Univ. 3 mm

The heat transfer and solidification processes that take place in a twin roll are largely affected by the velocity field that develops in the molten pool. Kasama et al.(1990) mentioned that surface ripples on the meniscus are directly related and determined by the surface quality of strips. They recommended that a coupled fluid flow and heat transfer analysis is very important for realistic modelling of a twin–roll caster.

Wang and Saucedo (1990) investigated flow patterns in the twin roll caster using a full–scale water model (305 mm roll diameter, 333 mm width) and reported on the effect of the feeding system on macroscopic flow near the `kissing point' or roll nip and on air entrainment. Through flow visualization, they suggested that a submerged pour box nozzle with a baffle plate and an internal overflow generated uniform flow speed distribution without air entrainment nor strong turbulence.

Tanaka et al. (1991) investigated relation among longitudinal cracks, columnar zone thickness, and surface waves in the mould. From their 0.6 scale (720 mm diameter roll) water model) they have seen that the wave magnitude on the meniscus could be reduced by increasing the depth of the nozzle outlet position.

Although a multitude of publications on conventional continuous casting operations and many experimental studies for the twin roll casting process have been published to date, very little attempt has been made so far to actually model twin–roll casting operations.

Kraus (1986) developed a very simple one–dimensional transient conduction heat transfer model for an inclined twin–roll CC process feeding two clad sheet. He used a finite–element method to solve the modelled equations and investigated a modelling parameter sensitivity in carbon steel system.

Masounave et al. (1988) reported on a two–dimensional heat conduction model for a

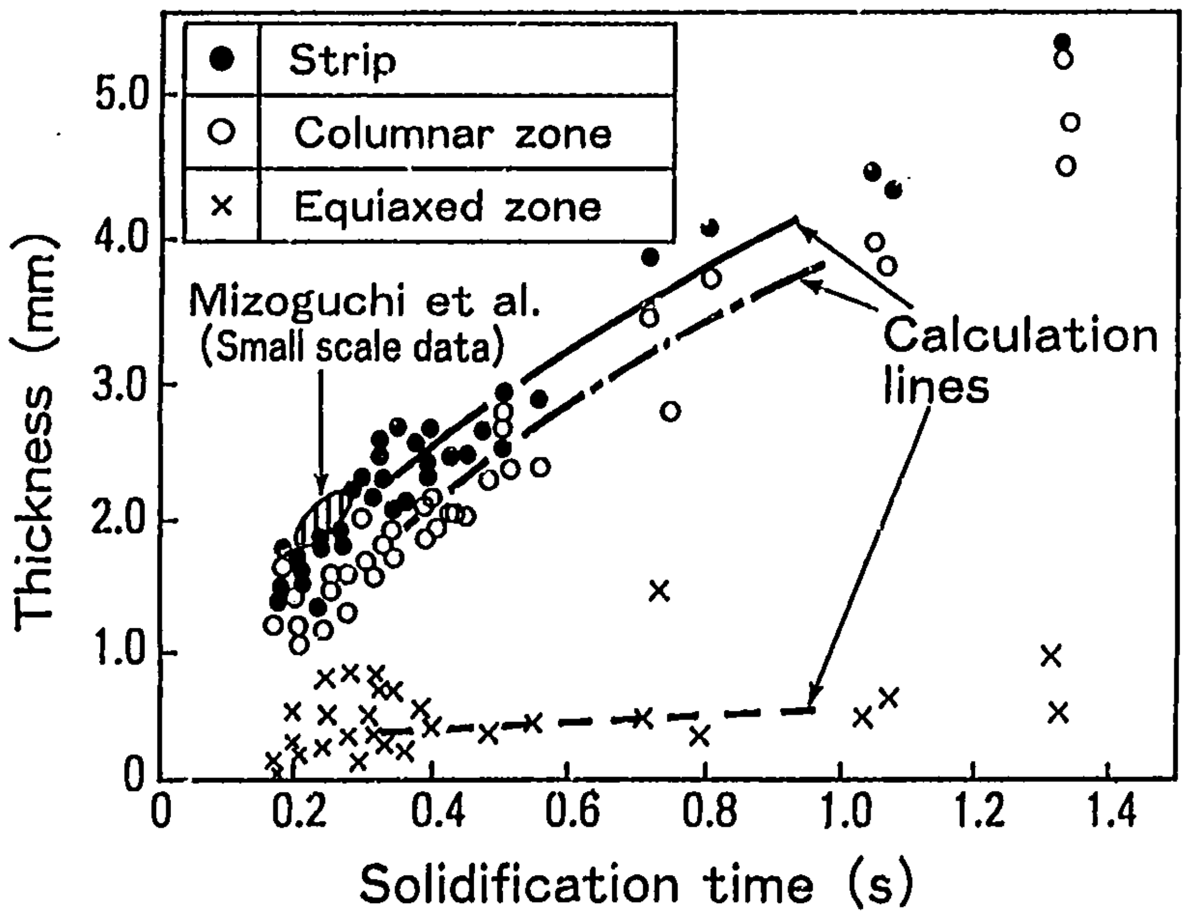

Figure 2.1 Relation between solidification time and thickness of strip, columnar or equiaxed zone

roll CC process. They adopted the equivalent heat capacity method to model solidification and, by assuming a linear relationship between temperature and the solid phase present, they calculated the solid fraction.

Bagshaw et al. (1986) developed a steady state two dimensional heat conduction model using a control volume based finite difference method. They also carried out experimental studies in an Al-Cu alloy system, using a horizontal twin roll caster, and determined heat transfer coefficients by fitting predicted strip exit temperature to experimental measurements. Later, they reported the effect of strip thickness and of roll material to strip temperature using their mathematical model (Bagshaw et al., 1991).

Miyazawa and Szekely (1981) appear to be the first to report fluid flow and heat transfer for the twin-roll CC process. These authors reported the two-dimensional, uncoupled fluid flow and heat transfer results for a pure aluminium system, after making a number of simplifying assumptions: velocity field in the liquid region were determined using total mass balance and the continuity of the liquid. Although their uncoupled analysis of the transport equations are not realistic, they discovered, nonetheless, that there exists a narrow range of casting parameters (i.e. the roll spacing, the angular velocity of the rolls, the feed rate of the material, and the physical properties of the material) that gives a stable mode of operation. Miyazawa et al. (1986, 1988) applied the model to stainless steel system and investigated the dependence of strip thickness on casting speed.

Recently, Saitoh et al.(1989) have reported a two-dimensional, uncoupled fluid flow and heat transfer model for a twin-roll CC process. Their simplified model equations are similar to those of Miyazawa and Szekely (1981). The moving phase-change boundary was handled using a boundary fixing method and the transformed equations for solid and liquid regions were solved separately by the usual explicit finite difference scheme. They have also carried out experiments in a laboratory scale twin-roll caster and compared their numerical results with those from experiments (Hojo et al., 1987). In their final comment, these authors have suggested that a thorough two-dimensional analysis, including full heat transfer and coupled fluid flow equations, will be required to obtain a more realistic picture of the twin-roll process.

Takuda et al. (1990) proposed another simple two dimensional, uncoupled fluid flow and heat transfer model. In their model, the velocity field in the mould is calculated by simple equations first and the stream lines are used for solving an energy equation as coordinate lines. Their model can not take account of the dependency of the energy field upon the velocity field.

From the above literature review, it appears that the mathematical modelling of a twin-roll CC process is in its infancy and is far from complete. So far, mere preliminary studies have appeared in the literature.

2.2 Turbulent Model

In turbulent flow, motions of fluid are irregular, time-dependent and accompanied by fluctuations in velocity. In order to understand the complex flow, it is necessary to solve the momentum equations and the continuity equation simultaneously. The solutions can only be obtained by using a numerical procedure because of the nonlinear character of the equations set.

A wide variety of approaches for simulating turbulent flows have been developed over the past two decades. In the most fundamental approach, full or direct turbulent simulation (FTS or DNS), the Navier-Stokes equations are solved directly. The important details of turbulence are, however, very small scale in character and solving the equation directly without a turbulence model requires very fine grids; for example certain flows whose Reynolds number is 10^4 needs 10^9 grids to solve. Such calculations are very difficult and expensive to carry out, because even using today's powerful supercomputer, hundreds of hours of computations are required.

Deardorff (1970) developed the large eddy simulation (LES) model which solves filtered Navier-Stokes equations and yields the large scale components of the fluid motion. Although LES is a very strong tool for investigating turbulence in detail at a relatively low cost (vis-a-vis FTS), unfortunately, it also requires a supercomputer (e.g. Moin & Kim, 1982).

For practical reasons, cost and desired accuracy, Reynolds-averaged Navier-Stokes (RANS) calculations are the most popular turbulence models today. RANS is chiefly based on the concept of the Reynolds stresses arising from cross-correlations of fluctuating components of velocities($-\rho u'v'$). Using the Reynolds stress term, turbulent shear stress is written as follows, of velocities($-\rho\overline{u'v'}$). Using the Reynolds stress term, turbulent shear stress is written as follows,

$$\tau = \rho\nu\frac{\partial\overline{u}}{\partial y} - \rho\overline{u'v'} \tag{2.8}$$

where the flow is assumed to be a shearing stress flow whose velocity gradient is in the y-direction.

Boussinesq (1877) suggested that the Reynolds stress could be replaced by the product of mean velocity gradient and a quantity termed the 'turbulent viscosity', through analogy with Newton's law of viscosity as follows,

$$-\rho\overline{u'v'} = \mu_t\frac{\partial\overline{u}}{\partial y} \tag{2.9}$$

Unlike the laminar viscosity (μ), the turbulent viscosity (μ_t) is not a property of the fluid, but is largely determined by the structure of turbulence at each point within the flow system. In order to estimate the turbulent viscosity, Prandtl (1925) proposed an algebraic relation through analogy with mean free path in molecular kinetic theory as follows, which has become known as the mixing-length hypothesis (or the momentum transfer theory).

$$\mu_t = \rho l_m^2\left|\frac{\partial\overline{u}}{\partial y}\right| \tag{2.10}$$

where l_m is mixing length and is determined by experiments usually.
Von Karman (1930) proposed the similarity hypothesis as follows,

$$l_m \propto \left|\frac{\partial\overline{u}/\partial y}{\partial^2\overline{u}/\partial y^2}\right| \tag{2.11}$$

However, the mixing-length model, often called a 'zero equation model', is not very popular, because the length scale is not determined solely by local properties of the mean flow but is influenced by properties at other locations in the vicinity.

To take into account the local character of turbulence, Kolmogorov (1942) has proposed the time-averaged turbulence kinetic energy, 'k', with the following definition,

$$k \equiv \frac{1}{2}\left(\overline{\Sigma u'^2 + \Sigma v'^2} \right) \tag{2.12}$$

where k is determined from the solution of a convective transport equation. Using the time-averaged turbulence kinetic energy, turbulent viscosity is represented as follows,

$$\mu_t = \rho k^{\frac{1}{2}} l \tag{2.13}$$

where 'l' is the length scale, which is prescribed algebraically in the 'one equation model', or is calculated from transport equations in the 'two equation model'.

The k-ϵ turbulence model, proposed by Jones and Launder (1972), has been one of the most popular models of turbulence because of its wide applicability and engineering accuracy. The 'ϵ' is the isotropic dissipation rate of turbulence energy defined by $k^{1.5}/l$. The scalar transport variables k and ϵ are determined from solutions of the convective transport equations, and the turbulent viscosity, μ_t, is given by

$$\mu_t = \frac{C_\mu f_\mu \rho k^2}{\epsilon} \tag{2.14}$$

where C_μ is a constant and f_μ is a damping function of the turbulent Reynolds number, which is equal to unity when the flow is fully turbulent. In the standard high Reynolds number k-ϵ model, f_μ is assumed unity in the whole region and experimentally-established boundary conditions are applied near the wall. In many turbulent flows, the turbulent properties near the wall are functions of only the normal-distance Reynolds number, y_+, and the direct effects of molecular viscosity far enough from the wall are not important. Commonly, the empirical wall functions used, are as follows :

$$\frac{u}{u^*} = \begin{cases} \frac{1}{K'}\ln(Ey^*) & (16 < y^* < 200) \\ y^* & (0 < y^* < 16) \end{cases} \tag{2.15}$$

Although numerous works using the high Reynolds number k-ϵ model have been reported, there is a strong debate as to the value of the model for complex flows (Launder, 1984) because the wall functions are based on experimental data for parallel flows in simple shear. Thus curved surfaces and recirculating flows are not applicable, though commonplace.

Jones and Launder (1972, 1974) proposed a low Reynolds number form of the k-ϵ model that does not require these wall functions. They have introduced viscous diffusion terms and additional terms into the k and ϵ equations to account for the non-isotropic dissipation processes. An exponential function of the local turbulent Reynolds number was used as the damping function f_μ. In this model, the boundary condition, $u = v = k = \epsilon = 0$ on the wall, can be adopted. They reported that the model provided good agreement with measurements and predictions in wall boundary flow, pipe flow, and channel flow systems. Following Jones and Launder, several investigators revised or developed other low Reynolds number k-ϵ models.

Launder and Sharma (1974) applied a low Reynolds number model, which is almost similar to the Jones & Launder model (1974) except for the damping function and coefficient C_μ, to model the flow generated by a rotating disc. In spite of the fact that the system contains very high gradients of swirl velocity in the vicinity of the disc (spin Reynolds number up to 4 x 10^5), predictions of velocities, heat and mass transfer were in close agreement with experimental data.

Lam and Bremhorst (1981) developed a new form of low Reynolds number k-ϵ model which does not include additional terms in the k and ϵ equations. In their model, the turbulent viscosity is a function of not only the local turbulent Reynolds number but also of the location. Although the model requires a certain values of ϵ on the wall boundary, the equations are relatively simpler than the Jones & Launder model. They validated their model for a fully developed turbulent pipe flow problem.

Chien (1982) proposed another form a low Reynolds number model where k and ϵ

equations have different additional terms. The model is based on an assumption that the 'logarithmic-law' near the wall is applicable even in the viscous sub-layer. He applied it to a fully turbulent channel flow and a turbulent boundary layer flow over a flat plate, and showed that the model gave better predictions than that of the Jones & Launder model.

Patel et al. (1984) tested several different versions of the k-ϵ turbulent model in a variety of boundary layers, namely, flat-plate, sink flow, strong pressure gradient, and equilibrium adverse pressure gradient, and concluded that the low Reynolds number models of Launder & Sharma (1974), Chien (1982), Lam & Bremhorst (1981), and Wilcox & Rubesin performed considerably better than the others in the simple case of a flat-plate boundary layer flow. In the equilibrium adverse pressure gradient boundary layer, the models by Chien and Lam & Bremhorst overestimated the skin-friction coefficient, whereas Launder & Sharma and Wilcox & Rubesin yielded satisfactory results. The models by Launder & Sharma, and Chien, achieved the best representation of experimental data in the favourable pressure gradient boundary layer system and in the sink flow system respectively.

Henkes and Hoogendoorn (1988) investigated the low Reynolds number k-ϵ models in the natural convection boundary layer problem and showed that Jones & Launder's, Lam & Bremhorst's and Chien's model gave the best results in predicting the velocity profiles.

A number of numerical works on turbulent flow and heat transfer have appeared in the metallurgical literature, in particular, concerning ladles (e.g. Mazumdar & Guthrie,1990), tundishes (e.g. Joo,1989) and conventional continuous casters (e.g. Thomas, 1990).

Dubke et al. (1988) investigated fluid flow in the electromagnetic stirring of continuous cast strands by using both numerical and experimental methods. In the model equations, the high Reynolds number k-ϵ model and the Lam-Bremhorst type low Reynolds number k-ϵ model were along used with the Maxwell equations. They calculated two-dimensional steady fluid flow at the transverse cross section and the third dimension was taken into account by depth-averaging. The model considered neither a mushy region nor heat transfer, and it was checked against experimental values obtained with mercury.

Thomas et al. (1990) studied two-dimensional turbulent fluid flow in a continuous casting system using FIDAP (a commercial CFD software from Fluid Dynamics Int., Evaston Illinois).

transfer model for a continuous casting system. The model equations were again solved using FIDAP. They investigated the effects of several important parameters after adopting fixed–shell thickness approach.

Farouk et al. (1991) presented a numerical model for the twin belt caster system using the Jones–Launder type low Reynolds number k–ε model along with the simple solidification model, where it was assumed arbitrarily that the molecular viscosity in the mushy region was twenty times of that in the liquid region. They investigated the temperature distribution in some alloy systems and the inclusion trajectory.

Summing up, the k–ε turbulent model, in particular, the low Reynolds number form, is recognized to be an efficient model and has become very popular recently. Very few researchers in the metallurgical field, however, have studied turbulent flow and heat transfer in an enclosure of arbitrary geometry such as the mould of a twin roll caster.

2.3 Body Fitted Coordinates

One of the most important steps required to achieve an accurate numerical solution of the transport equations involves the proper location of the nodal points in the flow region affected by the boundary, because in many differential systems, the boundary conditions have a dominant influence on the character of the solution. An appropriate approach to deal with geometric complexities is the generation of a curvilinear coordinate system with coordinate lines coincident with all boundaries. In this approach a computational domain of arbitrary shape is mapped onto a simple shaped domain in the transformed coordinate system.

The most popular methods for numerical grid generation by using differential system technique were introduced by Thompson et al. (1977). In the method, a system of elliptic equations are solved to generate the grid.

The general transformation from the physical plane (x,y) to the transformed plane (ξ,η) equations are solved to generate the grid.

The general transformation from the physical plane (x,y) to the transformed plane (ξ,η) is given by $\xi=\xi(x,y)$, $\eta=\eta(x,y)$.

Derivatives are transformed as follows;

$$\frac{\partial f}{\partial x} = \frac{1}{J}\left(\left(\frac{\partial y}{\partial \eta}\right)\left(\frac{\partial f}{\partial \xi}\right) - \left(\frac{\partial y}{\partial \xi}\right)\left(\frac{\partial f}{\partial \eta}\right) \right) = \frac{y_\eta f_\xi - y_\xi f_\eta}{J} \tag{2.16}$$

$$\frac{\partial f}{\partial y} = \frac{1}{J}\left(\left(\frac{\partial x}{\partial \xi}\right)\left(\frac{\partial f}{\partial \eta}\right) - \left(\frac{\partial x}{\partial \eta}\right)\left(\frac{\partial f}{\partial \xi}\right) \right) = \frac{x_\xi f_\eta - x_\eta f_\xi}{J} \tag{2.17}$$

where J is the Jacobian of the transformation;

$$J = \left(\frac{\partial x}{\partial \xi}\right)\left(\frac{\partial y}{\partial \eta}\right) - \left(\frac{\partial x}{\partial \eta}\right)\left(\frac{\partial y}{\partial \xi}\right) = x_\xi y_\eta - x_\eta y_\xi \tag{2.18}$$

The basic concept of the body fitted coordinate scheme is to generate transformation functions such that all boundaries coincide with coordinate lines. The coordinate lines, therefore, should be taken as solutions of an elliptic boundary value problem with one of these as constant on the boundaries. Figure 2.2 shows an example of the two-dimensional field transformation.

In body fitted coordinates, all governing equations and boundary conditions are transformed using the coordinate transformation and solved in the transformed domain.

Methods for the body fitted coordinate system for fluid flow problems can be roughly grouped into the following key features (Karki & Patankar, 1988) :

1. orthogonal or non-orthogonal grid system,
2. staggered or non-staggered grid arrangement,
3. co-variant physical or curvilinear velocity components as the dependent variables in the momentum equations.

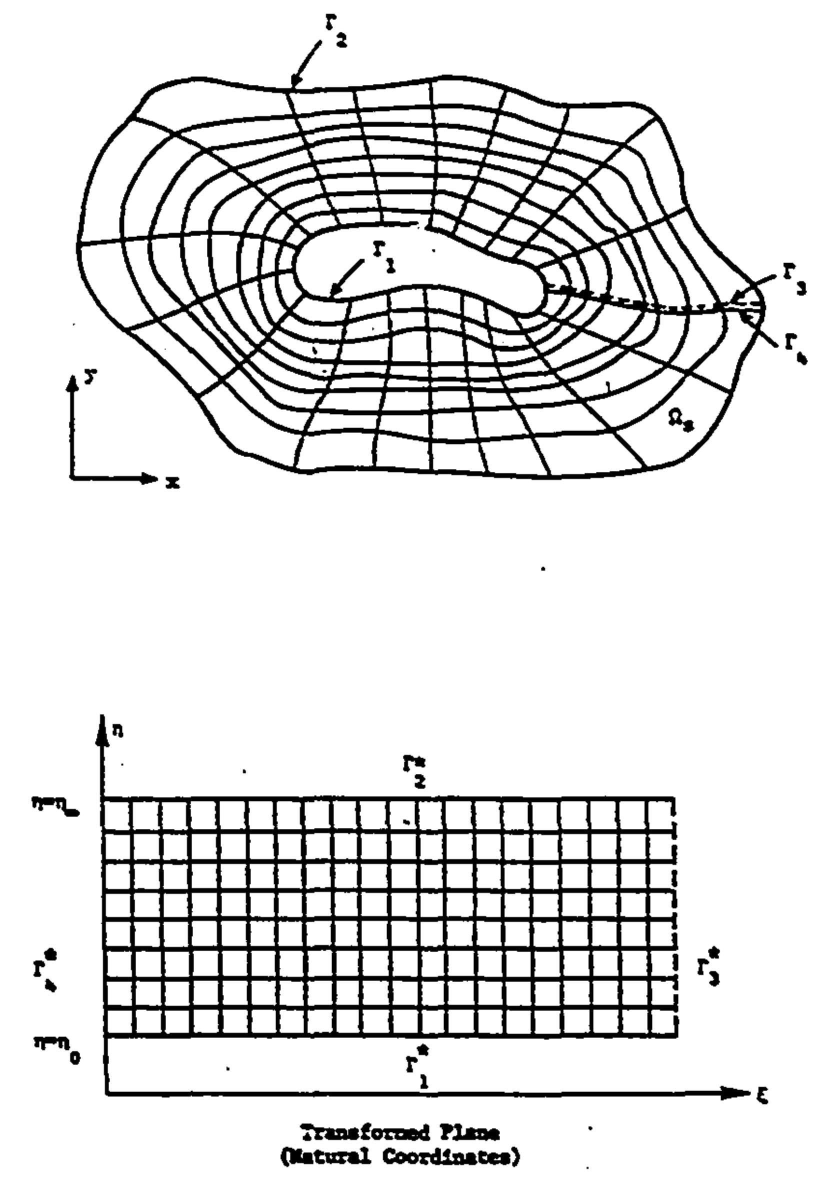

Figure 2.2 Physical and transformed planes (Thompson el al, 1974)

Barfield (1970) developed a mapping technique to generate orthogonal grids. He showed only a numerical scheme for interpolating lines between the orthogonal curvilinear mesh lines.

The method for orthogonal coordinate systems has been well developed, for instance Pope (1978) solved turbulent gas flow problems in a diffuser using the k-ϵ model. The attraction to use orthogonal coordinate systems lie in the fact that the equations of motion are considerably simpler than those for a non-orthogonal coordinate systems, and boundary conditions can be applied easily. Computational time might be also saved slightly. However, methods for the orthogonal coordinate system have limited applicability. In particular, it can not be strictly applied for the non-orthogonally intersecting boundaries.

Concerning a method for non-orthogonal coordinate systems, Thompson et al. (1985) describe the generation procedure for grid formation in detail. The method has become very popular recently, because of its wide applicability.

McWhorter and Sadd (1980) applied the non-orthogonal body-fitted coordinate to a two-dimensional steady state heat conduction problem of an eccentric circular annulus, as the first application of this method to problems of heat conduction.

It is very important for fluid flow problems to deal with velocity components properly. In a staggered arrangement, the locations of the velocity components are displaced from those of the scalars to avoid a wavy velocity field being acceptable to the continuity equation and checker board pressure field owing to make the pressure difference between two adjacent grid points become the natural driving force for the velocity component location between these grid points (Patankar, 1980). Unless a staggered grid arrangement is employed, a special technique is required to avoid the oscillations of the velocity and pressure field (Rhie & Chow, 1983).

As the dependent variables in the momentum equations, the covalent physical velocity components are more popularly employed than the curvilinear velocities. It is because the conservation equations in the curvilinear velocity formulation contain additional curvature source terms arising from the special variation of the velocity components. These source terms often cause difficulty in the numerical convergence of the model equations.

Shyy et al.(1985) applied a fully staggered grid system to solve two-dimensional steady hybrid, second-order upwind and QUICK, for discretizing the convection terms in the momentum equations.

Karki and Patankar (1988) solved two-dimensional steady state laminar flow problems in a tube with a constriction, and natural convection problems in concentric and eccentric annuli using non-orthogonal body-fitted coordinate with a staggered grid arrangement. They reported a good agreement with experimental data.

Hadjisuphocleous et al. (1988) applied non-orthogonal body-fitted cöordinates to a two-dimensional transient natural convection problem in a cooling cavity. They also adopted the staggered grid system and the physical covalent velocity components as the dependent variables in the momentum equations.

Although quite a few studies exist which have adopted body-fitted coordinate in analysing turbulence flow and associated heat transfer problems, to author's knowledge, no researcher has yet applied the body-fitted coordinate apprach to model turbulent flow in a metallurgical process that additionally incorporates coupled solidification.

2.4 Numerical Model For Solidification

Heat in the wedge-shaped pool is transferred both by convection and by molecular diffusion and eddy conduction. In addition, in the mushy zone, the latent heat is released.

In the thin solidified strip on the rolls, heat is transferred purely by conduction. Heat is removed through intense internal cooling of the fast moving rolls. During the phase change of molten steel, three distinct regions are present: a solid region, a totally liquid region, and a mushy region consisting of liquid dispersed among solid dendrites.

The majority of numerical studies to date on solidification consider only the conductive heat transfer mechanism, because the boundaries between the regions are determined by heat transfer. However, in the physical systems which involve partial or fully liquid phases, not only conduction effects but also convection effects, are important. In predominantly forced convection systems such as a strip caster, it is plausible that convective heat transfer dominates over transfer. However, in the physical systems which involve partial or fully liquid phases, not only conduction effects but also convection effects, are important. In predominantly forced convection systems such as a strip caster, it is plausible that convective heat transfer dominates over conduction.

An early numerical approach for dealing with convection-diffusion controlled isothermal phase changes is reported by Sparrow et al.(1977). They modelled natural convective melting of pure salt in a tube using deforming-transformed grids. They assumed a small time lag between the heat delivery to the interface and the resulting interface motion. Fluid flow and heat transfer in the liquid region were solved assuming that the interface is fixed during this small time interval. Numerical grid generation, accordingly, was revised at each time interval, requiring intensive computational effort for implementation.

Brent et al. (1988) presented a numerical solidification model based on the enthalpy-porosity technique which allowed a fix-grid solution in convection-diffusion problems. They investigated a melting problem of pure gallium in a cavity. In the enthalpy-porosity approach, the evolution of the latent heat is accounted for by defining a source term in the energy equation. The momentum equations included additional terms which dominate over the others in the solidifying control volume so as to force velocity values in solid regions to zero. The additional terms had no influence in liquid regions.

In pure materials, isothermal phase change occurs, and the numerical methodology for solidification is relatively simple. In many practical situations in metallurgy, however, materials are not pure but are alloys which have liquid-solid regions of co-existence (mushy region) which affect fluid and energy flows. In such cases, during the phase change, the evolution of latent heat has a functional relationship with temperature as opposed to the step change associated with an isothermal phase change. The total specific enthalpy of the material (the total heat content) can be expressed as

$$H = h + \Delta H, \quad h = \int_{T_{ref}}^{T} C_p dT + h_{ref} \tag{2.19}$$

$$\Delta H = f(T) \tag{2.20}$$

'H' is the sum of sensible heat h and the nodal latent heat ΔH, where the nodal latent heat is in the range $0 \leq \Delta H \leq \lambda$; λ is the latent heat of solidification.

Szekely and Jassal (1978) presented numerical and experimental works for ammonium chloride solidification in a two-dimensional slot. They employed D'Arcy Law source approach in the momentum equations and a linear correlation between the liquid fraction and permeability in the inter-dendritic region ; the permeability function was obtained from the analogy to Poiseuille's law for the flow of a viscous fluid through a circular capillary. They solved the momentum and energy equations at each region independently at each step, and obtained good agreement between the numerical results of temperature distribution and measurement.

Voller and Parkash (1987) applied the enthalpy-porosity method to mushy region phase change problems using PHOENICS (a commercial CFD software from CHAM). They solved the convection-diffusion problem in the liquid and mushy region, and the conduction problem in the solid region simultaneously using the D'Arcy law source approach. In the model, the mushy region is assumed to consist of only dendritic columnar, and inter-dendritic flow is treated as a flow in a porous media employing the Carman-Kozeny equation (Carman, 1937) for permeability. The relationship between the liquid mass fraction and temperature was taken to be linear. They carried out parametric studies for the solidus-liquidus temperature range in a two-dimensional transient natural convection solidification problem in a cavity using Dirichlet boundary conditions.

Shyy and Chen (1990) studied a similar natural convection problem with phase change in a cavity using an adaptive grid computational technique with a weighting function for velocity. For the solidification model, the same enthalpy-porosity technique employing the Carman-Kozney equation was used. Although they did not validate the model experimentally, they have reported on the important influence of Ra, Pr, and Stefan number on the energy field.

Very recently Shyy et al.(1992) presented advanced work where the adaptive grid technique was used on the solidification problem of a titanium ingot casting. They solved two-dimensional convection-diffusion problems in conjunction with the enthalpy-porosity technique, along with a modified k-ϵ turbulent model. They investigated some qualitative features of the ingot at two casting speeds (2×10^{-4} and 4×10^{-4} m/s) and two levels of gravity (normal g and 10^{-5}g). They mentioned that the k-ϵ model predicted a thicker mushy region compared to that predicted by a zero-equation turbulence model and proposed that the latter model seems to offer more consistent results as compared with experimental observations.

Given the above literature survey, it appears that the numerical modelling of phase changes in an alloy system is still in an evolutionary stage and that very few investigations have modelled solidification under the influence of very strong forced convection motions similar to those encountered in a twin roll strip caster.

TWIN DRUM CASTER

3.1 General Characteristics of Vertical Twin Roll Caster

Of the various strip continuous casting processes for directly casting steels that are equivalent to, or better than, conventional hot rolled strips, the twin roll casting is among the more developed systems (ref. Table 1).

A typical twin roll caster is characterized by a pair of internally cooled counter-rotating rolls fixed on parallel axes, with the cylindrical faces separated by a gap at the centre which is equal to the thickness of the strip to be cast. Liquid metal is supplied continuously and solidified on the water-cooled rolls. In the steel industry the top-feeding twin roll caster is the most popular system of the several designs available due to advantages of productivity and equivalent surface quality on both sides of the strip being produced. Figure 3.1 provides a schematic diagram of a vertical twin roll caster which is mathematically modelled in this study. It has equal diameter rolls and the top feeding system is from a delivery nozzle.

Although the twin roll casting system has attracted the attention of all materials processing industries, steel companies in particular have been developing it due to large potential profits that can be achieved through a reduction in processing costs. In the aluminium industry, the twin roll caster acts as a powerful rolling mill, as well as a solidifying machine, since solidification is completed well before the roll bite point. Unfortunately, in most of the steel industries, the 'kissing point' of solidified shells should be practically coincident with the roll bite point, because of the large rolling forces otherwise generated by premature solidification. This demands accurate design and control of the twin roll caster for steel industry applications.

The twin-roll casting process, as applied to steel, has some particularly significant

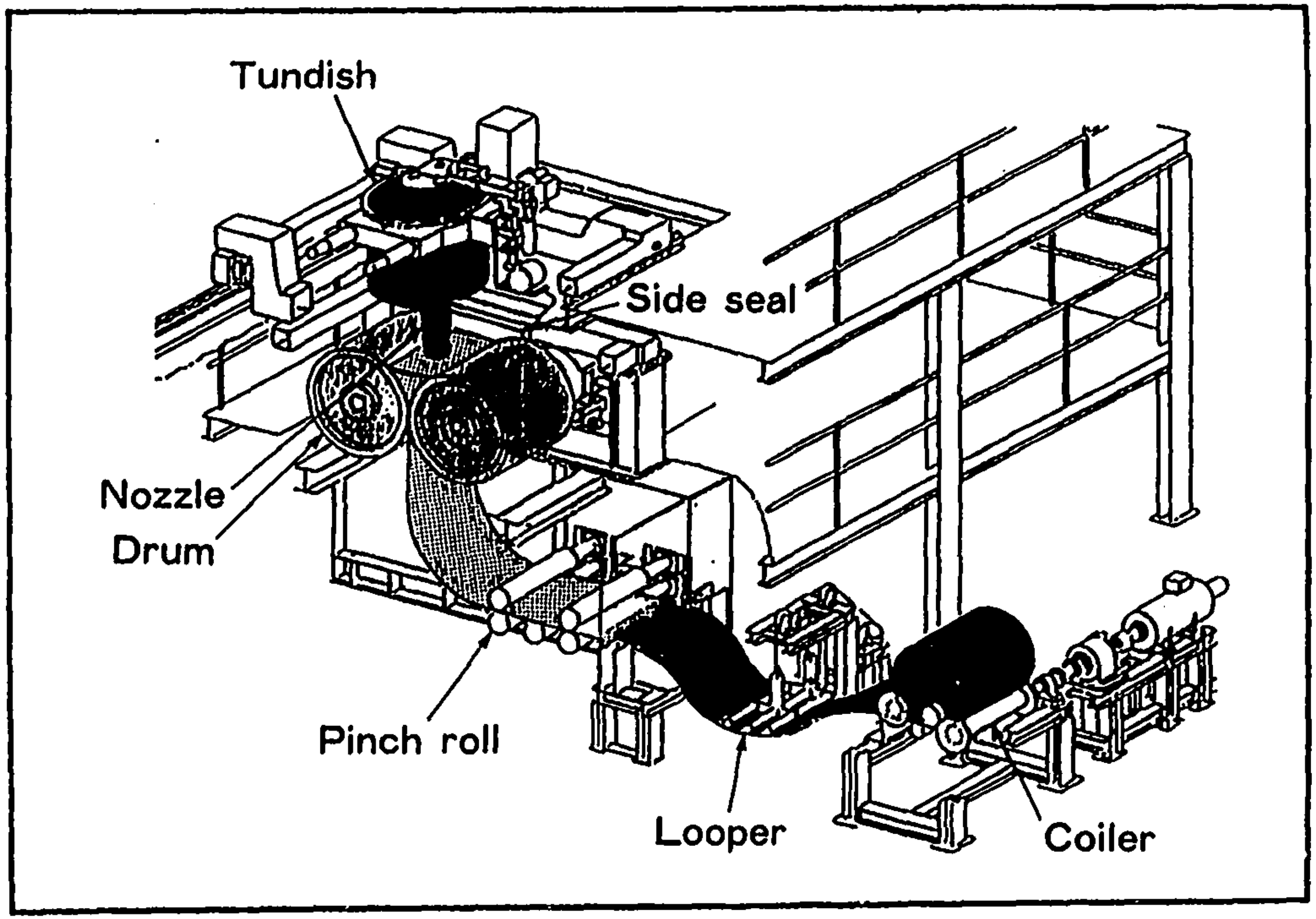

Figure 3.1 3-D schematic diagram of twin roll caster

characteristics. These are:

1. A solidification rate that is significantly higher than conventional slab casters because of no casting powder in the mould.
2. Friction free casting, in that the solidified shell moves at the same velocity as the rolls.
3. Predicting and controlling the location of the 'kissing point' is essential.
4. Heat extraction capacity is much higher than single-roll casters and the quality of the two strip surfaces can be the same due to both side cooling.

Owing to the higher rates of solidification, higher speeds through the mould and the lower thermal mass undergoing solidification (i.e. thin strip vs.thick slab) the process has been found to be extremely sensitive to slight variations in thermal flows and metal-mould interactions. The fluid flow in the mould considerably affects heat transfer, the thickness of solid shell and the location of the 'kissing point'.

3.2 The N.S.C. Twin Drum Caster

3.2.1 Solidified Shell Thickness

A twin roll casting program has been undertaken in a corporative effort between Nippon Steel Corp.(N.S.C.) and Mitsubishi Heavy Industries Ltd. with a semi-industrial experimental unit installed at Hikari Works of N.S.C. The experimental unit is a vertical type, top feeding, equal diameter, twin roll (drum) caster, using a submerged nozzle to deliver molten steel, and is named the twin drum caster. Figure 3.2 shows a photograph of the twin drum caster.

The machine has a 10-ton melt capacity which can produce 800 mm width strip between 1200 mm diameter drums. Since 1989, the machine has been producing cast austenitic stainless

The demonstration plant of twin-drum strip continuous casting process at the Hikari Works indicates the future elimination of the hot-rolling process.

Figure 3.2 Twin Drum Caster

steel coil on a test basis. A plant layout of the caster and equipment specifications are given in Figure 3.3, and Table 3, respectively.

The molten steel is supplied to the tundish fitted with induction heating from an electric furnace, and is poured between water-cooled drums via a controlled stopper-rod and a refractory nozzle. For stable operation, fully automatic casting control systems are employed. The liquid level is controlled using a meniscus detector as a sensor and a tundish stopper nozzle as an actuator. The drum gap and drum force are controlled using gap sensors, hydraulic servo-mechanics and drum motors. The constant-drum-gap control system is preferably adopted to the constant-drum-force control system according to the variation of strip thickness at test runs. In the system, during casting, the thickness of the strip and drum force are continuously detected, and the feed-back system controls the casting speed and drum gap to obtain the assigned thickness. The drum force is determined to satisfy strip thickness, casting stability and strip quality. The cast strip is joined to a dummy sheet taken up on the coiler, and the ends of the drums are sealed by preheated refractory plates. Solidification becomes completed in the vicinity of the drum gap.

Figure 3.4 shows the relation between casting speed and strip thickness in 304 typed stainless steel casting. Variations in strip thickness are less than ± 3 % using the constant-drum-gap control system. This relation gives information about the correlation between solidified shell thickness and contact time on the roll as following,

$$d_s = 4.83t^{0.60} \qquad (0.2 < t \text{ [sec]} < 1.2) \qquad [mm] \qquad (3.1)$$

Although the form of the equation is the same as equations (2.3), (2.4) & (2.7), values of the fitting parameters are different in each equation.

The empirical equation (3.1) tends to have the largest thickness. It suggests the biggest cooling rate. The equation (2.3) of Kasama et al. was obtained partially using the same machine at N.S.C.(twin drum caster) as the equation (3.1). Consequently these two equations are quite similar, but not the same. The equation (2.4) of Hlinka et al. was obtained after fitting parameters

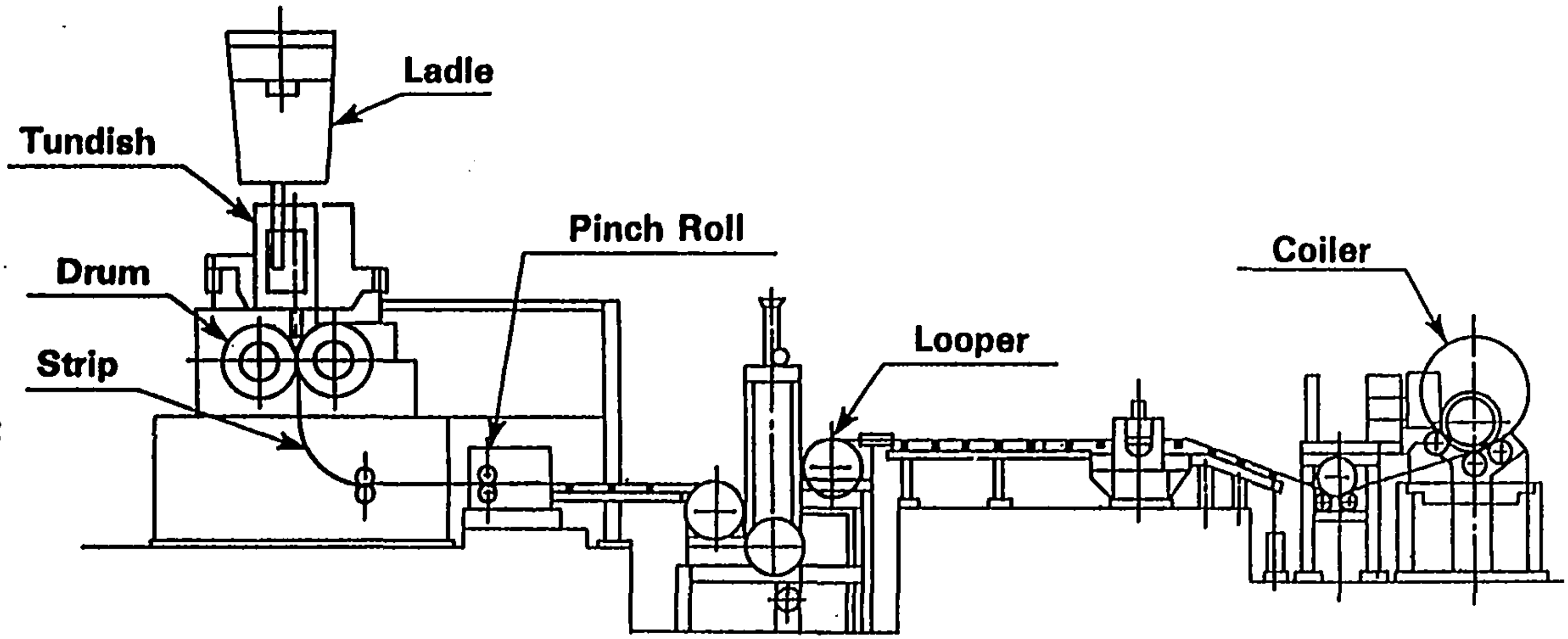

Figure 3.3 Pilot plant apparatus of twin drum caster

Table 3 Specifications of the twin drum caster

Items	Specifications
Type	Twin drums
Ladle capacity	10 ton
Tundish capacity	1.6 ton
Casting speed	20～130 m/min
Strip thickness	1.6～5.0 mm
Drum width	800 mm
Drum diameter	1200 mm
Drum sleeve	Cu + Ni plating
Coiler type	Up-coiler

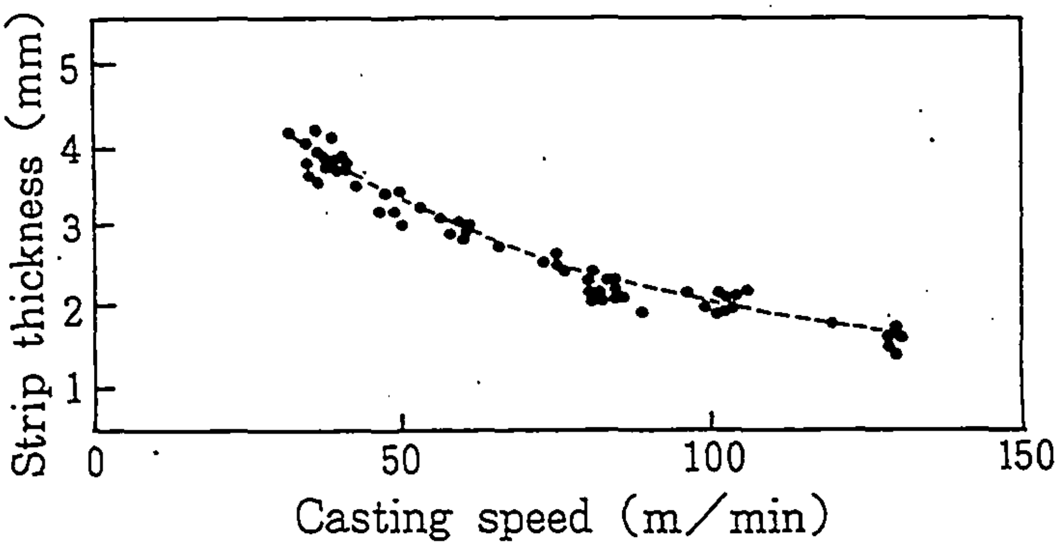

Figure 3.4 Relation between casting speed and strip thickness

to the data of Bethlehem Steel Corporation (BSCO), NKK, Kawasaki Steel Corporation (KSC) and NSC. An important point is that the correlation depends on not only the contact time but also on other factors of the machine and operation, and therefore can not be determined unequivocally.

Although these correlations provide very important information on how to obtain the desired strip thickness, the dependence of strip thickness on the other factors such as the delivery system of molten steel or its superheat is still unknown.

3.2.2 Surface Cracking

During the first stage of experiments conducted at N.S.C, fine longitudinal cracks occasionally occurred along the strip's surfaces. Figure 3.5 shows the microstructure around a typical longitudinal crack. The crack usually has a depth of about 100–300 μm and is about 10 cm in length.

Local solidification delay exists around the crack, indicated by the thinner thickness of the columnar crystal zone than the average. Figure 3.6 sketches the deviation of the columnar zone thickness across the wide section of a typical strip with the longitudinal cracks. The longitudinal cracks were observed at the location thinner thickness of the columnar zone. The critical deviation ratio of the longitudinal crack formation is about 80 % of the average thickness of the columnar zone.

In addition to above the fact, it was found that the magnitude of surface waves on the meniscus in the mould was related to the amount of the longitudinal cracks, during casting.

From the above experimental results, it is apparent that the fluid flow conditions of molten steel influence heat transfer and solidification phenomena, and the relation between coupled momentum and energy transport with solidification should be ascertained. Unfortunately, it is very difficult to find out the effects of each factor by experimental works alone because of the complexities of the phenomena, and a good mathematical model is therefore a necessity.

Most of the material treated in the Section 3.2 is derived from a N.S.C. report (Yamada et al. 1992).

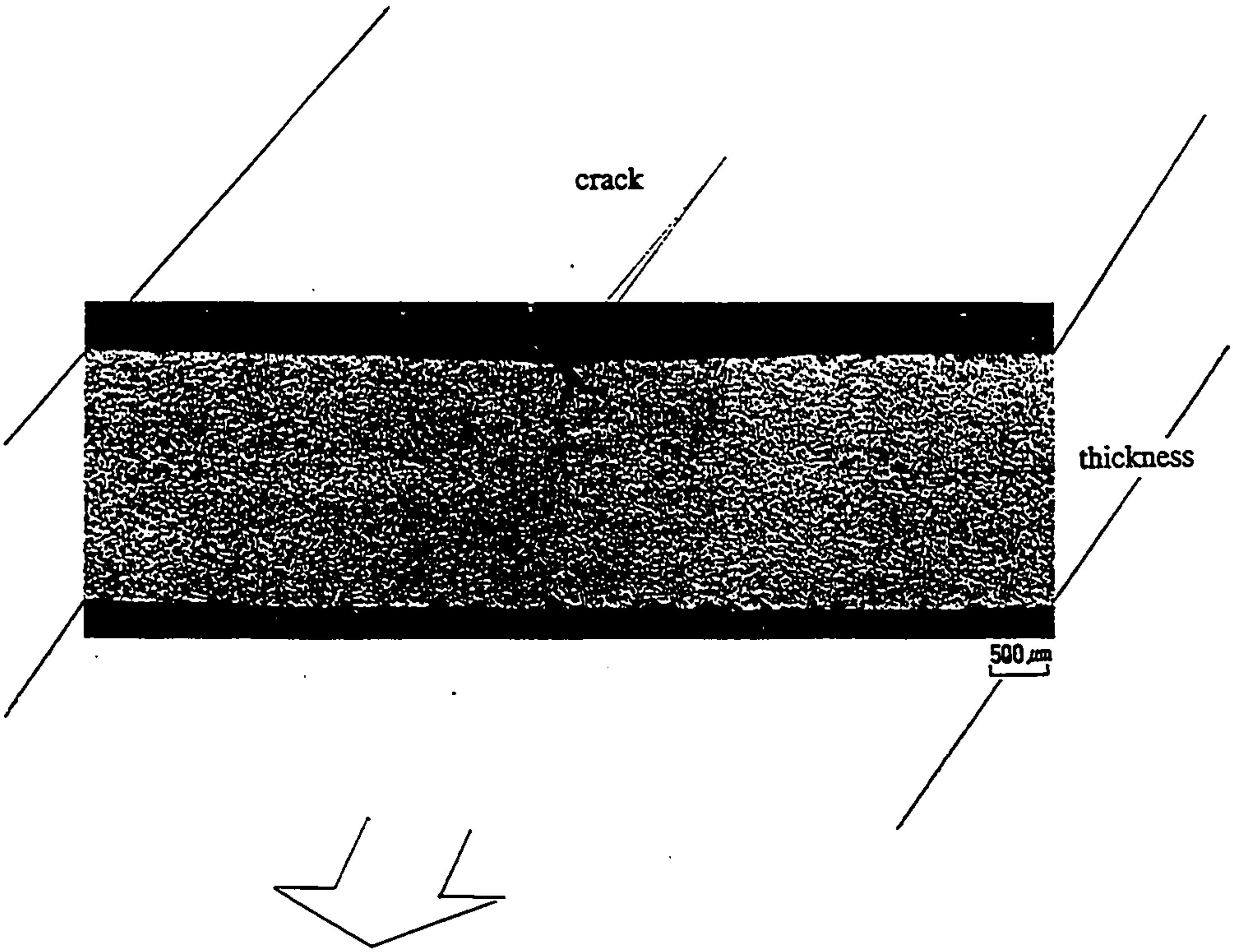

Figure 3.5 Transverse cross section around a longitudinal crack

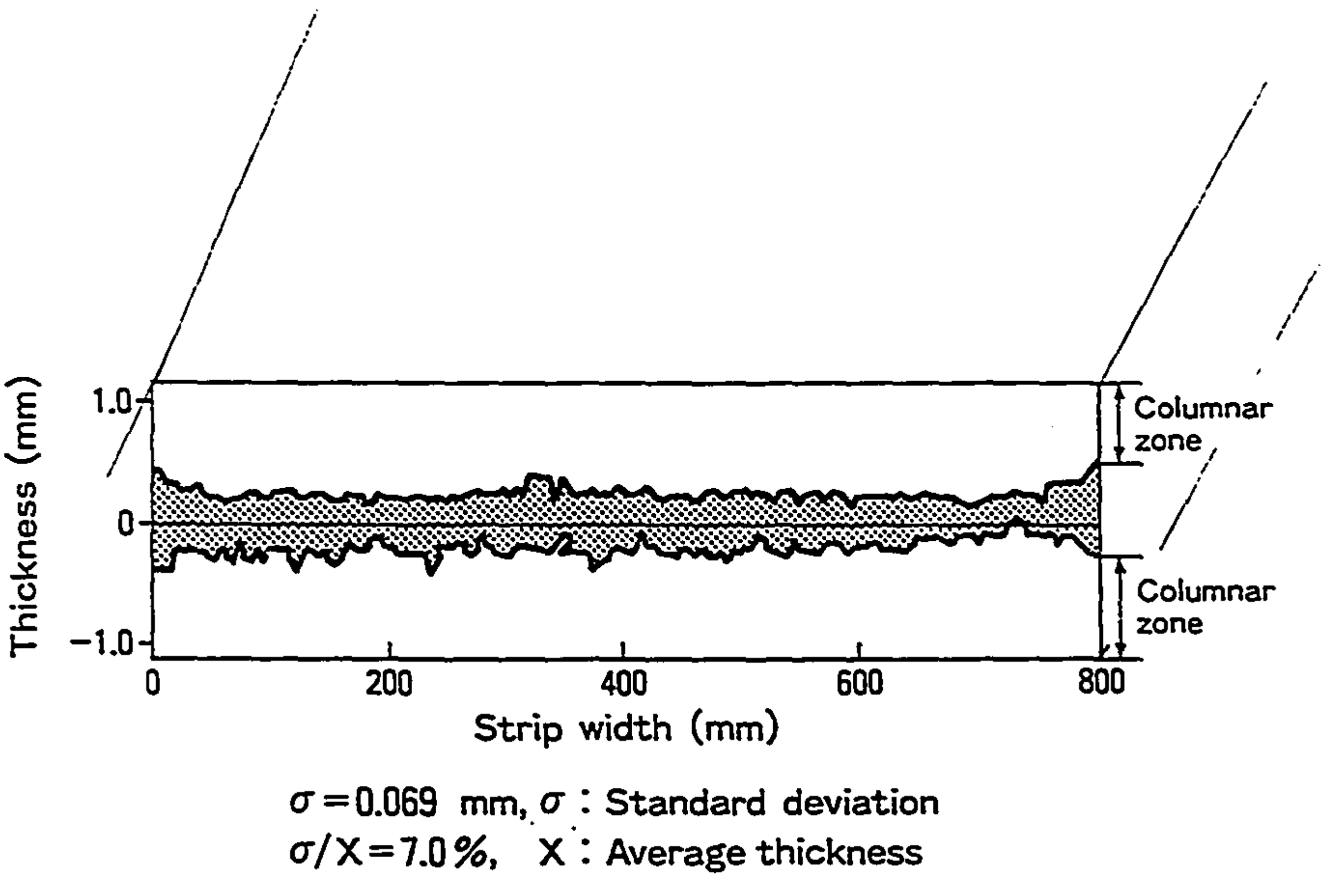

Figure 3.6 Deviation of columnar zone thickness

MATHEMATICAL FORMULATION OF THE PROBLEM

4.1 Introduction

Numerical modelling gives us useful information at relatively low cost (vis–a–vis physical models) about flows and the energy conditions in the mould during the design stage of such casters. In spite of the importance of modelling a twin–roll caster, few attempts accounting for fluid flow (Miyazawa & Szekely, 1981; Saitoh et al., 1989) have been made to model this caster system to date. This may be partly due to the fact that the problem posed is quite difficult in that a turbulence modelling of flow, heat transfer and solidification in an arbitrarily shaped geometry is required. Specifically, the modelling complexities of a twin–roll caster can be listed as follows:

1. The model should consider coupled fluid flow and heat transfer using the properties of liquid steel which has a low Prandtl number and a high Rayleigh number.
2. The model should consider turbulence, laminar and buffer region due to the existence of the mushy region whose boundaries are not clear.
3. The modelling region is of arbitrary wedge–shaped geometry. Neither Cartesian nor cylindrical coordinates is applicable without large solution errors.
4. The process contains a high speed moving boundary (roll), inlet–outlet conditions with a submerged nozzle and a free–surface.
5. The solidification phenomenon of the alloy must be considered.
6. For cost effectiveness, and from an industrial point of view, it is more appropriate that simulations be performed not by a supercomputer but using a personal

personal computer.

To resolve these complexities, the following mathematical approach has been adopted:

1. Control volume based finite difference method
2. Low Reynolds number k-ϵ turbulent model
3. Non-orthogonal body fitted coordinate system
4. Staggered grid adaptation
5. Enthalpy-porosity technique
6. Under-relaxation technique

4.2 Governing Equations

4.2.1 General Form of Governing Equations

Continuity equation (conservation of mass):

$$\frac{\partial \rho}{\partial t} + \nabla \cdot (\rho \vec{V}) = 0 \tag{4.1}$$

Navier-Stokes equation (integral equation of momentum):

$$\frac{D\vec{V}}{Dt} = \frac{\partial \vec{V}}{\partial t} + u\frac{\partial \vec{V}}{\partial x} + v\frac{\partial \vec{V}}{\partial y} + w\frac{\partial \vec{V}}{\partial z} = \vec{F} - \frac{1}{\rho}\nabla p + \vec{f} \tag{4.2}$$

The left term represents mass per unit volume times acceleration, the first right term is the external force, the second one is pressure force and the third one is the viscous force.

Conservation of energy :

$$\frac{De}{Dt} + \frac{D}{Dt}\left(\frac{V^2}{2}\right) = \vec{V}\cdot\vec{F} - \vec{V}\cdot\frac{1}{\rho}\nabla p + \vec{V}\vec{f} - \frac{p}{\rho}\nabla\cdot\vec{V} + \frac{\Phi}{\rho} + \frac{Q}{\rho} \tag{4.3}$$

The first left term represents rate of gain of internal energy per unit volume, the second one is rate of gain of kinematic energy. The first right term represents work done on fluid by external forces, the second one is work done by pressure force, the third one is work done by viscous force, the fourth one is work done by isobaric change of unit volume, the fifth one is heat generation by viscous dissipation and the last term is energy input.

Considering Newtonian incompressible fluid flow, equations (4.1)-(4.3) can be revised as follows respectively,

Continuity equation:

$$\nabla\cdot\vec{V} = 0 \tag{4.4}$$

Momentum equation:

$$\frac{D\vec{V}}{Dt} = \vec{F} - \frac{1}{\rho}\nabla p + \nu\nabla^2\vec{V} \tag{4.5}$$

Energy equation:

$$C_p\frac{DT}{Dt} = \frac{\kappa}{\rho}\nabla^2 T + \frac{\Phi}{\rho} \tag{4.6}$$

Also the general form of the governing equations for mass/fluid/energy/scalar component transport processes can be written in the form

$$\frac{\partial}{\partial t}(\rho\phi) + \nabla\cdot(\rho\vec{V}\phi) = \nabla\cdot(\Gamma_\phi\nabla\phi) + S_\phi \tag{4.7}$$

where ϕ represents dependent valuables (e.g. u,v,w,T etc.) and S_ϕ is a source term.

4.2.2 Laminar Flow

In case of laminar flow, the shear stress force is proportional to the local velocity gradient (Newton's law of viscosity), so that governing equations of motion are relatively simple. Considering two-dimensional fluid flow and heat transfer, the equations in the Cartesian coordinate system (x-y) can be written as follows;

$$\underbrace{\frac{\partial \rho\phi}{\partial t}}_{(transient\ term)} + \underbrace{\frac{\partial(\rho u\phi)}{\partial x} + \frac{\partial(\rho v\phi)}{\partial y}}_{(convection\ term)} = \underbrace{\frac{\partial}{\partial x}\left(\Gamma_\phi \frac{\partial \phi}{\partial x}\right) + \frac{\partial}{\partial y}\left(\Gamma_\phi \frac{\partial \phi}{\partial y}\right)}_{(diffusion\ term)} + \underbrace{S(x,y)}_{(source\ term)} \qquad (4.8)$$

Continuity equation :

$$\phi = 1, \ \Gamma_\phi = 0, \ S(x,y) = 0 \qquad (4.9)$$

u-momentum equation :

$$\phi = u, \ \Gamma_\phi = \mu, \ S(x,y) = -\frac{\partial p}{\partial x} \qquad (4.10)$$

v-momentum equation (the gravity is in the y-direction):

$$\phi = v, \ \Gamma_\phi = \mu, \ S(x,y) = -\frac{\partial p}{\partial y} + \rho g \qquad (4.11)$$

To take into account the buoyancy effect, employing the Boussinesq approximation, which uses the first order Taylor-series expansion, equation (4.11) is revised as follows,

$$\phi = v, \ \Gamma_\phi = \mu, \ S(x,y) = -\frac{\partial p}{\partial y} + \beta\rho_{ref}g\,(T - T_{ref}) \qquad (4.12)$$

Energy equation :

$$\phi = T, \ \Gamma_\phi = \frac{\kappa}{C_p}, \ S(x,y) = 0 \qquad (4.13)$$

Concentration equation (without reaction):

$$\phi = C, \;\; \Gamma_\phi = D_{dif}, \;\; S(x,y) = 0 \tag{4.14}$$

4.2.3 Turbulent Flow

As mentioned in Chapter 2, the shear stress in turbulence has a Reynolds stress term and a turbulent model is necessary to simulate the flow.

In the present work, the Jones & Launder type low Reynolds number k-ϵ turbulent model (1972) is employed for the following reasons;

1. Of the various kinds of turbulent model, with a view of both accuracy and cost, the two equation model is preferable to the others. Additionally, the k-ϵ model has been the most tested in various systems.
2. The wall function treatment of the standard high Reynolds number k-ϵ model is not available for the solidification problem of alloy because boundaries between solid and liquid region are ambiguous owing to the presence of a mushy region. The low Reynolds number k-ϵ model does not need the wall function treatment.
3. The problems involve not only fully turbulent flow but also laminar flows and semi-turbulent flows. The low Reynolds number k-ϵ model is therefore preferable.
4. According to the literature survey (chapter 2.2), of the various low Reynolds number models, the Jones & Launder type model showed better predictions compared with the other similar models in both natural convection and forced convection problems with strong pressure gradients.
5. Since the location of the solidification boundary is ambiguous, it is difficult to employ a low Reynolds number k-ϵ model that uses the distance from the wall, such as required by the Lam & Bremhorst type (1980).

Using the general form of the transport equation (equation (4.8)), governing equations can be written by the Jones & Launder low Reynolds turbulent model as follows;

u-momentum equation :

$$\phi = u, \quad \Gamma_\phi = \mu+\mu_t$$
$$S(x,y) = -\frac{\partial p}{\partial x} + \frac{\partial}{\partial x}\left((\mu+\mu_t)\frac{\partial u}{\partial x}\right) + \frac{\partial}{\partial y}\left((\mu+\mu_t)\frac{\partial v}{\partial x}\right) \tag{4.15}$$

v-momentum equation with the Boussinesq approximation :

$$\phi = v, \quad \Gamma_\phi = \mu+\mu_t$$
$$S(x,y) = -\frac{\partial p}{\partial y} + \frac{\partial}{\partial x}\left((\mu+\mu_t)\frac{\partial u}{\partial y}\right) + \frac{\partial}{\partial y}\left((\mu+\mu_t)\frac{\partial v}{\partial y}\right) + \beta_0\rho_{ref}g(T-T_{ref}) \tag{4.16}$$

Energy equation :

$$\phi = T, \qquad \Gamma_\phi = \frac{\kappa}{\rho C_p} + \frac{\kappa_t}{\rho C_p}, \qquad S(x,y) = 0 \tag{4.17}$$

Turbulent kinematic energy equation:

$$\phi = k, \quad \Gamma_\phi = \mu+\frac{\mu_t}{\sigma_k}$$
$$S(x,y) = \mu_t\left[2\left(\left(\frac{\partial u}{\partial x}\right)^2 + \left(\frac{\partial v}{\partial y}\right)^2\right) + \left(\frac{\partial u}{\partial y} + \frac{\partial v}{\partial x}\right)^2\right] - \rho\epsilon - 2\mu\left(\left(\frac{\partial k^{0.5}}{\partial x}\right)^2 + \left(\frac{\partial k^{0.5}}{\partial y}\right)^2\right) \tag{4.18}$$

Dissipation rate of turbulent energy equation :

$$\phi = \epsilon, \quad \Gamma_\phi = \mu+\frac{\mu_t}{\sigma_\epsilon}$$
$$\begin{aligned} S(x,y) = {} & C_1\mu_t\left[2\left(\left(\frac{\partial u}{\partial x}\right)^2+\left(\frac{\partial v}{\partial y}\right)^2\right)+\left(\frac{\partial u}{\partial y}+\frac{\partial v}{\partial x}\right)^2\right]\frac{\epsilon}{k} - C_2\rho(1-0.3\exp(-Re^{2}))\frac{\epsilon^2}{k} \\ & + 2\frac{\mu\mu_t}{\rho}\left(\left(\frac{\partial^2 u}{\partial x^2}\right)^2 + \left(\frac{\partial^2 u}{\partial y^2}\right)^2 + \left(\frac{\partial^2 v}{\partial x^2}\right)^2 + \left(\frac{\partial^2 v}{\partial y^2}\right)^2\right) \end{aligned} \tag{4.19}$$

Here, the turbulent viscosity, μ_t, is given by

$$\mu_t = \frac{C_\mu f_\mu \rho k^2}{\epsilon} \tag{4.20}$$

$$f_\mu = \exp\left(\frac{-2.5}{(1 + Re^t/50)} \right), \quad Re^t = \frac{\rho k^2}{\mu \epsilon} \tag{4.21}$$

where the turbulent model constants are:

$$C_\mu = 0.09, \quad C_1 = 1.44, \quad C_2 = 1.92, \quad \sigma_k = 1.0, \quad \sigma_\epsilon = 1.3 \tag{4.22}$$

The turbulent thermal conductivity, κ_t, in the energy equation (4.17) is evaluated from,

$$\kappa_t = \frac{C_p \mu_t}{Pr_t} \tag{4.23}$$

where Pr_t is the turbulent Prandtl number. A value of 0.9 for Pr_t is often used for air or water systems. Since for the liquid metal system the Pr_t is not known, its value has been taken to be 0.9.

4.2.4 Non-Dimensionalization

For simplicity of programming, and to make the effect of each parameter clear, a non-dimensional form of the governing equations and boundary conditions have been employed in the present work. Thus the following dimensionless variables are used for non-dimensionalization:

$$\bar{u} = \frac{u}{U_r}, \quad \bar{v} = \frac{v}{U_r}, \quad \bar{x} = \frac{x}{D}, \quad \bar{y} = \frac{y}{D}, \quad \bar{k} = \frac{k}{U_r^2}, \quad \bar{\epsilon} = \frac{\epsilon D}{U_r^3}, \quad \bar{P} = \frac{(p + \rho_0 g y)}{\rho U_r^2} \tag{4.24}$$

$$\bar{h} = \frac{h}{h_{in}}, \quad Re = \frac{U_r D}{\nu}, \quad Re_t = \frac{U_r D}{\nu_t}, \quad Gr = \frac{g\beta_0 D^3 (T_h - T_c)}{\nu^2}, \quad Pr = \frac{\mu C_p}{\kappa} \quad (4.25)$$

where D represents a characteristic length, whose choice will be discussed in the next chapter.

4.3 Body Fitted Coordinates

4.3.1 Numerical Grid Generation

The second step in the analysis is to introduce a transformation of coordinate that maps the physical domain (x–y plane) onto a rectangular computational domain (ξ–η plane).

The relationship between partial derivatives of a function f with respect to physical and transformed variables is well known (Thomson, 1985). The first and second order derivatives are summarized in following matrix equation,

$$\begin{bmatrix} \frac{\partial f}{\partial \xi} \\ \frac{\partial f}{\partial \eta} \\ \frac{\partial^2 f}{\partial \xi^2} \\ \frac{\partial^2 f}{\partial \xi \partial \eta} \\ \frac{\partial^2 f}{\partial \eta^2} \end{bmatrix} = \begin{bmatrix} \frac{\partial x}{\partial \xi} & \frac{\partial y}{\partial \xi} & 0 & 0 & 0 \\ \frac{\partial x}{\partial \eta} & \frac{\partial y}{\partial \eta} & 0 & 0 & 0 \\ \frac{\partial^2 x}{\partial \xi^2} & \frac{\partial^2 y}{\partial \xi^2} & (\frac{\partial x}{\partial \xi})^2 & 2\frac{\partial x}{\partial \xi}\frac{\partial y}{\partial \xi} & (\frac{\partial y}{\partial \xi})^2 \\ \frac{\partial^2 x}{\partial \xi \partial \eta} & \frac{\partial^2 y}{\partial \xi \partial \eta} & \frac{\partial x}{\partial \xi}\frac{\partial x}{\partial \eta} & \frac{\partial x}{\partial \xi}\frac{\partial y}{\partial \eta} + \frac{\partial x}{\partial \eta}\frac{\partial y}{\partial \xi} & \frac{\partial y}{\partial \xi}\frac{\partial y}{\partial \eta} \\ \frac{\partial^2 x}{\partial \eta^2} & \frac{\partial^2 y}{\partial \eta^2} & (\frac{\partial x}{\partial \eta})^2 & 2\frac{\partial x}{\partial \eta}\frac{\partial y}{\partial \eta} & (\frac{\partial y}{\partial \eta})^2 \end{bmatrix} \begin{bmatrix} \frac{\partial f}{\partial \xi} \\ \frac{\partial f}{\partial \eta} \\ \frac{\partial^2 f}{\partial x^2} \\ \frac{\partial^2 f}{\partial x \partial y} \\ \frac{\partial^2 f}{\partial y^2} \end{bmatrix} \quad (4.26)$$

Equation (4.26) can be solved using the reciprocal matrix, and the transformed derivatives are written as follows;

$$\frac{\partial f}{\partial x} = \frac{1}{J}\left(\frac{\partial y}{\partial \eta}\frac{\partial f}{\partial \xi} - \frac{\partial y}{\partial \xi}\frac{\partial f}{\partial \eta} \right) \tag{4.27}$$

$$\frac{\partial f}{\partial y} = \frac{1}{J}\left(-\frac{\partial x}{\partial \eta}\frac{\partial f}{\partial \xi} + \frac{\partial x}{\partial \xi}\frac{\partial f}{\partial \eta} \right) \tag{4.28}$$

$$\begin{aligned}
\frac{\partial^2 f}{\partial x^2} = & \left((\frac{\partial y}{\partial \eta})^2\frac{\partial^2 f}{\partial \xi^2} - 2\frac{\partial y}{\partial \xi}\frac{\partial y}{\partial \eta}\frac{\partial^2 f}{\partial \xi \partial \eta} + (\frac{\partial y}{\partial \xi})^2\frac{\partial^2 f}{\partial \eta^2} \right) / J^2 \\
& + [\left((\frac{\partial y}{\partial \eta})^2\frac{\partial^2 y}{\partial \xi^2} - 2\frac{\partial y}{\partial \xi}\frac{\partial y}{\partial \eta}\frac{\partial^2 y}{\partial \xi \partial \eta} + (\frac{\partial y}{\partial \xi})^2\frac{\partial^2 y}{\partial \eta^2} \right)\left(\frac{\partial x}{\partial \eta}\frac{\partial f}{\partial \xi} - \frac{\partial x}{\partial \xi}\frac{\partial f}{\partial \eta} \right) \\
& + \left((\frac{\partial y}{\partial \eta})^2\frac{\partial^2 x}{\partial \xi^2} - 2\frac{\partial y}{\partial \xi}\frac{\partial y}{\partial \eta}\frac{\partial^2 x}{\partial \xi \partial \eta} + (\frac{\partial y}{\partial \xi})^2\frac{\partial^2 x}{\partial \eta^2} \right)\left(\frac{\partial y}{\partial \xi}\frac{\partial f}{\partial \eta} - \frac{\partial y}{\partial \eta}\frac{\partial f}{\partial \xi} \right)] / J^3
\end{aligned} \tag{4.29}$$

$$\begin{aligned}
\frac{\partial^2 f}{\partial x \partial y} = & -\left(\frac{\partial x}{\partial \eta}\frac{\partial y}{\partial \eta}\frac{\partial^2 f}{\partial \xi^2} - (\frac{\partial x}{\partial \xi}\frac{\partial y}{\partial \eta} + \frac{\partial x}{\partial \eta}\frac{\partial y}{\partial \xi})\frac{\partial^2 f}{\partial \xi \partial \eta} + \frac{\partial x}{\partial \xi}\frac{\partial y}{\partial \xi}\frac{\partial^2 f}{\partial \eta^2} \right) / J^2 \\
& - [\left(\frac{\partial x}{\partial \eta}\frac{\partial y}{\partial \eta}\frac{\partial^2 y}{\partial \xi^2} - (\frac{\partial x}{\partial \xi}\frac{\partial y}{\partial \eta} + \frac{\partial x}{\partial \eta}\frac{\partial y}{\partial \xi})\frac{\partial^2 y}{\partial \xi \partial \eta} + \frac{\partial x}{\partial \xi}\frac{\partial y}{\partial \xi}\frac{\partial^2 y}{\partial \eta^2} \right)\left(\frac{\partial x}{\partial \eta}\frac{\partial f}{\partial \xi} - \frac{\partial x}{\partial \xi}\frac{\partial f}{\partial \eta} \right) \\
& - \left(\frac{\partial x}{\partial \eta}\frac{\partial y}{\partial \eta}\frac{\partial^2 x}{\partial \xi^2} - (\frac{\partial x}{\partial \xi}\frac{\partial y}{\partial \eta} + \frac{\partial x}{\partial \eta}\frac{\partial y}{\partial \xi})\frac{\partial^2 x}{\partial \xi \partial \eta} + \frac{\partial x}{\partial \xi}\frac{\partial y}{\partial \xi}\frac{\partial^2 x}{\partial \eta^2} \right)\left(\frac{\partial y}{\partial \xi}\frac{\partial f}{\partial \eta} - \frac{\partial y}{\partial \eta}\frac{\partial f}{\partial \xi} \right)] / J^3
\end{aligned} \tag{4.30}$$

$$\begin{aligned}
\frac{\partial^2 f}{\partial y^2} = & \left((\frac{\partial x}{\partial \eta})^2\frac{\partial^2 f}{\partial \xi^2} - 2\frac{\partial x}{\partial \xi}\frac{\partial x}{\partial \eta}\frac{\partial^2 f}{\partial \xi \partial \eta} + (\frac{\partial x}{\partial \xi})^2\frac{\partial^2 f}{\partial \eta^2} \right) / J^2 \\
& + [\left((\frac{\partial x}{\partial \eta})^2\frac{\partial^2 y}{\partial \xi^2} - 2\frac{\partial x}{\partial \xi}\frac{\partial x}{\partial \eta}\frac{\partial^2 y}{\partial \xi \partial \eta} + (\frac{\partial x}{\partial \xi})^2\frac{\partial^2 y}{\partial \eta^2} \right)\left(\frac{\partial x}{\partial \eta}\frac{\partial f}{\partial \xi} - \frac{\partial x}{\partial \xi}\frac{\partial f}{\partial \eta} \right) \\
& + \left((\frac{\partial x}{\partial \eta})^2\frac{\partial^2 x}{\partial \xi^2} - 2\frac{\partial x}{\partial \xi}\frac{\partial x}{\partial \eta}\frac{\partial^2 x}{\partial \xi \partial \eta} + (\frac{\partial x}{\partial \xi})^2\frac{\partial^2 x}{\partial \eta^2} \right)\left(\frac{\partial y}{\partial \xi}\frac{\partial f}{\partial \eta} - \frac{\partial y}{\partial \eta}\frac{\partial f}{\partial \xi} \right)] / J^3
\end{aligned} \tag{4.31}$$

where the quantity, J, is the Jacobian and is given by,

$$J = \frac{\partial x}{\partial \xi}\frac{\partial y}{\partial \eta} - \frac{\partial x}{\partial \eta}\frac{\partial y}{\partial \xi} \tag{4.32}$$

Since the basic idea of the transformation is to generate transformation functions such that all boundaries coincide with coordinate lines, the rectangular coordinate (ξ,η) are taken as solutions of some suitable elliptic boundary value problems with one of these coordinates constant on the boundaries. In the present study, the simplest elliptic equation, Laplace's equation, is employed for generating the system.

$$\frac{\partial^2\xi}{\partial x^2} + \frac{\partial^2\xi}{\partial y^2} = 0 \tag{4.33}$$

$$\frac{\partial^2\eta}{\partial x^2} + \frac{\partial^2\eta}{\partial y^2} = 0 \tag{4.34}$$

All numerical computation should be carried out in the rectangular transformed plane. Accordingly, it is necessary to interchange the roles of dependent and independent variables. Using equations (4.29)- (4.31), equations (4.33)-(4.34) are transformed as follows:

$$\alpha\frac{\partial^2 x}{\partial\xi^2} - 2\beta\frac{\partial^2 x}{\partial\xi\partial\eta} + \gamma\frac{\partial^2 x}{\partial\eta^2} = 0 \tag{4.35}$$

$$\alpha\frac{\partial^2 y}{\partial\xi^2} - 2\beta\frac{\partial^2 y}{\partial\xi\partial\eta} + \gamma\frac{\partial^2 y}{\partial\eta^2} = 0 \tag{4.36}$$

where

$$\alpha = \left(\frac{\partial x}{\partial\eta}\right)^2 + \left(\frac{\partial y}{\partial\eta}\right)^2 \tag{4.37}$$

$$\beta = \frac{\partial x}{\partial\xi}\frac{\partial x}{\partial\eta} + \frac{\partial y}{\partial\xi}\frac{\partial y}{\partial\eta} \tag{4.38}$$

$$\gamma = \left(\frac{\partial x}{\partial\xi}\right)^2 + \left(\frac{\partial y}{\partial\xi}\right)^2 \tag{4.39}$$

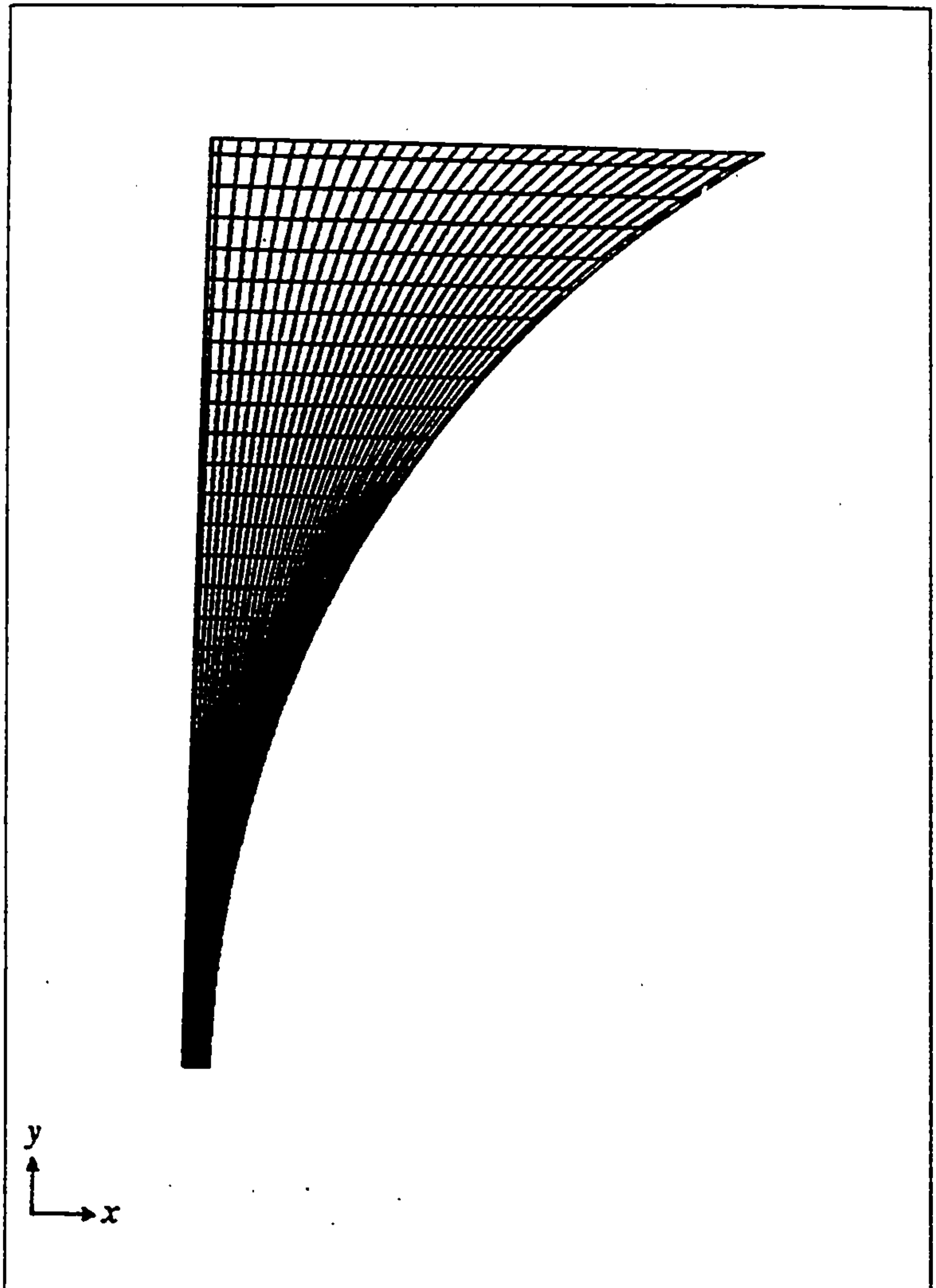

Figure 4.1 Grid formation in the physical plane

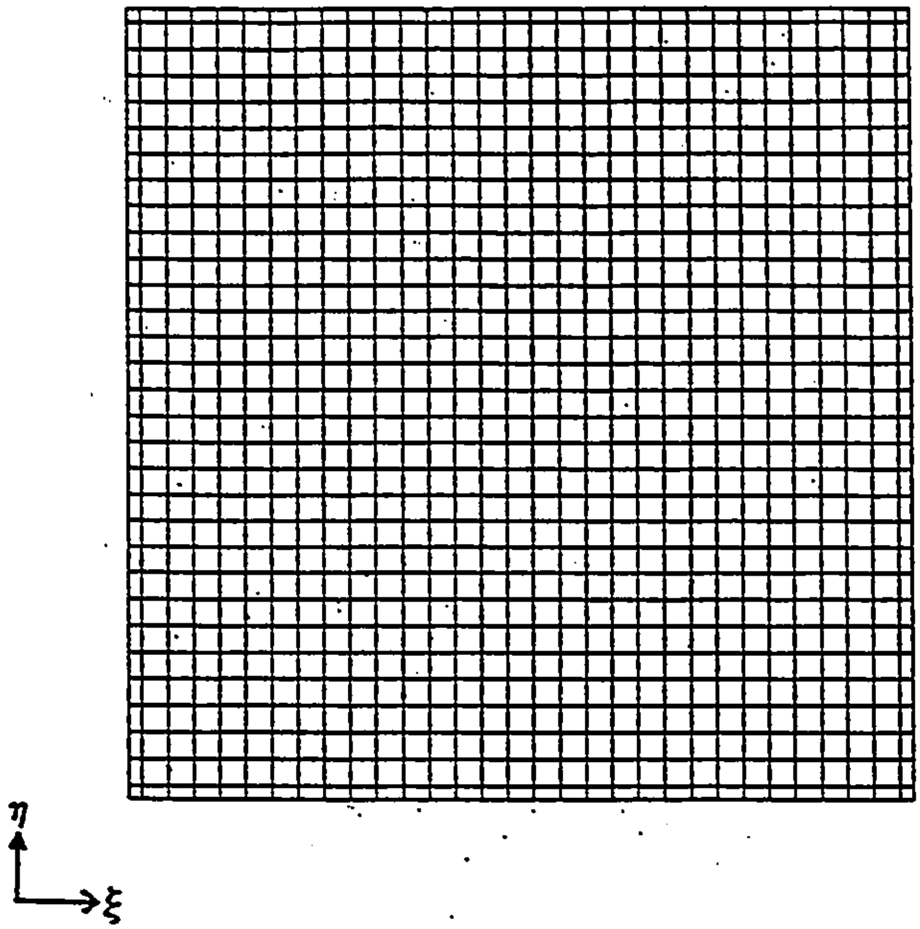

Figure 4.2 Grid formation in the transformed plane

The variables of derivatives on each node were determined numerically, solving equations.(4.35)-(4.36) on a uniform rectangular grid $\Delta\xi,\Delta\eta$, using the Gauss-Seidal method. This system is a quasi-linear elliptic system with Dirichlet boundary conditions for the physical coordinate in the transformed plane. When the factor β is set equal to zero, each coordinate line is perpendicular to each other, and the system is called the orthogonal coordinate system.

Figure 4.1 and Figure 4.2 show 32 x 32 nodes grid structure in the physical plane and in the transformed plane, respectively. In the transformed domain, uniformed rectangular coordinate system ($\Delta\xi=\Delta\eta=1$) and type B-grid formation (Patankar, 1980) are employed to simplify discretized equations and boundary conditions.

4.3.2 Transformation of Governing Equations

The governing equations (4.8)-(4.19) were transformed from the Cartesian physical plane (x,y) to the body fitted coordinate system (ξ,η) using the relations given by equations (4.27)-(4.31). In the transformation, the non-orthogonal coordinate system was adopted because of its wide applicability for a geometry. Additionally, in the transformed equations, not the curvilinear velocities but the co-variant physical velocities (u & v) are used as dependent variables in momentum, energy and k, ϵ equations.

Considering incompressible fluid, the general form of the governing equation (4.8) is transformed into,

$$J\frac{\partial\phi}{\partial t}+\frac{\partial(U\phi)}{\partial\xi}+\frac{\partial(V\phi)}{\partial\eta}=\left[\frac{\partial}{\partial\xi}\left(\Gamma_\phi\frac{\alpha}{J}\frac{\partial\phi}{\partial\xi}-\Gamma_\phi\frac{\beta}{J}\frac{\partial\phi}{\partial\eta}\right)+\frac{\partial}{\partial\eta}\left(\Gamma_\phi\frac{\gamma}{J}\frac{\partial\phi}{\partial\eta}-\Gamma_\phi\frac{\beta}{J}\frac{\partial\phi}{\partial\xi}\right)\right]+S(\xi,\eta) \quad (4.40)$$

where the contra-variant velocities U, V are

$$U=u\left(\frac{\partial y}{\partial\eta}\right)-v\left(\frac{\partial x}{\partial\eta}\right),\qquad V=v\left(\frac{\partial x}{\partial\xi}\right)-u\left(\frac{\partial y}{\partial\xi}\right) \quad (4.41)$$

Source terms and coefficient Γ_ϕ can be written in turbulent system as follows,

Continuity equation :

$$\phi = 1, \quad \Gamma_{\phi} = 0, \quad S(\xi,\eta) = 0 \tag{4.42}$$

u-momentum equation :

$$\phi = u, \quad \Gamma_{\phi} = \nu + \nu_t \tag{4.43}$$

$$\begin{aligned} S(\xi,\eta) = & -\left(\frac{\partial y}{\partial \eta}\right)\left(\frac{\partial P}{\partial \xi}\right) + \left(\frac{\partial y}{\partial \xi}\right)\left(\frac{\partial P}{\partial \eta}\right) + \frac{1}{J}\Big[\left(\frac{\partial y}{\partial \eta}\frac{\partial \nu_t}{\partial \xi} - \frac{\partial y}{\partial \xi}\frac{\partial \nu_t}{\partial \eta} \right)\left(\frac{\partial y}{\partial \eta}\frac{\partial u}{\partial \xi} - \frac{\partial y}{\partial \xi}\frac{\partial u}{\partial \eta} \right) \\ & + \left(-\frac{\partial x}{\partial \eta}\frac{\partial \nu_t}{\partial \xi} + \frac{\partial x}{\partial \xi}\frac{\partial \nu_t}{\partial \eta} \right)\left(\frac{\partial y}{\partial \eta}\frac{\partial v}{\partial \xi} - \frac{\partial y}{\partial \xi}\frac{\partial v}{\partial \eta} \right) \Big] \end{aligned} \tag{4.44}$$

v-momentum equation :

$$\phi = v, \quad \Gamma_{\phi} = \nu + \nu_t \tag{4.45}$$

$$\begin{aligned} S(\xi,\eta) = & -\left(\frac{\partial x}{\partial \xi}\right)\left(\frac{\partial P}{\partial \eta}\right) + \left(\frac{\partial x}{\partial \eta}\right)\left(\frac{\partial P}{\partial \xi}\right) + \frac{1}{J}\Big[\left(\frac{\partial y}{\partial \eta}\frac{\partial \nu_t}{\partial \xi} - \frac{\partial y}{\partial \xi}\frac{\partial \nu_t}{\partial \eta} \right)\left(-\frac{\partial x}{\partial \eta}\frac{\partial u}{\partial \xi} + \frac{\partial x}{\partial \xi}\frac{\partial u}{\partial \eta} \right) \\ & + \left(-\frac{\partial x}{\partial \eta}\frac{\partial \nu_t}{\partial \xi} + \frac{\partial x}{\partial \xi}\frac{\partial \nu_t}{\partial \eta} \right)\left(-\frac{\partial x}{\partial \eta}\frac{\partial v}{\partial \xi} + \frac{\partial x}{\partial \xi}\frac{\partial v}{\partial \eta} \right) \Big] + Jg\beta_{ref}(T - T_{ref}) \end{aligned} \tag{4.46}$$

Energy equation :

$$\phi = T, \quad \Gamma_{\phi} = \frac{\kappa}{C_p} + \frac{\kappa_t}{C_p}, \quad S(\xi,\eta) = 0 \tag{4.47}$$

Turbulent energy equation :

$$\phi = k, \quad \Gamma_{\phi} = \nu + \frac{\nu_t}{\sigma_t} \tag{4.48}$$

$$S(\xi,\eta) = \frac{\nu_t}{J} \Big[\alpha\left((\frac{\partial u}{\partial \xi})^2+(\frac{\partial v}{\partial \xi})^2\right) - 2\beta\left((\frac{\partial u}{\partial \xi})(\frac{\partial u}{\partial \eta})+(\frac{\partial v}{\partial \xi})(\frac{\partial v}{\partial \eta})\right) + \gamma\left((\frac{\partial u}{\partial \eta})^2+(\frac{\partial v}{\partial \eta})^2\right)$$

$$+ (\frac{\partial y}{\partial \eta})^2(\frac{\partial u}{\partial \xi})^2 - 2\frac{\partial y}{\partial \eta}\frac{\partial y}{\partial \xi}\frac{\partial u}{\partial \xi}\frac{\partial u}{\partial \eta} + (\frac{\partial y}{\partial \xi})^2(\frac{\partial u}{\partial \eta})^2 + (\frac{\partial x}{\partial \eta})^2(\frac{\partial v}{\partial \xi})^2 - 2\frac{\partial x}{\partial \xi}\frac{\partial x}{\partial \eta}\frac{\partial v}{\partial \xi}\frac{\partial v}{\partial \eta} \tag{4.49}$$

$$+ (\frac{\partial x}{\partial \xi})^2(\frac{\partial v}{\partial \eta})^2 -2 \Big(\frac{\partial x}{\partial \eta}\frac{\partial y}{\partial \eta}\frac{\partial u}{\partial \xi}\frac{\partial v}{\partial \xi} - \frac{\partial x}{\partial \xi}\frac{\partial y}{\partial \eta}\frac{\partial u}{\partial \eta}\frac{\partial v}{\partial \xi} - \frac{\partial x}{\partial \eta}\frac{\partial y}{\partial \xi}\frac{\partial u}{\partial \xi}\frac{\partial v}{\partial \eta}$$

$$+ \frac{\partial x}{\partial \xi}\frac{\partial y}{\partial \xi}\frac{\partial u}{\partial \eta}\frac{\partial v}{\partial \eta} \Big) \Big] - J\rho\epsilon - \frac{2\nu}{J} \Big[\alpha(\frac{\partial k^{0.5}}{\partial \xi})^2 - 2\beta\frac{\partial k^{0.5}}{\partial \xi}\frac{\partial k^{0.5}}{\partial \eta} + \gamma(\frac{\partial k^{0.5}}{\partial \eta})^2 \Big]$$

Dissipation rate of turbulent energy equation :

$$\phi = \epsilon, \quad \Gamma_\phi = \nu + \frac{\nu_t}{\sigma_\epsilon} \tag{4.50}$$

$$S(\xi,\eta) = \frac{C_1 f_1 \nu_t \epsilon}{J\,k} \Big[\alpha\left((\frac{\partial u}{\partial \xi})^2+(\frac{\partial v}{\partial \xi})^2\right) - 2\beta\left((\frac{\partial u}{\partial \xi})(\frac{\partial u}{\partial \eta})+(\frac{\partial v}{\partial \xi})(\frac{\partial v}{\partial \eta})\right) + \gamma\left((\frac{\partial u}{\partial \eta})^2+(\frac{\partial v}{\partial \eta})^2\right)$$

$$+ (\frac{\partial y}{\partial \eta})^2(\frac{\partial u}{\partial \xi})^2 - 2\frac{\partial y}{\partial \eta}\frac{\partial y}{\partial \xi}\frac{\partial u}{\partial \xi}\frac{\partial u}{\partial \eta} + (\frac{\partial y}{\partial \xi})^2(\frac{\partial u}{\partial \eta})^2 + (\frac{\partial x}{\partial \eta})^2(\frac{\partial v}{\partial \xi})^2 - 2\frac{\partial x}{\partial \eta}\frac{\partial x}{\partial \xi}\frac{\partial v}{\partial \xi}\frac{\partial v}{\partial \eta}$$

$$+(\frac{\partial x}{\partial \xi})^2(\frac{\partial v}{\partial \eta})^2-2 \left(\frac{\partial x}{\partial \eta}\frac{\partial y}{\partial \eta}\frac{\partial u}{\partial \xi}\frac{\partial v}{\partial \xi} - \frac{\partial x}{\partial \xi}\frac{\partial y}{\partial \eta}\frac{\partial u}{\partial \eta}\frac{\partial v}{\partial \xi} - \frac{\partial x}{\partial \eta}\frac{\partial y}{\partial \xi}\frac{\partial u}{\partial \xi}\frac{\partial v}{\partial \eta} + \frac{\partial x}{\partial \xi}\frac{\partial y}{\partial \xi}\frac{\partial u}{\partial \eta}\frac{\partial v}{\partial \eta} \right) \Big]$$

$$-JC_2(1-0.3\exp(-Re_t^2))\frac{\epsilon^2}{k} + 2\nu\nu_t\Big[\frac{1}{J} \left((\frac{\partial y}{\partial \eta})^2(\frac{\partial^2 u}{\partial \xi^2}) - 2\frac{\partial y}{\partial \eta}\frac{\partial y}{\partial \xi}\frac{\partial^2 u}{\partial \xi \partial \eta} + (\frac{\partial y}{\partial \xi})^2(\frac{\partial^2 \bar{u}}{\partial \eta^2}) \right)$$

$$+ \frac{1}{J^2} \Big(\left((\frac{\partial y}{\partial \eta})^2\frac{\partial^2 y}{\partial \xi^2}-2\frac{\partial y}{\partial \xi}\frac{\partial y}{\partial \eta}\frac{\partial^2 y}{\partial \xi \partial \eta}+(\frac{\partial y}{\partial \xi})^2\frac{\partial^2 y}{\partial \eta^2}\right) (\frac{\partial x}{\partial \eta}\frac{\partial u}{\partial \xi}-\frac{\partial x}{\partial \xi}\frac{\partial u}{\partial \eta})$$

$$+ \left((\frac{\partial y}{\partial \eta})^2\frac{\partial^2 x}{\partial \xi^2}-2\frac{\partial y}{\partial \xi}\frac{\partial y}{\partial \eta}\frac{\partial^2 x}{\partial \xi \partial \eta}+(\frac{\partial y}{\partial \xi})^2\frac{\partial^2 x}{\partial \eta^2} \right) (\frac{\partial y}{\partial \xi}\frac{\partial u}{\partial \eta} - \frac{\partial y}{\partial \eta}\frac{\partial u}{\partial \xi}) \Big]$$

$$+ \frac{1}{J}\left((\frac{\partial x}{\partial \eta})^2\frac{\partial^2 u}{\partial \xi^2} - 2\frac{\partial x}{\partial \eta}\frac{\partial x}{\partial \xi}\frac{\partial^2 u}{\partial \xi \partial \eta} + (\frac{\partial x}{\partial \xi})^2\frac{\partial^2 u}{\partial \eta^2} \right) \tag{4.51}$$

$$+ \frac{1}{J^2}\ (\left((\frac{\partial x}{\partial \eta})^2\frac{\partial^2 y}{\partial \xi^2} - 2\frac{\partial x}{\partial \xi}\frac{\partial x}{\partial \eta}\frac{\partial^2 y}{\partial \xi \partial \eta} + (\frac{\partial x}{\partial \xi})^2\frac{\partial^2 y}{\partial \eta^2} \right) (\frac{\partial x}{\partial \eta}\frac{\partial u}{\partial \xi} - \frac{\partial x}{\partial \xi}\frac{\partial u}{\partial \eta})$$

$$+ \left((\frac{\partial y}{\partial \eta})^2\frac{\partial^2 x}{\partial \xi^2} - 2\frac{\partial x}{\partial \xi}\frac{\partial x}{\partial \eta}\frac{\partial^2 x}{\partial \xi \partial \eta} + (\frac{\partial x}{\partial \xi})^2\frac{\partial^2 x}{\partial \eta^2} \right) (\frac{\partial y}{\partial \xi}\frac{\partial u}{\partial \eta} - \frac{\partial y}{\partial \eta}\frac{\partial u}{\partial \xi})\ ]$$

$$+ \frac{1}{J}\left((\frac{\partial y}{\partial \eta})^2\frac{\partial^2 v}{\partial \xi^2} - 2\frac{\partial y}{\partial \eta}\frac{\partial y}{\partial \xi}\frac{\partial^2 v}{\partial \xi \partial \eta} + (\frac{\partial y}{\partial \xi})^2\frac{\partial^2 v}{\partial \eta^2} \right)$$

$$+ \frac{1}{J^2}\ (\left((\frac{\partial y}{\partial \eta})^2\frac{\partial^2 y}{\partial \xi^2} - 2\frac{\partial y}{\partial \xi}\frac{\partial y}{\partial \eta}\frac{\partial^2 y}{\partial \xi \partial \eta} + (\frac{\partial y}{\partial \xi})^2\frac{\partial^2 y}{\partial \eta^2} \right) (\frac{\partial x}{\partial \eta}\frac{\partial v}{\partial \xi} - \frac{\partial x}{\partial \xi}\frac{\partial v}{\partial \eta})$$

$$+ \left((\frac{\partial y}{\partial \eta})^2\frac{\partial^2 x}{\partial \xi^2} - 2\frac{\partial y}{\partial \xi}\frac{\partial y}{\partial \eta}\frac{\partial^2 x}{\partial \xi \partial \eta} + (\frac{\partial y}{\partial \xi})^2\frac{\partial^2 x}{\partial \eta^2} \right) (\frac{\partial y}{\partial \xi}\frac{\partial v}{\partial \eta} - \frac{\partial y}{\partial \eta}\frac{\partial v}{\partial \xi})\ ]$$

$$+ \frac{1}{J}\left((\frac{\partial x}{\partial \eta})^2\frac{\partial^2 v}{\partial \xi^2} - 2\frac{\partial x}{\partial \eta}\frac{\partial x}{\partial \xi}\frac{\partial^2 v}{\partial \xi \partial \eta} + (\frac{\partial x}{\partial \xi})^2\frac{\partial^2 v}{\partial \eta^2} \right)$$

$$+ \frac{1}{J^2}\ (\left((\frac{\partial x}{\partial \eta})^2\frac{\partial^2 y}{\partial \xi^2} - 2\frac{\partial x}{\partial \xi}\frac{\partial x}{\partial \eta}\frac{\partial^2 y}{\partial \xi \partial \eta} + (\frac{\partial x}{\partial \xi})^2\frac{\partial^2 y}{\partial \eta^2} \right) (\frac{\partial x}{\partial \eta}\frac{\partial v}{\partial \xi} - \frac{\partial x}{\partial \xi}\frac{\partial v}{\partial \eta})$$

$$+ \left((\frac{\partial x}{\partial \eta})^2\frac{\partial^2 x}{\partial \xi^2} - 2\frac{\partial x}{\partial \xi}\frac{\partial x}{\partial \eta}\frac{\partial^2 x}{\partial \xi \partial \eta} + (\frac{\partial x}{\partial \xi})^2\frac{\partial^2 x}{\partial \eta^2} \right) (\frac{\partial y}{\partial \xi}\frac{\partial v}{\partial \eta} - \frac{\partial y}{\partial \eta}\frac{\partial v}{\partial \xi})\ ]$$

4.4 Modelling of Solidification Phenomena

4.4.1 Latent Heat Formulation

In using a fixed grid approach for the analysis of the solidification problem, the main difficulty is taking account of mass and heat transfer conditions in the vicinity of the phase change. The basic approach for tackling the problem is to define appropriate volume source terms for the governing equations.

In this study, the enthalpy formulation is adopted for the analysis of solidification heat transfer. Using the general form, equation (4.8), the following energy equation is used instead of equation (4.17).

$$\phi = h, \quad \Gamma_\phi = \frac{\kappa}{\rho} + \frac{\kappa_t}{\rho}, \quad S(x,y) = -\frac{\partial \Delta H}{\partial t} - \frac{\partial u \Delta H}{\partial x} - \frac{\partial v \Delta H}{\partial y} \tag{4.52}$$

where ΔH is the nodal latent heat defined as a function of temperature, and the equation is written in the simple Cartesian coordinate system. In the equation (4.52), obviously, the first term at the right in the source terms is the transient term being zero for steady state problems, while the second and third terms are the convective terms being zero for problems, where conduction is the only mode of heat transfer.

The treatment of latent heat is a major problem in phase change problems. In an alloy system, since the latent heat is associated with the liquid fraction in the mushy region, the local latent heat contribution term, ΔH, can be generally written by

$$\Delta H = \begin{cases} \lambda & T > T_L \\ \lambda f_L(T) & T_L > T > T_S \\ 0 & T < T_S \end{cases} \tag{4.53}$$

where λ is the latent heat, $f_L(T)$ is the local fraction of liquid, T_L the liquidus temperature at which solid starts to form and T_S is the temperature at which complete solidification is attained. In the case of a pure metal, T_L is identical to T_S because the phase change is isothermal. Note that the nature of the latent heat evolution in the mushy zone solely depends on the form of the local liquid-fraction-temperature relationship, i.e. $f_L(T)$.

The functional relationship should be both continuous and differential. In this study, a simple linear form is adopted. In non-dimensional form, the following relationships have been used for $f_L(T)$.

$$f_L(T) = \begin{cases} 1 & T > T_L \\ \dfrac{T-T_S}{T_L-T_S} & T_L > T > T_S \\ 0 & T < T_S \end{cases} \tag{4.54}$$

4.4.2 Enthalpy-Porosity Technique

In the solidification problem of an alloy system, fluid flow equations are applicable in both the fully liquid region and the mushy region. The enthalpy-porosity approach has been employed to formulate the equations for the conservation of momentum along with the following simplifying assumptions.

1. In the mushy region, the solid part only consists of dendritic columnar, and the structure is assumed to be isotropic in the unit volume.
2. The interdendritic flow in the mushy region is similar to fluid flow in porous media, and the flow velocity through the volume element is linearly related to pressure gradient; i.e., D'Arcy's law applies.
3. Any entrained crystallites in the liquid are assumed to have no effect on physical properties.

Figure 4.3 shows a schematic of dendritic columnar growth in the mould cavity or sump of the twin drum caster. When inertial effects are negligible, D'Arcy's law assumes the usual form as

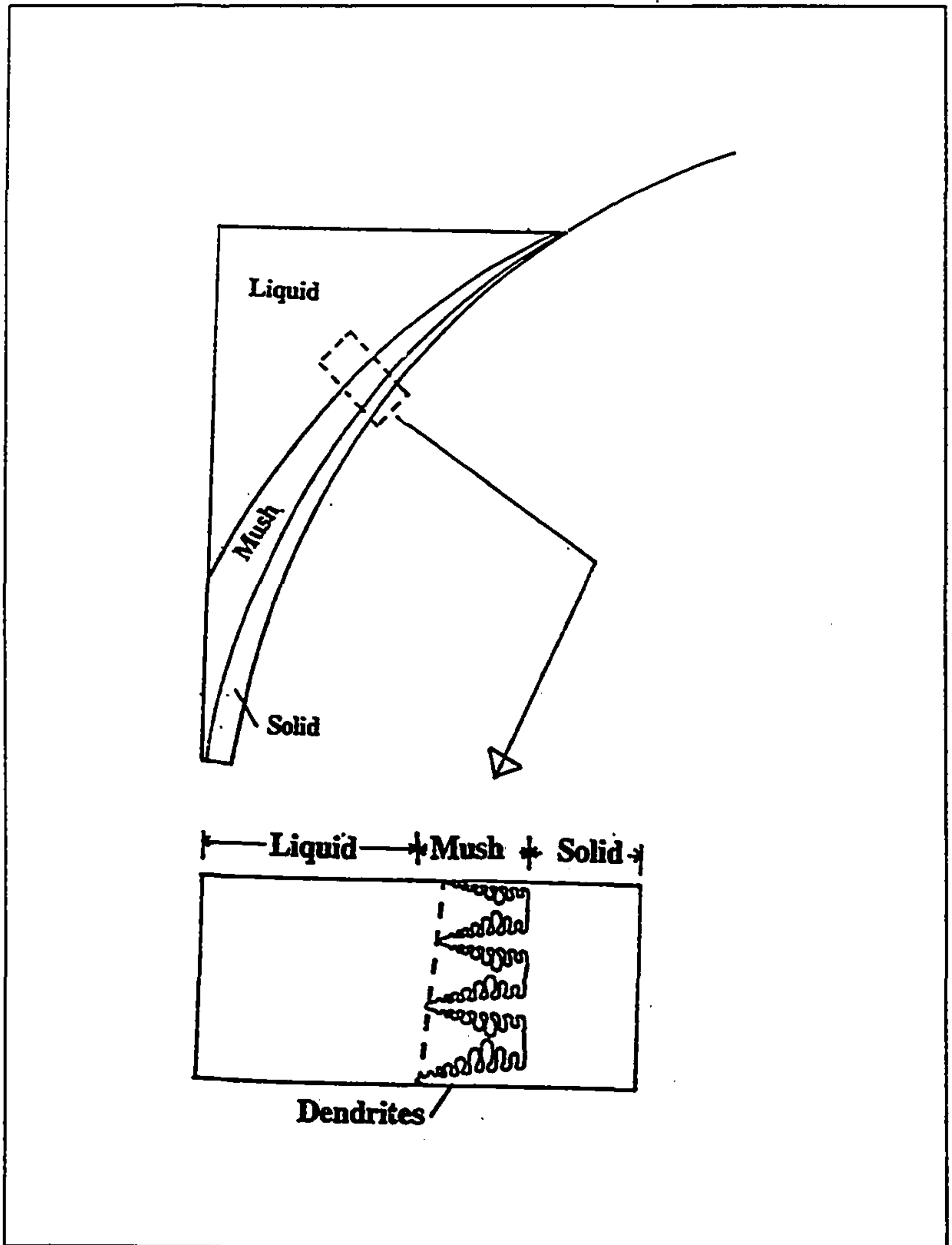

Figure 4.3 Schematic of columnar dendritic structure

$$\vec{V} = -\frac{K}{\mu}\left(\nabla p - \rho \vec{g} \right) \tag{4.55}$$

where V is the superficial velocity and K is the specific permeability of the porous media.

Coupling equation (4.55) with the governing equation (general form (4.8)), the momentum equations (4.10)–(4.11) can be reformulated as follows;

$$\phi = u, \quad \Gamma_\phi = \mu, \quad S(x,y) = -\frac{\partial p}{\partial x} + A(u-u_r) \tag{4.56}$$

$$\phi = v, \quad \Gamma_\phi = \mu, \quad S(x,y) = -\frac{\partial p}{\partial y} - \rho g + A(v-v_r) \tag{4.57}$$

The difference between the general form of the momentum equations and its modified form is only the additional terms in the source function S(x,y). It is important to chose an appropriate parameter, A, called the `porosity function', to model the modified equations. The porosity function is given by,

$$A = -\frac{\mu}{K} \tag{4.58}$$

The specific permeability, K, is a key parameter in the modelling of flow through a porous medium. Using the Blake–Kozeny equation to describe the flow through the porous media, the permeability can be written as,

$$K = C' \frac{l_c^2 f_L^3}{(1 - f_L)^2} \tag{4.59}$$

where C' is a constant and l_c is a characteristics length.

In the present work, the following equation has been used for the porosity function.

$$A = -\frac{\mu}{C'lc^2}\frac{(1-f_L)^2}{f_L^3} \approx -C''\frac{(1-f_L)^2}{f_L^3 + b} \tag{4.60}$$

Figure 4.4 illustrates the correlation between A and f_L when C'' is unity. The value of b is introduced to avoid zero division, and we have chosen a value of 10^{-3} from the point of view of the experimental fact that the critical liquid fraction to allow a flow is approximately 0.3. C'' is a constant to account for the mushy region, and should be defined as the condition that all interdendritic velocities in solid elements is zero. The actual value of C'' is somewhat arbitrary and will be discussed later.

Practically, the effect of A is as follows: In a fully liquid region, the liquid fraction f_L, is equal to unity, A is apparently zero and has no influence. Then equations (4.56) and (4.57) become identical with equations (4.10) and (4.11). In the mushy region, particularly at $f_L < 0.3$, the value of A will dominate other terms in the momentum equations. In the solid region, A has a large value and will swamp all other terms in the equations, and will force the velocity u to u_r i.e., equal to the roll velocity.

4.5 Boundary Condition

4.5.1 Roll Surface

The system contains the moving roll boundary whose tangential velocity is equal to the casting speed. So velocity components u and v on the roll boundary have the following values,

$$u = -U_r \sin\Theta, \quad v = -U_r \cos\Theta \tag{4.61}$$

where U_r is the casting speed, and Θ is the angular position of the node on the roll surface as illustrated in Figure 4.5.

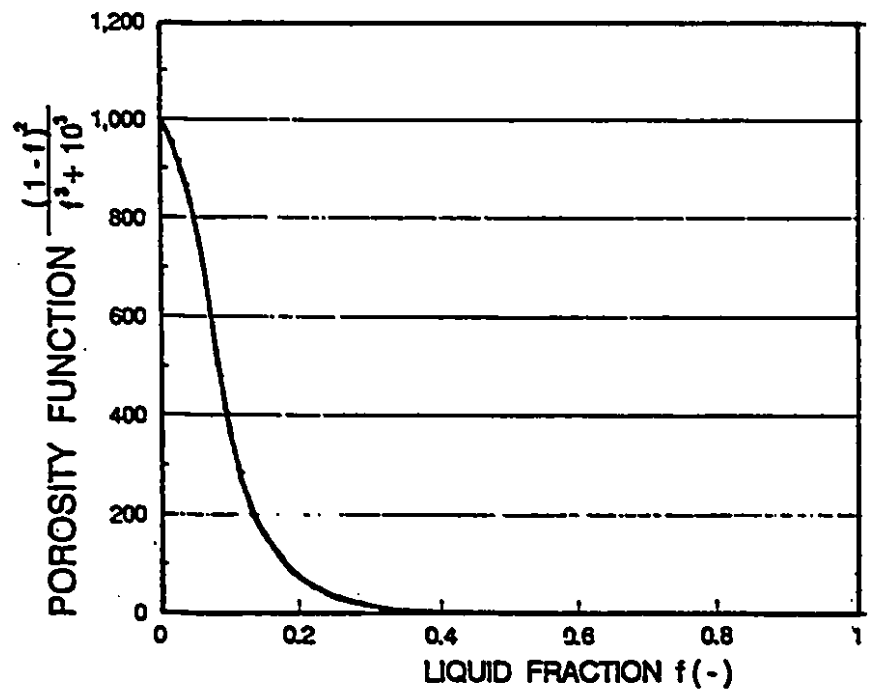

Figure 4.4 Porosity function for momentum equation

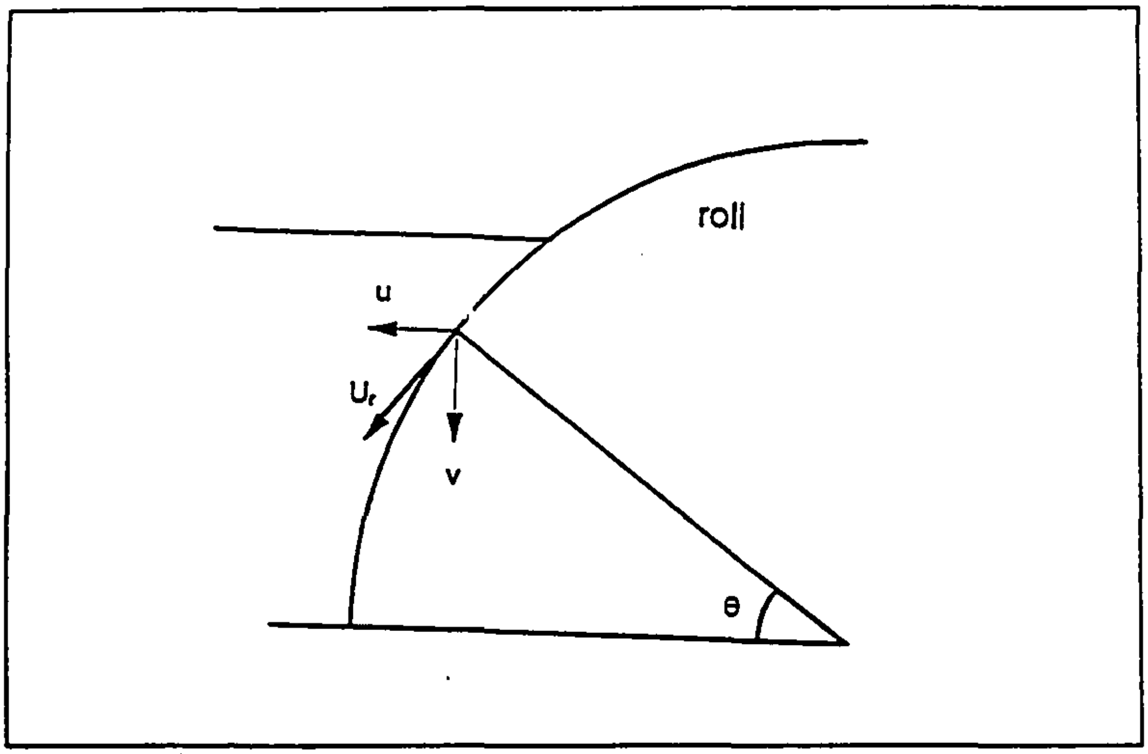

Figure 4.5 Schematic of position

In the Jones & Launder type low Reynolds number model, the turbulent energy k and the rate of dissipation of turbulent energy ϵ are equal to zero on the roll because there is no velocity fluctuation at the solid wall. As a result, boundary conditions for k and ϵ are written as,

$$k = \epsilon = 0 \tag{4.62}$$

The roll is water cooled, and the heat is taken out from the mould through the rolls. In this study, four kinds of boundary conditions were used for the energy equation.
These are:

1. Dirichlet condition I

$$T_{roll} = T_r = constant \tag{4.63}$$

2. Dirichlet condition II

$$T_{rollI} = T_r(x,y) \tag{4.64}$$

3. Newman condition I

$$q_{roll} = -\frac{k}{C_p}\frac{\partial h}{\partial n_\xi} = -\frac{k}{C_p J\sqrt{\alpha}}\left(\alpha\frac{\partial h}{\partial \xi} - \beta\frac{\partial h}{\partial \eta}\right) = constant \tag{4.65}$$

4. Newman condition II

$$q_{roll} = -\frac{k}{C_p J\sqrt{\alpha}}\left(\alpha\frac{\partial h}{\partial \xi} - \beta\frac{\partial h}{\partial \eta}\right) = h_i(T-T_\infty) \tag{4.66}$$

where h_i is local heat transfer coefficient and T_∞ is the ambient temperature.

4.5.2 Symmetric Axis

In order to save on computational costs, a symmetric half of the domain has been taken for calculations. Considering the steady state, all variables should be symmetrical about the vertical centre line. Since the ξ-coordinate lines are perpendicular to the central axis, boundary conditions on the symmetrical axis can be written as:

$$u = 0, \quad \frac{\partial \phi}{\partial \xi} = 0, \quad (\phi = v, k, \epsilon, h) \tag{4.67}$$

4.5.3 Free surface

The top surface of the mould is assumed flat and horizontal, and the free slip boundary condition is adopted for the momentum equations. From the condition that shear stress is equal to zero, the boundary condition for velocities can be written as,

$$v = 0, \quad J\frac{\partial v}{\partial \xi} - \beta\frac{\partial u}{\partial \xi} + \gamma\frac{\partial u}{\partial \eta} = 0 \tag{4.68}$$

Concerning the energy, turbulent energy and rate of energy dissipation equations, adiabatic boundary conditions were employed. The adiabatic boundary condition in a general form can be written as:

$$\beta\frac{\partial \phi}{\partial \xi} - \gamma\frac{\partial \phi}{\partial \eta} = 0 \qquad (\phi = k, \epsilon , h) \tag{4.69}$$

In case of a molten metal on an (oxidized) substrate, a large contact angle on the roll is expected owing to its large surface tension and non-wetting characteristics. Therefore, the meniscus shape of the corner between the top free surface and a roll is not sharp as in the water system but should be determined by the surface tension and the friction force on the moving wall. It is one of the unknown factors of this process, and an appropriate shape was guessed from experimental data under static conditions. Figure 4.6 shows the relation between liquid height and properties.(Jimbo et al. 1992)

The insulated boundary condition is used there.

4.5.4 Inlet & Outlet

From the mass balance i.e.,(width of nozzle) × (inlet velocity) = (strip thickness) × (casting speed), the inlet velocity boundary condition at the nozzle can be obtained :

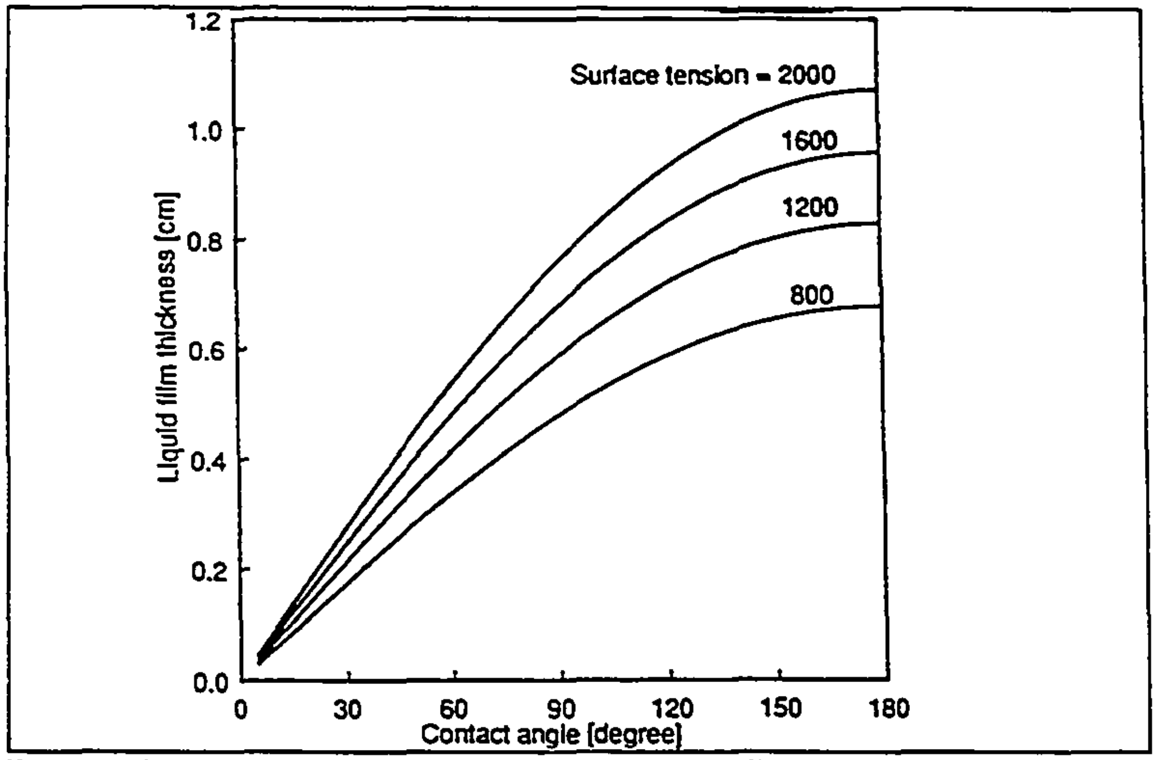

Figure 4.6 Relation between contact angle and liquid film thickness

$$u_{in} = 0, \quad v_{in} = \frac{dU_r}{D_{in}} \tag{4.70}$$

where D_{in} represents the width of the inlet nozzle slot, d is the strip thickness and U_r is the casting speed. Values for k and ϵ are fixed by fitting in with the inlet velocity, and using the coefficients at the fully turbulent condition for an air system (Murakami et al., 1988). The inlet enthalpy is known from the melt pouring temperature.

$$k_{in} = 0.05(u_{in}^2+v_{in}^2), \quad \epsilon_{in} = \frac{C_\mu k_{in}^{1.5}}{0.03D_{in}}, \quad h_{in} = \int_{T_{ref}}^{T_{in}} C_p dT_{in} \tag{4.71}$$

In practice, a submerged nozzle made of refractory is often used to deliver molten metal. Both in the domain and on boundaries of the submerged nozzle, all fluid elements are fixed at zero velocities, while appropriate thermal properties of a refractory e.g. (Al_2O_3) are used for the equation.

$$u_n = v_n = k_n = \epsilon_n = 0, \quad \Gamma_{h_n} = \frac{\kappa_n}{C_{p,n}} \tag{4.72}$$

For the outlet flow boundary, a fully developed condition was used. Since η–coordinate lines are almost perpendicular to the outlet boundary, the outlet condition can be written as,

$$u = 0, \quad \frac{\partial \phi_{out}}{\partial \eta} = 0, \quad (\phi = v, k, \epsilon, h) \tag{4.73}$$

4.6 Numerical Procedure

4.6.1 Discretization

The governing equations were discretized by an averaging procedure over small control volumes surrounding the nodal points. A staggered grid adjustment was employed for the location of the dependent variables in which all scalar variables were located at the geometric centres of the control volumes while velocities were calculated at the centres of the faces to avoid unrealistic fluctuations of pressure, in what is called a 'checker–board pressure' field.

Figure 4.7 and Figure 4.8 show parts of the two–dimensional grid structures on the physical plane and the transformed plane, respectively. The line joining the grid points E, P and W represent x–direction (or ξ–direction) while the line joining the nodes N, P and S represent the y–direction (or η–direction). Control volumes are shown by dashed lines, and points e, w, n and s lie on each interface of the control volume around the point P. In the rectangular transformed plane, the grid point is always at the centre of the control volume because a B–type grid (Patankar, 1980) was employed.

The finite–difference approximation to the conservation laws was used by taking the integral of the transformed governing equation (4.40) over the control volume. The resulting form at steady state is written as,

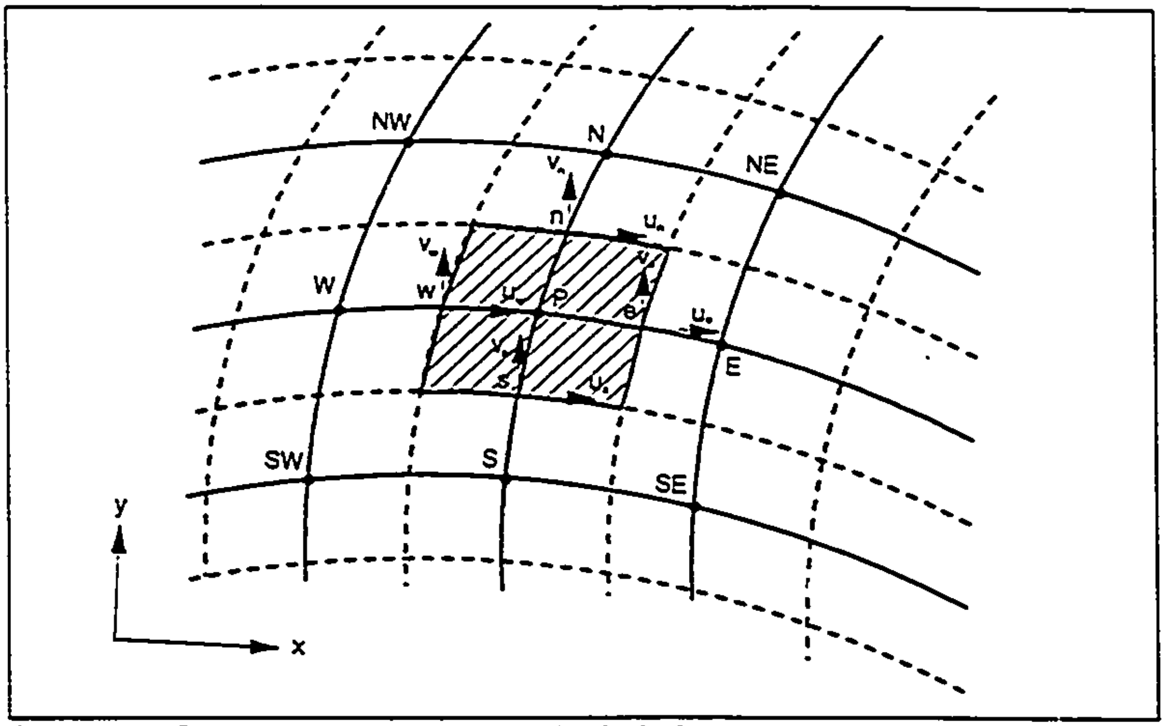

Figure 4.7 Grid representation in the physical plane

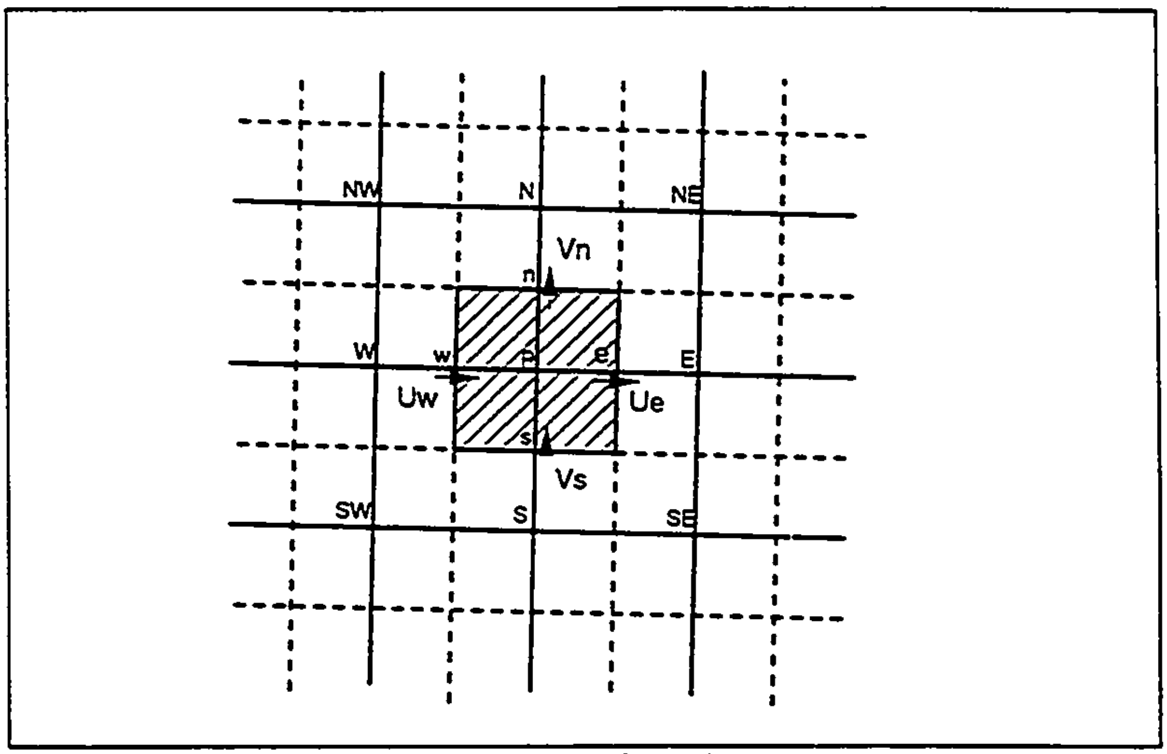

Figure 4.8 Grid representation in the transformed plane

$$[\ U\phi\delta\eta\ ]_w^e + [\ V\phi\delta\xi\ ]_s^n =$$
$$\left[\ \frac{\Gamma_\phi}{J}(\alpha\frac{\partial\phi}{\partial\xi} - \beta\frac{\partial\phi}{\partial\eta})\delta\eta\ \right]_w^e + \left[\ \frac{\Gamma_\phi}{J}(\gamma\frac{\partial\phi}{\partial\eta} - \beta\frac{\partial\phi}{\partial\xi})\delta\xi\ \right]_s^n + S(\xi,\eta)\delta\xi\delta\eta \tag{4.74}$$

usually $\delta\xi = \delta\eta = 1$ to render computations simple.
Equation (4.74) is formally of the same form as the finite-difference equation derived in Cartesian coordinates, while the relation between ϕ_P and neighbouring variables is :

$$a_P\phi_P = a_E\phi_E + a_W\phi_W + a_N\phi_N + a_S\phi_S + S_P \tag{4.75}$$

where the coefficients a involve the flow properties of convection and diffusion, and S_P involves the cross derivatives, the pressure gradients, the buoyancy force, etc.

In the convection-diffusion formulation of numerical fluid analysis, the treatment of convective terms is very important. Integration of the control volume with the first order derivative terms, like the convective terms, has the cental difference form of the natural outcome of a Taylor-series formula, which does not contain its own value. Unless using enough fine grid formation, such a discretized equation often gives unrealistic solutions like 'wiggles' satisfying only the continuity in a control volume.

To avoid the unrealistic solutions, following schemes are used to evaluate the convective terms:

$$a_E = \Gamma_e A(|F_e|) + MAX(\ -\bar{U}_e\ ;\ 0\ ) \tag{4.76}$$

$$a_W = \Gamma_w A(|F_w|) + MAX(\ -\bar{U}_w\ ;\ 0\ ) \tag{4.77}$$

$$a_N = \Gamma_n A(|F_n|) + MAX(\ -\bar{V}_n\ ;\ 0\ ) \tag{4.78}$$

$$a_S = \Gamma_s A(|F_s|) + MAX(\ -\bar{V}_s\ ;\ 0\ ) \tag{4.79}$$

where

$$F_e \equiv \frac{\bar{U}_e}{\Gamma_e}, \quad F_w \equiv \frac{\bar{U}_w}{\Gamma_w}, \quad F_n \equiv \frac{\bar{V}_n}{\Gamma_n}, \quad F_s \equiv \frac{\bar{V}_s}{\Gamma_n} \tag{4.80}$$

1. Upwind scheme (Courant et al., 1952)

$$A(|F|) = 1 \tag{4.81}$$

2. Hybrid scheme (Spalding, 1972)

$$A(|F|) = MAX(\ 0,\ 1-0.5|F|\ ) \tag{4.82}$$

3. Power law scheme (Patankar, 1979)

$$A(|F|) = MAX(\ 0,\ (1-0.1|F|)^5\ ) \tag{4.83}$$

4.6.2 Algorithm

A modified SIMPLER (Semi-Implicit Method for Pressure Linked Equations Revised, Patankar, 1980) procedure has been devised to resolve the velocity-pressure coupling problem in non-orthogonal curvilinear coordinates. The sequence developed for the solution procedure is discussed below.

1. Generate grid formation and store the coefficients for transformation.
2. Guess initial values for all dependent variables and calculate the contra-variant velocities U and V using an initial velocity field and calculate the coefficients for the momentum equations. For instance, the discretized momentum equations for u_e and v_e are obtained by integrating the momentum equations over the control volume around the point e, as follows,

$$u_e = \frac{\sum a_{nb}u_{nb}}{a_e} + \frac{B_e^u}{a_e} - \frac{\Delta V}{a_e}\left(\frac{P_E - P_P}{(\Delta\xi)_e}\left(\frac{\partial y}{\partial \eta}\right)_e - \frac{P_N+P_{NE}-P_S-P_{SE}}{4(\delta\eta)_e}\left(\frac{\partial y}{\partial \xi}\right)_e \right) \tag{4.84}$$

$$v_n = \frac{\sum a_{nb} v_{nb}}{a_n} + \frac{B_n^v}{a_n} - \frac{\Delta V}{a_n}\left(\frac{P_N - P_P}{\Delta\eta}\left(\frac{\partial x}{\partial \xi}\right)_n - \frac{P_{NE} + P_E - P_{NN} - P_W}{4(\delta\xi)_n}\left(\frac{\partial x}{\partial \eta}\right)_n \right) \tag{4.85}$$

$$U_e = u_e\left(\frac{\partial y}{\partial \eta}\right)_e - v_e\left(\frac{\partial x}{\partial \eta}\right)_e \tag{4.86}$$

$$V_e = v_e\left(\frac{\partial x}{\partial \xi}\right)_e - u_e\left(\frac{\partial y}{\partial \xi}\right)_e \tag{4.87}$$

where the coefficients B_e^u and B_n^v are the source terms excluding the pressure terms. Similar equations around the points *w* and *s* can be obtained. The value v_e can be obtained by interpolating values *n, ne, s* and *se*.

3. Construct the pressure equation and solve it.

$$\begin{aligned} a_P P_P &= a_E P_E + a_W P_W + a_N P_N + a_S P_S \\ &\quad + \frac{a_{NE} P_{NE} + a_{NW} P_{NW} + a_{SE} P_{SE} + a_{SW} P_{SW}}{B_f} + B \end{aligned} \tag{4.88}$$

where

$$B = (\langle U_w \rangle - \langle U_e \rangle)\Delta\eta_P + (\langle V_s \rangle - \langle V_n \rangle)\Delta\xi_P \tag{4.89}$$

Considering the effect of the second neighbouring terms B_f is small, it is assumed to be zero to avoid fluctuations in the solutions during implementation. The pseudo-velocities $\langle u \rangle$ and $\langle v \rangle$ are defined as follows,

$$\langle U \rangle = \langle u \rangle\left(\frac{\partial y}{\partial \eta}\right) - \langle v \rangle\left(\frac{\partial x}{\partial \eta}\right) \tag{4.90}$$

$$\langle V \rangle = \langle v \rangle\left(\frac{\partial x}{\partial \xi}\right) - \langle u \rangle\left(\frac{\partial y}{\partial \xi}\right) \tag{4.91}$$

$$i.e. \quad \langle u_e \rangle = \frac{\sum a_{nb} u_{nb} + B_e^u}{a_P}, \quad \langle v_e \rangle = \frac{\sum a_{nb} v_{nb} + B_e^v}{a_P} \tag{4.92}$$

4. With the new pressure field, the momentum equations are solved. The TriDigonal Matrix Algorithm (TDMA) is used for the solver.
5. Solve the pressure correction, $P'=P-P^*$, using equation (4.93).

$$\begin{aligned} a_P P'_P &= a_E P'_E + a_W P'_W + a_N P'_N + a_S P'_S \\ &+ a_{NE} P'_{NE} + a_{NW} P'_{NW} + a_{SE} P'_{SE} + a_{SW} P'_{SW} + B' \end{aligned} \tag{4.93}$$

$$B' = (U_w - U_e)\Delta\eta_P + (V_s - V_n)\Delta\xi_P \tag{4.94}$$

where, also, the second neighbouring terms are neglected.

6. Correct velocities. Cartesian velocity corrections are calculated from,

$$u'_e = u_e - u_e^* = -\frac{\Delta V}{a_e - \sum a_{nb}} \left(\frac{P'_E - P'_P}{(\Delta\xi)_e} \left(\frac{\partial y}{\partial \eta}\right)_e - \frac{P'_N + P'_{NE} - P'_S - P'_{SE}}{4(\delta\eta)_e} \left(\frac{\partial y}{\partial \xi}\right)_e \right) \tag{4.95}$$

$$v'_n = v_n - v_n^* = -\frac{\Delta V}{a_n - \sum a_{nb}} \left(\frac{P'_N - P'_P}{\Delta\eta} \left(\frac{\partial x}{\partial \xi}\right)_n - \frac{P'_{NE} + P'_E - P'_{NW} - P'_W}{4(\delta\xi)_n} \left(\frac{\partial x}{\partial \eta}\right)_n \right) \tag{4.96}$$

Similar expressions can be written for u_w' and v_s'.

7. Solve equations for energy, k and ϵ, and calculate turbulent viscosity and porosity at each node if necessary.
8. Repeat steps 1 through 7 until convergence is reached.

The above solution procedure has been used on many test problems and have been found to be stable and gives reasonable time requirements for computations.

4.6.3. Technique for Convergence

The successive under-relaxation (SUR) method was used to solve the system of finite difference equations. It was found SUR aided convergence quite favourably.

$$\phi_{i,j}^{N+1'} = \phi_{i,j}^{N'} + \omega(\phi_{i,j}^{N+1} - \phi_{i,j}^{N'}) \qquad (0 < \omega < 1) \tag{4.97}$$

where N denotes iteration level and $\phi_{i,j}^{N+1}$ is the most recent value of $\phi_{i,j}$, $\phi_{i,j}^{N}$ is the value from the previous iteration as adjusted by previous application of this formula, and $\phi_{i,j}^{N+1'}$ is the newly adjusted or "better guess" for $\phi_{i,j}$ at the (N+1)-th iteration level.

The convergence criterion is, at all nodes,

$$\frac{(\phi_{i,j}^{N} - \phi_{i,j}^{N-1})}{\phi_{ref}^{N}} < 0.00001 \tag{4.98}$$

where $\tilde{\omega}$ is the relaxation factor, $\phi_{i,j}^{N}$ is the value of u, v, h, k, ϵ at the (i,j)-th grid node after the N-th iteration cycle.

FLUID FLOW AND HEAT TRANSFER IN A WEDGE-SHAPED POOL

5.1 Introduction

In this chapter, several examples of fluid flow simulations in a wedge-shaped pool are performed so as to obtain a fundamental understanding of the system. The physical domain along with the generated grid lines are shown in Figure 5.1 along with the type B-grid structure (Patankar, 1980) which is generated by the non-orthogonal body fitted coordinate scheme. The non-dimensional equation (5.1) is solved for dependent variables.

$$\frac{\partial(U\phi)}{\partial\xi}+\frac{\partial(V\phi)}{\partial\eta} = \left[\frac{\partial}{\partial\xi}\left(\Gamma_\phi\frac{\alpha}{J}\frac{\partial\phi}{\partial\xi} - \Gamma_\phi\frac{\beta}{J}\frac{\partial\phi}{\partial\eta} \right)+\frac{\partial}{\partial\eta}\left(\Gamma_\phi\frac{\gamma}{J}\frac{\partial\phi}{\partial\eta} - \Gamma_\phi\frac{\beta}{J}\frac{\partial\phi}{\partial\xi} \right) \right] + S(\xi,\eta) \tag{5.1}$$

where the contra-variant velocities U, V are

$$U = \bar{u}\left(\frac{\partial\bar{y}}{\partial\eta}\right) - \bar{v}\left(\frac{\partial\bar{x}}{\partial\eta}\right), \qquad V = \bar{v}\left(\frac{\partial\bar{x}}{\partial\xi}\right) - \bar{u}\left(\frac{\partial\bar{y}}{\partial\xi}\right) \tag{5.2}$$

where also ϕ is a non-dimensional variable, ξ and η are dimensionless coordinates.

For discretization of convective terms, the aforementioned 'upwind scheme' (equation (4.95)) was used. A relaxation factor of 0.5 was used for variables u, v, k and ϵ, and it took about 4000 iterations to obtain converged solutions.

The effects of Reynolds number ($10 \sim 10^7$), boundary conditions (wall & free-slip), velocity of inlet flow and characteristic length, D, are discussed. In particular, the velocity profile in the vicinity of the surface of the moving roll is investigated in detail, and features of fluid flow structure in both laminar and turbulence are discussed.

Further, the heat transfer problems, including both the natural and forced convection in

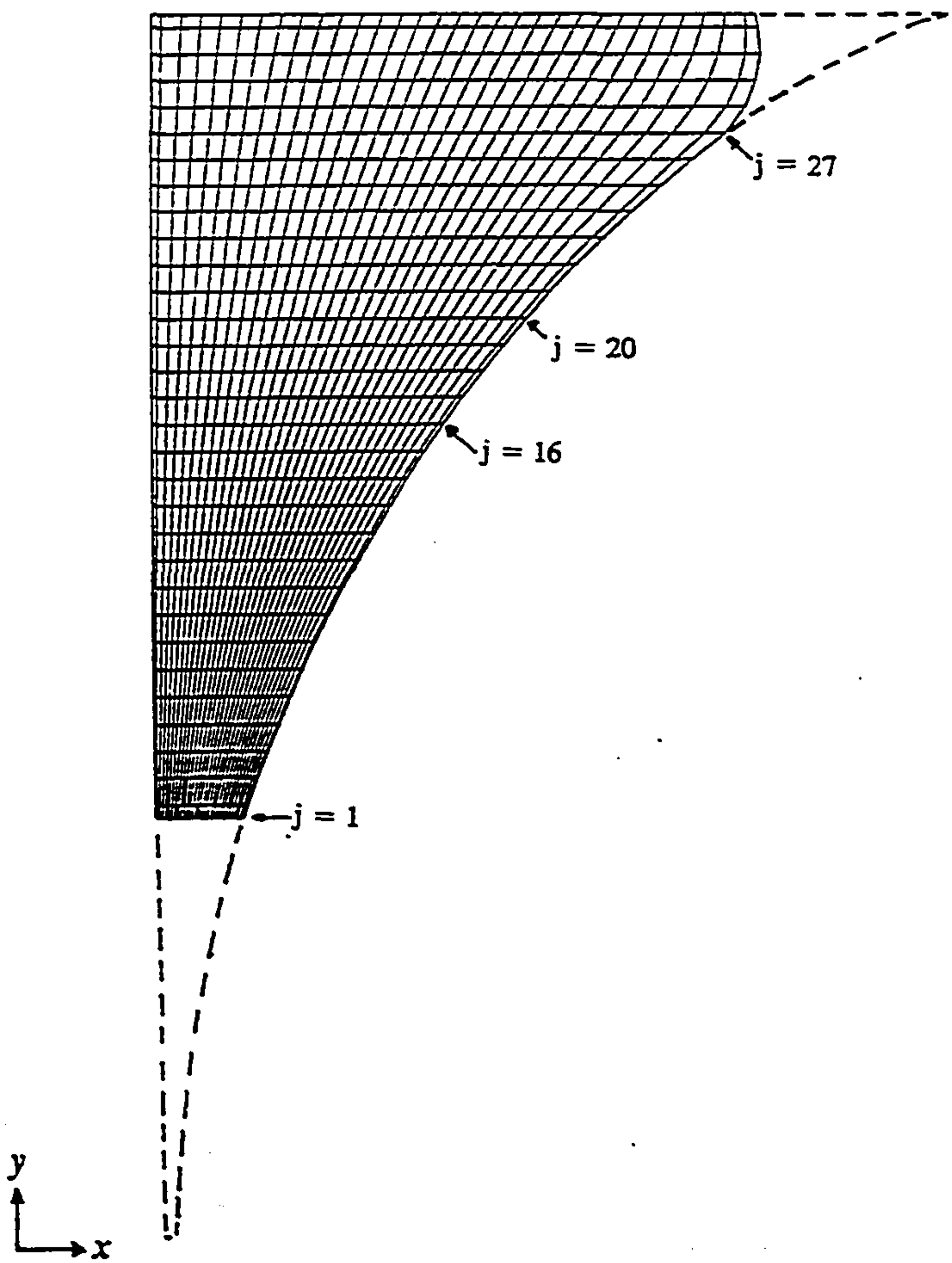

Figure 5.1 Grid structure in the physical domain

the system are investigated. The effects of Reynolds number, buoyancy force and turbulent heat transfer are also discussed. Finally, the fluid flow model is validated by comparing experimental data of an aqueous experimental model in Hikari Works at N.S.C. with present computations.

5.2 Closed System

5.2.1. Laminar Flow

Laminar momentum transport in a wedge-shaped system with a moving roll surface were first investigated, computationally. The laminar momentum equations are obtained using the following coefficients and source terms in equation (5.1).

$$\phi = \bar{u},\ \ \Gamma_\phi = \frac{1}{Re},\ \ S(\xi,\eta) = -\left(\frac{\partial \bar{y}}{\partial \eta}\right)\left(\frac{\partial \bar{P}}{\partial \xi}\right) + \left(\frac{\partial \bar{y}}{\partial \xi}\right)\left(\frac{\partial \bar{P}}{\partial \eta}\right) \tag{5.3}$$

$$\phi = \bar{v},\ \ \Gamma_\phi = \frac{1}{Re},\ \ S(\xi,\eta) = -\left(\frac{\partial \bar{x}}{\partial \xi}\right)\left(\frac{\partial \bar{P}}{\partial \eta}\right) + \left(\frac{\partial \bar{x}}{\partial \eta}\right)\left(\frac{\partial \bar{P}}{\partial \xi}\right) + J\,\frac{Gr}{Re^2}\frac{(\bar{h} - \bar{h}_c)}{(\bar{h}_h - \bar{h}_c)} \tag{5.4}$$

Steady state results of the velocity field in a closed domain surrounded by walls are shown in Figure 5.2 ($u = v = 0$ on all boundaries). The radius of the roll, R, was chosen as the characteristic length for the Reynolds number which was varied from 10 to 10^4.

It is seen that fluid near the moving roll boundary is pulled down and that a large recirculation is developed to satisfy mass balance. The top left corner of the domain becomes a stagnant zone owing to the stationary meniscus surface. Very similar flow profiles were obtained at Re=10 and Re=100.

The flow profile at $Re=10^3$ shows a relative decrease in the thickness of the downwards flow near the roll surface, and a relatively weaker counter flow from the bottom. In the case of $Re=10^4$, the downwards flow on the roll becomes much thinner compared to the other cases. Since the definition of Reynolds number is the ratio between inertial force and viscous force,

$Re=UD/\nu$, a large Reynolds number means either a large scale length, a high speed, or a low kinematic viscosity. The trend in the numerical results seems physically realistic and one notes that the length scale for velocity is represented by dimensionless arrows equal to u/U_r.

A converged solution to the fluid flow equations was obtained for Reynolds number more than $2x10^4$ only when a turbulent model was employed. Empirically, it is well known that the low critical Reynolds number is 2300 and the high critical Reynolds number is approximately $5x10^4$ for a pipe flow: When the Reynolds number of a flow is smaller than the lower critical Reynolds number, the flow remains in laminar conditions despite any disturbances in the entry flow. When the Reynolds number is larger than the high critical Reynolds number, the flow shifts from laminar to turbulent flow, independent of any external disturbances (Iwanami & Hirayama, 1983).

Figure 5.3 and Figure 5.4 provide qualitative plots of non–dimensional velocities for the downward flow near the roll, as a function of normal distance from the surface of the roll. Six representative points are shown in Figure 5.1 (j=16~20) around the centre of an arc of the roll surface. As seen in Figure 5.3(a) and Figure 5.3(b), at low Reynolds number flow, velocities near the wall (roll) decreased linearly with normal distance (R–square of each regression is higher than 99%), like laminar flow on a flat plate. The difference among values at each j point may have been caused by the effects of the curved surface and closed boundaries. Figure 5.4(c) shows that velocities near the roll at Re=1000 decrease in a logarithmic manner similar to the near wall region for turbulent flow over a flat surface; in this case, the root mean square of each regression is also higher than 99%. Further, in the case of $Re=10^4$ (Figure 5.4), the best regression of velocities near the roll is obtained not by a logarithmic curve but with a power law fitted curve. Obviously the structure of each flow is distinct.

To investigate the influence of boundary conditions other than the roll boundary, flow simulations for $Re=10\sim10^4$ were performed using a symmetrical boundary condition for the left and free surface boundary condition at the top. (see equation (4.82)–(4.83)) These boundary conditions are rather similar to that of a symmetric half of the mould of a twin roll caster. Figure 5.5(a)~(d) show the results of velocity fields.

Since the flow slips freely on the left and top boundaries, the recirculating flow is much stronger and boundary layers on the roll are thicker than that for stationary wall conditions

(Figure 5.2). The stagnant zone at the left top corner also disappeared for this condition.

5.2.2. Turbulent Flow

Although the aforementioned results were obtained in low Reynolds systems, a real twin roll casting system has a much higher Reynolds number; for instance, Reynolds numbers range from 10^5~10^6 in the twin drum caster at N.S.C..

Figure 5.6 shows velocity field for Re=10^4~10^7. The flow simulations were performed using Jones & Launder type low Reynolds number k–ε turbulent model with free–slip boundary condition on the top along with the symmetric boundary condition at the left. In the case of Re=10^4, the turbulent viscosity is almost negligible (turbulent energy $k < 10^{-27}$), and the flow can be regarded as laminar. Figure 5.6 (a) is identical with that of the laminar model (Figure 5.5(d)).

When the Reynolds number is greater than 10^5, the non–dimensional velocity profile becomes independent of Reynolds number, as shown in Figure 5.6.

Figure 5.7 shows the relationship between velocity in vicinity of the roll surface and normal distance from the surface, similar to Figure 5.3a and Figure 5.3b. Not only can the relation between velocity and normal distance be expressed by similar logarithmic curves, but the velocity profiles near the roll are also practically identical with each other, the flow structure becomes independent of Reynolds number in this turbulent system for Re > 10^5.

Figure 5.9 and Figure 5.10 show profile of turbulent kinematic energy and of dissipation rate of turbulent energy, respectively. The strongest turbulence develops at the vicinity of the moving roll surface because of the large velocity field. Another large turbulent energy region develops at the left top corner because of the interaction of strong upwards flow. The weakest turbulence region lies around the centre part of the domain because of the flow stagnant zone at the centre of the recirculation. The region of high dissipation rate of turbulent energy also exists in the vicinity of the roll surface.

The profiles of turbulent kinetic energy and those of dissipation rate of turbulent energy for three different Reynolds number are very similar to each other. In particular, the results of Re=10^6 and Re=10^7 are practically identical.

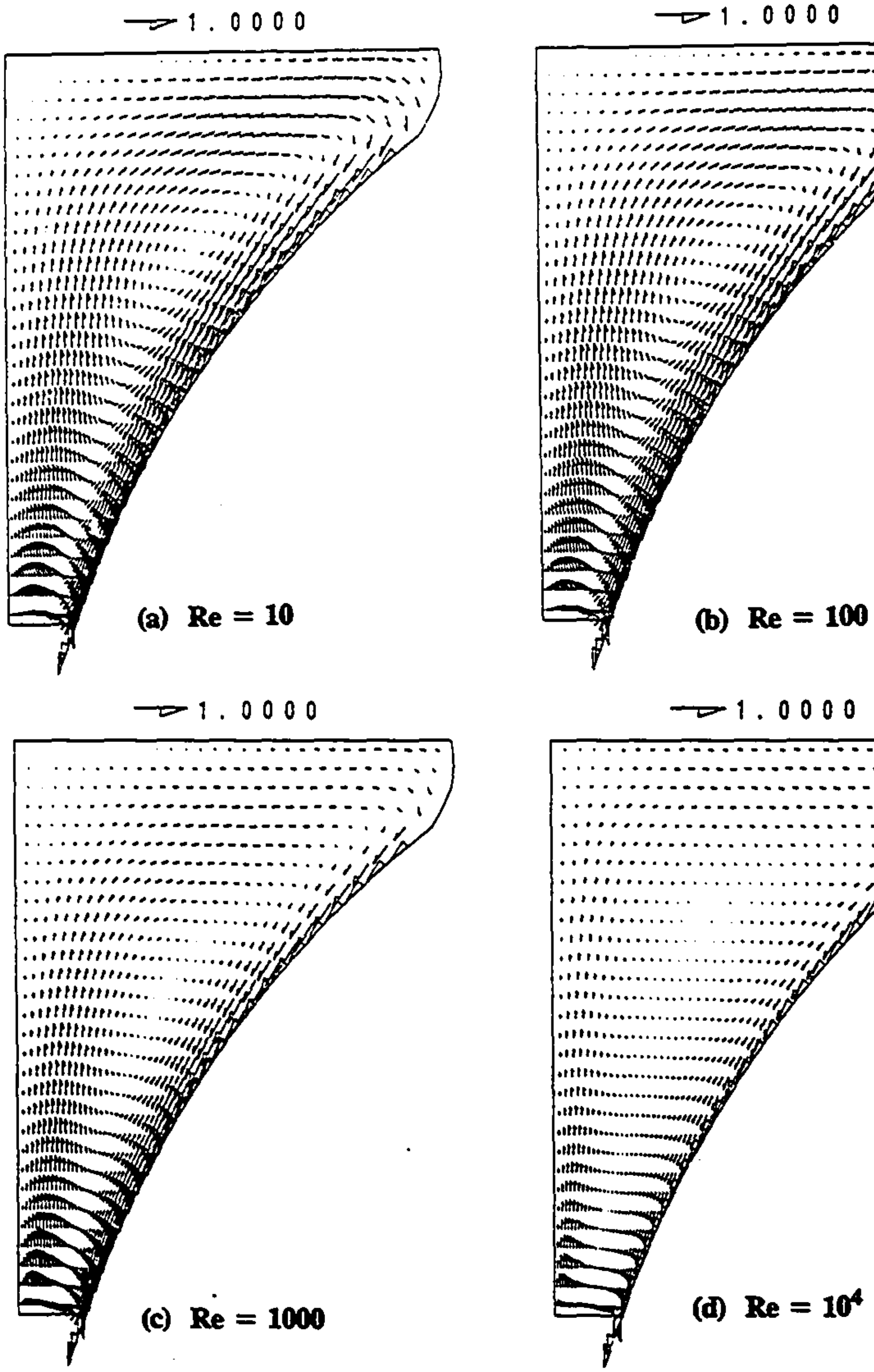

Figure 5.2 Non-dimensional velocity profile in the closed domain surrounded by walls

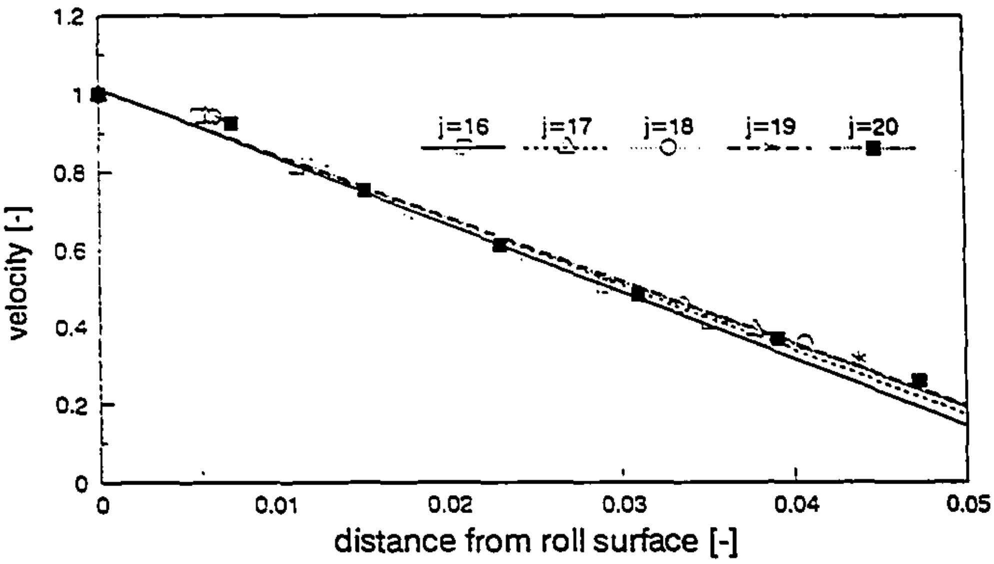

(a) Re=10

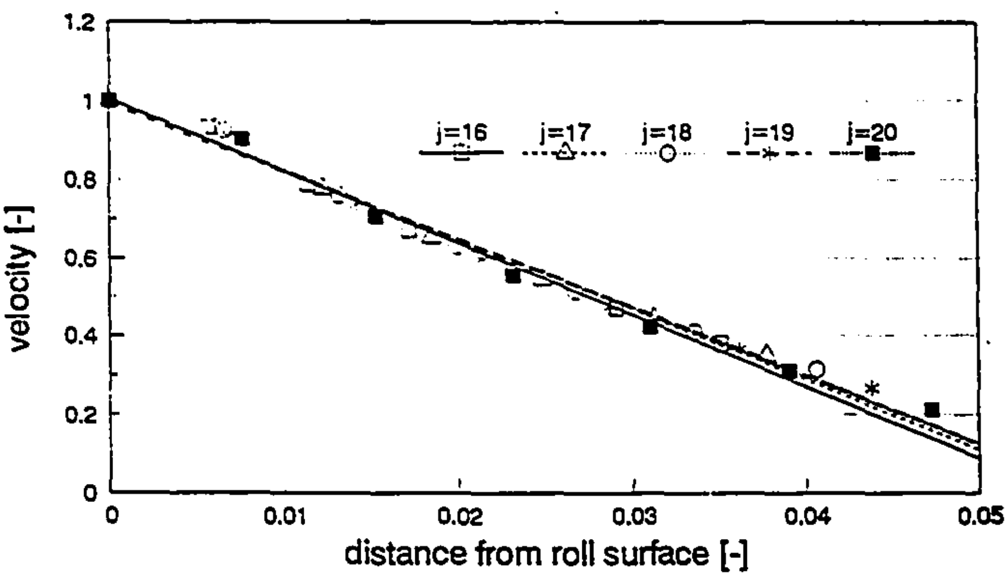

(b) Re=100

Figure 5.3 Relation between velocity and normal distance from roll (I)

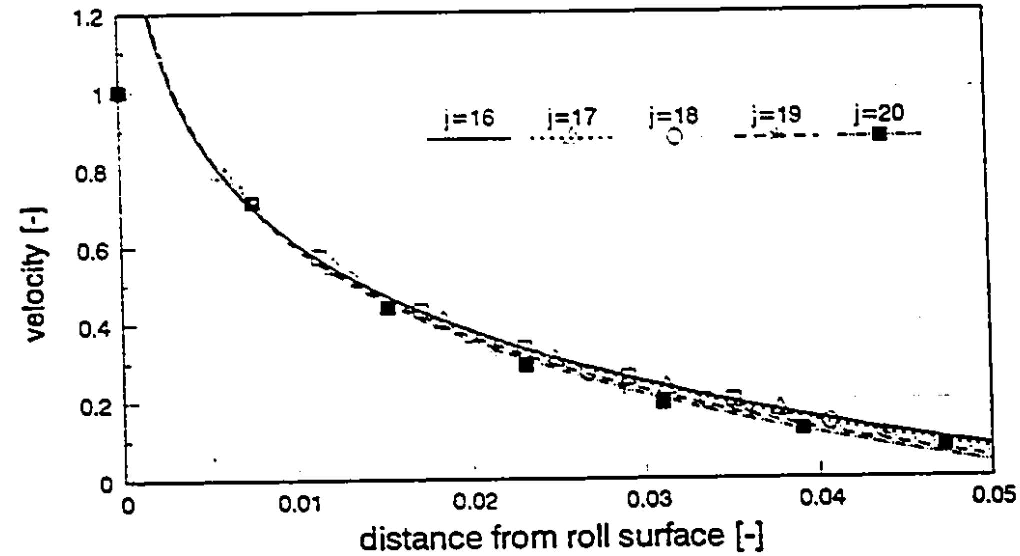

(c) Re=1000

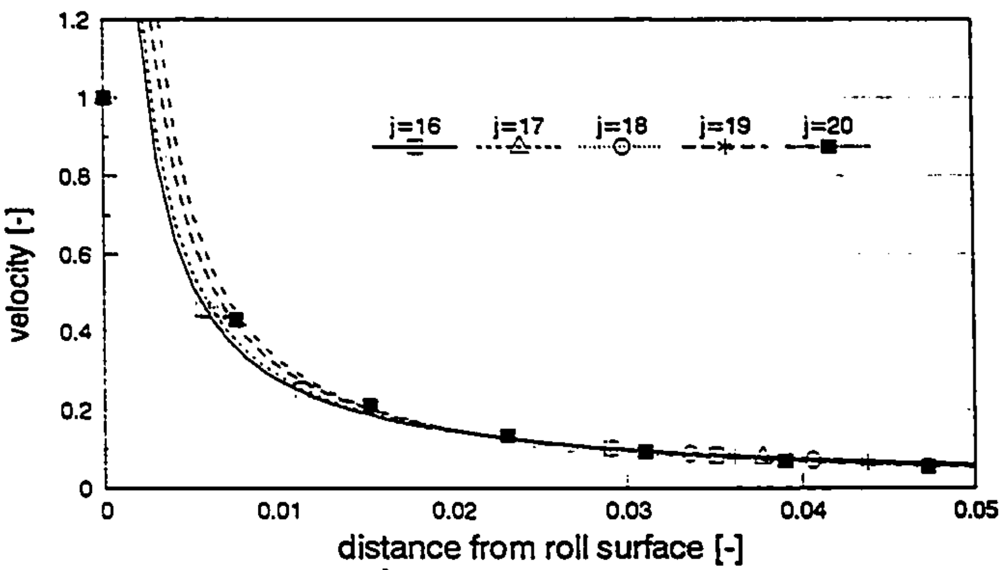

(d) Re=10000

Figure 5.4 Relation between velocity and normal distance from roll (II)

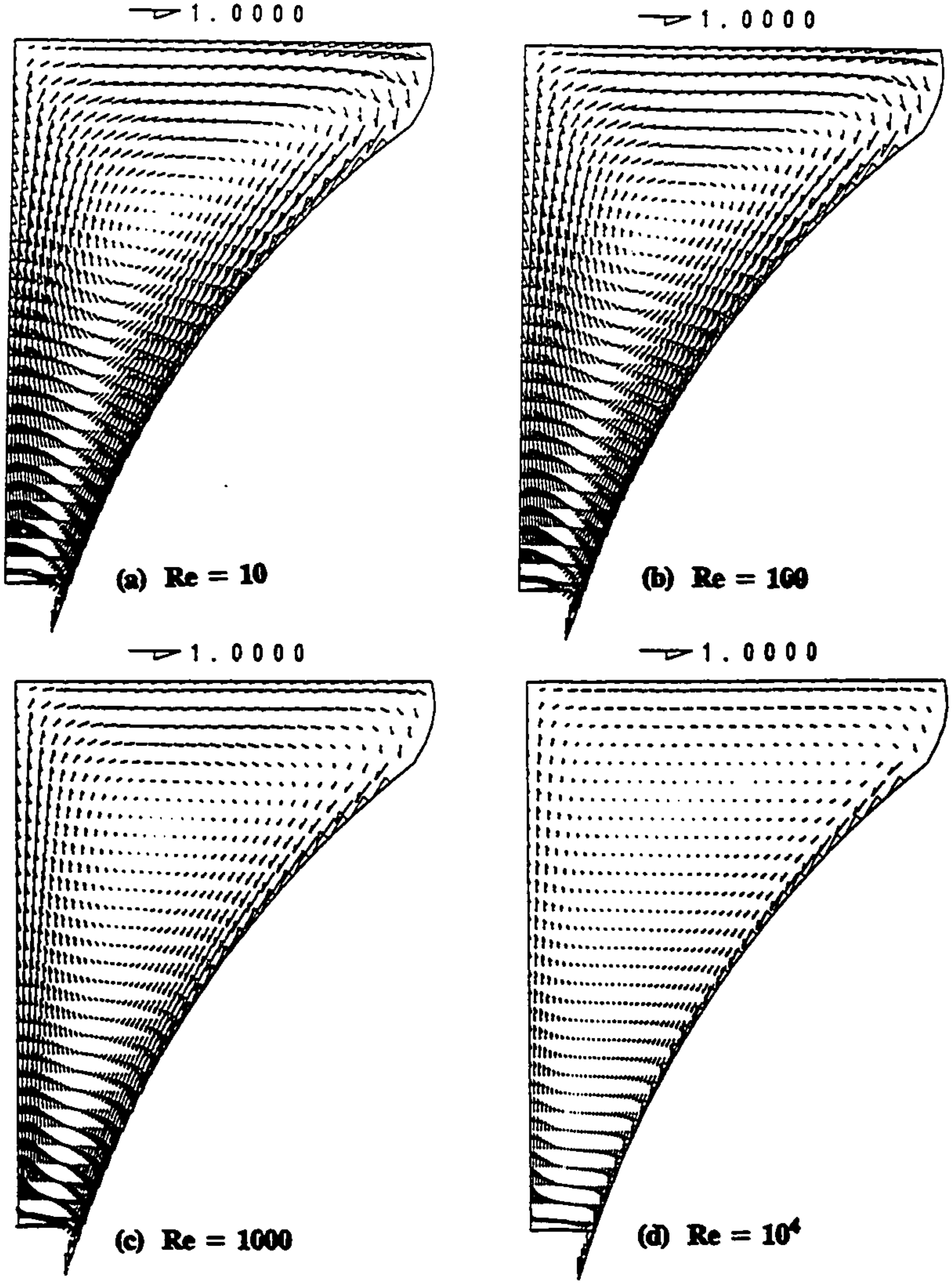

Figure 5.5 Non-dimensional velocity profile with free surface and symmetric axis

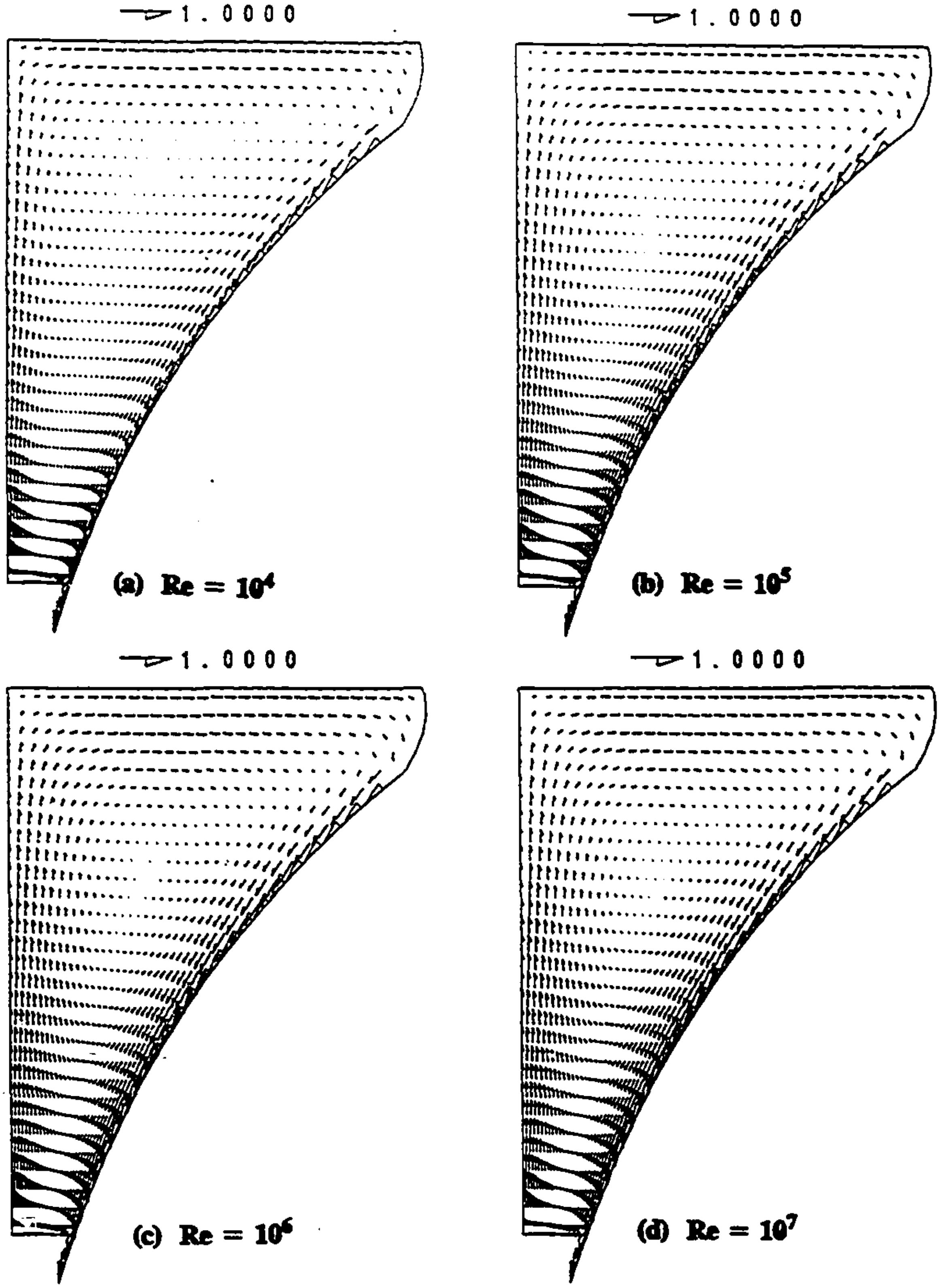

Figure 5.6 Non-dimensional velocity profile in closed domain using the turbulent model

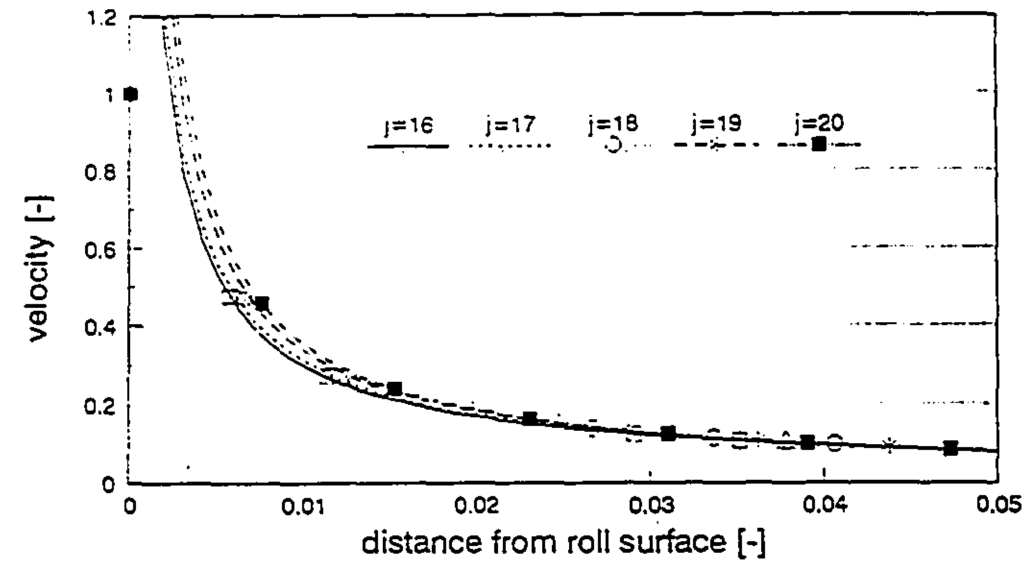

(a) Re = 10^4

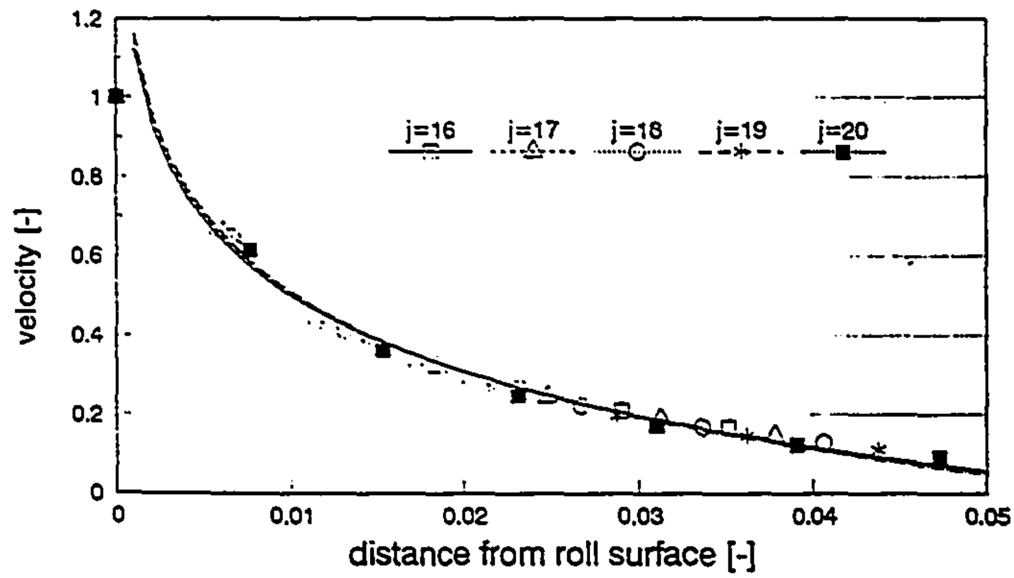

(b) Re = 10^5

Figure 5.7 Relation between velocity and normal distance (III)

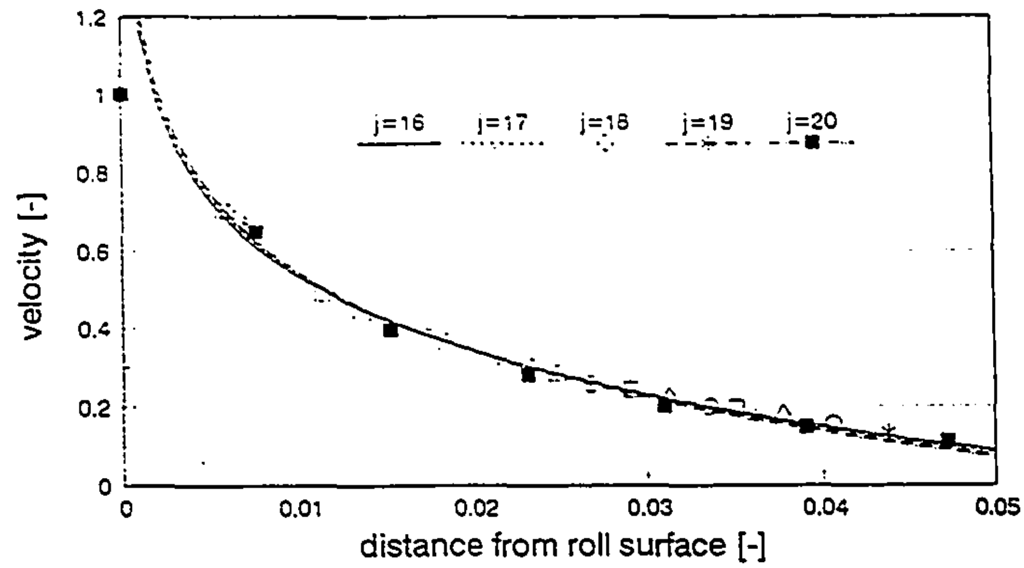

(c) Re = 10^6

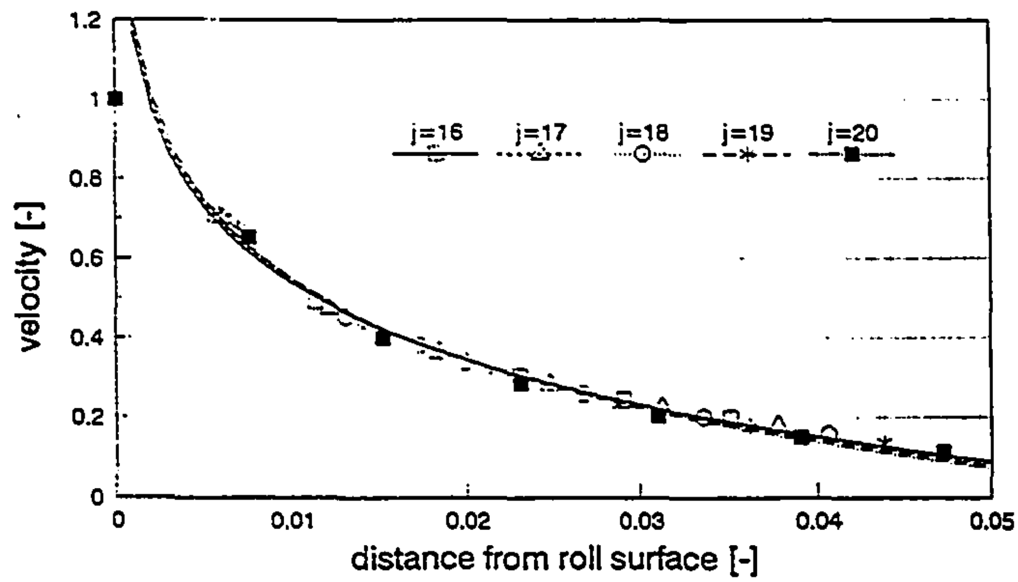

(d) Re = 10^7

Figure 5.8 Relation between velocity and normal distance (IV)

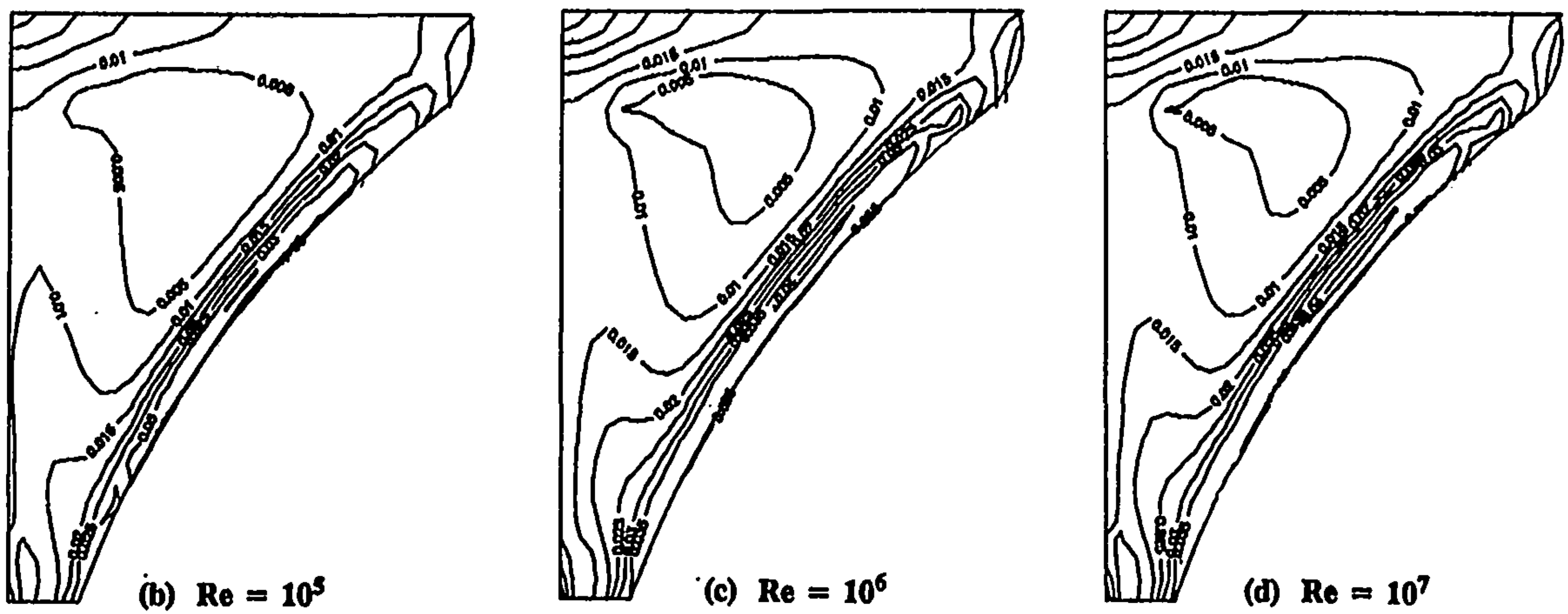

(b) Re = 10^5 (c) Re = 10^6 (d) Re = 10^7

Figure 5.9 Profile of non-dimensional turbulent kinetic energy

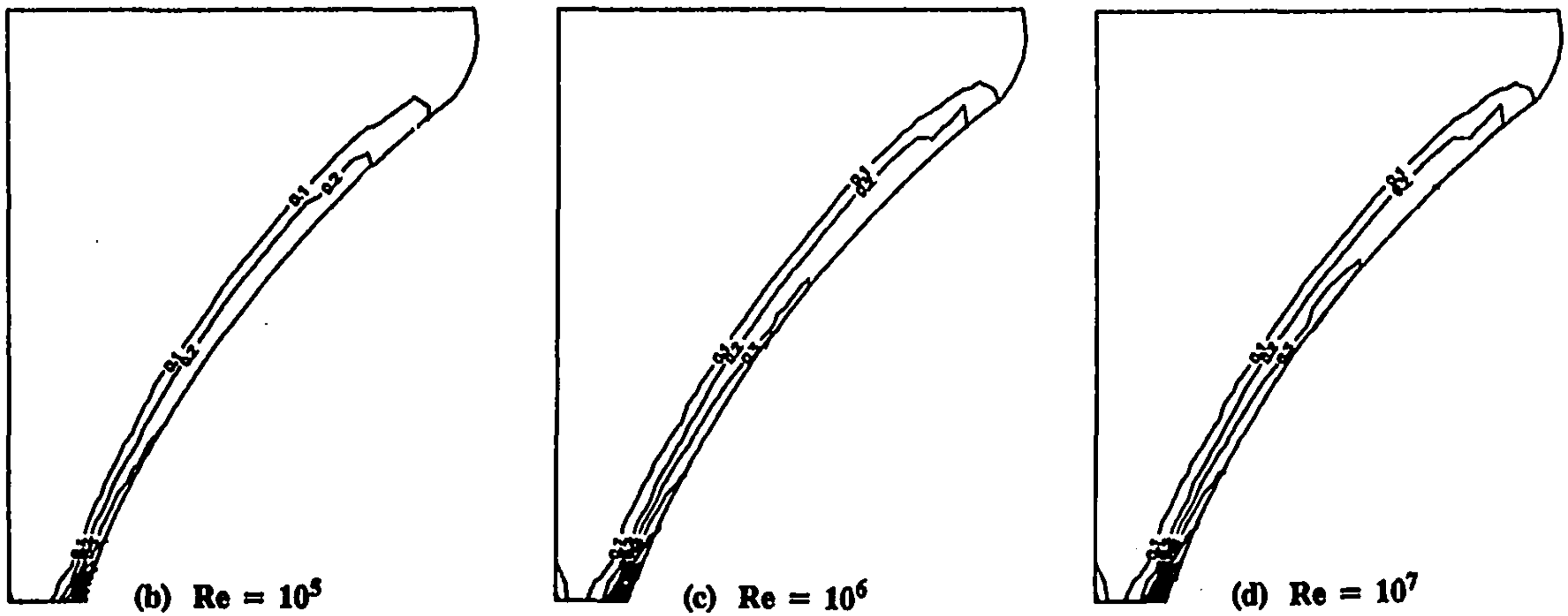

Figure 5.10 Profile of non-dimensional turbulent energy dissipation

5.3 Inlet–Outlet System

The effect of inlet velocity was investigated for the same system. Figure 5.11 shows the vector plots of the velocity fields for four different inlet conditions; v_{in}=0.1, 0.2, 0.33, 0.5 of the tangential velocity of the roll surface. The Reynolds number of the flows is 10^5, the symmetric boundary condition on the left and the free surface boundary condition on the top was used. The inlet flow at the top free surface covers five nodal distance.

Figure 5.11(a) shows that when the velocity of inlet flow is equal to 0.1, the inlet flow is too weak to penetrate against the upward flow along the symmetric boundary. As a result the macroscopic flow is similar to that of the closed system. At the outlet boundary on the bottom, a counter flow exists because of mass conservation within the domain.

When the non–dimensional velocity of inlet flow is equal to 0.2 (Figure 5.11(b)), the inlet flow penetrates slightly, and a relatively small recirculation zone is developed.

When the velocity of inlet flow is 0.33 or larger (Figure 5.11(c)–(d)), the strong inlet flow penetrates vertically through the domain to the bottom. Two counter rotating recirculation zones develop, resulting from two strong downwards flows at both sides. The thickness of the downwards flow along the rolls decreases owing to the inlet flow compared with that of the closed system.

Figure 5.12 shows profiles of turbulent kinetic energy. A strong turbulent region develops along the roll surface. In the case of a large inlet velocity (Figure 5.11(c) and (d)), the region where the turbulent energy is the largest lies just under the two recirculation zones. The flows for these cases are complicated and are a result of the influence of two downwards flows.

Similarly, Figure 5.13 shows profiles for the dissipation rate of turbulent energy. A high rate of dissipation exists along the roll surface, and the region for the highest rate of dissipation corresponds with the zone of highest turbulent energy.

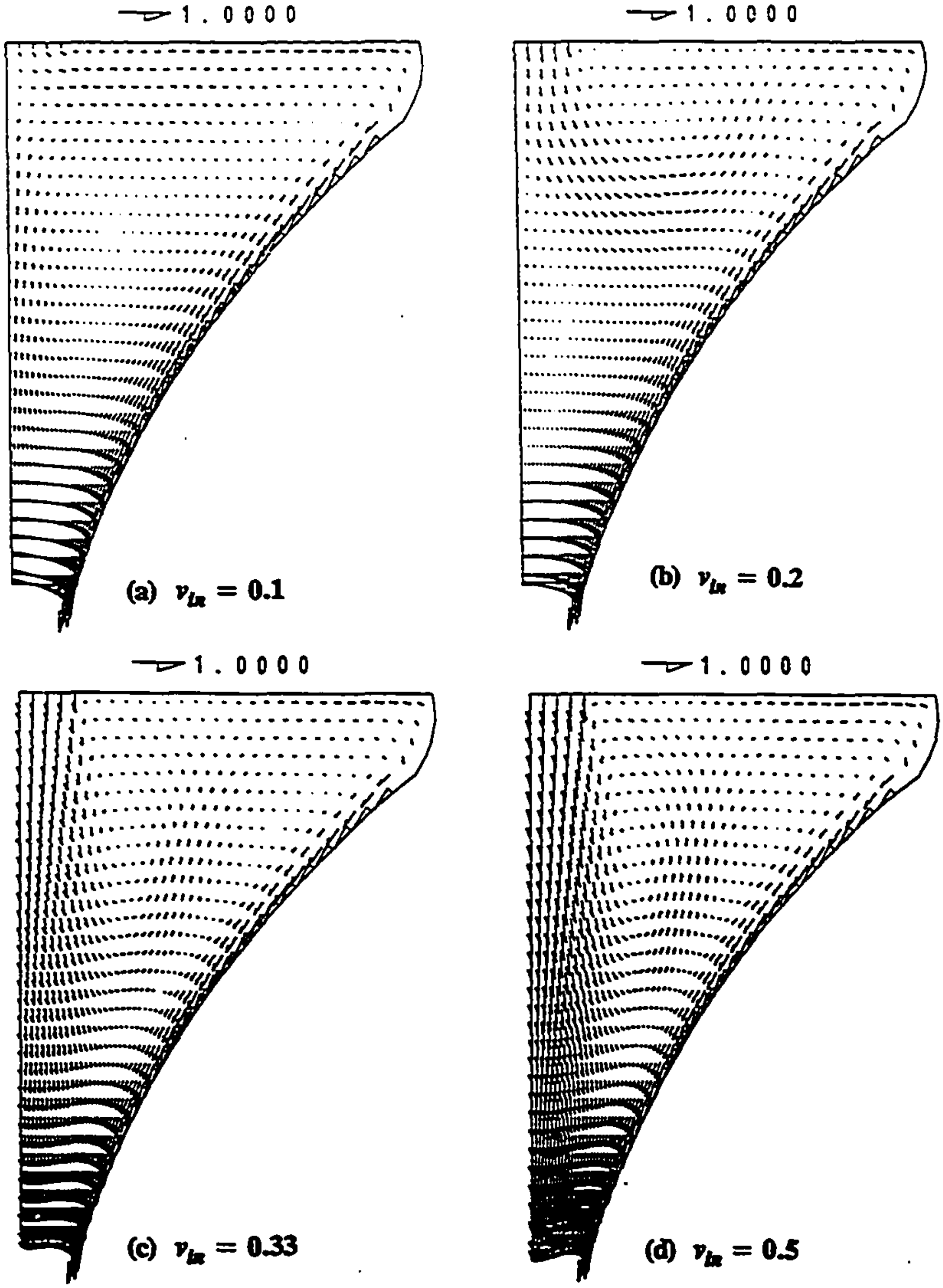

Figure 5.11 Non-dimensional velocity profile in the inlet-outlet system

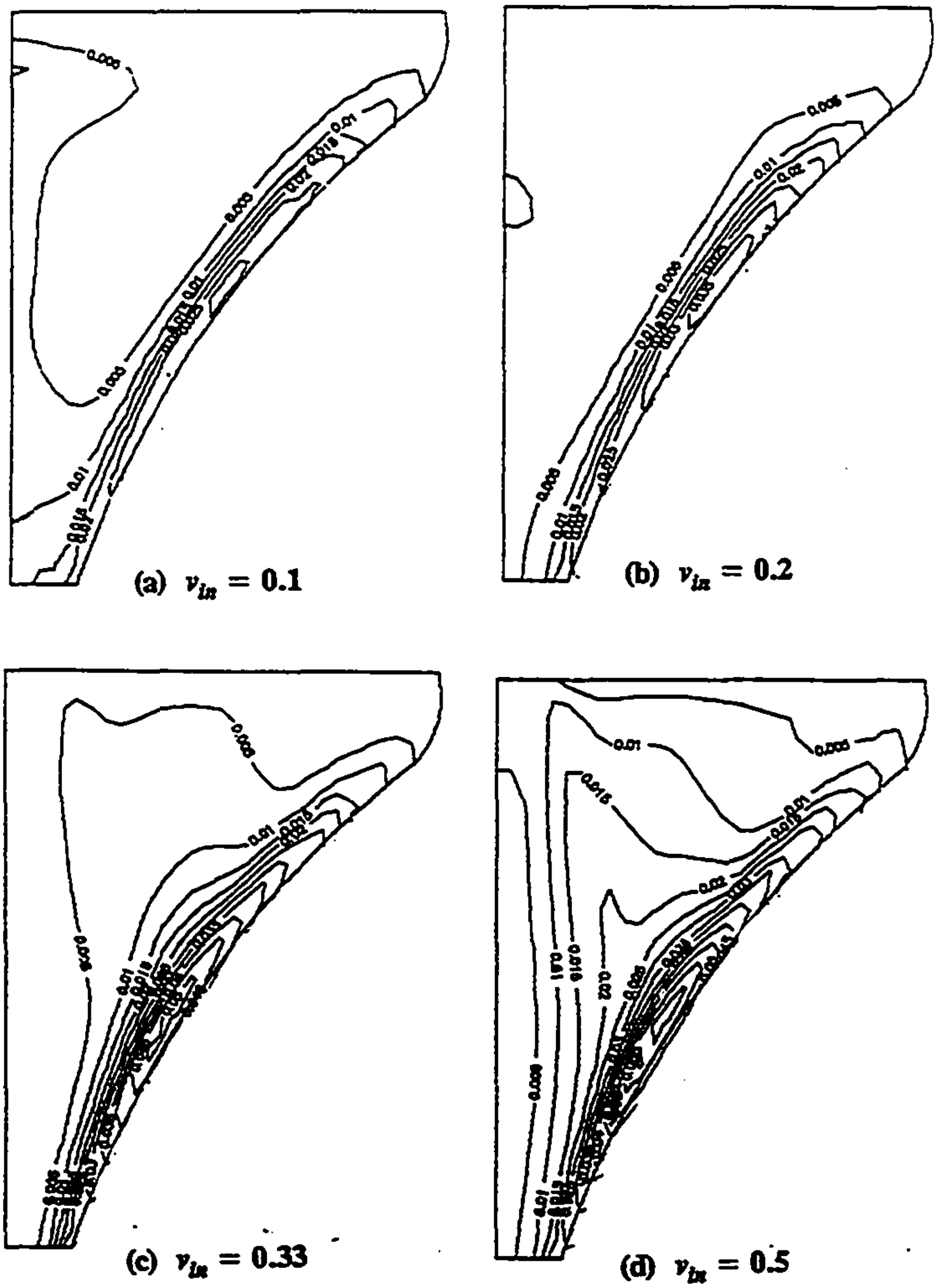

Figure 5.12 Profile of turbulent kinetic energy in inlet-outlet system

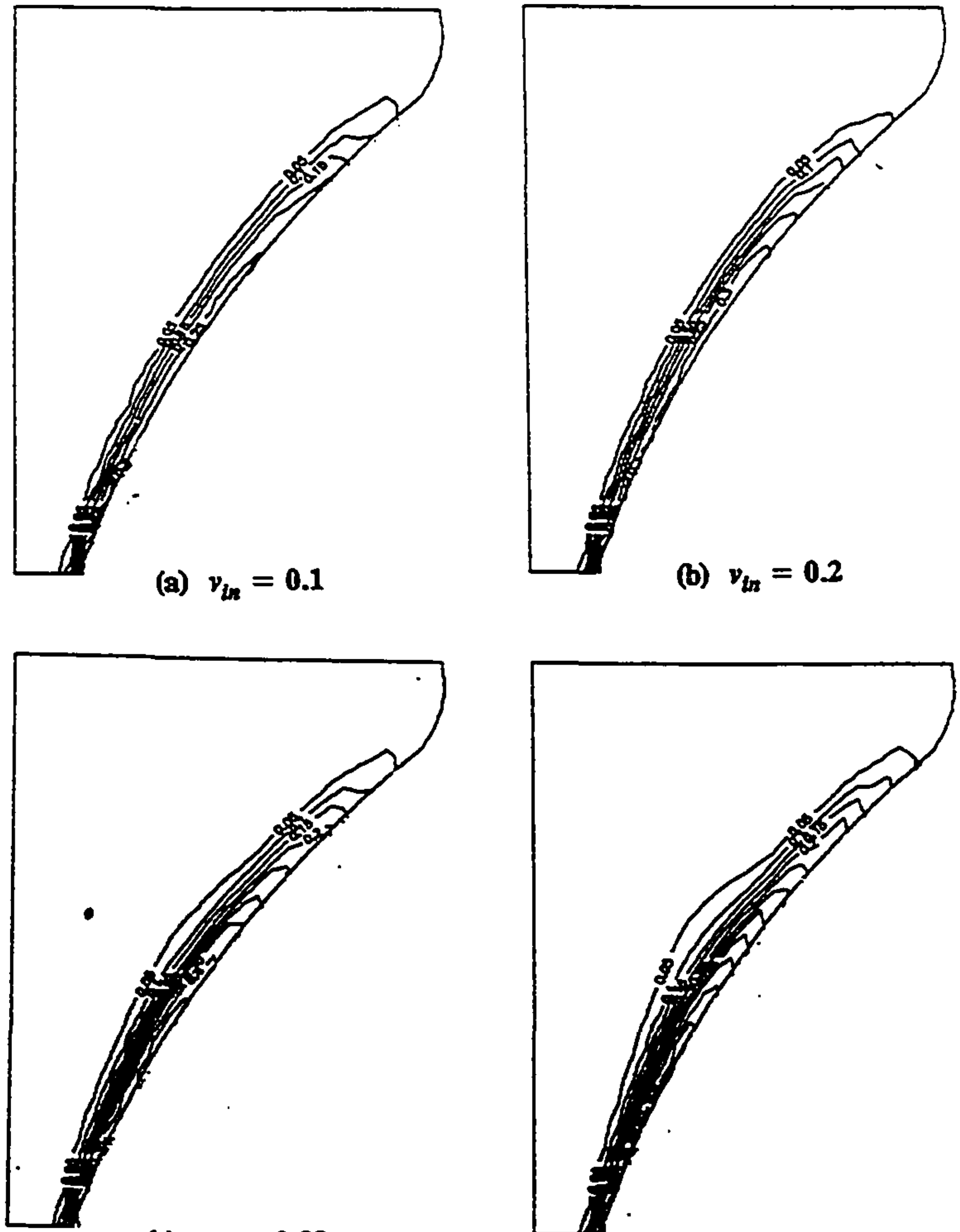

(a) $v_{in} = 0.1$ (b) $v_{in} = 0.2$

(c) $v_{in} = 0.33$ (d) $v_{in} = 0.5$

Figure 5.13 Profile of rate of dissipation in inlet-outlet system

5.4 Heat Transfer

5.4.1 Effects of Buoyancy Force

In practical twin roll casting systems, heat transfer must be considered in concert with fluid flow. Figure 5.14(a) shows the velocity vector profile of molten steel when the Prandtl number is 0.158 and the Rayleigh number is 10^8. The dimensionless velocity of the inlet flow was fixed at 0.5 and the Reynolds number at 10^5. The Dirichlet boundary condition was used on the roll surface ($\theta=0$), while the inlet temperature was the highest ($\theta=1$). These conditions correspond to a casting speed of 10 m/min and a superheat of 68K for the twin drum caster at N.S.C.. It shows that the inlet flow penetrates up to the exit and that two recirculation zones are developed by the inlet flow and fluid drawn by the moving roll.

Figure 5.14(b) shows the velocity profile when the Reynolds number is equal to 10^5 but without heat transfer i.e. isothermal condition. As seen, Figure 5.14(a) and Figure 5.14(b) are very similar to each other, and no influence of buoyancy forces on the flow can be observed. A comparison between these two figures clearly demonstrates that forced convection dominates over natural convection under such flow conditions.

Figure 5.15(a) shows the velocity field for molten steel when the Reynolds number is lowered to 10^3. The heat transfer boundary conditions correspond to those of Figure 5.14(a). In this condition, the inlet flow does not penetrate deeply but moves horizontally along the top surface, and turns down along the roll surface. This is because of the strong influence of the buoyancy force on the hot inlet flow which is later cooled by the roll surface.

Figure 5.15(b) shows the velocity profile when the Reynolds number is equal to 10^3 but for isothermal conditions. This figure also shows that the inlet flow diffuses earlier compared to that for the high Reynolds number condition (Figure 5.14(b)). Two recirculation zones are still observed for an isothermal sump, which is very different from the flows in Figure 5.15(a) for the non–isothermal situation. A comparison between Figure 5.15(a) and Figure 5.15(b) demonstrates that natural convection dominates over forced convection, and that the buoyancy effect is very important for the prediction of the flow field under such low Reynolds number flows.

Figure 5.16 shows isotherms corresponding to $Re=10^5$ and $Re=10^3$. In the case of $Re=10^5$, Gr/Re^2, which is a measure of the ratio of free to forced convection (see equation (5.4)), is much smaller than one, so the effects of natural convection is very small, and the isotherms expand vertically. In the case of $Re=10^3$, Gr/Re^2 is larger than one, so natural convection seems to strongly influence the flow field, and the isotherms expand horizontally.

5.4.2 Effects of Turbulent Heat Transfer

In order to ascertain effects of turbulent heat transfer, a simulation was performed after neglecting the turbulent heat transfer coefficient. Figure 5.17 shows the velocity profile and isotherms when Reynolds number is equal to 10^5, Rayleigh number is equal to 10^8, and turbulent heat conductivity, κ_t, is equal to zero under identical boundary conditions to those for Figure 5.14. The velocity profile is very similar to Figure 5.14(a), probably because the effect of natural convection is negligible. However, isotherms are quite different from those in Figure 5.16(a). Without turbulent heat transport, much less heat is transported through the roll because of a small thermal diffusivity. As a result, the temperature gradient in vincity ofthe roll surface is much smaller. This signifies that the heat conduction model predicts a low temperature field even after accounting for fluid flow.

Figure 5.18 shows the local Nusselt numbers on the roll when the non-dimensional ambient temperature, θ_∞, is assumed -20°C. The local Nusselt number, *Nu*, was obtained numerically using the following equation;

$$Nu = - \frac{\Theta}{(\theta_{roll} - \theta_\infty)J\sqrt{\alpha}} \left(\alpha \frac{\partial \theta}{\partial \xi} - \beta \frac{\partial \theta}{\partial \eta} \right) \tag{5.5}$$

where Θ is the angle between a location on the roll and the first contact point (see Figure 5.18). As seen, when the turbulent heat transfer is taken into account, the local Nusselt number is much higher compared to the other case and heat transfer coefficient correspondingly estimated from numerical results becomes higher. In author's opinion, it seems that heat transfer coefficients in twin roll casters (ref. Table 2) were underestimated by previous researchers because they used heat conduction models.

5.4.3 Effects of Characteristic Length

The characteristic length, D, determines the overall Reynolds number and other important variables, and it is necessary to discuss a suitable dimension for its choice.

In all aforementioned calculations, the radius of the roll was employed as the characteristic length because it was considered to be the most important dimension with respect to the design of a twin roll caster. Usually the characteristic length of a closed domain such as a duct is defined as D = 4(cross-sectional area)/(wetted perimeter), although there is some controversy in the use of this definition in such a two-dimensional arbitrary geometry. The characteristic length for parallel flow between two walls should be the thickness of the slit, and that of the flow in a cavity is usually the dimension of the narrow width. From the point of view of heat transfer to a plate, the length of the arc of the roll surface could be reasonably defined as being the characteristic length. To cofirm effect of the characteristic length, two performances were carried out.

Figure 5.19 shows the results of the velocity profile which were calculated using two different characteristic length, the 4(cross-sectional area)/(wetted perimeter) and the length of the arc of the roll surface, under identical conditions. These characteristic lengths, D, represent values of 0.245 x (radius) and 0.845 x (radius), respectively for the two cases. No significant difference in results is observed upon their use, and the results are truly identical with Figure 5.14(a). Also isotherms in both cases, which are shown in Figure 5.20, are identical with Figure 5.16(a). No effect of the choice of the characteristic length was found.

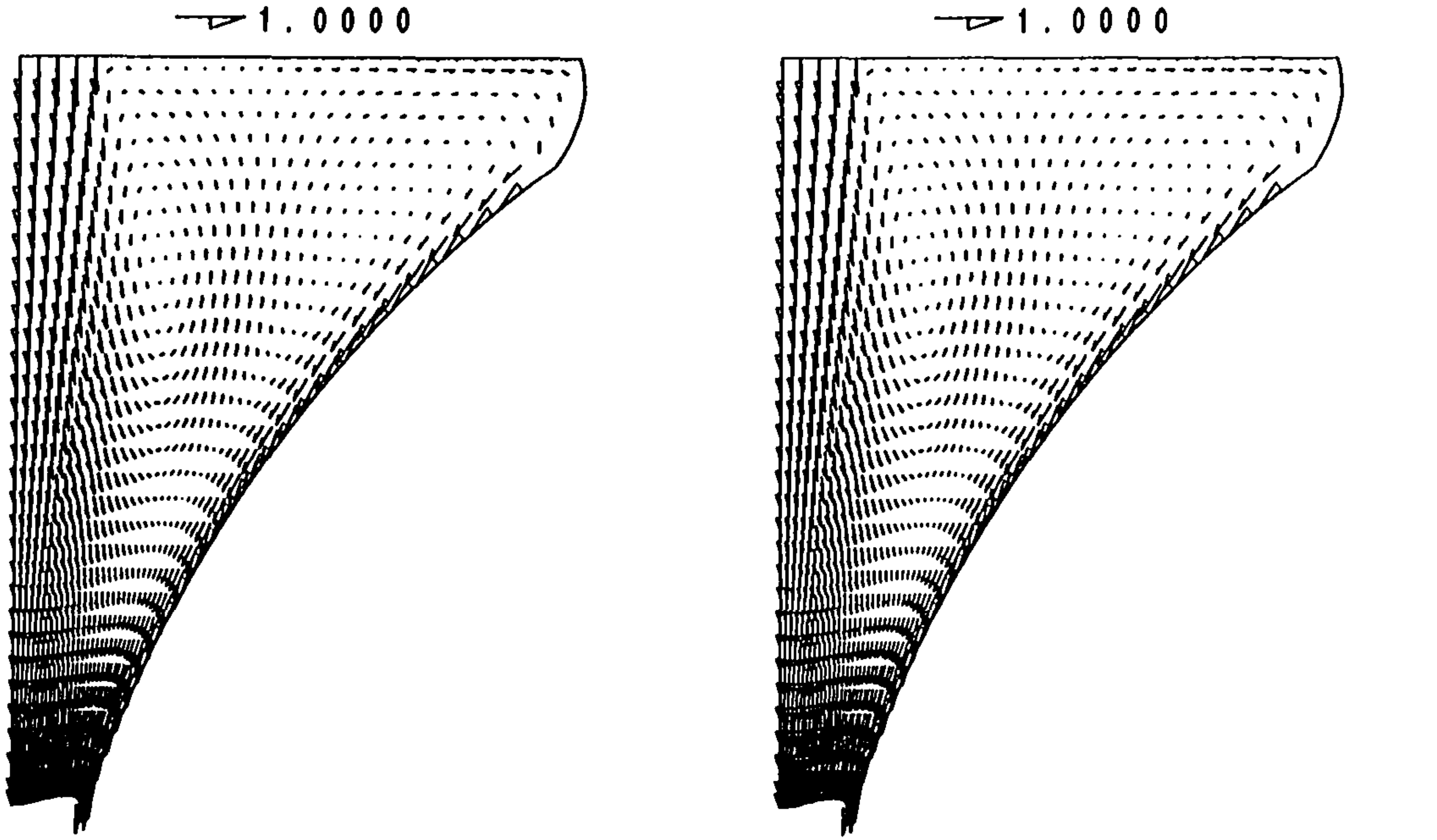

(a) Ra=10^8, Pr=0.158

(b) isothermal condition

Figure 5.14 Non-dimensional velocity profile, Re=10^5, v_{in}=0.5

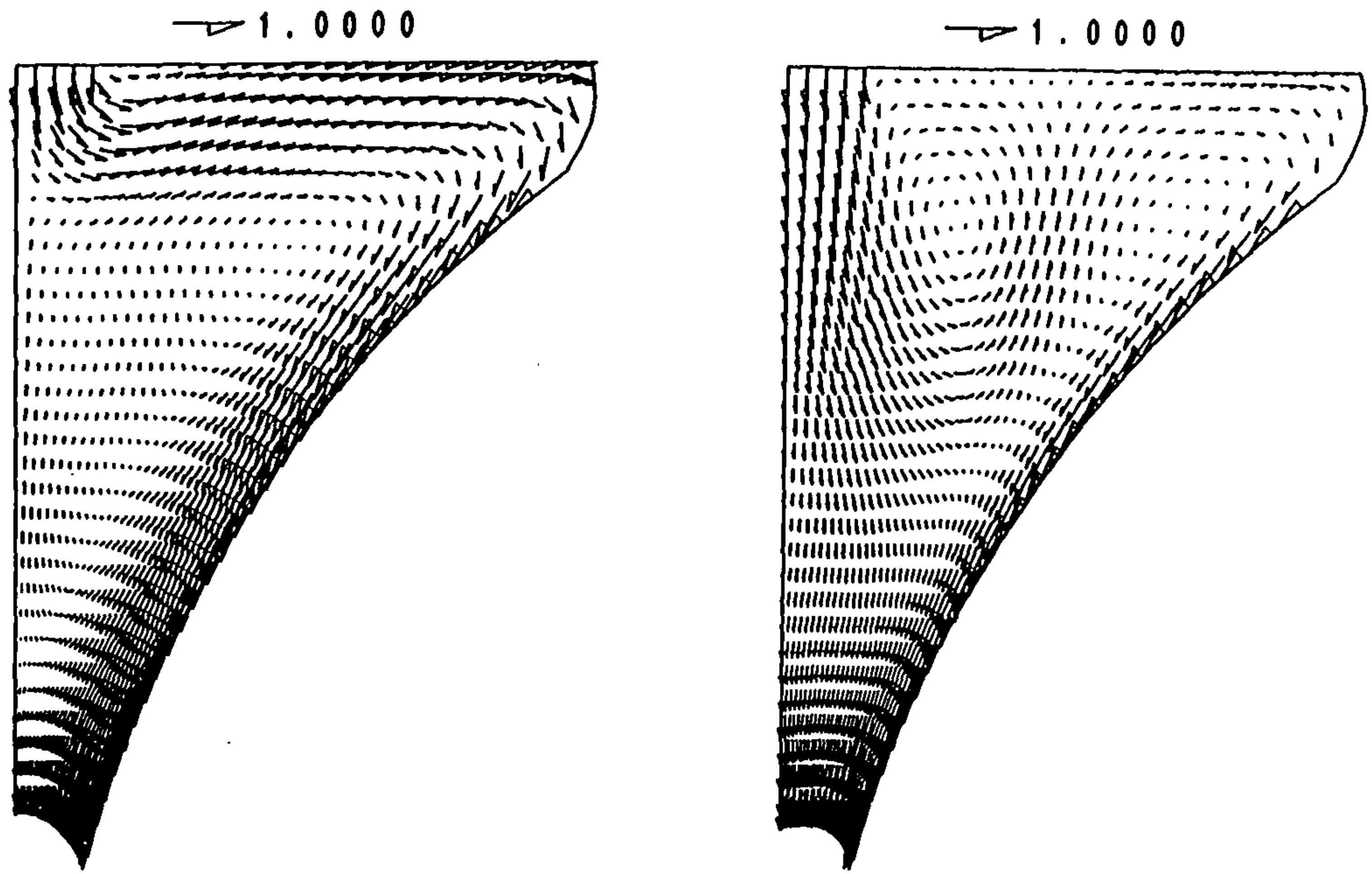

(a) Ra=10^8, Pr=0.158 (b) isothermal condition

Figure 5.15 Non-dimensional velocity profile, Re=10^3, v_{in}=0.5

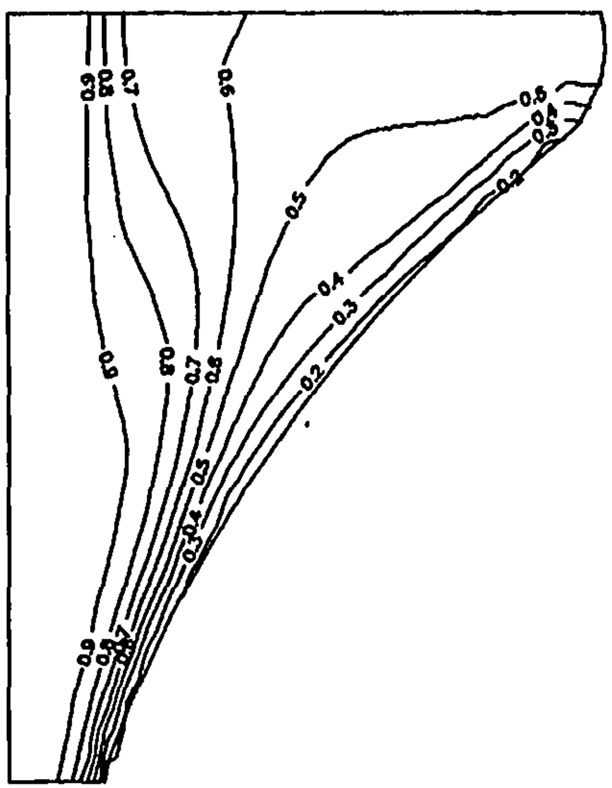

(a) Re = 10^5

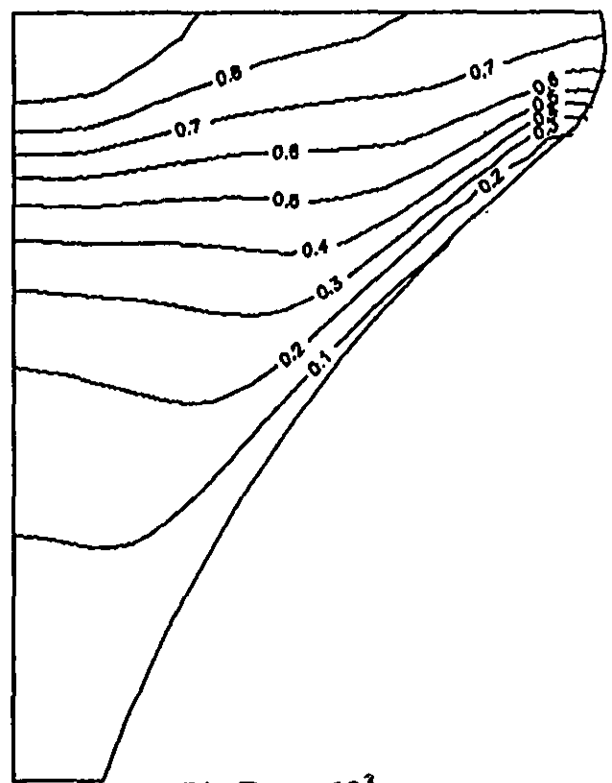

(b) Re = 10^3

Figure 5.16 Temperature profile, $\theta_{in}=1.0$, $\theta_{roll}=0.0$

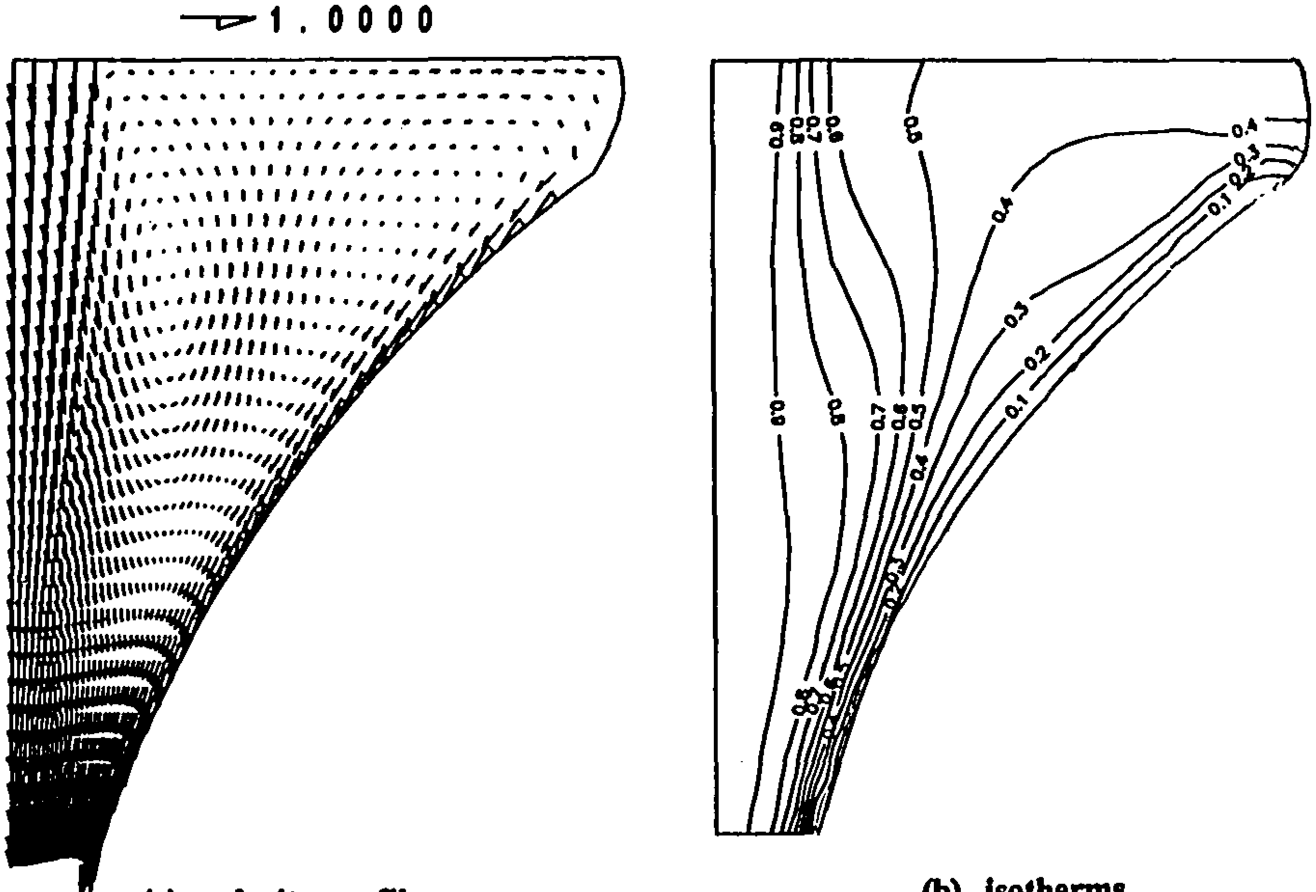

(a) velocity profile

(b) isotherms

Figure 5.17 Computed results without turbulent heat transfer

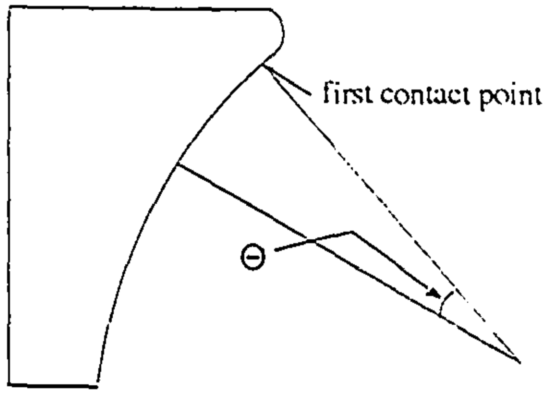

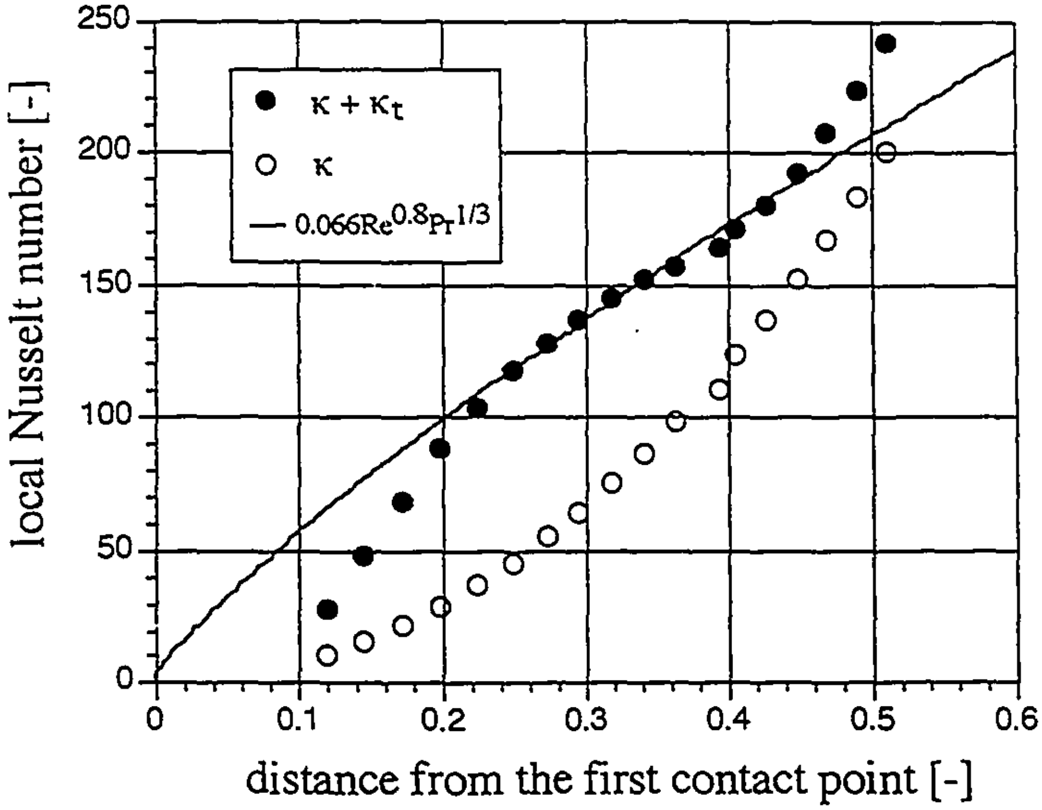

Figure 5.18 Local Nusselt number ($Re=10^5$,$Ra=10^8$,$Pr=0.158$)

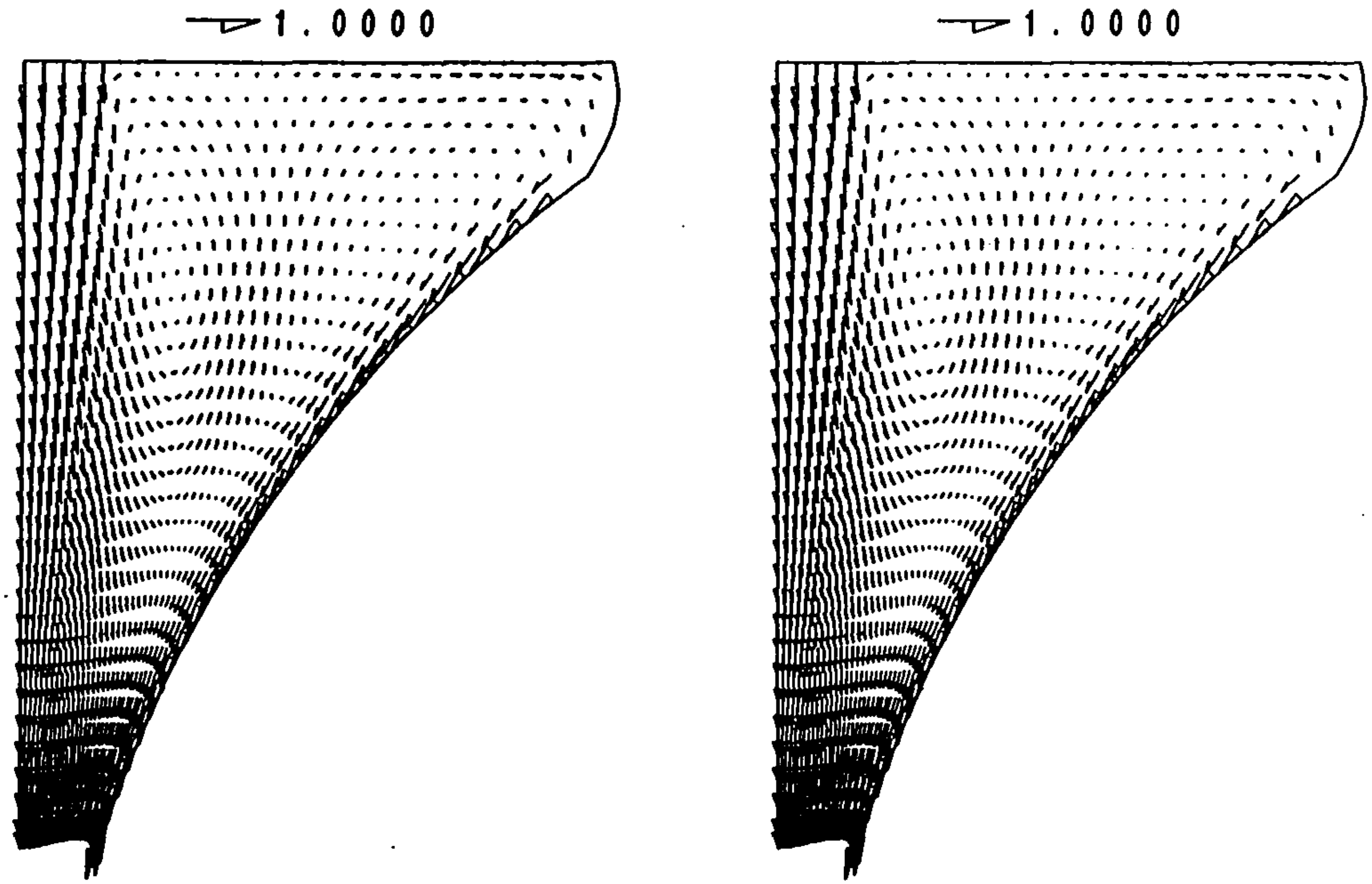

(a) D = 0.245 R

(b) D = 0.845 R

Figure 5.19 Non-dimensional velocity profile for two kinds of charcteristic length

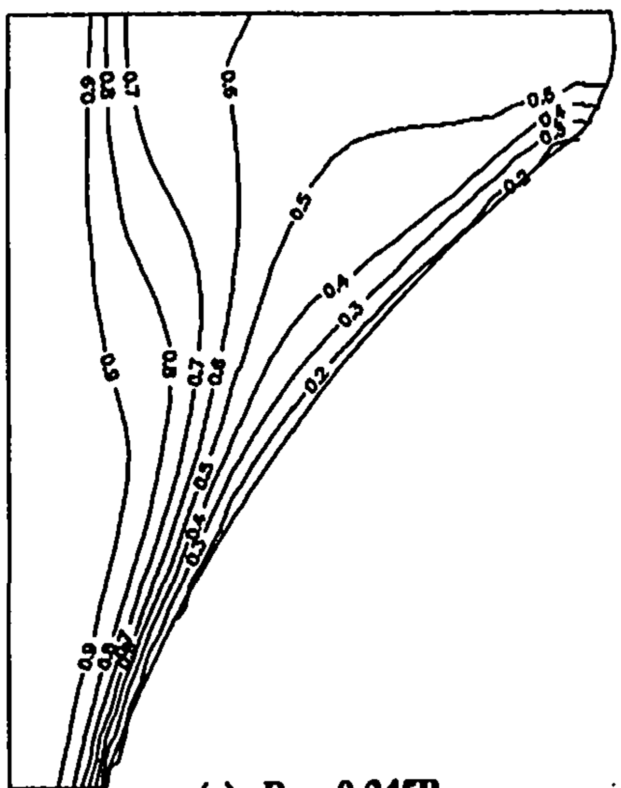

(a) $D = 0.245R$

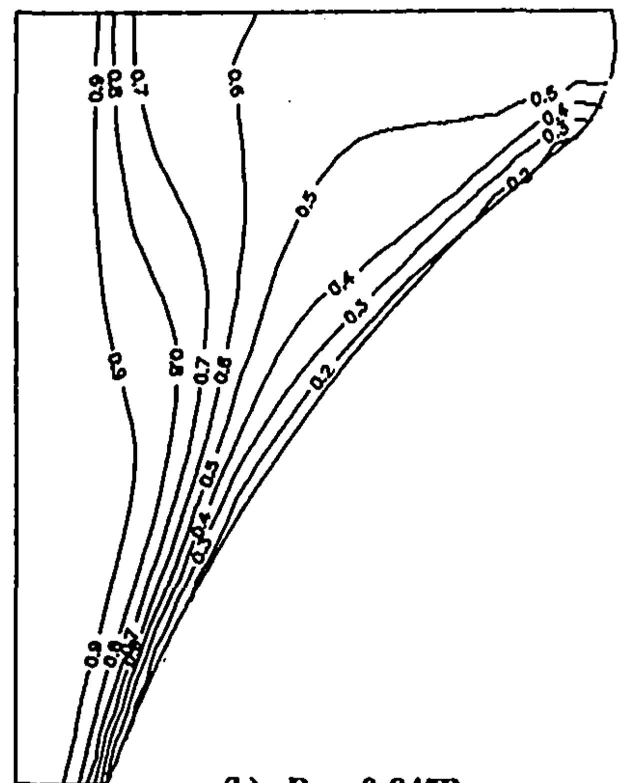

(b) $D = 0.845R$

Figure 5.20 Isotherms for two kinds of charcteristic length

5.5 Verification

To verify the fluid flow model, a numerical result was compared with an experimental result from a water model which was carried out in the Hikari Works of N.S.C. The water model has a scale of 0.6 as large as the actual twin drum caster so as to be able to respect Froude number (inertia force/gravity force, v^2/gD) and Weber number (inertia force/surface tension, $\rho D v^2/\sigma$). Table 4 provides a comparison of specifications between the water model and the actual twin drum caster.

Table 4 Specifications of the water model

	water model	twin drum caster
roll diameter	720 mm	1200 mm
mould width	480 mm	800 mm
casting speed	0.51 m/sec	0.66 m/sec
mass flow rate	4.67 kg/sec	16.7 kg/sec
meniscus level	40•	40•

The flow of the dye injected through the nozzle was traced and recorded on a video machine, while the velocity distribution was observed through the video record.

Figure 5.21 illustrates the transient dye distribution from a vertical submerged nozzle to the mould. The dye is injected vertically and diffuses isotropically at first. Owing to the moving roll, the dye tends to spread down, and it takes time to spread to upper part of the mould. Stagnant regions are observed at both sides of the nozzle near the top surface.

To compare the experimental results with the model, numerical simulations were carried out using a grid structure equivalent to the boundaries shown in Figure 5.22.

Figure 5.23 shows the predicted velocity field for a symmetric half of the mould for the following specific set of operating conditions; casting speed = 0.51m/s, velocity of inlet flow = 0.57m/s, pool of depth = 0.2m. The inlet flow penetrates into the centre of the mould, and creates a large recirculation. On the other hand, the moving roll causes another big recirculation.

This results in two asymmetrical counter rotating recirculation zones within the wedge-shaped pool. A small eddy is also seen to develop at the corner between the nozzle and the surface of the pool. This region may therefore be stagnant.

To compare the numerical result and the flow visualisation in the water model, the spread of the injected dye was simulated using the mathematical model. In the model calculations, the unsteady state convective-diffusive mass transport equation for dye movement was solved using the prior calculated steady state velocity field (Figure 5.23). While implementing the governing mass fraction transport equation (non-dimensional form of equation (4.40) and (5.6)).

$$\phi = \chi_A, \quad \Gamma_\phi = \frac{1}{Sc\ Re} + \frac{1}{Sc_t Re_t}, \quad S(\xi,\eta) = 0 \tag{5.6}$$

where χ_A is the mass fraction of A, and Sc_t, the turbulent Schmidt number. The latter was taken to be unity on the reasonable assumption that the concentration profile is determined by the velocity profile. Figure 5.24 illustrates the concentration profile of the dye at 0.1–0.3 second after injection. The behaviour of dye spreading into the pool is clearly observed. Figure 5.25 illustrates the concentration profiles after 0.5–0.7 second.

Figure 5.26 provides a comparison between the computational and the experimental result. Here, the one percent concentration lines are drawn in Figure 5.26(a) and compared with the results of the flow visualisation. They show very good agreement and demonstrate that the fluid flow model can, at least, qualitatively, explain fluid flow phenomena in the wedge-shaped pool of a twin roll caster.

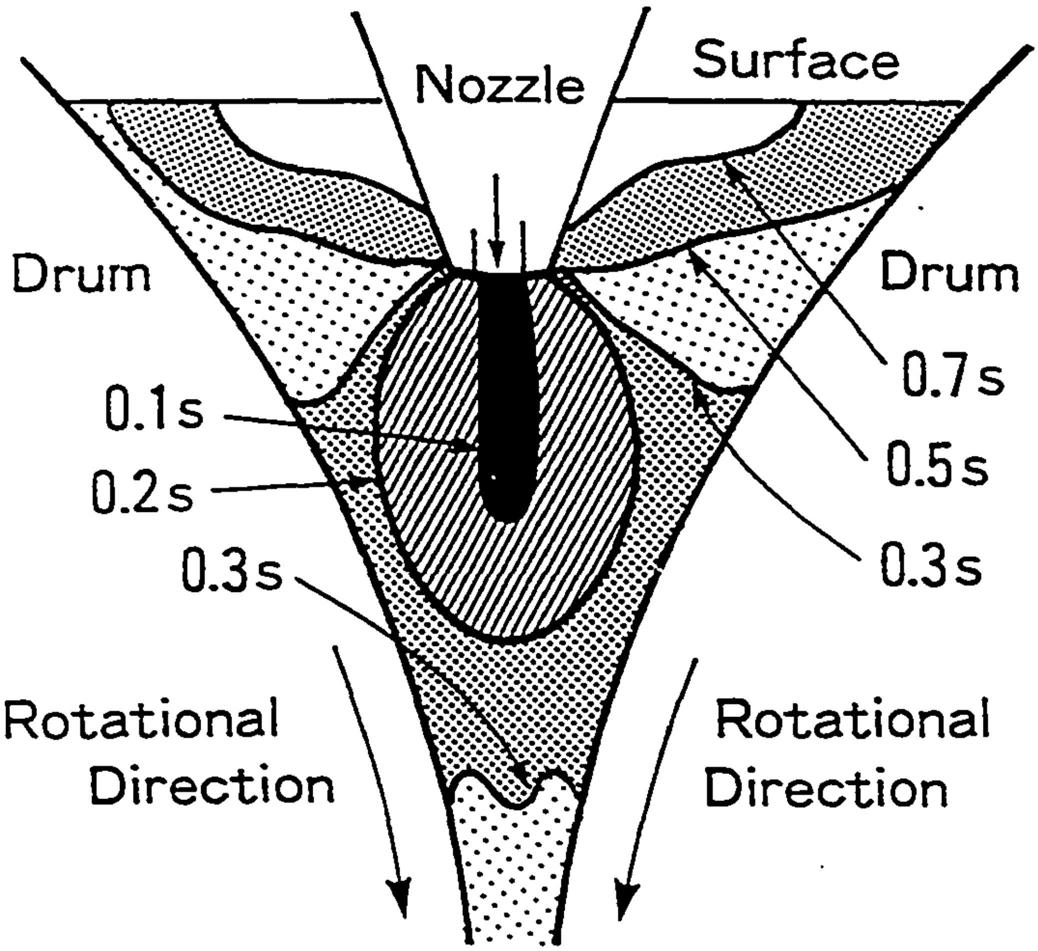

Figure 5.21 Visualisation of flow by dye injection

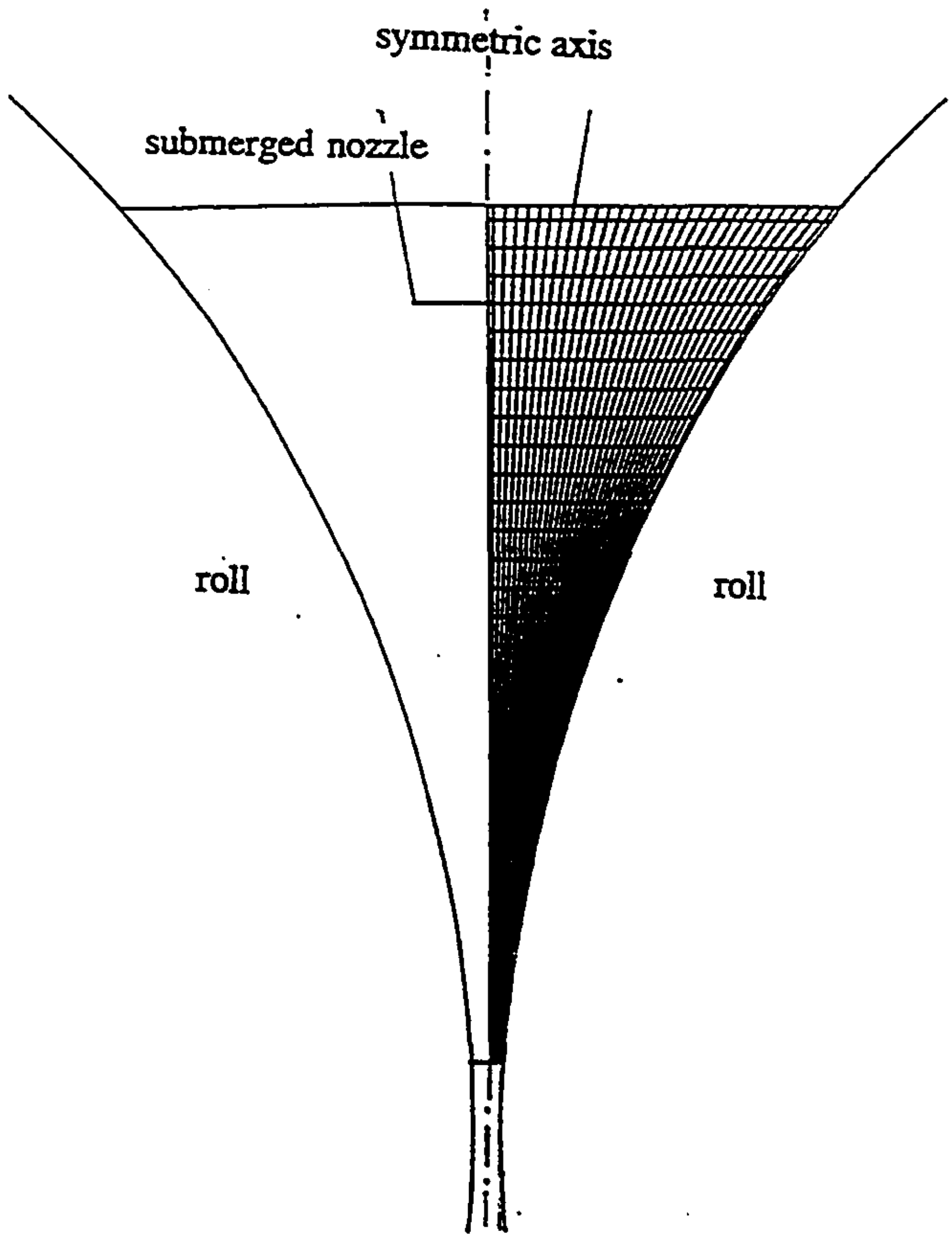

Figure 5.22 Grid formation for the water model

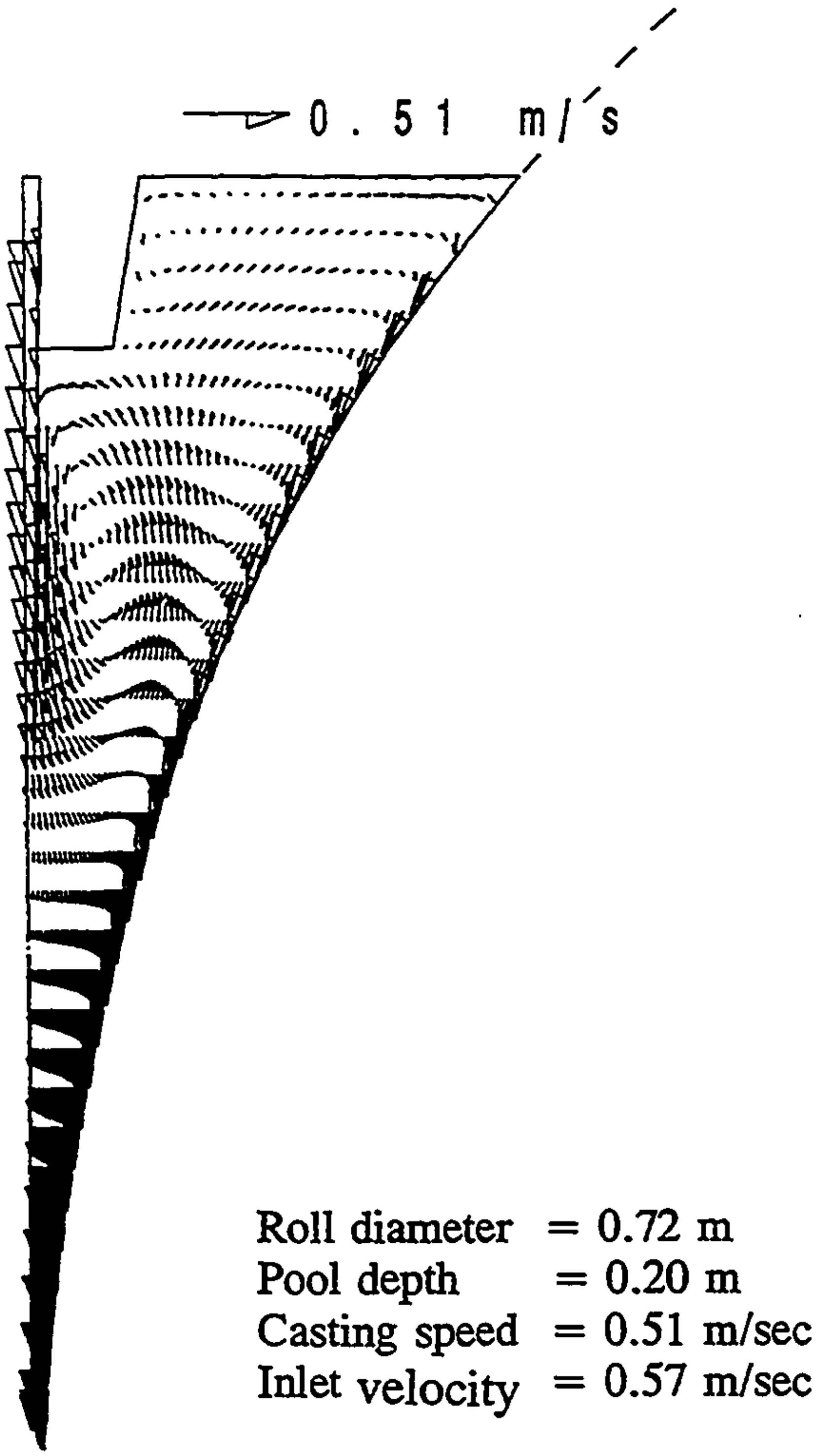

Figure 5.23 Velocity profile of the water model

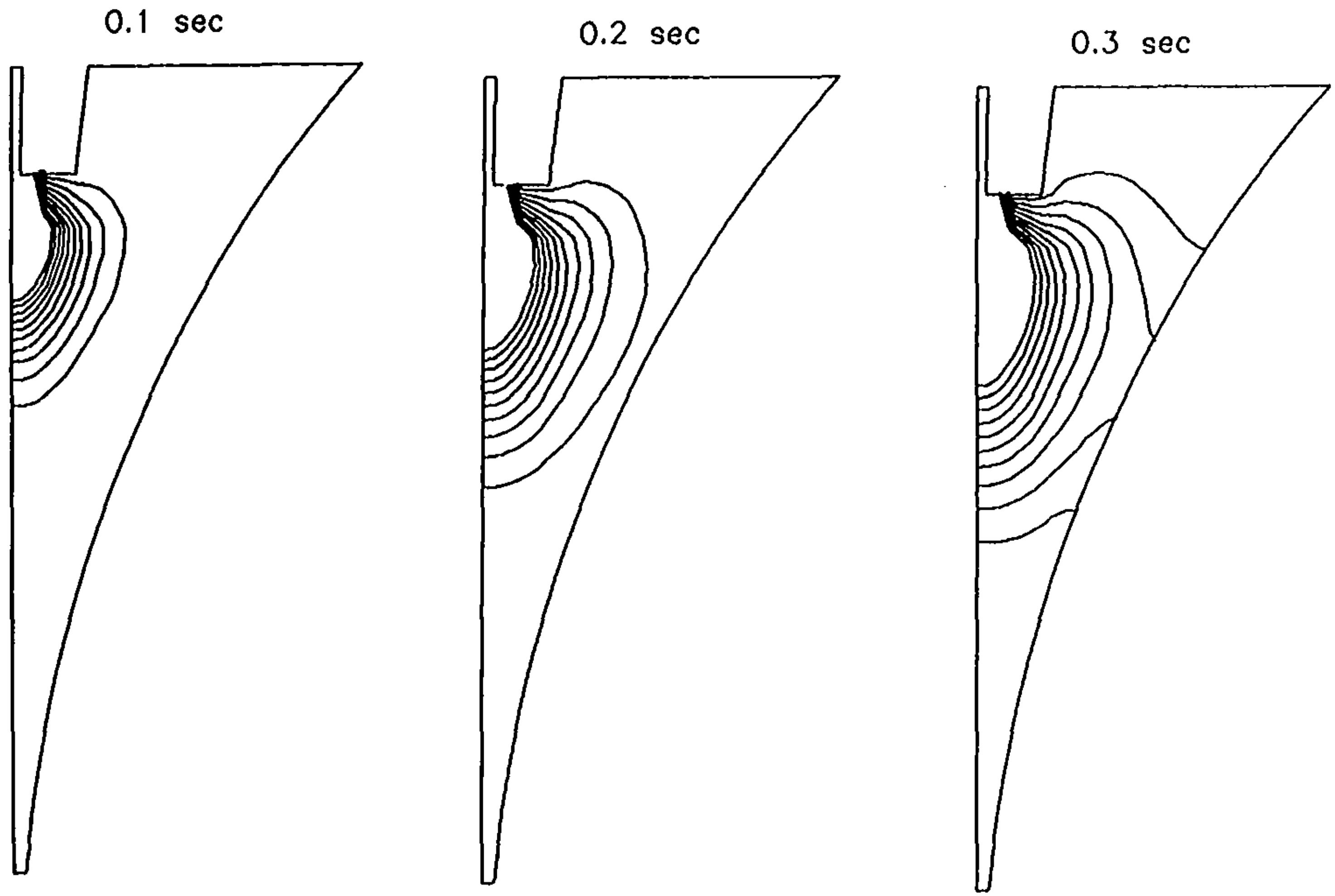

Figure 5.24 Concentration profile of dye (0.1 ~ 0.3 sec)

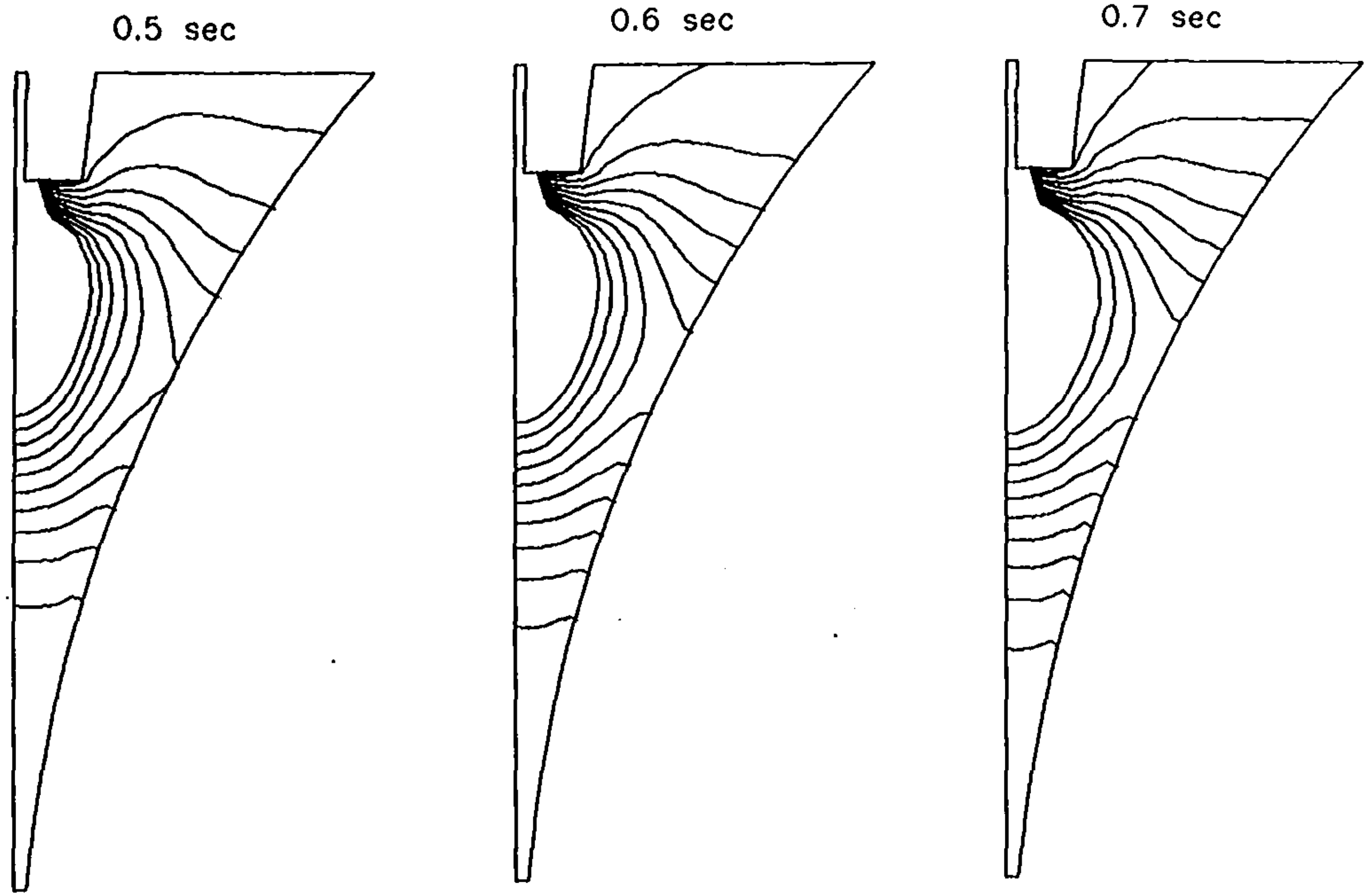

Figure 5.25 Concentration profile of dye (0.5~0.7 sec)

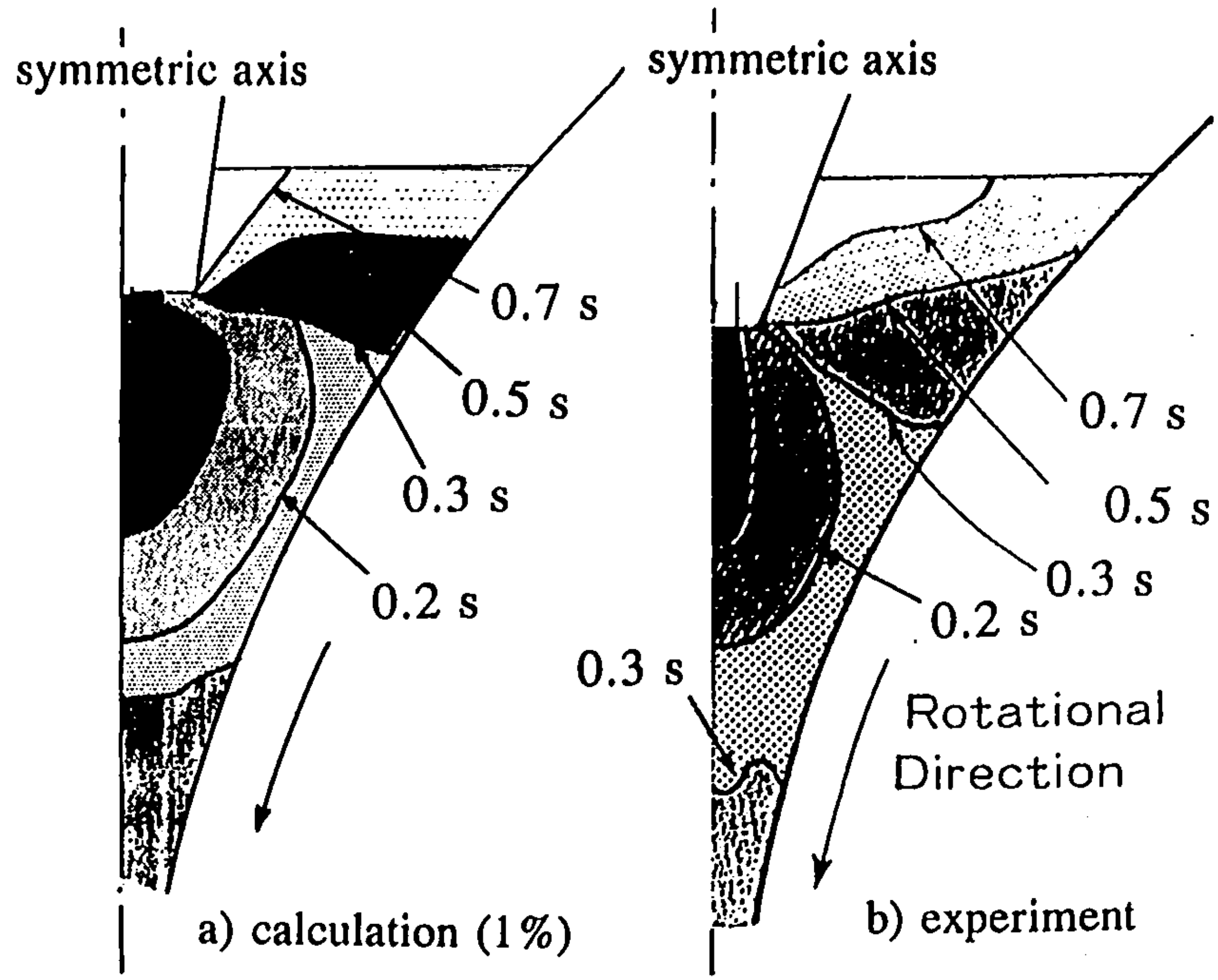

Figure 5.26 Comparison between computational and experimental results

5.6 Summary

A general mathematical model of turbulent transport processes has been developed for an arbitrary wedge-shaped pool. Several flow characteristics of the system were identified using the model. These are summarized below:

1. In the closed system, the critical Reynolds number based on the radius of the roll as the characteristic dimension is around 2×10^4. As such, a turbulent model is required to predict an flow in the actual twin roll casting systems which operate at $Re \sim 10^5$ to 10^8.
2. The momentum boundary layer thickness on the roll surface decreases with increasing Reynolds number or velocity of the inlet flow. Also, boundary conditions at the vertical axis of symmetry and at the free surface affect the flow structure near the roll. Therefore, the model for the twin roll caster has to take into account realistic boundary conditions, particularly inlet conditions.
3. Numerical solutions of macroscopic flows are in good agreement with experimental data from a prototype water model.
4. The model incorporated turbulent energy transport, and the energy field does not affect the fluid flow field significantly in the twin roll casting process of steel because forced convection dominates over natural convection in this system. Turbulent heat transfer, however, influences the energy field, and the diffusion heat conduction model seems not to be applicable.
5. The choice of the characteristic length does not influence the modelling results for the twin roll system.

Part of the work in this chapter has been already presented and published in the ISS Proceedings of the Toronto conference, held April 1992 (Murakami et al., 1992).

NUMERICAL ANALYSIS of FLUID FLOW, HEAT TRANSFER and SOLIDIFICATION in A TWIN ROLL CASTER

6.1 Introduction

In this chapter, a model of coupled turbulent fluid flow, heat transfer and solidification in a vertical twin roll caster is introduced. Numerical simulations are performed in Sn−15%Pb alloy system that previous researchers studied experimentally. Unlike the fluid flow model in chapter 5, the energy field can affect the velocity field greatly owing to the co-existence of a liquid-solid region (mushy region). This is large enough to influence fluid flow conditions in alloy systems. As a result, the stability of the computations is much lower than that of only fluid flow calculations. Both the initial conditions and the choice of the under-relaxation factors are very important to obtain converged solutions. A relaxation factor of 0.2 was used for the energy equation, together with relaxation factors starting from an initial value of 0.4 at the beginning of each implementation to a maximum of 0.7 for the other variables. Step-change boundary conditions were used to create good initial conditions.

The purpose of this chapter is to describe the effects of several parameters in the solidification model in detail and to demonstrate the importance of the solidification model in predicting flow and energy conditions in the twin roll casting system. The effects of the porosity function, particularly the effects of the resistance coefficient of the function were investigated. They are strongly related to the energy profile in the mould. Computations were carried out using different kinds of boundary conditions for the energy equation. Also, the effects of turbulent Prandtl number and of inlet temperature, are discussed.

The results are compared with the experimental data (Hojo et al., 1987) in detail, and with an analytical solution using the Virtual Adjunct Method (Clyne and Garcia, 1981).

6.2 Effects of the porosity function coefficient

The solidification of a binary alloy is a very complicated phenomenon, and modelling was one of the most difficult parts of this research work. In the model, it was assumed that solidification occurs with equilibrium at the solid-liquid interface, and that the rate of solidification is controlled only by the rate of heat transfer within the mushy region. The diffusion of solute in the solid is negligible, but we assume that the composition of the interdendritic liquid can be specified by the local temperature.

In order to compare present computations with the experimental results of Hojo et al. (1987), the same specifications as those used by the latter, and shown in Table 5, were employed for calculations.

Table 5 Input data for computations

roll diameter	89 mm
pool depth	30 mm
nozzle entrance (not submerged)	2 mm
casting speed	1.87 m/min
strip thickness	3.2 mm
inlet temperature	213 °C
roll temperature	17 °C
properties (Sn-15%Pb)	
viscosity	1.8×10^{-3} Pa.s
density	7200 kg/m^3
heat conductivity	21 W/m.K
specific heat	230 J/kg.K
latent heat	1.59×10^{5} J/kg
solidus temperature	183 °C
liquidus temperature	208 °C

non-dimensional number	
Reynolds number (Re)	4620
Prandtl number (Pr)	0.02
Rayleigh number (Ra)	4×10^4
Grashof number (Gr=Ra/Pr)	8×10^6
representative length (D)	46.1 mm

Two types of boundary conditions for the energy equation, Dirichlet condition I and Neumann condition II, have been adopted. The following concrete boundary conditions have been chosen to account for the experimental fact that the temperature of the surface of the strip just after the roll bite point fluctuated between 100°C and 160°C.

Dirichlet condition I : constant temperature T_0=150°C on the surface

Neumann condition II : heat transfer coefficient $h_i=4500/t^{0.547}$ on the surface

where 't' is the contact time [second] and the exponent '0.547' was referred by Hlinka et al.'s paper (1988). The heat transfer coefficient is in the order of magnitude found by previous researchers on small, twin roll casters (refer to Table 2 in Chapter 2).

A Jones and Launder type low Reynolds number k-ϵ turbulent model was used for all computations in this chapter. Without a turbulent model, no converged solution has been obtained. With reference to the computational results, the non-dimensional distance between the roll surface and the nearest node, y^+ (=distance x u^*/ν), was in the order of magnitude 10, so it was reasonable that this turbulent model be adopted.

Wide variations in the resistance coefficient of the porosity function, C", were used in order to study its effect on transport pattern in the presence of the solid-liquid phase change. In this study, all governing equations are non-dimensional, and C" is induced from equation(4.60) as follows,

$$C'' = \frac{U}{D}\frac{\nu}{C' l_c^2} \tag{6.1}$$

where l_c is a characteristic length related to the primary dendrite arm space and the secondary dendrite arm space. This value must also depend on the angle between the flow and the dendrite arms, so that it is very difficult to find a constant value relevant to all systems. In spite of the importance of this coefficient, very few research works to study its effect have been reported. In this model, the value of C" is determined, so as to fit results to experimental facts.

Figures 6.1–6.5 show velocity profiles and isotherms using the Dirichlet condition for various values of C".

Figure 6.1 shows results at C" = 0. In this case, the solidification phenomenon does not affect fluid flow because there exists no resistance from either a solid or a mushy region. Only the latent heat affects the energy field. Gr/Re^2 is 0.37, and the effect of natural convection is relatively small. Therefore, like a fluid flow of the aqueous experiments, the inlet flow penetrates along the centre line of the mould and generates a large recirculation in the pool. The moving roll causes a downward flow and a counter rotating flow develops. The thickness of the downward flow layer near the roll surface is small. A stagnant point of the flow, which was observed in the flow using a submerged nozzle, does not appear.

The isothermal lines correspond to the flow field. Hot metal flow from the entrance causes a high temperature region along the symmetric boundary. A cold region develops around the top right corner. The domain seems to be separated to two regions, hot and cold, by the upward flow between two recirculations.

The same result, practically, was obtained at C" = 0.001.

Figure 6.2 shows results at C" = 0.01. Both velocity profile and isotherms are distinct from Figure 6.1. The inlet flow from the entrance does not penetrate to the roll bite point but dissipates around the half depth of the pool. Recirculation caused by the inlet flow is relatively small. A downward flow near the roll surface develops well because a solid–mushy region, defined as the temperature below the liquidus temperature, is dragged down by the underlying solid. The force (resistance), however, is not enough strong to pull whole of the dendritic region. The final thickness of the solidified shell is larger than that of C" = 0.

Figure 6.3 shows results at C" = 0.1. A very strong downflow is observed near the surface of the roll, while the depth of the inlet flow's penetration reaches only one third of the total depth of the pool. Velocities at nodes near the roll surface are almost the same as the tangential velocity of the roll because of the large resistance in the 'solid' region. The solid region develops along the surface of the roll unlike profiles at smaller C", and metal is completely solidified before the roll bite point in this condition.

Compared with Figures 6.1(b) & 6.2(b), the temperature of the upper region of the wedged pool, particularly at the top surface, increases.

Since a constant temperature is assumed on all nodes of the right boundary, isotherms concentrate on the top right corner. In the real system, the flow at the corner may fluctuate, so a shape of the boundary and temperature might not be constant.

Figure 6.4 shows results at C" = 0.5. The thickness of a 'solidified' region on the roll is much thicker than that of C" = 0.1. Resistance is large enough to fix velocities in the solid/mushy region, so that the gradient of velocities in the downward flow is very small. Strong resistance in the mushy region also affects the flow, and no counter flow below the inlet flow is observed. In this case, the solid region occupies one third of the depth from the roll bite point, and after shell kissing point velocities are decided to conserve mass balance. The present model does not take account of deformation of the solidified shell, so velocities in the solid region might not correct.

Figure 6.5 shows results at C" = 2. A similar transport pattern to that for C" = 0.5 is obtained. Thickness of the solid region increases.

In case that the value of C" is more than 5, solutions of the computations diverged. The reason is considered that a strong downward flow in the solid region, whose velocities are forced to be fixed mathematically, break mass and momentum conservation in the wedged-shape computational domain. Since the present model does not handle deformation of the solid region, an object which contains a large solid region is not suitable for the model.

The assumption of constant temperature on the boundary may not be realistic. To confirm the effect of C", a similar investigation was carried out using the Neumann boundary condition.

Figure 6.6 shows a velocity profile and isotherms at $C^* = 0$, the local heat transfer coefficient is $4500/t^{0.547}$ W/m^2K. Inlet flow from the entrance penetrates vertically and mixing of the molten metal in the pool is low. The cold metal stays at the upper right zone and a large solid region (defined below T_s here) develops. The solid region disappears in the lower zone by attack from the hot metal inflow. It is distinct from that of the Direchlet condition, and also the fluid flow profile is slightly different because of the effect of the natural convection.

Figure 6.7 shows results at $C^* = 0.01$. In this case, similar profiles to those of the Dirichlet condition are obtained. The inlet flow is diffused half way down the pool, while the thickness of the downward flow near the roll surface increases. The solid region expands vertically, and the liquid region increases. Since an insolated boundary condition was used at the top right corner, isotherms there are parallel to each other. At the exit, or roll bite point, the thickness of the solidified shell was 0.6 mm, and the surface temperature of the shell 164°C. Intuitively, the shell profile appears to be physically unrealistic.

Figure 6.8 shows results at $C^* = 0.1$. Velocities in the solid region are fixed, and the solidified shell grows along the roll surface. The shell is slightly remelted in the narrow zone of the pool, and the final shell thickness is 0.76 mm, which is 48% of the distance between rolls. The temperature of surface is 159 °C there.

Figure 6.9 shows results at $C^* = 0.5$. The solidified shell develops along the roll surface, and the shells on both sides meet before the roll bite point. A counter flow is observed under the inlet flow, and its influence on the temperature field is also observed. Velocities toward the roll at the meniscus surface increase. It demonstrates that resistance in the lower zone increases. The temperature of the shell surface at the exit was 147 °C.

Figure 6.10 shows the results for $C^* = 2$. The solidified shells 'kiss' each other at depth of 20 mm into the pool. The inlet flow, therefore, does not penetrate deeply and but spreads horizontally near the meniscus. In this case, solutions were fluctuating and did not converge.

As already mentioned, the resistance coefficient C" exerts a significant influence upon both velocity profiles and energy profiles. Increase in the value C" increases the force to fix velocities in the mushy-solid region and gives physically more reasonable transport profiles. But also it increases a solid region and causes instability during computations, particularly in wedged-shape domains.

In the author's opinion, each solidification system has an intrinsically different resistance for the mushy region and has its own value of C" of the model, so that it is necessary for the model to be compared with experimental results in each instance. The velocity profile, at least, ought to satisfy the physical fact that the solid region moves down at the same velocity as the tangential velocity of the roll. And it may be observed that the value chosen for C" is sufficiently small enough to allow for significant flow in the mushy region at high local liquid fractions. From the points, the value C" $= 0.1 \sim 0.5$ were adopted for the model. This value is equivalent to $10^3 \sim 5\text{x}10^3$ in a dimensional system. Voller and Parakash (1987) chose $1.6\text{x}10^3$ for a cavity problem, and Brent et al. (1988) used $1.6\text{x}10^6$ for a pure gallium ingot system. Evidently, further research in this area is called for.

In the next section, the results are compared in detail with the experimental results of Hojo et al., reported in 1987.

6.3 Comparison with experimental data
– effects of a thermal boundary condition & validation –

Figures 6.11 and 6.12 show isotherms with various thermal boundary conditions.

Figure 6.11(a) illustrates the experimental result measured by Hojo et al. (1987) using 40 thermocouple, while (b) ~ (h) illustrate computational results. Conditions for each case are summarized in the following Table 6.

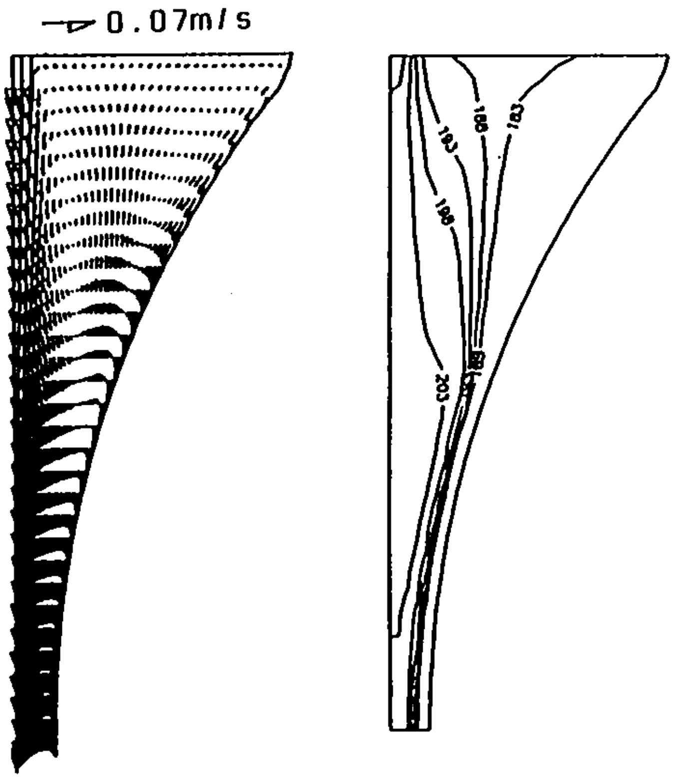

(a) velocity profile (b) isotherms

Figure 6.1 Fluid flow and temperature profile

resistance constant C" = 0
temperature of surface 150°C

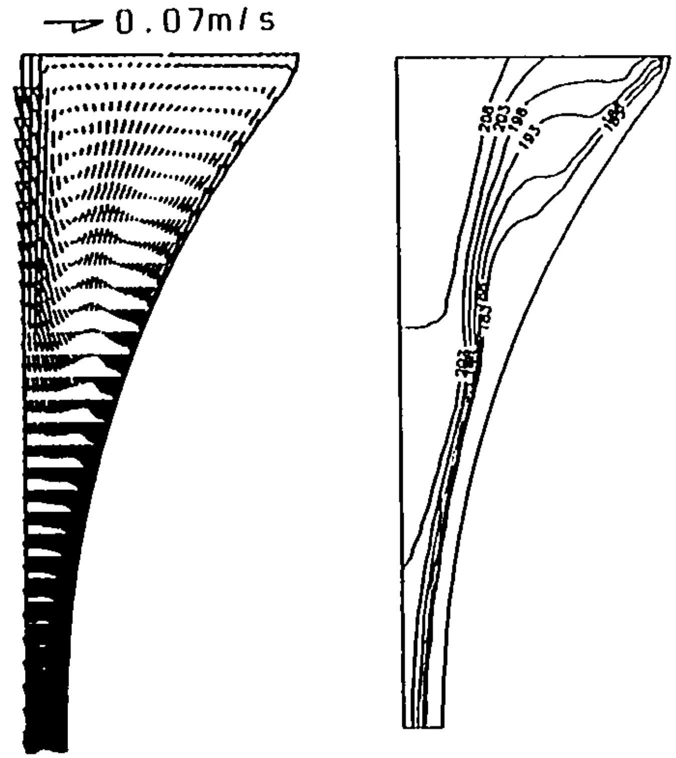

(a) velocity profile (b) isotherms

Figure 6.2 Fluid flow and temperature profile

resistance constant C" = 0.01
temperature of surface 150°C

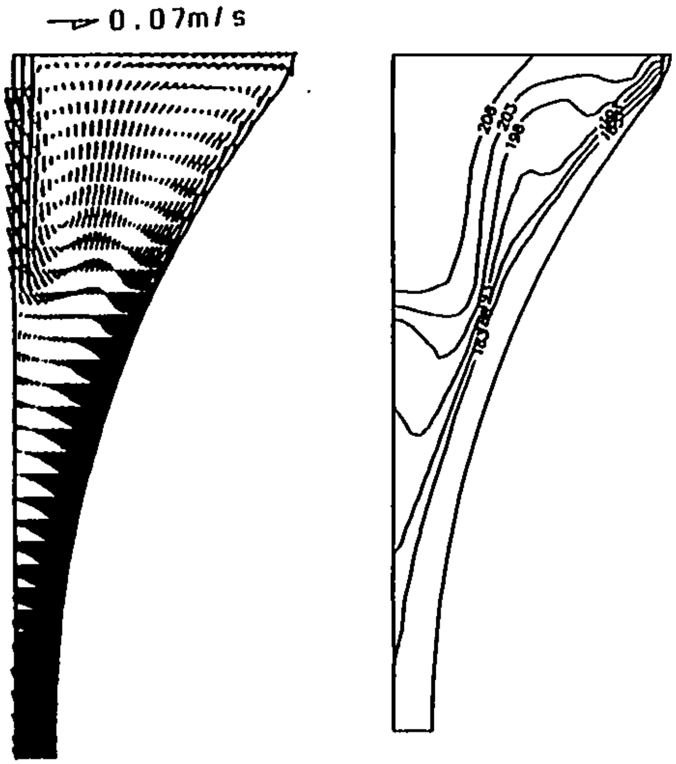

(a) velocity profile (b) isotherms

Figure 6.3 Fluid flow and temperature profile

resistance constant C" = 0.1
temperature of surface 150°C

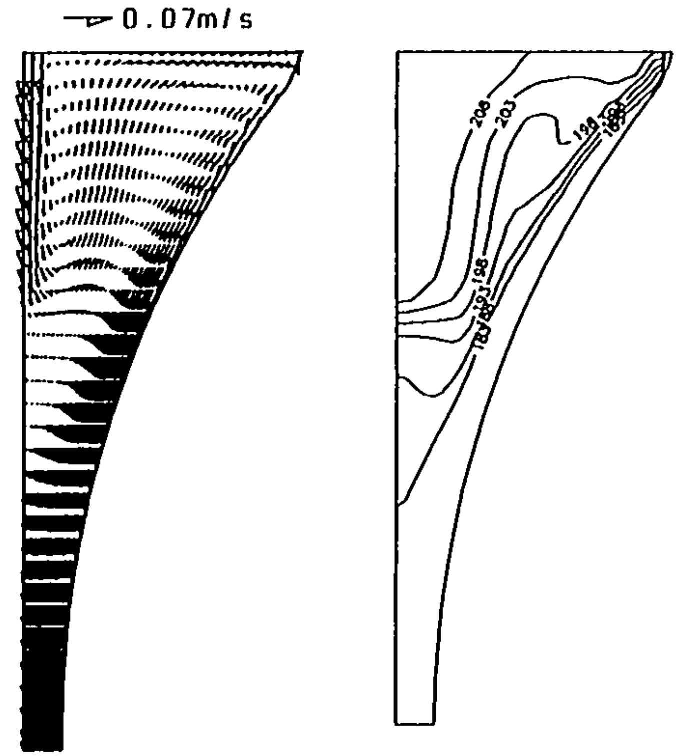

(a) velocity profile (b) isotherms

Figure 6.4 Fluid flow and temperature profile

resistance constant C" = 0.5
temperature of surface 150°C

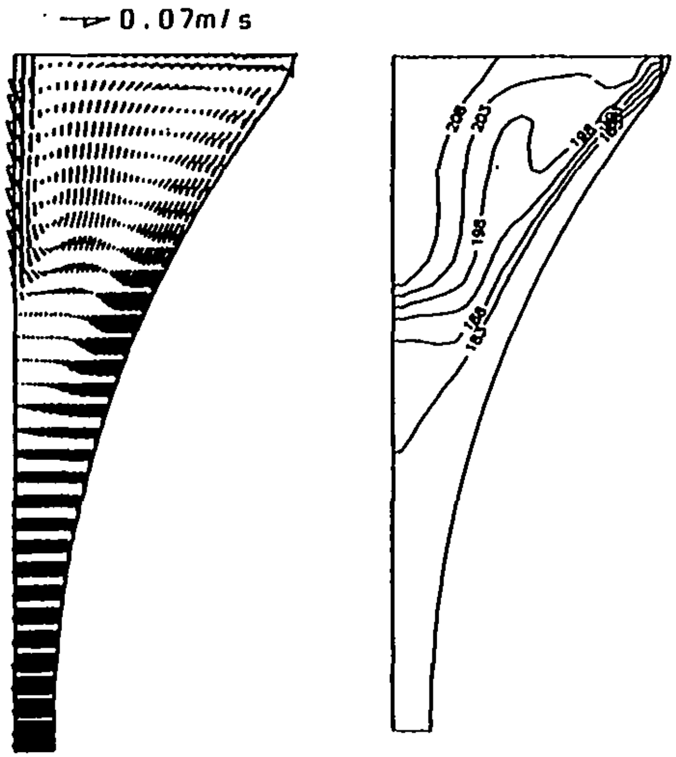

(a) velocity profile (b) isotherms

Figure 6.5 Fluid flow and temperature profile

resistance constant C" = 2.0
temperature of surface 150°C

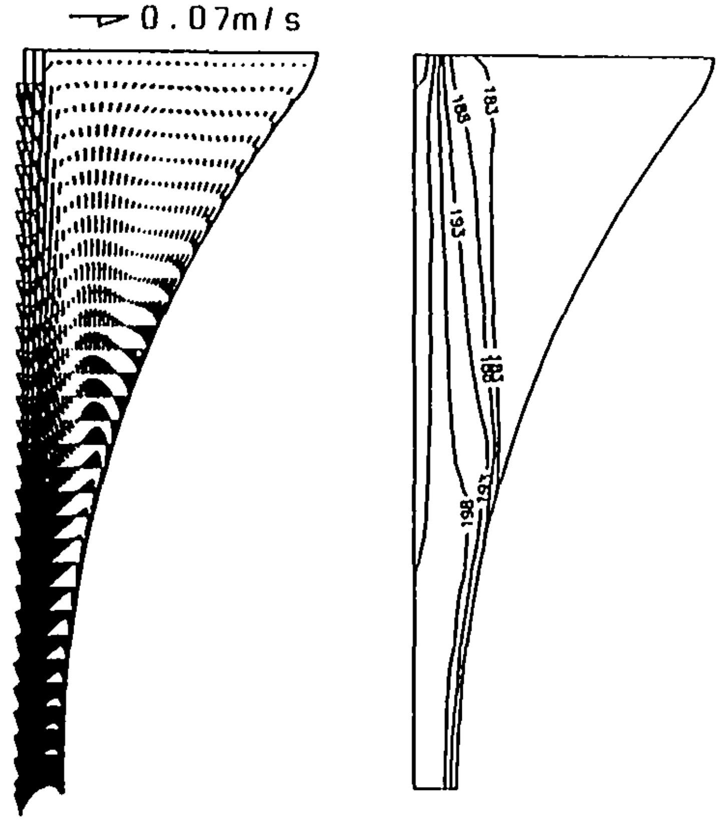

(a) velocity profile (b) isotherms

Figure 6.6 Fluid flow and temperature profile

resistance constant C" = 0.
heat transfer coefficient $4500/t^{0.547}$ W/m^{2}K

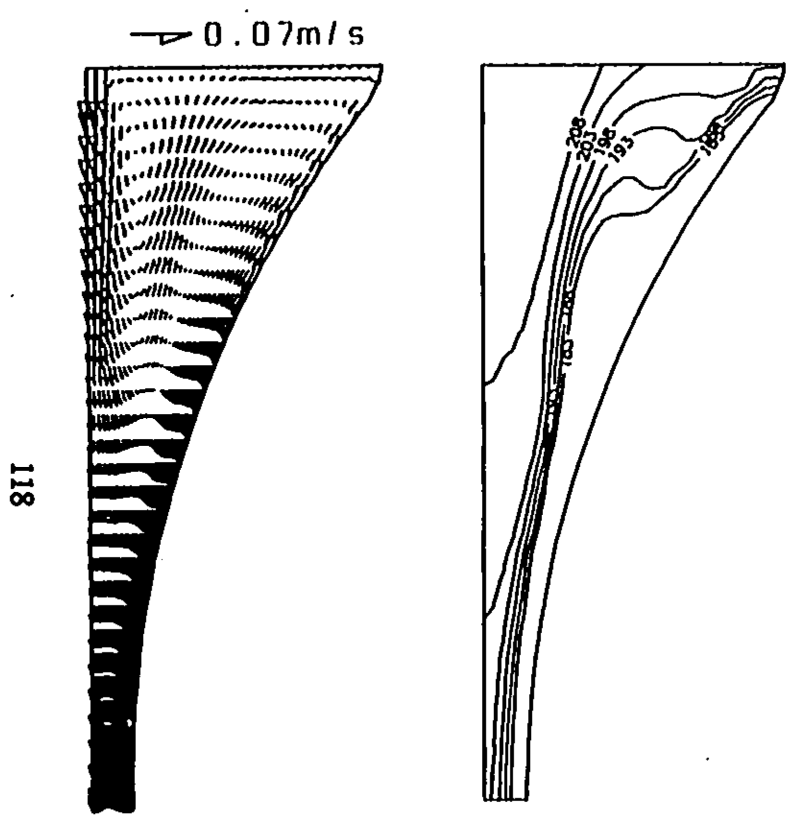

(a) velocity profile (b) isotherms

Figure 6.7 Fluid flow and temperature profile

resistance constant C" = 0.01
heat transfer coefficient $4500/t^{0.547}$ W/m^2K

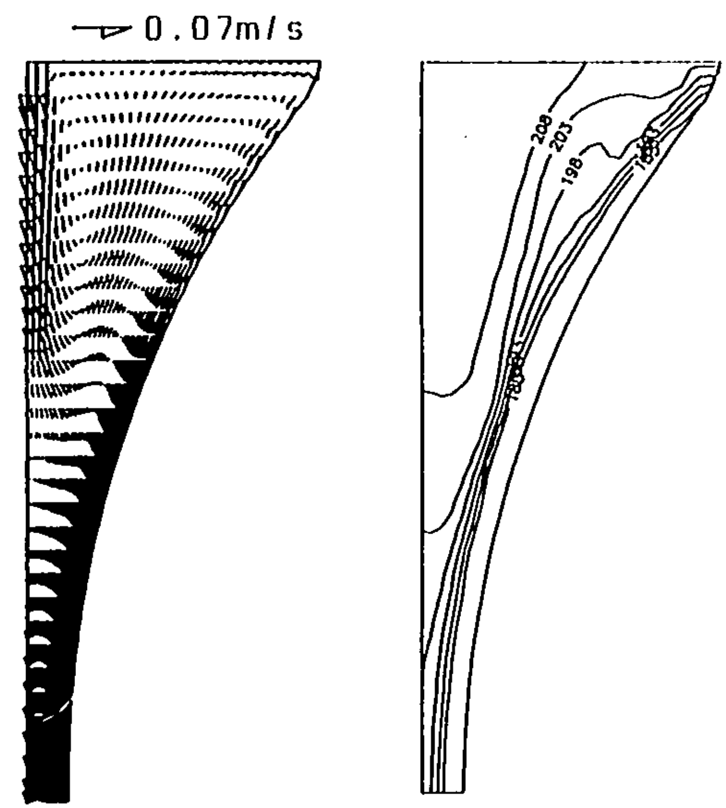

(a) velocity profile (b) isotherms

Figure 6.8 Fluid flow and temperature profile

resistance constant C" = 0.1
heat transfer coefficient $4500/t^{0.547}$ W/m^2K

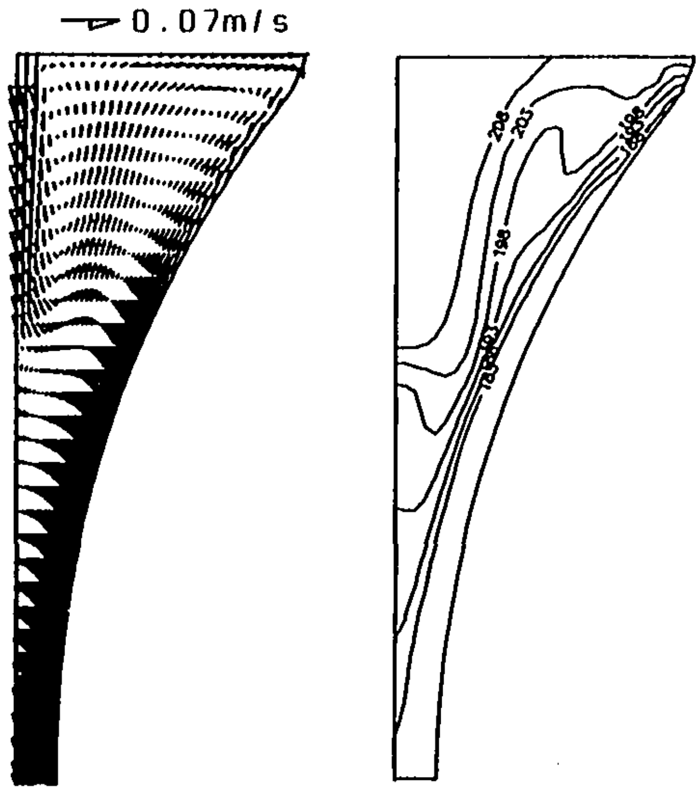

(a) velocity profile (b) isotherms

Figure 6.9 Fluid flow and temperature profile

resistance constant C" = 0.5
heat transfer coefficient $4500/t^{0.547}$ W/m²K

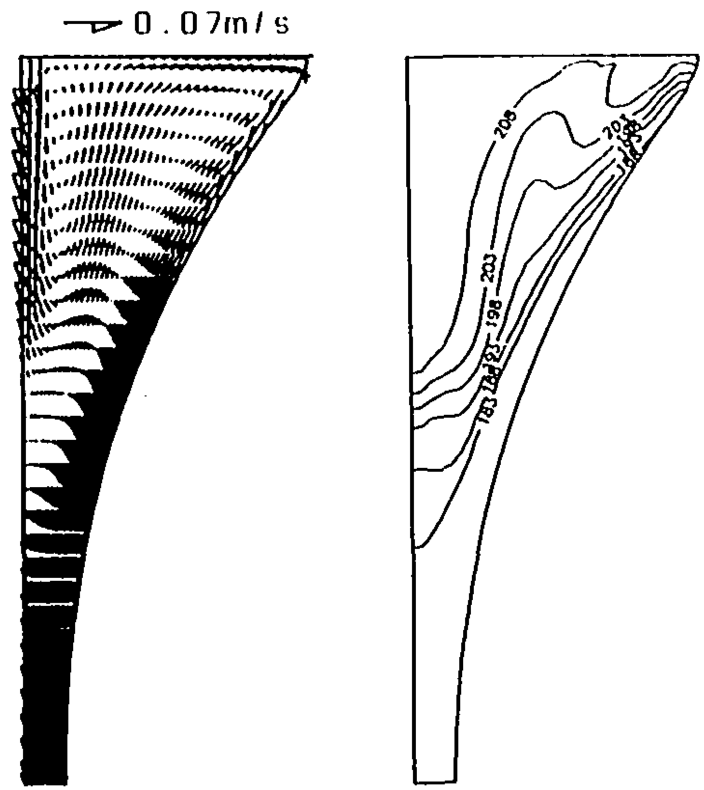

(a) velocity profile (b) isotherms

Figure 6.10 Fluid flow and temperature profile

resistance constant C" = 2.
heat transfer coefficient $4500/t^{0.547}$ W/m²K

Table 6 Conditions for Calculations

	C"	thermal boundary condition
case (b)	0.1	$T_0 = 150°C$
case (c)	0.1	$h_i = 4500/t^{0.547}$ W/m^{2}K
case (d)	0.5	$h_i = 4500/t^{0.547}$ W/m^{2}K
case (e)	0.3	$h_i = 4500/t^{0.547}$ W/m^{2}K
case (f)	0.5	$h_i = 4000/t^{0.547}$ W/m^{2}K
case (g)	0.5	$h_i = 4000/t^{0.6}$ W/m^{2}K
case (h)	0.5	$T_0 = 130 - 183°C$

In the experiment, the inlet flow generates a region of hot liquid around the centre line, while a large mushy region develops in the rest of the mould. The isothermal lines lie along the roll surface and the final thickness of the solidified shell is 1.42 mm. The shell seems to remelt and is thin near the middle of the sump. The computational results revealed similar temperature profiles to those of Hojo et al.'s experiment, particularly in the simulation of a large mushy region and a similar fully liquid region. Large or small, however, all computational results show the hot liquid region tends to spread horizontally near the meniscus surface unlike Hojo et al.'s data. It can be speculated that the resistance to flow in the mushy region is overestimated. For the same reason, the computational results show flat curves of the liquidus line crossing the boundary of symmetry.

Each of the 200°C isotherm lines in the computational results is very wavy instead of the straight cone-like experimental line shown in Figure 6.11(a). This is because the isotherms of the present calculations were steady state solutions and directly related to the flow field, the convective heat transfer dominating thermal diffusion phenomena.

Regarding the solidified shells, in case(b) and (d) the metal solidified before the roll bite point. In these two cases, the 190°C isotherms lie at similar locations to those found by Hojo et al.'s. The other results predict much thinner shells than those reported by Hojo et al.'s. Similarly, the 190°C line locates close to each shell. It is because the liquid fraction, where temperatures are less than 190°C, is expected to be less than 30%, and the region is expected to behave practically as though it were solid. Figure 6.12(h) illustrates the result using a Dirichlet boundary condition II wherein the temperature of the roll surface is fixed at a value varying linearly from the solidus temperature at the first point of contact point to 130°C at the roll bite point. Since the surface temperature is fixed relatively higher, the fully liquid region spreads widely near the meniscus.

To investigate thermal conditions in more detail, further comparisons were made and are now presented.

Figure 6.13 provides a comparison of the temperature along the vertical axis of symmetry of the mould. The solid red circle represents Hojo et al.'s data. Each computational result predicts an abrupt temperature curve between the 15 and 20 mm point. This zone represents the end point of the inlet flow beyond which the resistance becomes abruptly larger. Hojo et al.'s data reveals a similar temperature curve. Cases (d) and (g) also suggest good agreement with experiment. The abrupt curves in cases (b) & (d) near the roll bite point are related to the completion of solidification.

Figure 6.14 compares shell thicknesses correlated with the contact time between the metal and the roll. The contact time was calculated from the tangential velocity and the distance between the first contact point and the location on the roll. An analytical solution using the Virtual Adjunct Method (VAM) (Clyne & Garcia, 1981) was also obtained and is also illustrated.

Using VAM, the relation between shell thickness 'd' and contact time 't' are described by :

$$t = B_1 d^2 + B_2 d \qquad (6.2)$$

where

$$B_1 = \frac{1}{4 a_s \chi^2} \qquad (6.3)$$

$$B_2 = \frac{C_{ps}\rho_s}{\pi^{\frac{1}{2}}\chi \exp(\chi^2)\left(M^{\frac{1}{2}} + erf(\chi) \right) h_i} \qquad (6.4)$$

constant 'χ' is obtained by iterations from the following condition

$$\frac{\exp(-\chi^2)}{M + erf(\chi)} = \frac{m(T_{in}-T_S)\exp(-n^2\chi^2)}{(T_S-T_{roll})(1-erf(n\chi))} + \frac{\pi^{\frac{1}{2}}\lambda\chi}{C_{ps}(T_S-T_{roll})} \tag{6.5}$$

where $M = K_S C_{PS}\rho_S/K_m C_{Pm}\rho_m$, $m = K_L C_{PL}\rho_L/K_S C_{PS}\rho_S$, $n = a_S/a_L$, and the local heat transfer coefficient $h_i = 4500/t^{0.547}$ is used.

The analytical solution shows a root square curve of time, and is much lower values than numerical and experimental results. This discrepancy is thought to be related to the fact that VAM assumes the metal inlet flow is rectified along whole area of the meniscus surface. In this assumption, a shell might develop at a root square curve and shell growth is rather depressed. This analytical model can not account for influence of the inlet flow condition.

Hojo et al.'s data shows a characteristic curve, which demonstrates a pause in shell growth between 0.2 and 0.5 second. Although none of the computational results predict the Hojo et al.'s results quantitatively, the results of cases (b) and (d) have flat curves which mean a pause of the sheil growth between 0.4 and 0.6 second and show a similar trend. To understand quantitative differences, a more detailed investigation would seem to be required.

From the results shown in Figure 6.11 – 6.14, case (d) best predicts the Hojo et al.'s experimental results. Although one could get the better computational results through ad-hoc tuning, it is not important for us to create a result completely corresponding to the experimental one by arranging unknown boundary conditions. The purpose of the work is not to predict Hojo et al.'s data but to demonstrate the possibility of the numerical model for simulating transport phenomena in a twin roll caster and for investigating features of the system.

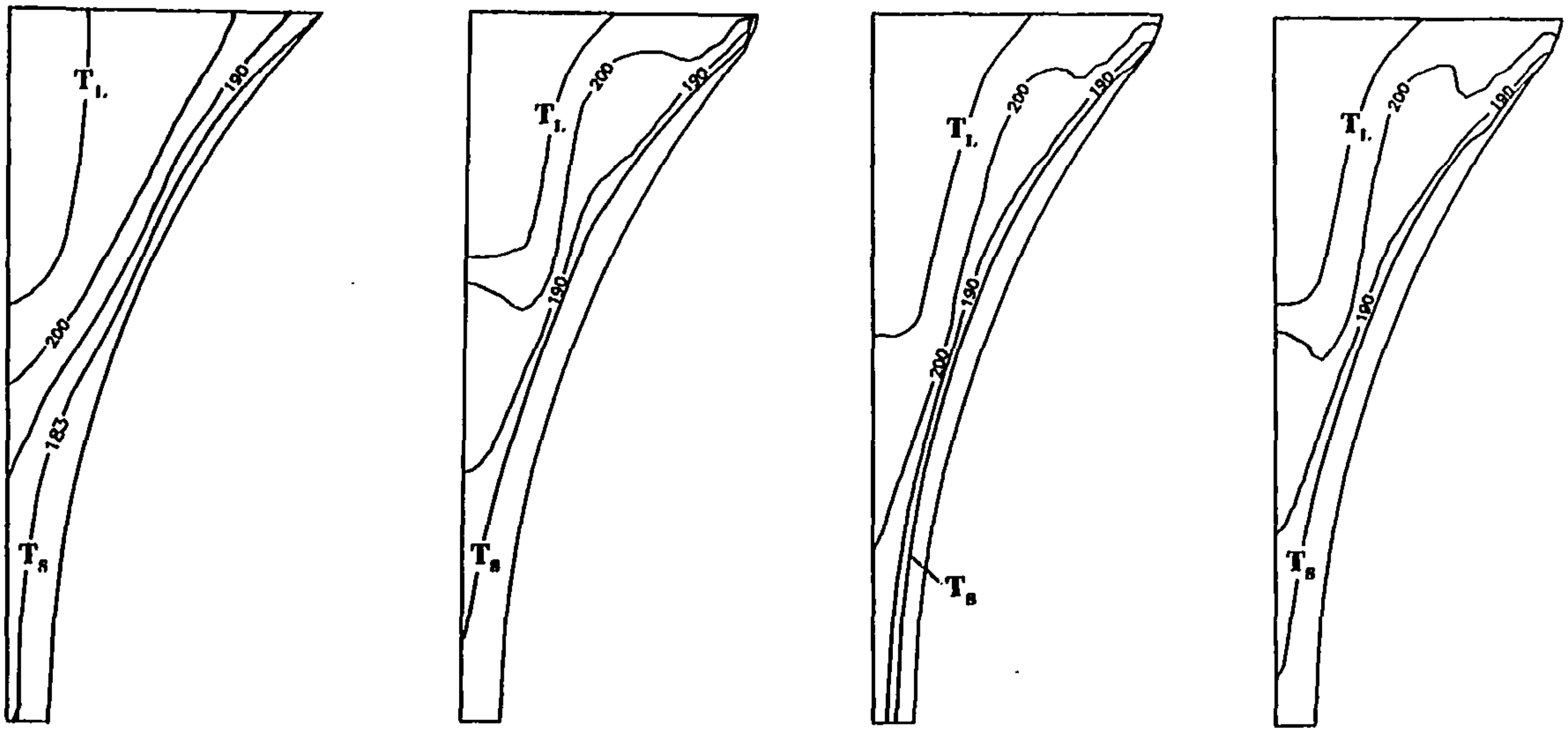

(a) **experiment**
Hojo et al (1987)

(b) **calculation**
$C'' = 0.1$
$T_0 = 150°C$

(c) **calculation**
$C'' = 0.1$
$h_i = 4500/t^{0.547}$ W/m^{2}K

(d) **calculation**
$C'' = 0.5$
$h_i = 4500/t^{0.547}$ W/m^{2}K

Figure 6.11 **Comparison of temperature profiles**

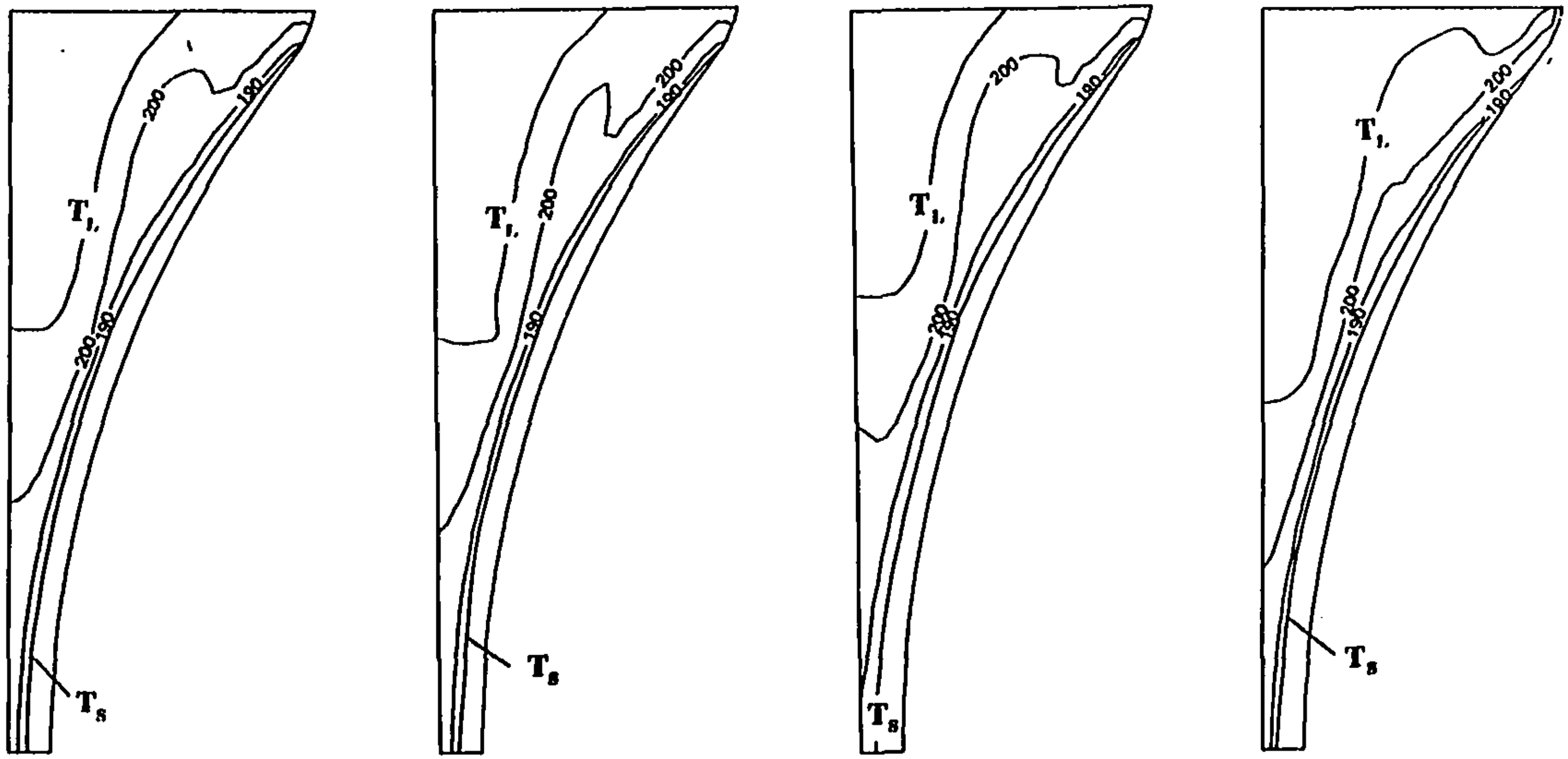

(e) calculation
$C'' = 0.3$
$h_l = 4500/t^{0.547}$ W/m²K

(f) calculation
$C'' = 0.5$
$h_l = 4000/t^{0.547}$ W/m²K

(g) calculation
$C'' = 0.5$
$h_l = 4000/t^{0.6}$ W/m²K

(h) calculation
$C'' = 0.5$
$T_0 = 130 \sim 183$°C

Figure 6.12 Comparison of temperature profiles

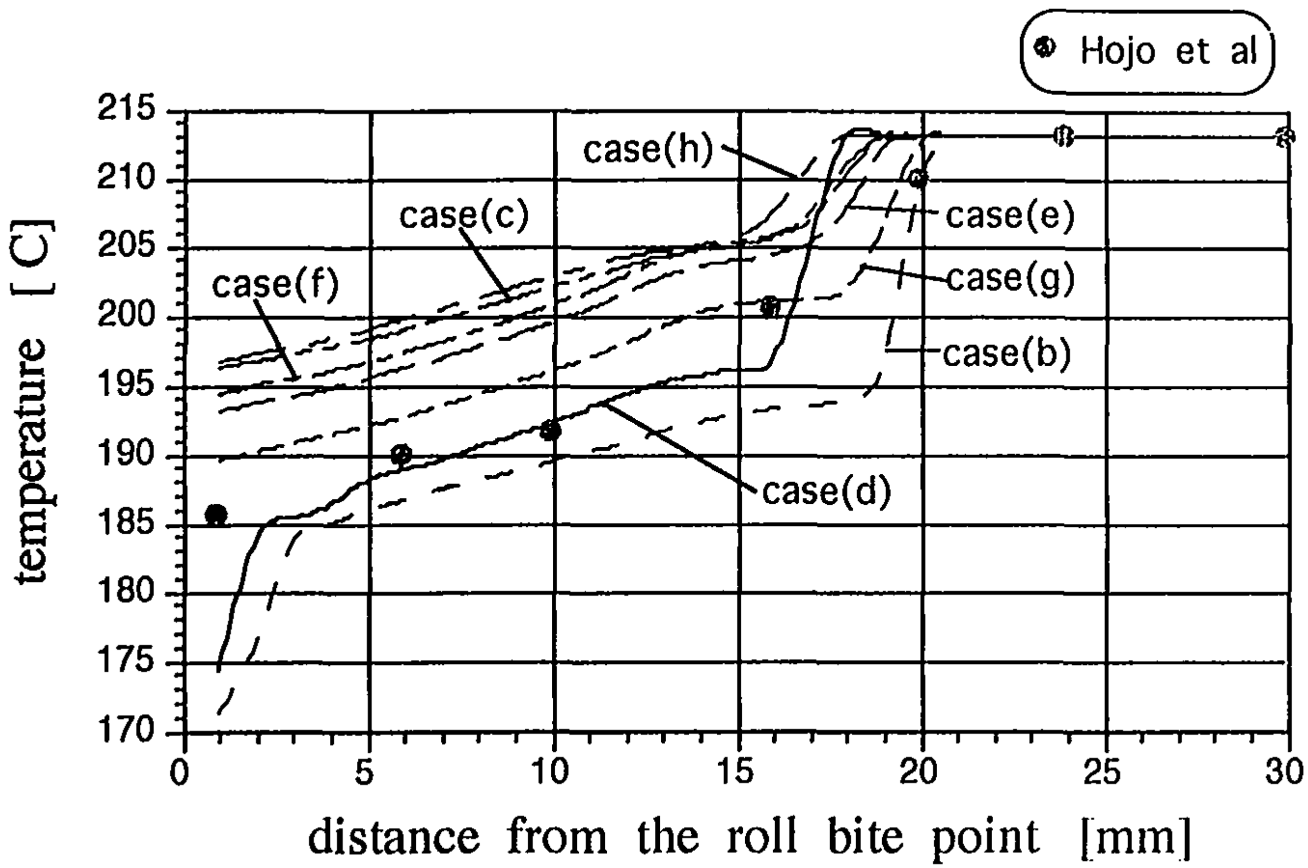

Figure 6.13 Temperature of the centre line of the mould

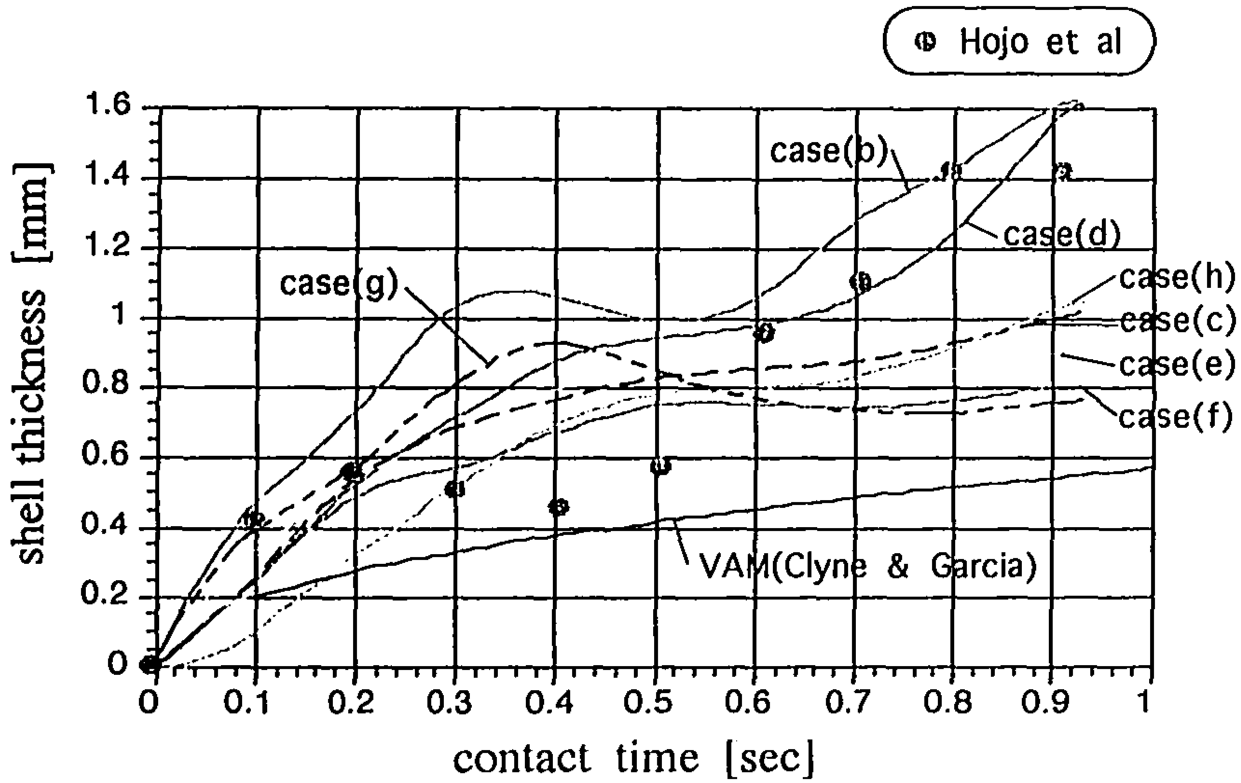

Figure 6.14 Relation between contact time and shell thickness

6.4 Effects of Turbulent Prandtl Number

The turbulent Prandtl number is one of the most important parameters influencing the transport of energy, and its effects are discussed in this section.

In turbulence, the shear stress 'τ' and heat flux 'q' are given, on the x–y plane, by,

$$\tau = \mu\frac{\partial\bar{u}}{\partial y} - \rho\overline{u'v'} \tag{6.6}$$

$$q_y = \kappa\frac{\partial\bar{T}}{\partial y} - \rho C_p\overline{T'v'} \tag{6.7}$$

where u'_i represents velocity fluctuation and T' is temperature fluctuation.
By analogy with Prandtl's mixing length hypothesis, the fluctuating components are expressed by,

$$\overline{u'v'} = -\nu_t\frac{\partial\bar{u}}{\partial y}, \qquad \overline{T'v'} = -\frac{\kappa_t}{\rho C_p}\frac{\partial\bar{T}}{\partial y} \tag{6.8}$$

Here the turbulent Prandtl number 'Prt' is defined as,

$$Pr_t = \frac{\nu_t}{\kappa_t/\rho C_p} = \frac{\mu_t C_p}{\kappa_t} \tag{6.9}$$

Many researchers have investigated the turbulent Prandtl number for a long time, mainly by experimental methods. Most of them, however, have investigated simple flow systems, for instance a pipe flow, and very few works have been carried out for complex geometries such as the twin roll caster mould.

Generally, the value 0.9 is used as the turbulent Prandtl number of air, and 1.0 is used for water. In practice, these values prove to be quite accurate in many cases, provided molecular conduction processes are relatively unimportant in comparison to turbulent transport process.

Concerning the value for hot liquid metal, however, no experimental data has been reported. The Prandtl number of a liquid metal is much smaller than 1 (e.g. 0.15 for steel and 0.01 for Al). As such, the heat conductive layer is thicker than the laminar sub-layer in turbulent heat transfer. Since eddies of turbulence easily lose their heat by conduction during their irregular motions, the transport of heat is considered smaller than that of momentum. To take into account such phenomena, a value which is larger than 1 is sometimes adopted for a liquid metal. Tani (1984) suggested $Pr_t = 2 - 3$ in a liquid metal.

To investigate effects of the turbulent Prandtl number in the system, several calculations, for various of $Pr_t = 0.5 - 5$, have been carried out.

Figure 6.15 shows isotherms at Prt = 1, 1.5, 2 and 3 when the resistance constant C" = 0.5, the heat transfer coefficient $h_i = 4500/t^{0.547}$. No big differencce is observed among them, but the thickness of the solidified shell at the roll bite point is slightly decreased with increase in Pr_t. When Pr_t is less than 1, the shell is completely solidified at the exit.

Figure 6.16 shows the temperature profile of the centre line of the mould. Except near the roll bite point, all results are very close. Also, very similar shell profiles to those measured were obtained in all cases, as shown in Figure 6.17.

Considering the results, the effects of Pr_t on the transport profile is very small in this system. The results demonstrate that convective heat transfer is much larger than conductive heat transfer in such systems.

Figure 6.18 shows the final thickness of the solidified shell at the roll bite point, at the contact time of 0.92 sec, correlated to the turbulent Prandtl number. Under the selected conditions, the prediction of the shell thickness at $Pr_t = 3$ coincided with the Hojo et al.'s result. The change of values seems to follow a curve tending towards a horizontal asymptote. The reason why the thickness is affected only near the roll bite point by variations in Pr_t, in spite of very little influence at other locations, is that the flow near the roll bite point is very small because of high resistance there. It demonstrates that heat conduction at the point is important enough to determine the inner quality of strip.

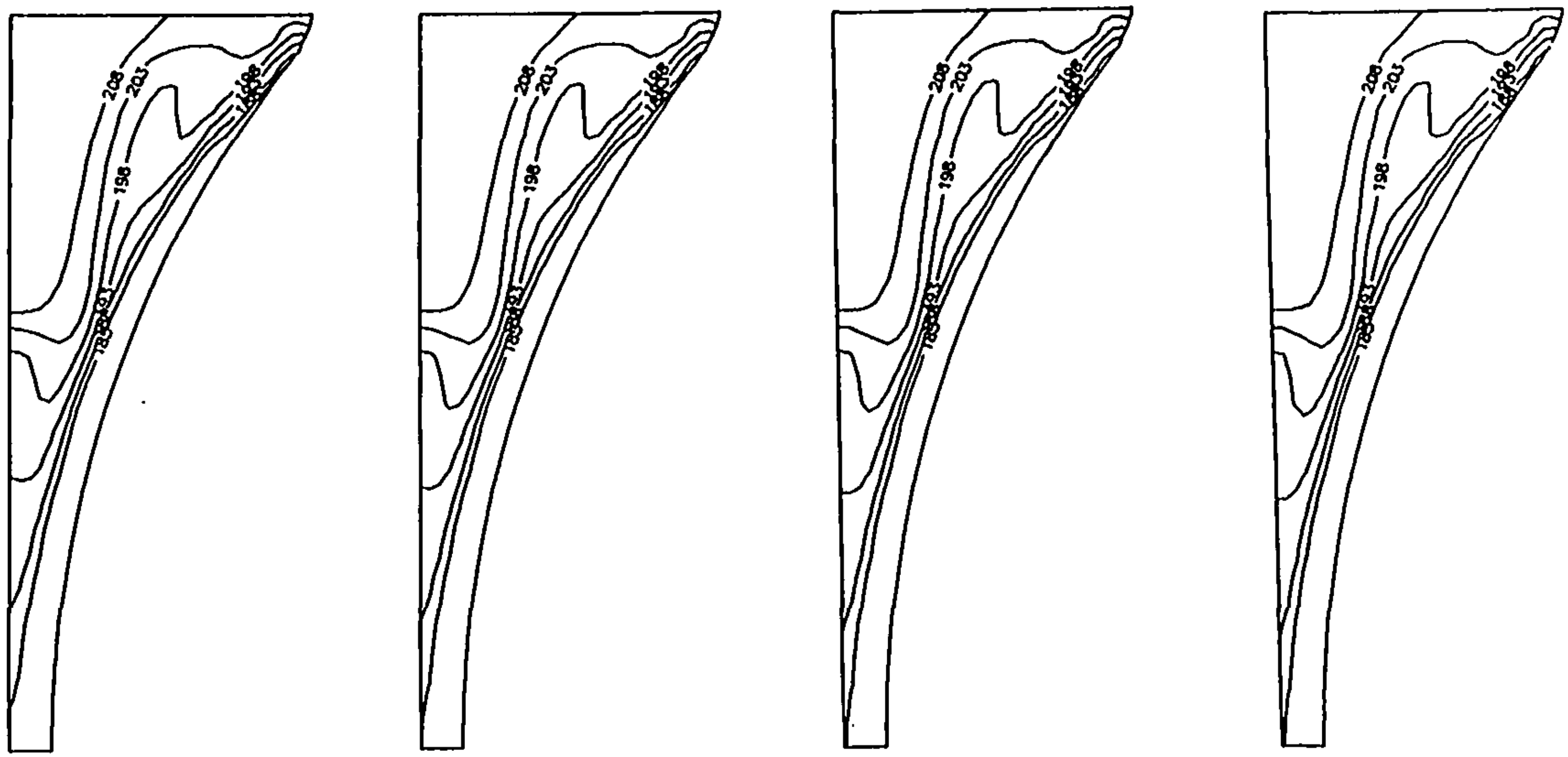

(a) Pr_t = 1.0 (b) Pr_t = 1.5 (c) Pr_t = 2.0 (d) Pr_t = 3.0

Figure 6.15 Comparison of temperature profiles for effects of turbulent Prandtl number ($C'' = 0.5$, $h_l = 4500/t^{0.547}$ W/m^2K)

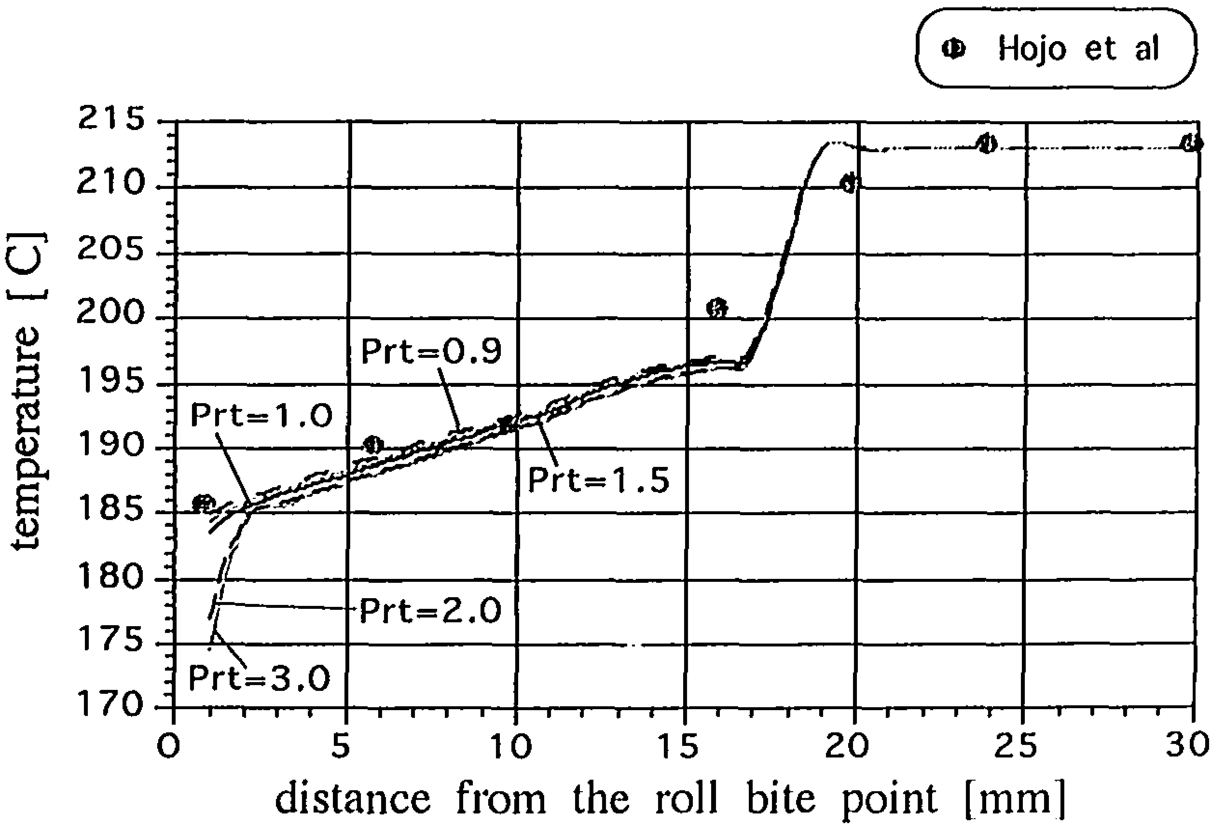

Figure 6.16 Temperature of the centre line of the mould
Effects of P_{rt} (C'' = 0.5, $h_i = 4500/t^{0.547}$ W/m^2 K)

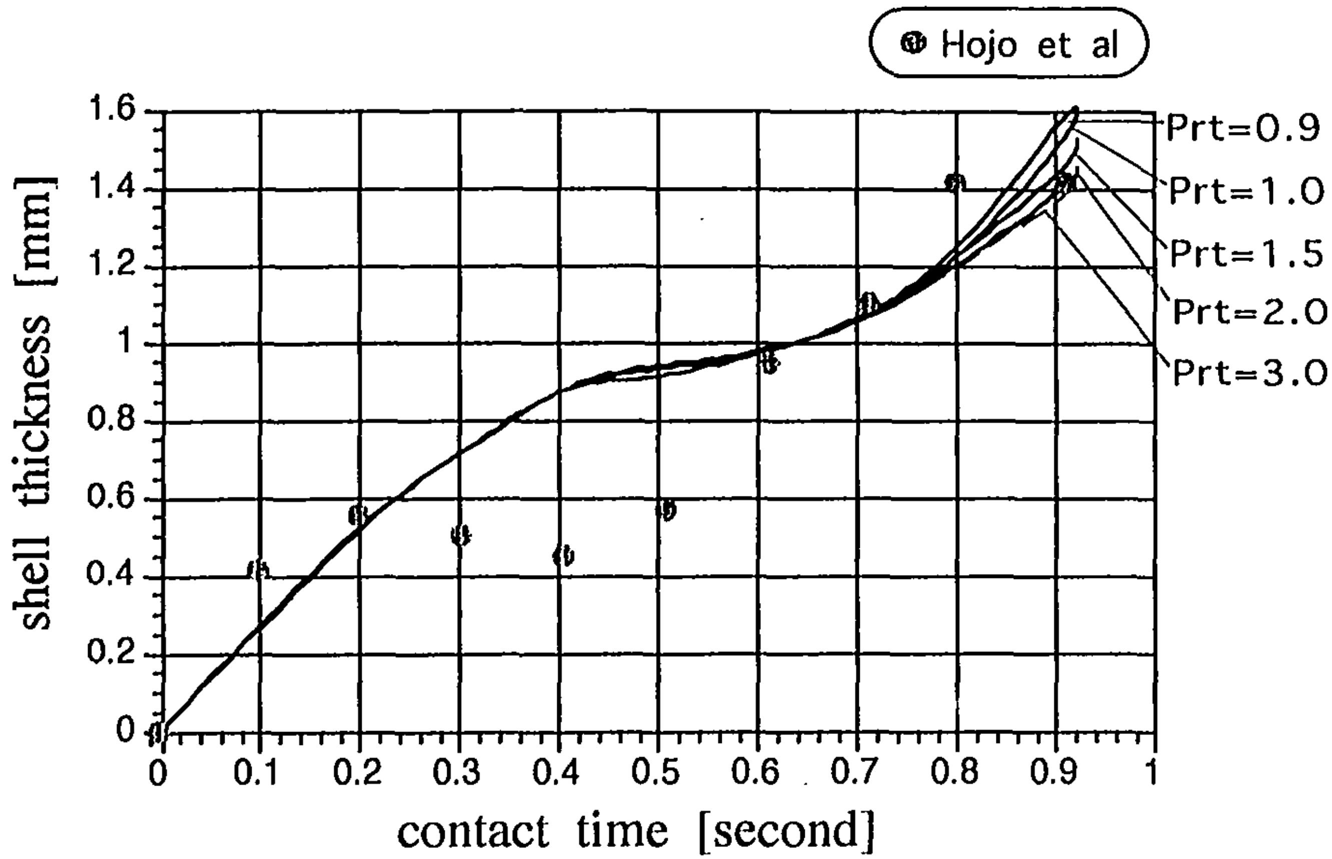

Figure 6.17 Relation between contact time and shell thickness
Effect of P_{rt} ($C'' = 0.5$, $h_i = 4500/t^{0.547} W/m^2K$)

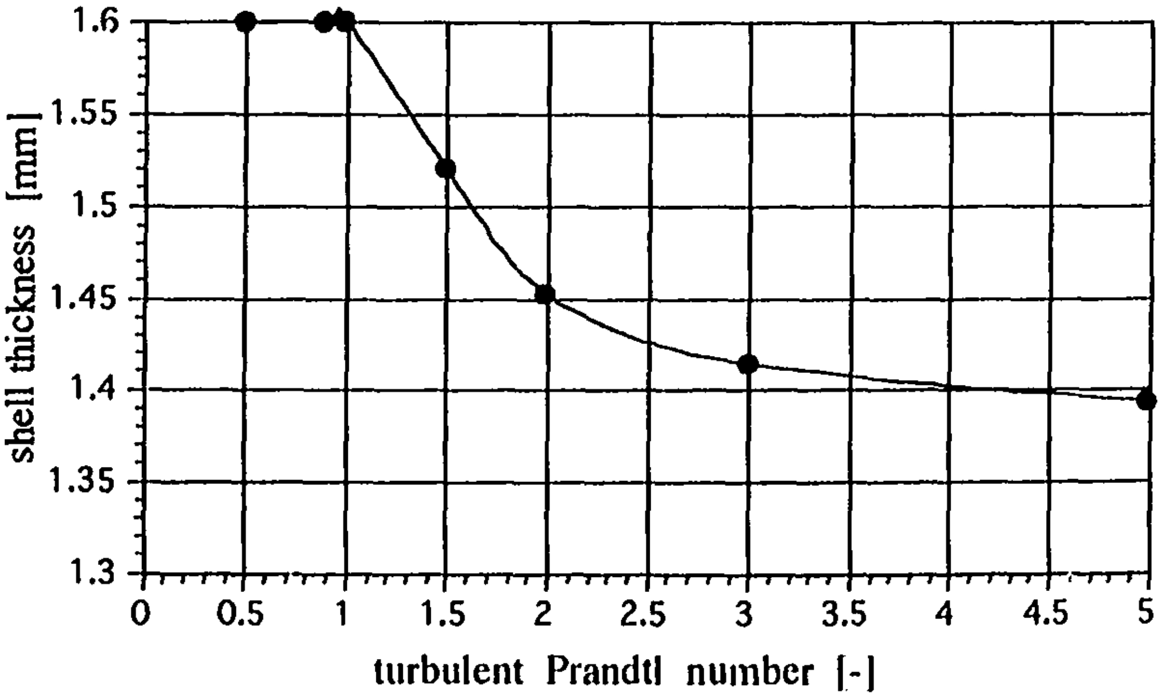

Figure 6.18 Relation between shell thickness and turbulent Prandtl number ($C'' = 0.5$, $h_l = 4500/t^{0.547}\,W/m^2K$)

6.5 Effects of Superheat

Superheat (or inlet temperature) is an important operational parameter in casting processes. In this section, the effects of superheat (SH) are investigated for four different values of superheat, SH = 1, 5, 10 and 20 K. Since the real thermal boundary condition is unknown for each case, the same heat transfer coefficient, $h_i = 4500/t^{0.547}$ W/m^{2}K, was used. The resistance constant C" and the turbulent Prandtl number Pr_t were fixed at 0.5 and 3.0, respectively.

Figure 6.19 shows a comparison of isotherms. Hojo et al. (1987) also measured temperatures at SH = 1 K, and their result are also shown.

When the superheat is 1 K (i.e. inlet temperature = 209°C) solidification is completed before the roll bite point in both calculations and Hojo et al.'s experiments. However, the location of their liquidus lines are very different from each other. In the computational result, a large liquid region exists, and it shows heat loss of the inlet flow is very small. Figure 6.19(a) illustrates a small liquid region experimentally and a very large mushy region, and difference of the superheat significantly influences a temperature profile. Although comparison among Figure 6.19(b) – (d) also shows that decrease of the super-heat increases the area of the mushy region, the amount of the increase is smaller than Hojo's results.

Hojo's temperature data fluctuated by more than ± 1 K, so both a more precise model and a more precise measurement are necessary to discuss these results quantitatively.

Figure 6.20 shows the temperature of the centre line of the mould.
Temperature lines at SH = 1, 5, 10 K in the lower zone within 15mm of the roll nip are very close. Hojo et al.'s data show the same tendency. It is considered that heat transfer near the kissing point of the shells is relatively small because of very little flow, particularly at conditions of small superheat. Temperature drops are also observed at the same position, and no temperature decrease of the inlet flow is observed under these conditions.

When the superheat is 20 K, the temperatures exhibit over-all increase. Negligible heat

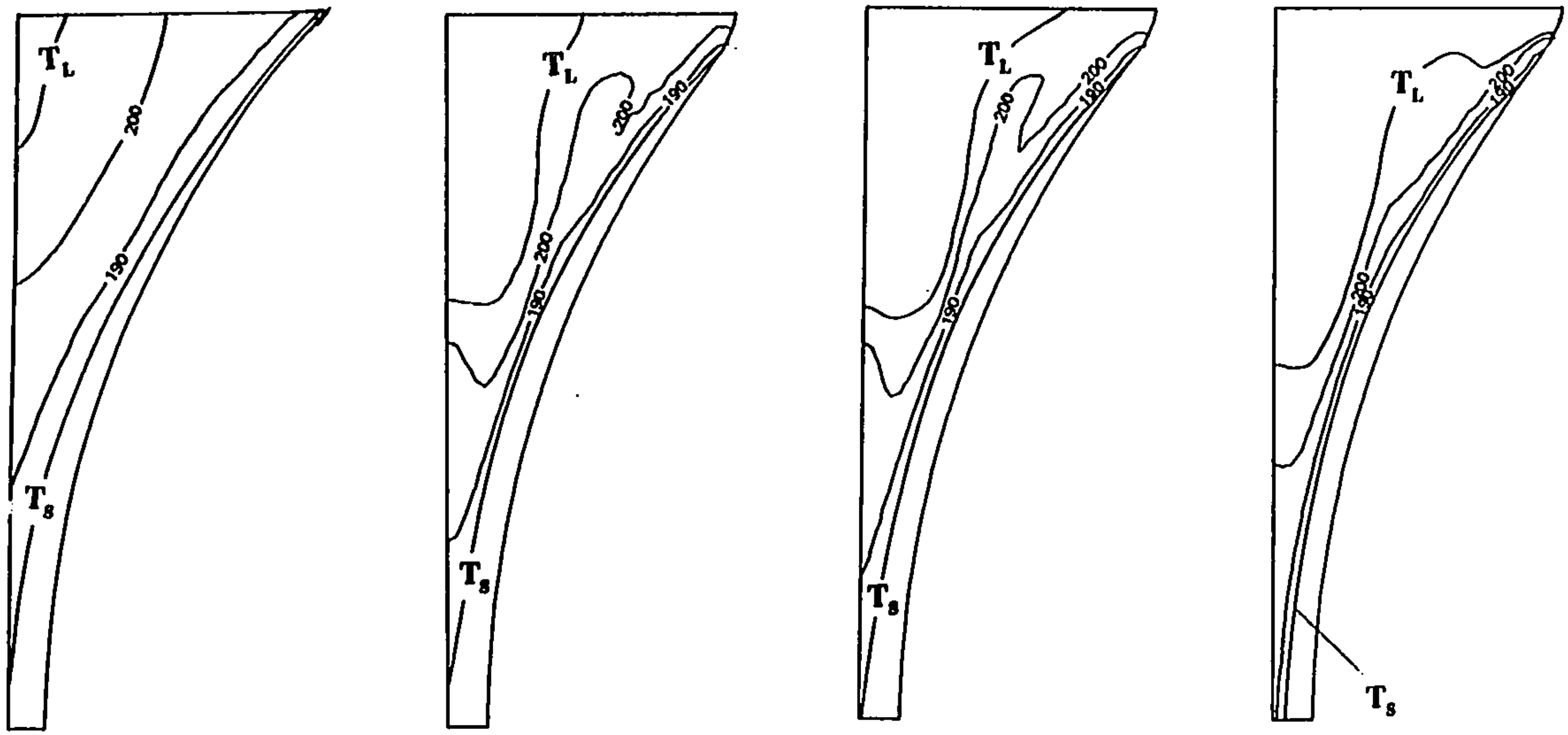

(a) SH = 1 K   (b) SH = 1 K   (c) SH = 10 K   (d) SH = 20 K

Hojo et al (1987)

Figure 6.19 Comparison of temperature profiles Effect of super-heat (SH)

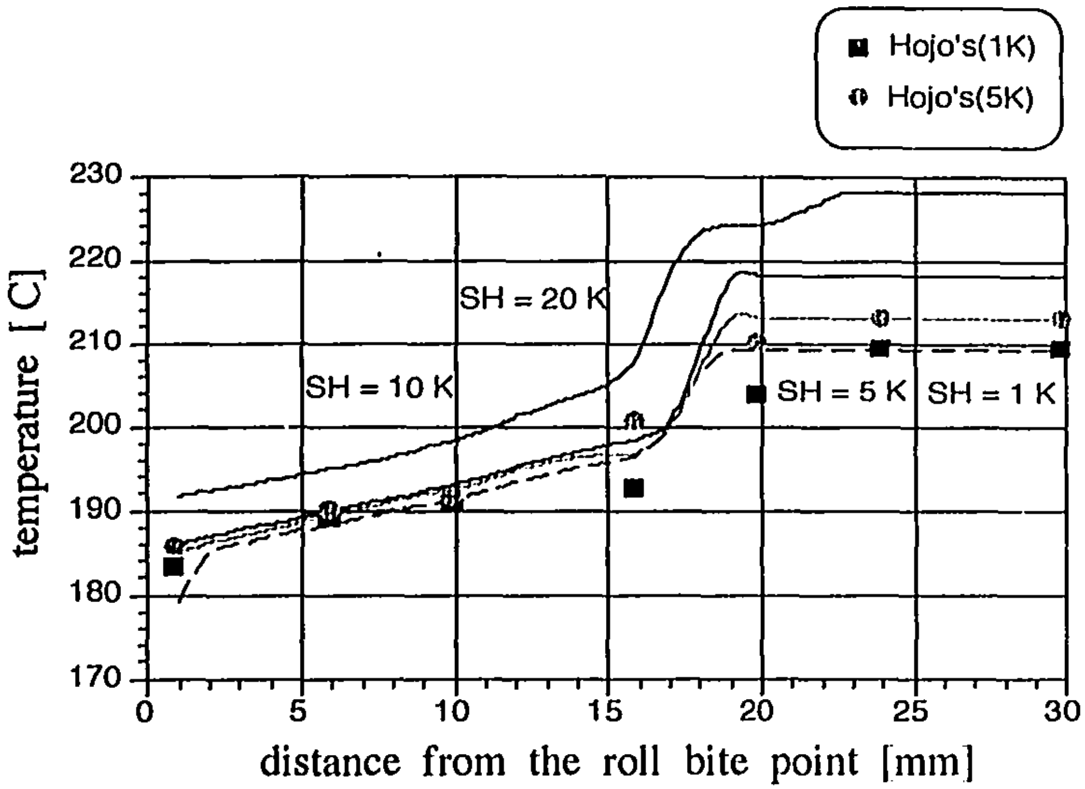

Figure 6.20 Temperature of the centre line of the mould
Effect of super-heat
($C'' = 0.5$, $h_l = 4500/t^{0.547} W/m^2K$, $Pr_t = 3.0$)

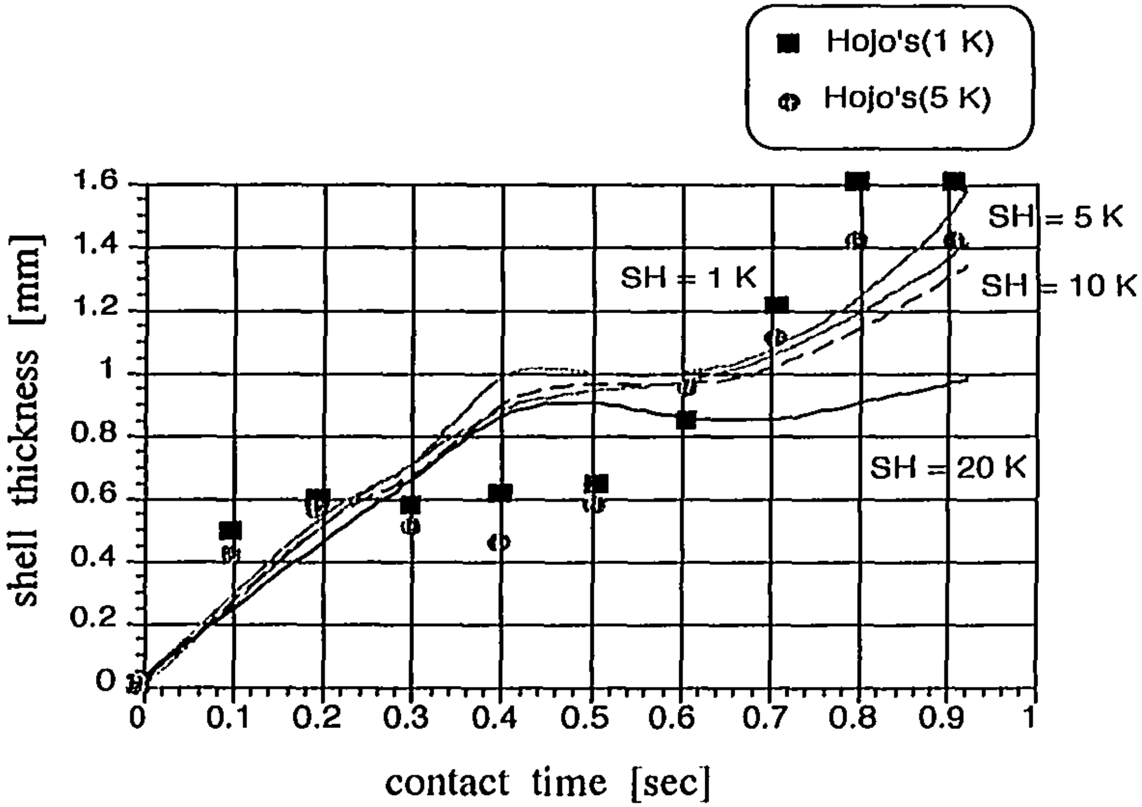

Figure 6.21 Relation between contact time and shell thickness
Effect of super-heat
(C" = 0.5, $h_l = 4500/t^{0.547}$ W/m²K, $Pr_t = 3.0$)

diffusion is observed in the end of the inlet flow.

Figure 6.21 provides a comparison of shell profiles.
All cases illustrate the same shell profiles before 0.4sec. The effects of the superheat appear near the exit. Hojo's data show qualitatively similar behaviour.

6.6 Summary

A mathematical model for solidification coupled with turbulence in a vertical twin roll caster has been developed. The effects of several important parameters in the model were investigated in the Sn-15%Pb alloy system, and the results were compared with Hojo et al.'s experimental results (1987).

These are summarized below :

1. The resistance constant for the additional term in the momentum equation to allow for mushy zone solidification significantly affects thermal conditions within the mould. In the model, a value of C" = 0.5 was properly chosen.

2. The model takes into account the effects of inlet flows and is able to predict the pause in shell growth and remelting phenomena. The computational results are in qualitative agreement with Hojo et al.'s temperature measurements, although Clyne's analytical solution did not predict a similar shell profile.

3. Increasing the turbulent Prandtl number decreased the final shell thickness. The over-all temperature profile, however, was not affected so much for the range of parameters studied. The result at the condition $Pr_t = 3$, C" = 0.5, local heat transfer coefficient $h_i=4500/t^{0.547}$ gave the best agreement with Hojo et al.'s

results.

4. Increasing the super-heat, decreases the area of the mushy and solid regions. Although the same tendency appeared in the experimental result, the computational result at SH = 1 K was not in quantitative agreement with Hojo et al.'s results.

From the points mentioned above, the model is an apparently useful tool for studying heat, mass and flow phenomena in twin roll casting processes. Further investigations for the industrial process using this model are discussed in the next chapter.

Chapter 7

COMPUTATIONAL STUDIES of TRANSPORT PROCESSES in A TWIN ROLL STAINLESS-STEEL CASTER

7.1 Introduction

In this chapter, several fluid flow simulations involving coupled heat transfer and solidification in stainless-steel systems are performed for the twin roll caster. The properties of austenitic stainless-steel 304 and specifications of the twin drum caster in N.S.C. are basically used for these performance predictions. The power-law scheme (equation(4.97)) was employed to discretize the convective terms in all the transport equations.

Unlike the simulations for the Sn–Pb system shown in chapter 6, the Reynolds number of the system is quite high. First, therefore, the effects of the number of grids are investigated in order to select an adequate grid density.

Next, the effects of important operating parameters are discussed: roll gap (10 – 30 mm), casting speed (40 – 120 m/min), super-heat (10 – 50 K), design of submerged nozzle, height of the pool, and heat transfer coefficient. Parameters concerned with the nozzle can have a large influence on the transport phenomena in the mould. However, so far, a study of such factors has been superficial. The selected parameters ; depth, size, thickness and direction of the inlet flow, are quantitatively investigated.

Lastly, the effects of the engineering factors for the design of the twin roll casting system are summarized using the computational results. The author believes that the computational results can give very important information for the design of the inlet system in the twin roll caster.

7.2 Grid Selection and Effects

A plant scale twin roll caster is a much larger piece of equipment than the laboratory scale caster considered in Chapter 6. As such, the Reynolds number of the system is very large. In general, a high Reynolds number flow (strong turbulence) requires a large number of grids for computations.

Here the question of influence of the number of grids is discussed.

Three kinds of grid densities, 32 x 32, 42 x 42 and 52 x 52, were employed in the investigation. Specifications and properties used in the computations are summarized in Table 7.

Table 7 Specifications and properties (stainless steel 304)

roll diameter	1.2 m
pool depth	0.386 m
nozzle entrance	15 ~ 18 mm
nozzle depth	44 mm
nozzle thickness	50 ~ 70 mm
casting speed	60 m/min
strip thickness	30 mm
inlet temperature	1464 °C
water temperature	20 °C
properties (SUS304)	
viscosity	7×10^{-3} Pa·s
density	7000 kg/m^3
heat conductivity	31 W/m·K
specific heat	700 J/kg·K
latent heat	2.64×10^5 J/kg
solidus temperature	1399 °C
liquidus temperature	1454 °C
properties (submerged-nozzle)	
density	2200 kg/m^3
heat conductivity	17 W/m·K
specific heat	1054 J/kg·K

non-dimensional numbers	
Reynolds number (Re)	4.8×10^5
Prandtl number (Pr)	0.158
Rayleigh number (Ra)	3.3×10^7
Grashoff number (Gr=Ra/Pr)	2.1×10^8
representative length (D)	0.419 m

Since boundary conditions of the surface on the roll for the energy equation were unknown, a Dirichlet condition II (eq. 4.64) was adopted: temperature of the roll surface is assumed to vary linearly from the solidus temperature at the first point of contact to 1266°C at the roll bite point. A relaxation factor of 0.3 was used for all equations (Dirichlet condition cases). A value of 10^{-7} was used for the convergence criteria for the energy equation. This is very crucial when discussing shell thickness. A value of 10^{-5} was used for the other equations for a convergence criterion.

Figure 7.1 illustrates grid formations for calculations. These formations were generated by solving Laplace equations (eqs. (4·33) – (4·34)). A value of 10^{-6} was used for convergence criteria of the numerical grid generation. When the residue was larger than 10^{-5}, numerical results did not make sense physically.

Although it takes much longer time to generate the grid for a larger grid density, fortunately, in the geometry modelled, parallel horizontal coordinate lines (x-coordinate) are available, and the author found the same grid formation and computational results could be obtained by dividing each x-coordinate line uniformly, without solving the Laplace equations. This approach to generate a grid system saved computational time and avoided numerical solution errors during grid generation.

Shaded portions in the Figures 7.1(a-c) represent submerged-nozzles. Their sizes are slightly different to each other owing to the grids. The resistant constant for solidification, C", was set equal to 1 for all calculations. Since the pilot plant twin roll equipment is much larger than the laboratory scale one, the curve shape of the meniscus surface at the top right corner, probably whose hight is about 10 mm, is not considered in the geometry.

Figure 7.2 shows computational results of velocity profiles. The results suggest a very similar flow pattern to that of the water model (Fig. 5.23), because the solidified shell and the high resistance mushy region are too small to influence the flow field significantly. It is also because the forced convection dominates over the natural convection in the system. In such a case we can say the water model is useful for studying the fluid motion in the mould.

All vector plots show almost the same flow pattern, and a comparison of the three figures (Fig. 7.2(a-c)) shows no clear differences.

Figure 7.3 gives profiles of the turbulent kinetic energy, 'k'. The inlet flow causes strong turbulence, and the highest point of the turbulent kinetic energy appears at the exit of the submerged-nozzle. The high energy zone expands vertically, the centre of the recirculation by the inlet flow being a region of high turbulent kinetic energy. Since the value of k is zero in the solid region, a large k-gradient exists near the roll, particularly in the lower region where the inlet flow impinges on the solidified shell. By contrast, the fluid flow in the upper region of the pool is very mild.

Comparison of the turbulent kinetic energy does not show a big difference among three kinds of grid density, although Figure 7.3(a) is slightly different from the others.

Figure 7.4 illustrates isotherms. Large mushy regions are observed in all cases owing to the relatively low super-heat condition. Large temperature gradients are observed near the roll surface and within the body of the submerged nozzle (made of refractory Al_2O_3-C).

A comparison among them tells that the higher grid density gives the lower temperature field in spite of the same boundary conditions. While the temperature of the meniscus of the result in the 32 x 32 grid density is higher than 1445°C, that in the 52 x 52 one is lower than 1440°C. Regarding the highest temperature region of the inlet, it seems reasonable to suppose that the smaller exit of the nozzle in a 42 x 42 grid density induces the smaller zone in Figure 7.4(b). Effects of the nozzle size will be discussed later.

Although the accuracy of the computational results cannot be discussed here for lack of precise measurements, generally speaking, the higher grid density gives the more accurate solutions in a finite difference method. However, the computational time increases almost geometrically with the number of grids. Table 8 indicates two representative temperature values and approximate computational time in each case.

Table 8 Comparison of temperature and CPU at various grid densities

grid density	T at meniscus (0.1m from centre)	T at centre roll bite point	CPU (386–33MHz + Math co-processor)
32 x 32	1445.3°C	1451.3 °C	1.1 days
42 x 42	1440.5°C	1449.9 °C	2.7 days
52 x 52	1437.9°C	1448.2 °C	8.8 days

Judging from computational time and accuracy, a 42 x 42 grid density was employed for the investigations described below.

7.3 Effects of Gap Between Rolls

The distance between the roll surfaces (roll gap) at the roll bite point limits the maximum strip thickness and may affect transport phenomena in the mould. Here the effects of roll gap are described.

Figure 7.5 shows predicted velocity profiles for three roll gaps; 30mm, 20mm, 10mm. Casting speed is 60 m/min, and the Dirichlet boundary condition II on the cold boundary is adopted for the energy equation (1399 → 1266°C). A decrease in the roll gap decreases the velocity of the inlet flow, due to a decrease of the inlet mass flow rate. A very mild flow was observed in the pool for the smallest gap (Figure 7.5(c)).

Decreases in the roll gap deforms the physical domain, and gives rise to instabilities during computations owing to large disproportion in grid size. It causes and requires a large number of iterations for converged solutions. Table 9 displays the number of total iterations and computational time.

Table 9 Number of iterations and CPU for convergence

roll gap	number of iterations	CPU (IBM386 33MHz)
30 mm	30000	2.7 days
20 mm	120000	11 days
10 mm	250000	23 days*

* : the results were obtained using a super-computer(FACOM VP2200), and CPU was estimated from the number of iterations, 11 and 23 days per one calculation are not practical time

Figure 7.6 illustrates isotherms for the same conditions as Figure 7.5. Decrease of the roll gap decreases temperature of the pool, because both inlet mass flow rate and inlet energy also decrease. In the case of a small roll gap, the lower region of the mould is relatively cold, for the hot inflow does not reach there.

One of the key pieces of information for engineers to design a twin roll casting system is the temperature profile (or the solid/liquid fraction) of the strip at the roll bite point. Figure 7.7 indicates the temperature of the roll at the bite point. All three cases have similar temperature profiles: temperature gradients within 1mm from the outside strip surface are very large, while gradient values are roughly equal.

Judging from the similarity of the temperature profile at the roll bite point and practical computational time, a value of 30 mm was employed for the roll gap for the remaining parametric studies.

7.4 Effects of Superheat

In the plant scale twin roll caster, controlling the liquid steel's superheat is not easy, because the inlet temperature depends upon upstream processes as well as the controls of the inlet system. Here the effects of superheat(SH) ranging between 10 K and 50 K are discussed, since this represents the range of possibilities in the pilot plant.

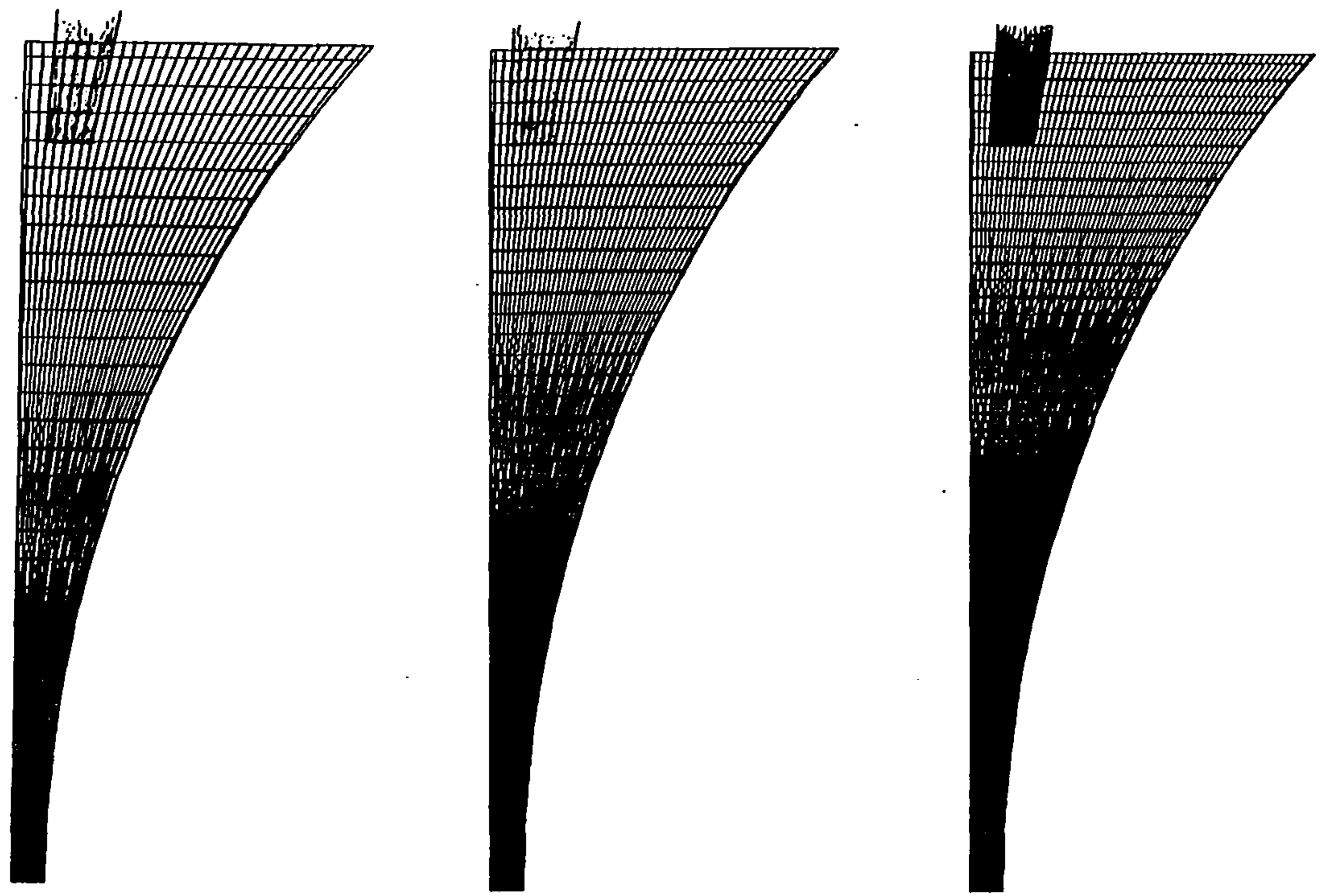

(a) 32 x 32

(b) 42 x 42

(c) 52 x 52

Figure 7.1 Grid Structure

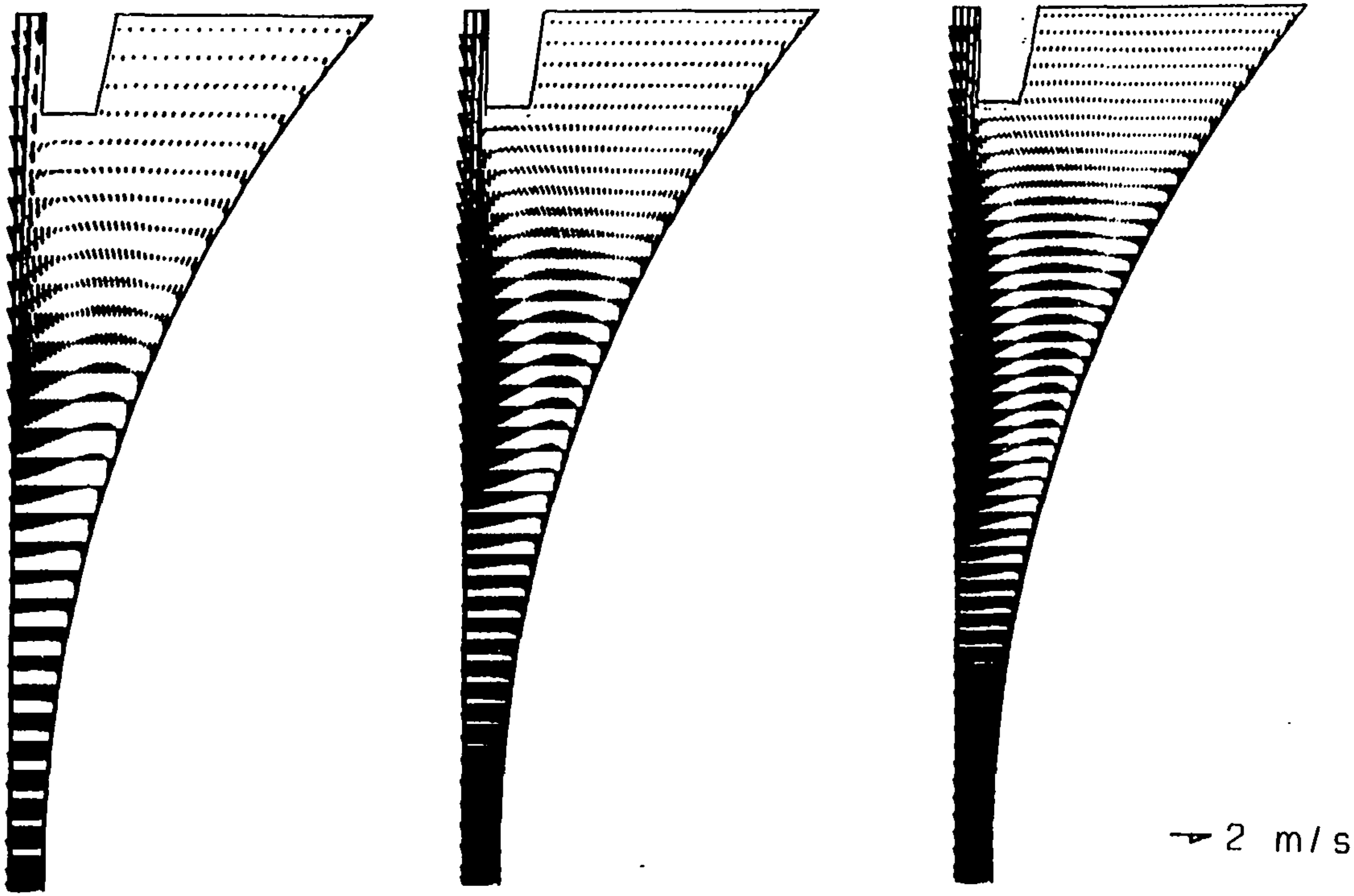

(a) 32 x 32 (b) 42 x 42 (c) 52 x 52

Figure 7.2 Comparison of velocity profiles
Effect of grid density (Re = 4.8×10^5, Pr = 0.158, Ra = 3.3×10^7)

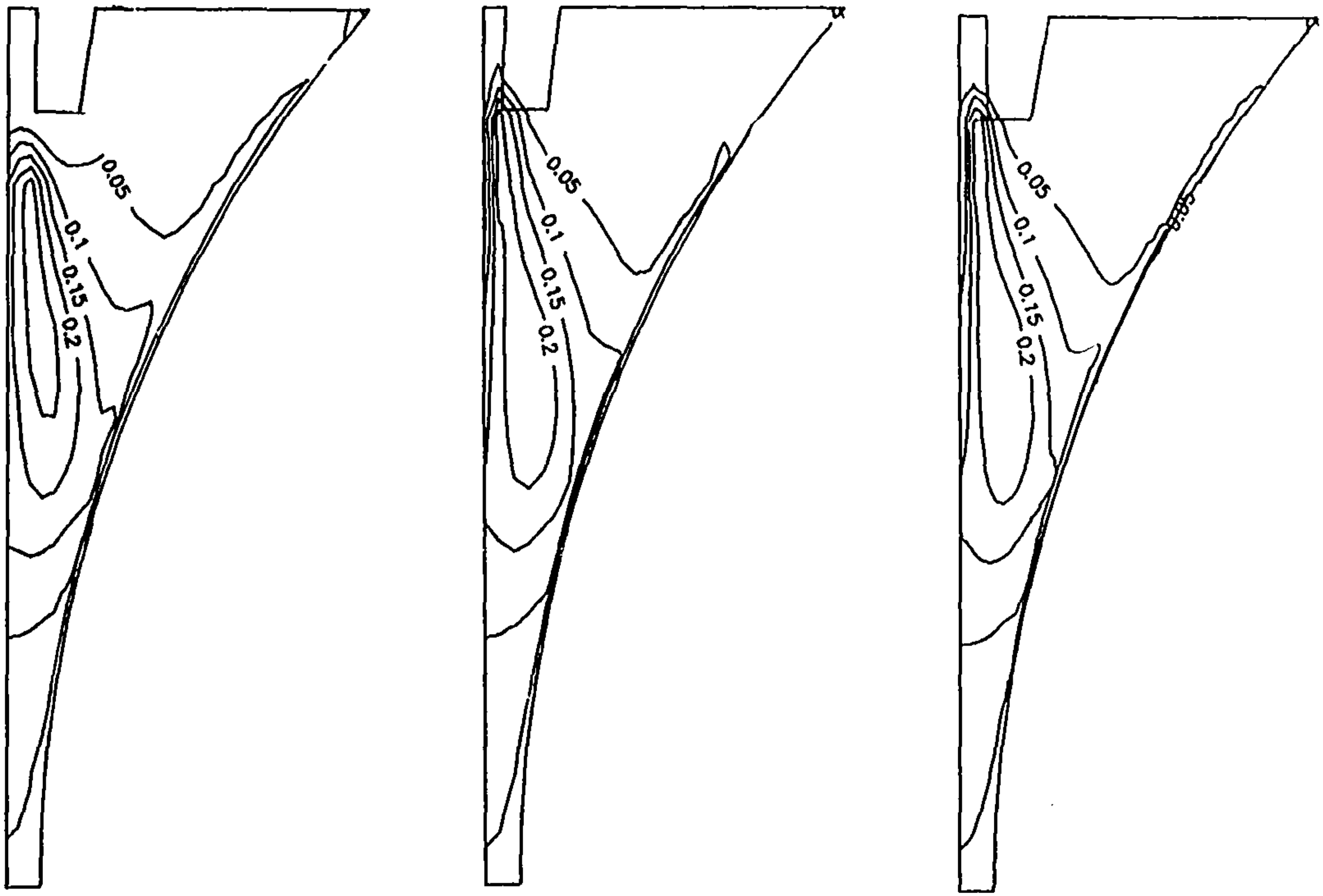

(a) 32 x 32 (b) 42 x 42 (c) 52 x 52

Figure 7.3 Comparison of turbulent energy profiles
Effect of grid density (Re = 4.8 x 10^5, Pr = 0.158, Ra = 3.3 x 10^7)

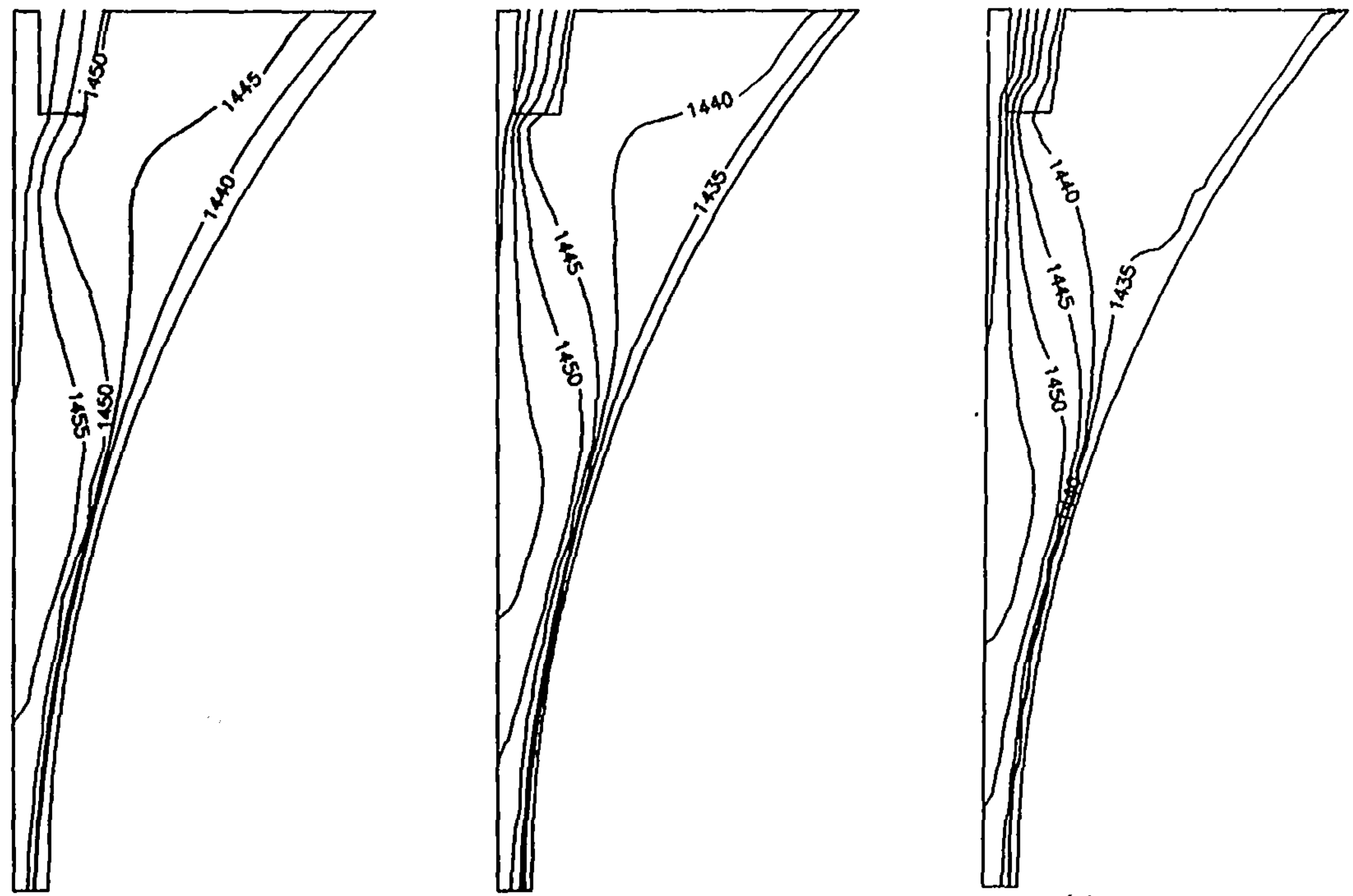

(a) 32 x 32

(b) 42 x 42

(c) 52 x 52

Figure 7.4 Comparison of temperature profiles
Effect of grid density ($Re = 4.8 \times 10^5$, $Pr = 0.158$, $Ra = 3.3 \times 10^7$)

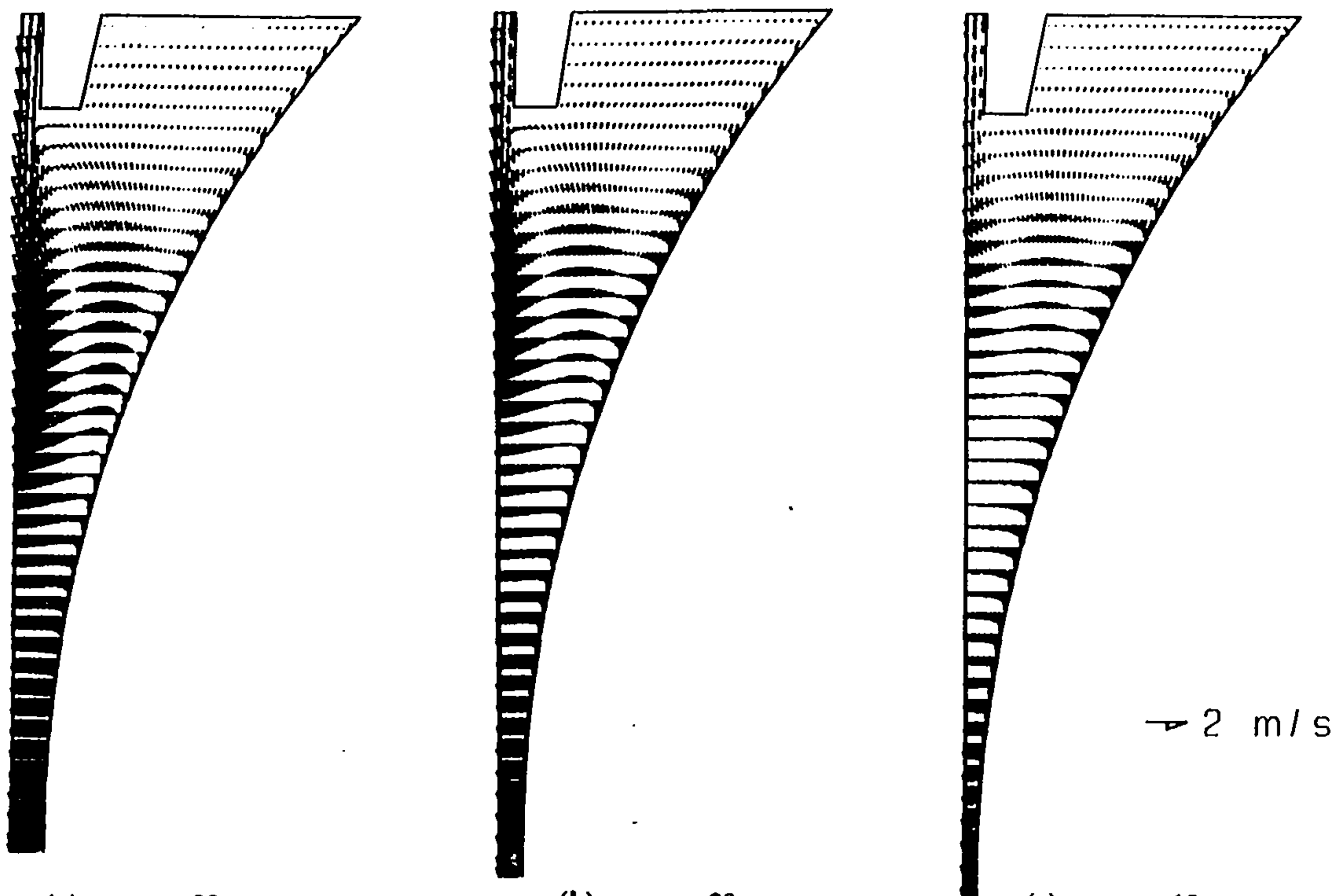

(a) gap = 30 mm (b) gap = 20 mm (c) gap = 10 mm

Figure 7.5 Comparison of velocity profiles
Effect of roll gap (casting speed = 60 m/min, super-heat = 20K)

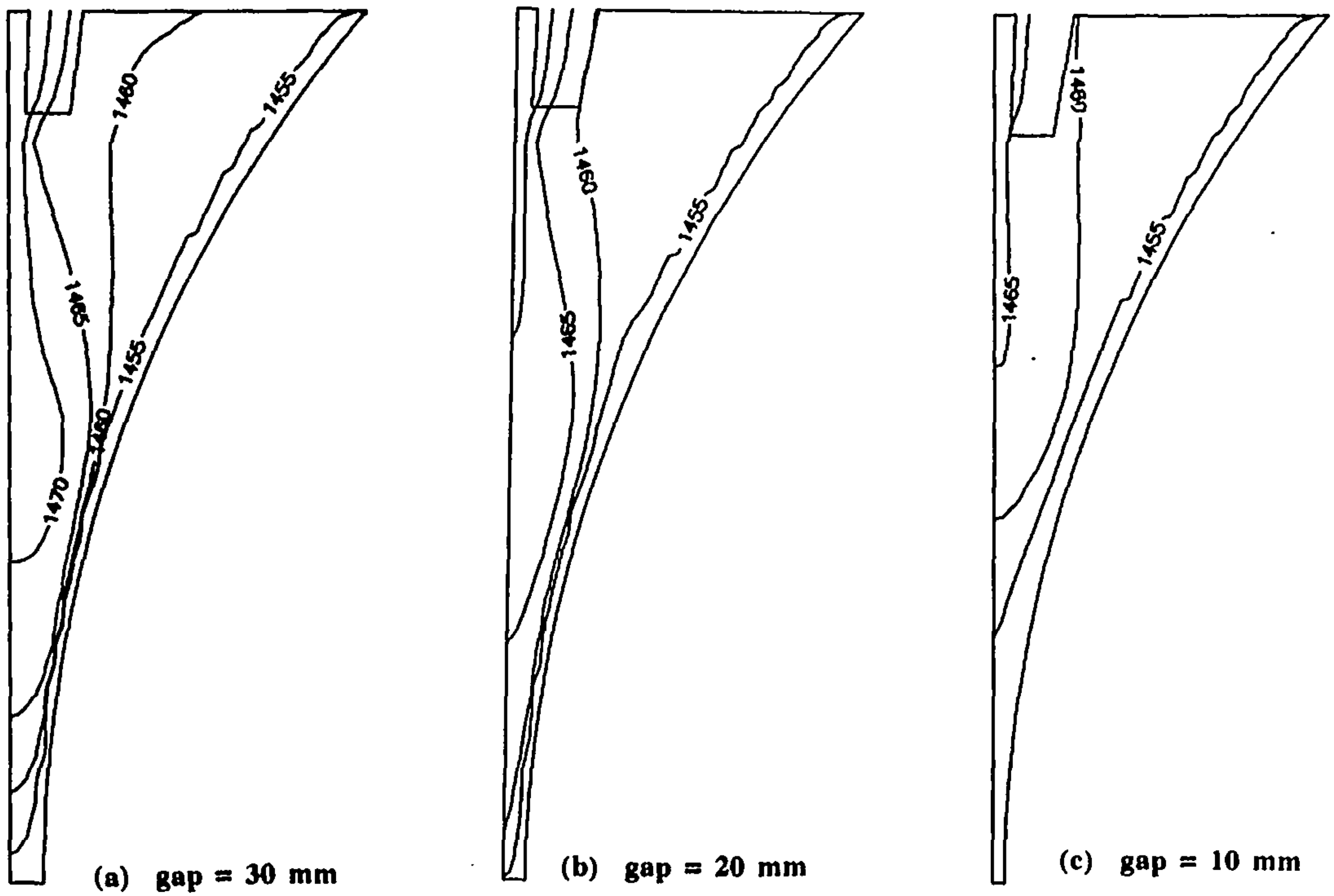

(a) gap = 30 mm (b) gap = 20 mm (c) gap = 10 mm

Figure 7.6 Comparison of temperature profiles
Effect of roll gap (casting speed = 60 m/min, super-heat = 20K)

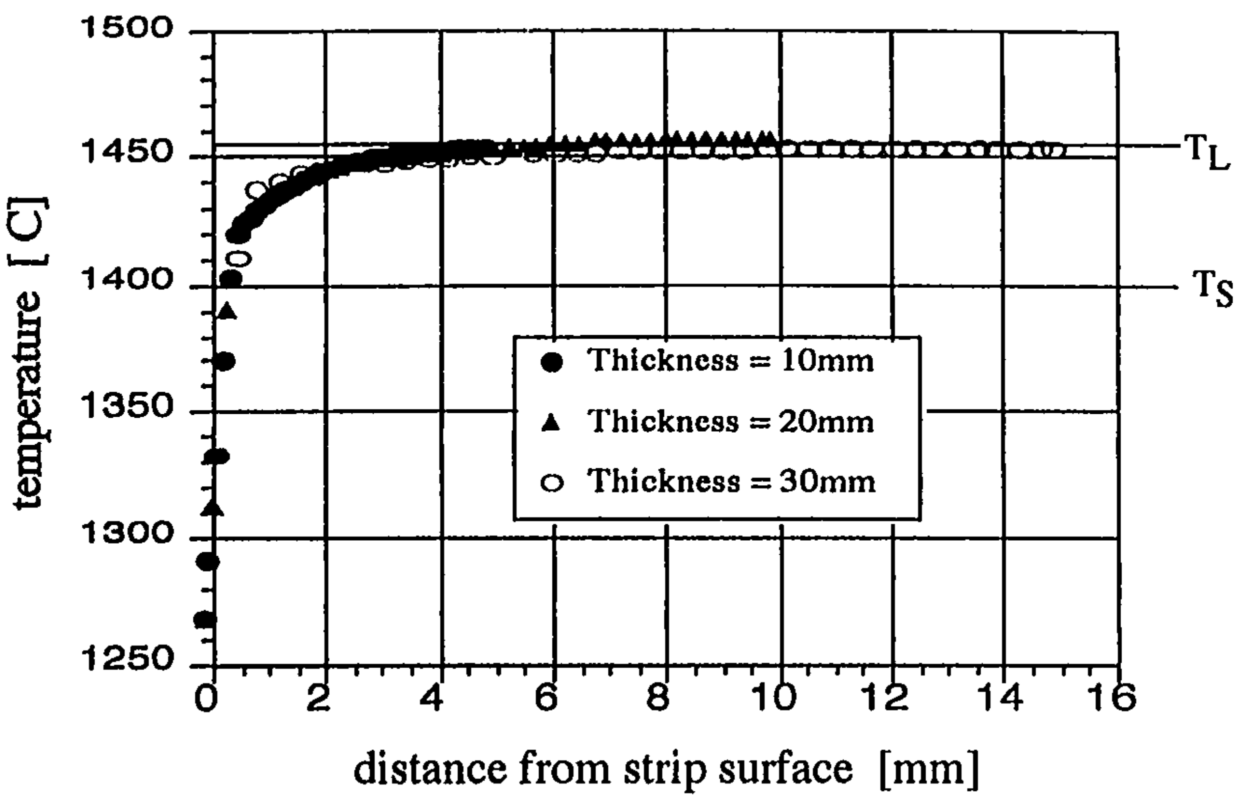

Figure 7.7 Temperature profile of the roll bite section at various roll gaps

Figure 7.8 illustrates temperature profiles for SH = 20 ~ 50 K. The same boundary conditions as Figure 7.6(b) are used on the roll. The bulk temperature in the pool depends upon the super-heat , particularly, increase of the inlet temperature increases temperature of the meniscus. The figure demonstrates that a very thin mushy region appears near the roll surface when the superheat is larger than 20 K, compared to that for SH = 10 K (Figure 7.6(b)). Increases in superheat decreases the thickness of the mushy region.

All isotherms have similar characteristic that the temperature gradient in the vicinity of the roll surface is very large and small near the meniscus.

The constant temperature of the strip surface at different superheat is open to the question, although the Dirichlet boundary condition leads to a better convergence of solution than the Neumann boundary conditions in this system.

Figure 7.9 shows predicted isotherms for different superheat using Neumann boundary conditions: a heat transfer coefficient h_i = 8000 W/m^{2}K, which Suichi et al(1991) reported using one-dimensional heat conduction model, was employed for the present calculations. Since the solidified shell is too thin to divide into some nodes in the upper mould, the thickness of the heat resistance in the vicinity of the roll surface was assumed to be constant. A relaxation factor 0.1 was used for the energy equation. The comparison in Figure 7.9 indicates that an increase in superheat proportionally increases the temperature within the mould. The bulk temperature in the pool for the Neumann boundary condition was essentially lower than that of the Dirichlet boundary condition. The over-all heat flux through the shell surface on the roll is calculated, to be approximately 10^7 W/m^2, which is in agreement with the value estimated on the basis of secondary dendrite arm spacing in the solidified strip (Miyazaki et al, 1990).

Figure 7.10 shows the temperature of the roll bite point (exit of the mould) for a Dirichlet boundary condition within 3 mm from the outside shell surface. There is a rapid temperature drop within 1 mm from the roll surface. The temperature gradient for conditions of higher superheat is larger than of lower super-heats due to the constant temperature (1266°C) of the strip surface.

Figure 7.11 shows the temperature of the roll bite point for the Neumann boundary condition. Although similar curves are observed, temperature of the strip surface increases following increase of the superheat; 1169.4°C (SH=10K), 1219.3°C (20K), 1314.7°C (30K), 1323.9°C (40K) and 1333.0°C (50K). Little solidified shell is observed for the case of high superheat.

7.5 Effects of Casting Speed

Figure 7.12 shows predicted velocity profiles for various casting speeds using the Neumann condition on the roll boundary (h_i = 8000 W/m^{2}K, SH = 10 K). Obviously all figures have the same flow pattern, and the absolute values change in proportion. This can be attributed to the fact that convective flows (inertial forces) dominate diffusive flows (viscous force), and also the solidified shell is thin enough to be neglected compared with the bulk region.

Figure 7.13 gives a comparison of isotherms at the various casting speeds. Unlike the velocity profile, the temperature profile is very greatly influenced by the casting speed condition. Increase of the casting speed increases the temperature in the pool and decreases the area of the solid and mushy regions. It is entirely reasonable to say that the decrease in contact time between the steel and the roll causes such phenomena.

Since the depth of the pool is constant, casting speed is identical to solidification time, which is the most important factor in the process. To reveal the effect, the relation between casting speed and solidified thickness is indicated in Figure 7.14. Solid circles designate experimental data (Yoshimura et al., 1991) and circles and solid lines designate the computational results. Computational results at three levels of liquid fraction (f_L=0.5, 0.6, 0.7) are plotted in the figure. The computational results demonstrate that an increase of casting speed linearly decreases thickness of the solidified shell. The experimental data indicates that increase in casting speed slowly decreases the thickness of the strip. Judging from only the results, we may say the liquid fraction at the centre of strips were around 0.6 until casting speed is less than 80 m/min, and it has larger value at higher casting speed. It is seen from Figure 7.14 that at low casting speeds under 80 m/min, a solidified shell forms on the roll surface, but for higher casting speeds, a solidified shell is very thin. This is due to the increase in turbulent heat flux at the shell surface at higher casting speeds. The constant convective cooling rate of h_i = 8000 W/m^{2}K appears to be too small to form a strip for the higher rates of casting. Concerning the thermal conditions for calculations might not be accurate, it cannot be discussed at the present for the lack of information. Further investigation for the point is being continued.

7.6 Effects of Nozzle Design

One of the most important and difficult points in the development of the twin roll casting system is designing the inlet system (a nozzle for pouring). Until today, neither any mathematical model to take into account this point has been developed, nor has any physical model provided sufficient information.

In this section, the effects of several parameters concerned the design of the nozzle are investigated in the stainless steel system, using the author's model. In the implementations, the same boundary conditions were used: casting speed = 60 m/min, super-heat = 20 K, heat transfer coefficient between the roll and the shell surface = 8000 W/m^{2}K.

7.6.1 Inside gap of the submerged nozzle

Figure 7.15 shows velocity profiles for various inflow entry ports ; total (full mould) inside gap of the nozzle is (a) 9 mm, (b) 15 mm, (c) 27 mm, (d) 40 mm. To avoid the influence of the size of the meniscus of the pool, the outside thickness of submerged nozzle is kept constant.

Figure 7.15(a) demonstrates that the strong inflow causes a strong counter flow and a strong recirculation. Any increase in entrance size decreases velocity of the inflow and the counter flow. In the case of 40 mm wide entrance, velocity of the inflow is smaller than casting speed, and the flow field is very mild in the mould.

Figure 7.16 illustrates isotherms for the same conditions as Figure 7.15. Figure 7.16(a) shows the lowest temperature field, and the mushy region occupies most of upper region in the pool in Figure 7.16(a) & (b). Increase of the entrance size increases bulk temperature and area of the liquid region. For the case of a wide entrance, the high temperature region is observed along the centre line of the mould.

On the other hand, the temperature of the outside surface of the solidified shell decreases as following increase of entrance size: temperature at the roll bite point is (a) 1219°C, (b) 1216°C, (c) 1169°C, (d) 1161°C.

From the results , the smallest entrance system has the largest negative heat flux through the roll. It seems reasonable to suppose that heat of the high speed and thin inflow easily diffuses into the mould owing to large turbulent heat transfer.

7.6.2 Depth of nozzle

The depth of the submerged nozzle affects the meniscus condition, which strongly improved the quality of the strip surface.

Figure 7.17 shows predicted velocity profiles for various nozzle depths. Strong flow in the pool is observed in the case of the most shallow submerged nozzle (Figure 7.17(a)). With increase in nozzle depth, flow in the pool becomes slower. Figure 7.17(d) demonstrates that too deep a nozzle gives rise to another recirculation along the nozzle surface.

Figure 7.18 indicates the u-velocity profile of the meniscus surface in the mould. Negative values in the figure means a flow towards the nozzle. In the case of nozzle depth = 5mm, a flow towards the roll is very strong, and the maximum velocity is larger than 0.5m/s.

Increase of the nozzle depth decreases velocities. In the case of the depth = 101mm, negative velocity is observed near the nozzle, and the velocities do not decrease compared with that of depth = 43mm. In the case of the depth = 130 mm, most of the velocities are negative and the flow of the meniscus surface directs the nozzle due to the counter recirculation. The absolute values of the velocities are around 0.1m/s.

Figure 7.19 illustrates predicted temperature profiles. With increasing nozzle depth, the nozzle temperature rises, and temperatures near the roll in the upper region decreases. For deep nozzles (Fig. 7.19(c) & (d)), temperatures at the top right corner of the nozzle decrease slightly due to the cold corner flow near the top surface. Velocity inside the nozzle is so large that heat transfer from the molten steel to the nozzle is very large. Therefore the longer nozzle easily becomes hot, and isotherms are influenced from the temperature of the nozzle. The deep nozzle also causes a relatively large remelting of the solidified shell as well as higher strip temperatures.

7.6.3 Outside thickness of the submerged nozzle

Flow and energy fields of three kinds of large submerged nozzle are investigated.

Figure 7.20 shows a predicted fluid flow and a temperature profile using a thick submerged nozzle; outside thickness is 221mm at the top surface and 174mm at the nozzle front, inside thickness = 15mm. The velocity profile demonstrates the outside thickness of the nozzle is so large that the flow between the nozzle and the roll is suppressed. The macroscopic flow pattern under the nozzle is similar to that of the thinner nozzle (Figure7.17(b)), because the region occupied by the nozzle is stagnant zone at even the case of the thinner nozzle. The temperature profile is, however, very much affected by the nozzle. A large temperature gradient can be observed in the nozzle, and the temperature at the top right corner is lower than that of the thinner nozzle.

Figure 7.21 shows a fluid flow and a temperature profile when the thick nozzle is submerged deeper; nozzle depth = 101 mm. The velocity profile is similar to Figure 7.17(c). Heat of the inlet flow is absorbed by the nozzle, temperatures near the roll surface are low: they are around 1330°C at the strip surface on the roll. However, heat loss to the outside of the mould through the nozzle was not considered in the calculation, and the temperature of the submerged nozzle may become much lower in the real plant system. Since the nozzle depth is larger than that of Figure 7.20, the temperature of the roll bite point is higher than that.

Figure 7.22 shows a fluid flow and a temperature profile in the case of a deep nozzle whose outside and inside thickness are large. The inlet flow is assumed to be arranged to the same velocity, although it is difficult in the real system.

The inflow smoothly penetrates towards the roll bite point, no large recirculation is observed in the flow field. The isotherms demonstrate that the nozzle divides the pool into hot and cold zones. Since the region between the nozzle and the roll is separated from the main flow, its temperature is very low. The inlet flow does not lose much heat because the flow is less turbulent and heat diffusion is smaller.

7.6.4 Horizontally impinging

Figure 7.23 shows a velocity profile and isotherms using a horizontal impinging of the molten steel; the size of the entrance of the inflow is 9.6 mm per one side. To make computations simple, the inlet flow is assumed to enter from the left boundary into the bulk, although it may come from the top in a realistic condition.

The velocity profile demonstrates the inflow goes straight towards the roll, and divides the pool vertically. Velocities near the meniscus are large (maximum 0.66 m/s), owing to the horizontal inflow. One large mild recirculation is caused by the moving roll. Compared with the flow field of the vertical impinging nozzle, the flow in the vicinity of the roll surface develops better, in spite of the turbulence near the top surface.

The isotherms demonstrate the bulk temperature in the pool is very high, and that the temperature of the meniscus is almost the same as the inlet temperature. It is seen that the solidified shell is remelted in the middle. On the contrary, temperature in the lower mould is relatively low, and the thickness of the solidified shell grows thicker than that of the vertical impinging nozzle.

Figure 7.24 shows fluid flow and temperature profiles for the case of a thick horizontal impinging nozzle. The size of entrance was doubled to half the inlet velocity. The inflow strikes the roll surface directly. Most of the inflow goes down along the roll surface after the strike. The region under the nozzle is stagnant. The part of the inflow goes up, and would stir the top corner strongly: in the calculation, the meniscus line is fixed.

The isotherms demonstrate temperature of the whole region in the mould is almost the same as the inlet temperature. It is because the hot inflow covers the cooling roll surface, in addition, most of the top surface is covered by the nozzle insulated at the top boundary.
In this condition, the solidified shell does not appear until the lower mould. Nevertheless, the temperature of the strip surface at the roll bite point is relatively low (1194°C).

The effect of the inlet system to the strip temperature is summarized.

Figure 7.25 shows temperature profiles of the roll bite point within 3mm from the strip surface for five representative submerged nozzles. The deep nozzle (depth = 101mm) indicates the highest temperature at the strip surface, and the thinnest solid region. The thick nozzle (outside thickness = 221 → 174 mm) causes a slightly colder and thicker strip, in spite of the same nozzle depth as that of the deep nozzle). The large entrance nozzle (inside thickness = 80 mm), which has the same nozzle depth and outside thickness, induces the lowest temperature at the strip surface, and the highest temperature at the centre of the strip. It is due to less turbulent heat transfer between the shell and the molten steel. The largest thickness of the solidified shell is observed in this case.

The horizontal impinging nozzle leads to relatively thick solidified shell, and the temperature at the centre of the strip is not high unlike the large entrance nozzle.

7.6.5 Height of pool

Figure 7.26 shows predicted velocity profile and isotherms employing the pool height = 0.3 m (angular position of the meniscus = 30°). The nozzle position is almost the same as the lower domain of Figure 7.17(c), and a similar flow profile is observed; the flow at the meniscus is directed towards the nozzle.

Figure 7.26(b) shows a higher temperature in the centre of the mould than that of a higher pool (Fig. 7.19), because of higher input energy per volume and a smaller distance between the nozzle and the exit of the flow. A large temperature gradient is observed above the point where the recirculation of the inflow strikes the downwards flow on the roll.

No convergence solution could be obtained for the case of a pool height of 0.52 m (angular position of the meniscus = 50°). In the higher pool, the physical domain is almost triangular, and both size and shape of grids of the top corner are very different from those at the bottom (roll bite point). It seems to be necessary to change the grid structure and the grid density.

7.7 Effects of Cooling Rate

One further parameter, cooling rate, is important for the mould. Sensitivity tests for the heat transfer coefficient between the strip surface and the roll are now carried out.

Figure 7.27 illustrates isotherms at various heat transfer coefficients; h_i = 10000 ~ 18000 W/m^{2}K. The predictions of velocity profiles are cut, because they are almost the same as that of h_i = 8000W/m^{2}K (Fig. 7.17(b)) due to a very thin solidified shell even in the case of 18000 W/m^{2}K.

Comparison of the isotherms demonstrate the general feature that an increase in the cooling rate decreases the bulk temperature in the mould: the temperature of the meniscus for h_i = 12000 W/m^{2}K (Fig. 7.27(b)) is about 5 degrees lower than for h_i = 10000 W/m^{2}K (Fig. 7.27(a)), and is about 15 degree lower than that of h_i = 8000 W/m^{2}K (Fig. 7.19(b)). However, no significant difference is observed in the upper mould between Figure 7.27(c) and (d).

Regarding the temperature near the roll bite point, increases in the heat transfer coefficient apparently decreases it, in any comparisons.

Figure 7.28 indicates the temperature of the roll bite section within 3 mm from the strip surface. A clear distinction can be made below 0.5 mm from the strip surface, which is completed solid. Using interpolation, the thickness for h_i = 18000 W/m^{2}K at the liquid fraction = 0.6 (3.5mm) is more than twice as large as that for h_i = 8000 W/m^{2}K (1.5mm)

7.8 Engineering Characteristic of Twin Roll caster

As has been mentioned above, the predictions that this model produces can give a wealth of important information for both designing and operating the twin roll casting system.

Here, we concentrated on the most interesting outputs for engineers of the twin roll caster; temperature and thickness of strip, flow and temperature condition of the meniscus surface of the mould. The data are summarized with predicable cost to keep each condition in Table 10 & 11.

Table 10 Characteristics of the twin roll caster I

	temperature of strip surface		thickness of strip (F_S=0.4)		shell remelting in the middle	
	high	low	thick	thin	large	small
roll gap	large	small	small*	large	large	small
casting speed	fast	slow	slow	fast	fast	slow
super-heat	high	low	low	high	high	low
nozzle depth	case by case		shallow	deep	deep	shallow
inside thickness	small	large	small	large	large	small
outside thickness	small	large	large	small	large	small
direction of inflow	vertical	horizon	horizon	vertical	vertical-lower zone horizon-upper zone	
pool height	low	high	high	low	low	high
cooling rate	small	large	large	small	large	small

* : The point is that the smaller roll gap causes the colder strip, although the maximum strip thickness is determined by the roll gap.

Table 11 Characteristics of the twin roll caster II

	temperature of meniscus surface		velocity of meniscus surface		predictable cost for equipment	
	high	low	large	small	high	low
roll gap	large	small	large	small	small	large
casting speed	fast	slow	fast	slow	fast	slow
super-heat	high	low	case by case		high	low
nozzle depth	shallow	deep	shallow	deep	deep	shallow
inside thickness	case by case		small	large	case by case	
outside thickness	small	large	small	large	large	small
direction of inflow	horizon	vertical	horizon	vertical	case by case	
pool height	low	high	low	high	case by case	
cooling rate	small	large	small	large	large	small

Quantitative tendency of each factor is described before.

With all the information that has been obtained from the computational studies using the model within limited conditions, the author believes the information can be quite useful for developing and operating better twin roll casting processes.

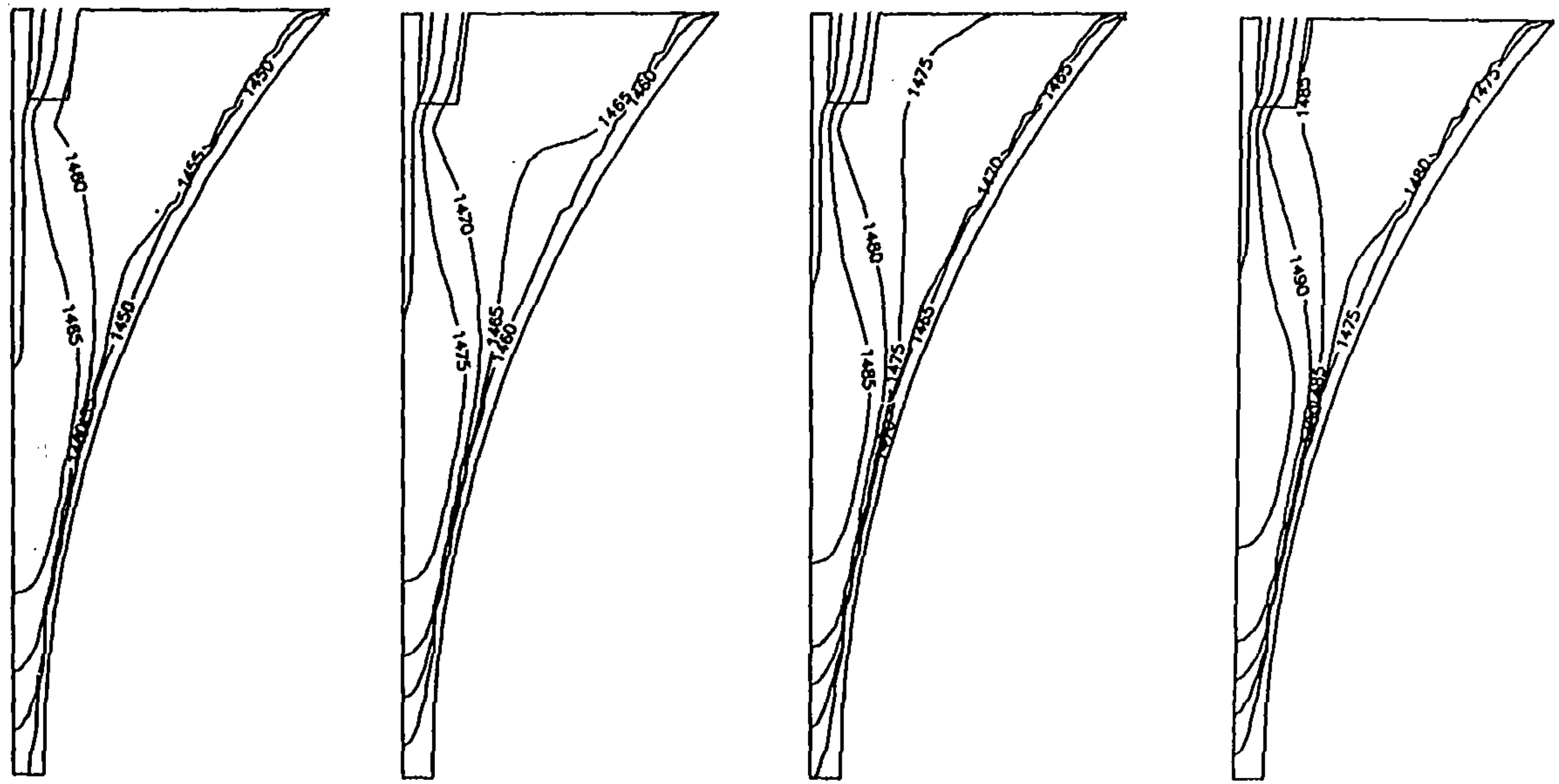

(a) SH = 20 K (b) SH = 30 K (c) SH = 40 K (d) SH = 50 K

Figure 7.8 Comparison of temperature profiles
Effect of super-heat(Dirichlet condition, casting speed = 60 m/min)

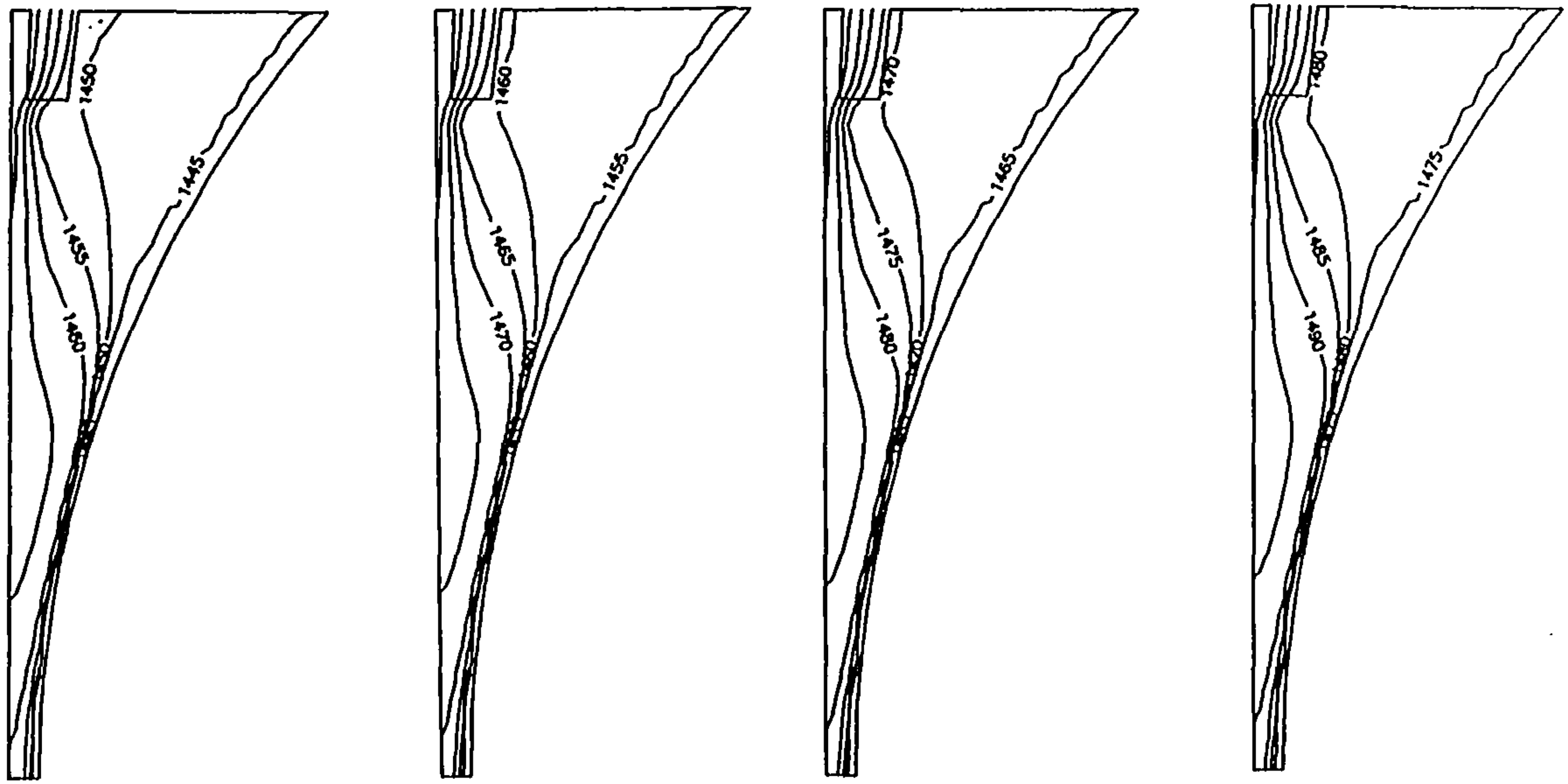

(a) SH = 20 K

(b) SH = 30 K

(c) SH = 40 K

(d) SH = 50 K

Figure 7.9 **Comparison of temperature profiles**
Effect of super-heat (Neumann condition, casting speed = 60 m/min)

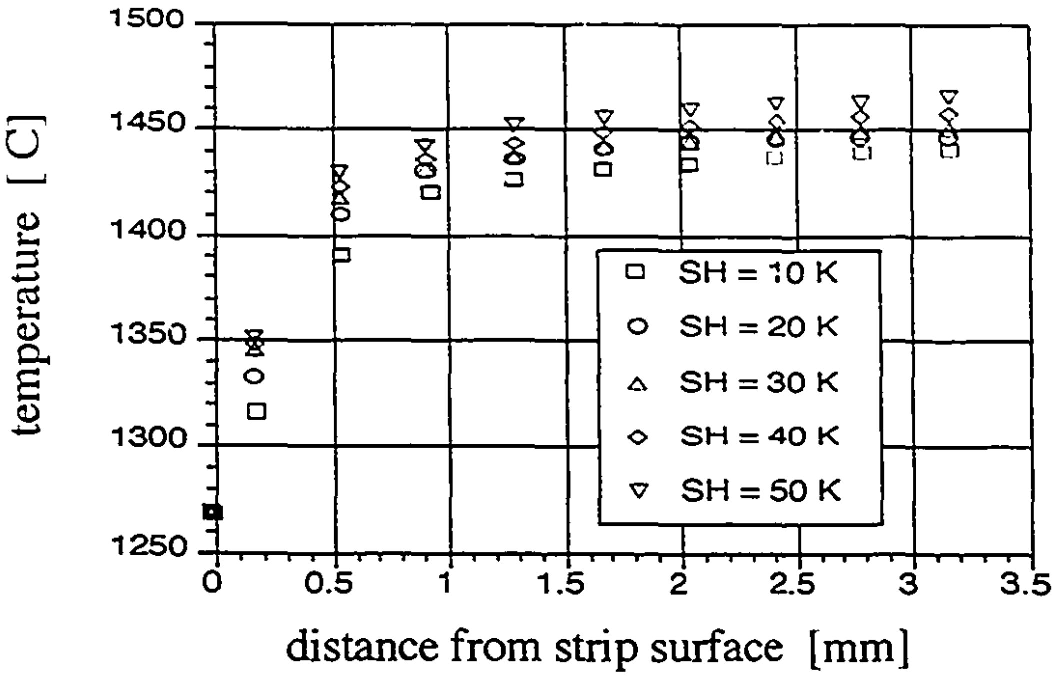

Figure 7.10 Temperature profile of the roll bite section Effect of super-heat (Dirichlet condition)

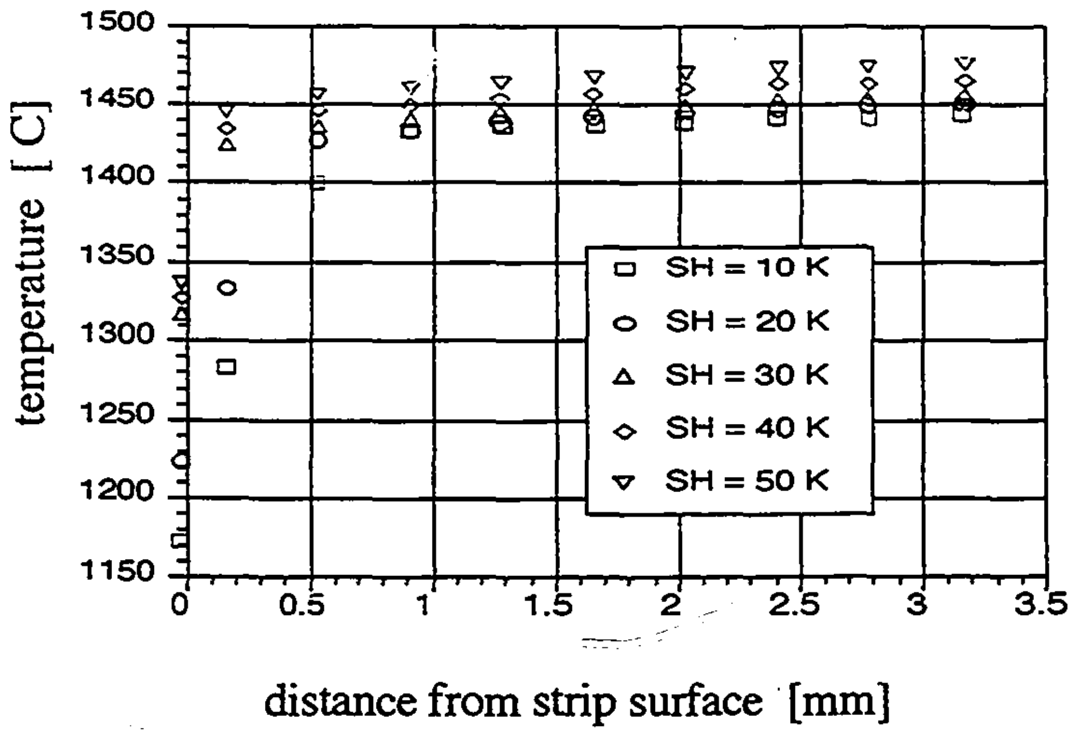

Figure 7.11 Temperature profile of the roll bite section Effect of super-heat (Neumann condition)

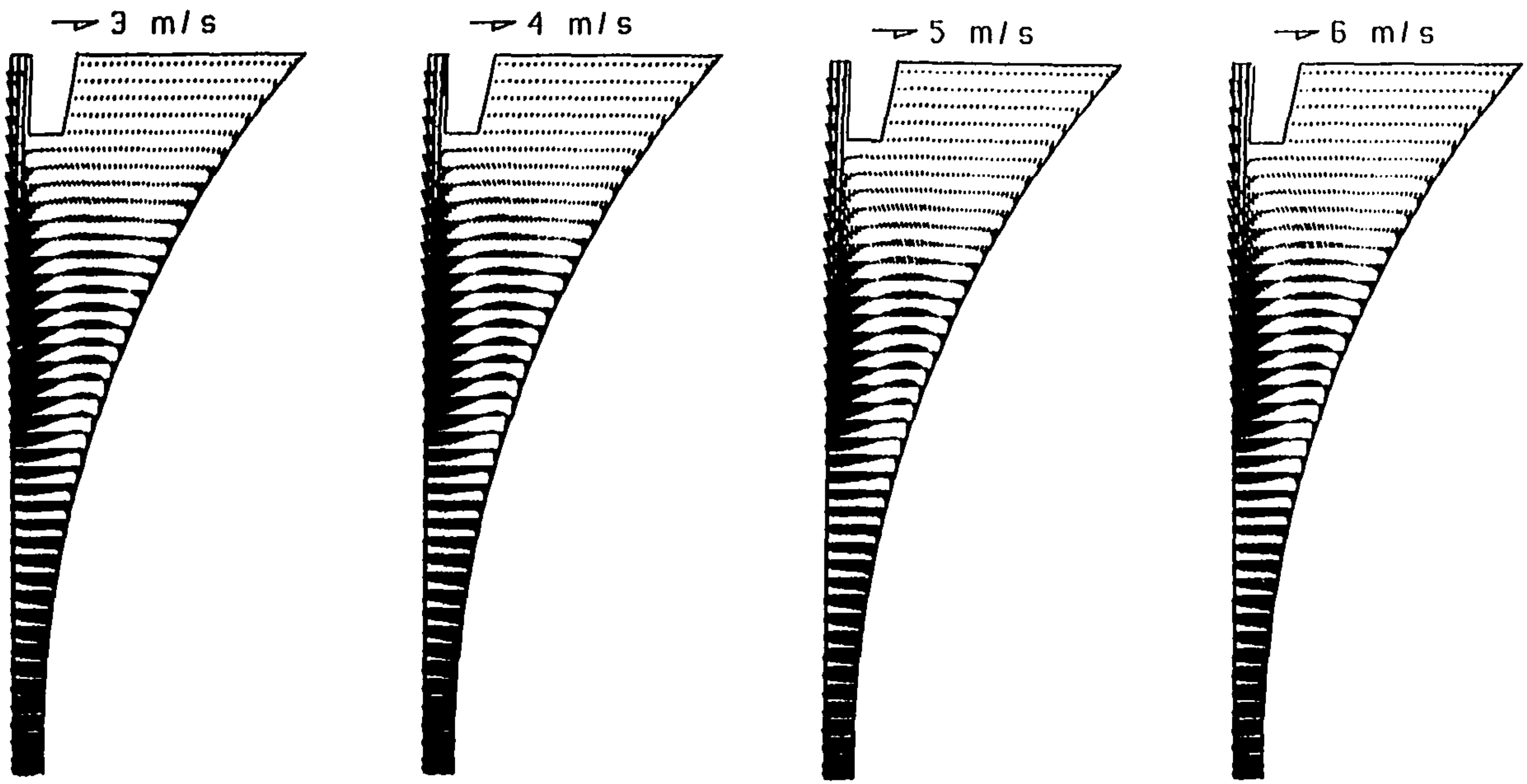

(a) 60 m/min (b) 80 m/min (c) 100 m/min (d) 120 m/min

Figure 7.12 Comparison of velocity profiles
Effect of casting speed(super-heat = 20 K, h_l = 8000 W/m^{2}K)

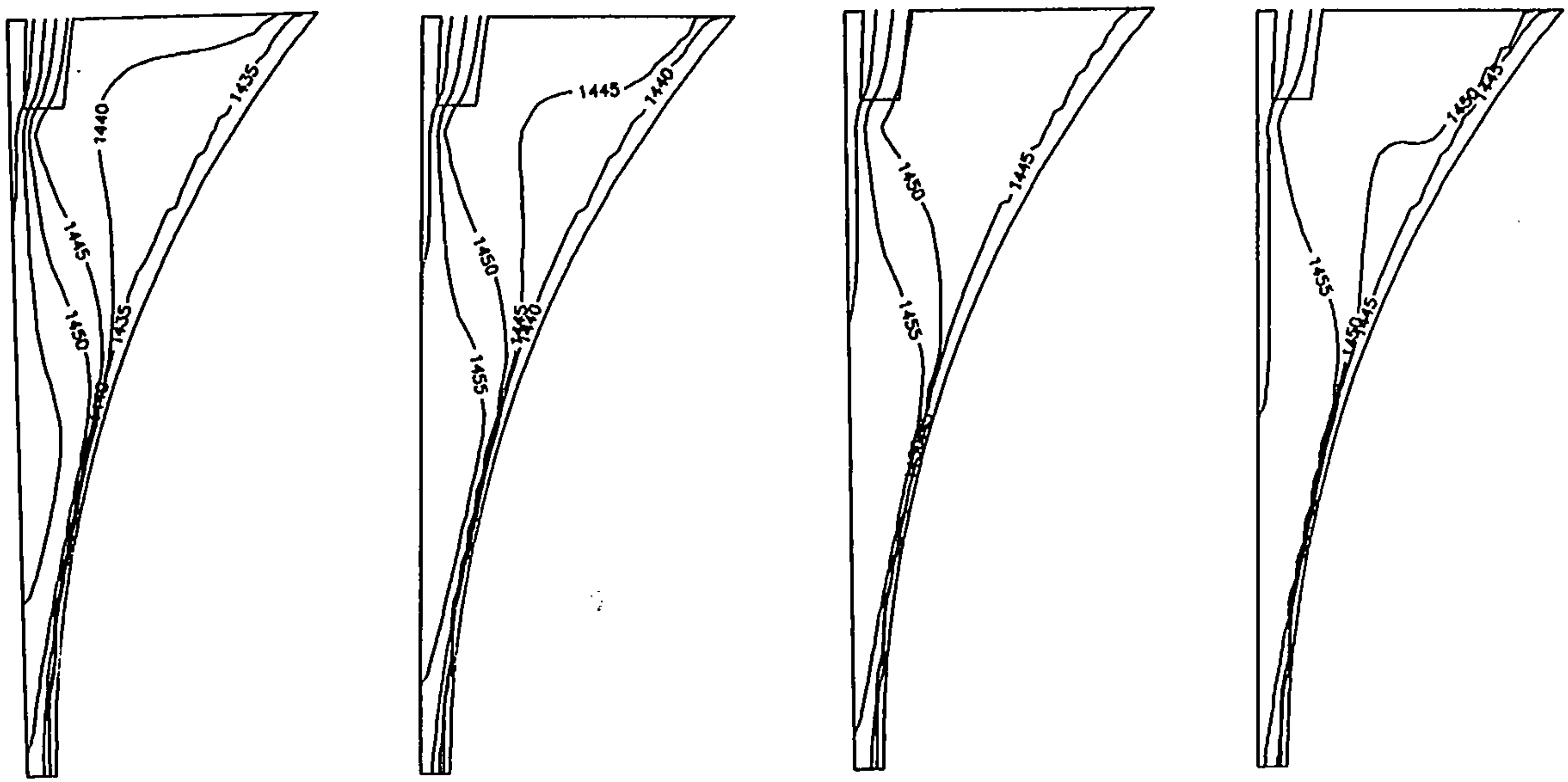

(a) 60 m/min (b) 80 m/min (c) 100 m/min (d) 120 m/min

Figure 7.13 Comparison of temperature profiles
Effect of casting speed(super-heat = 20 K, h_i = 8000 W/m^{2}K)

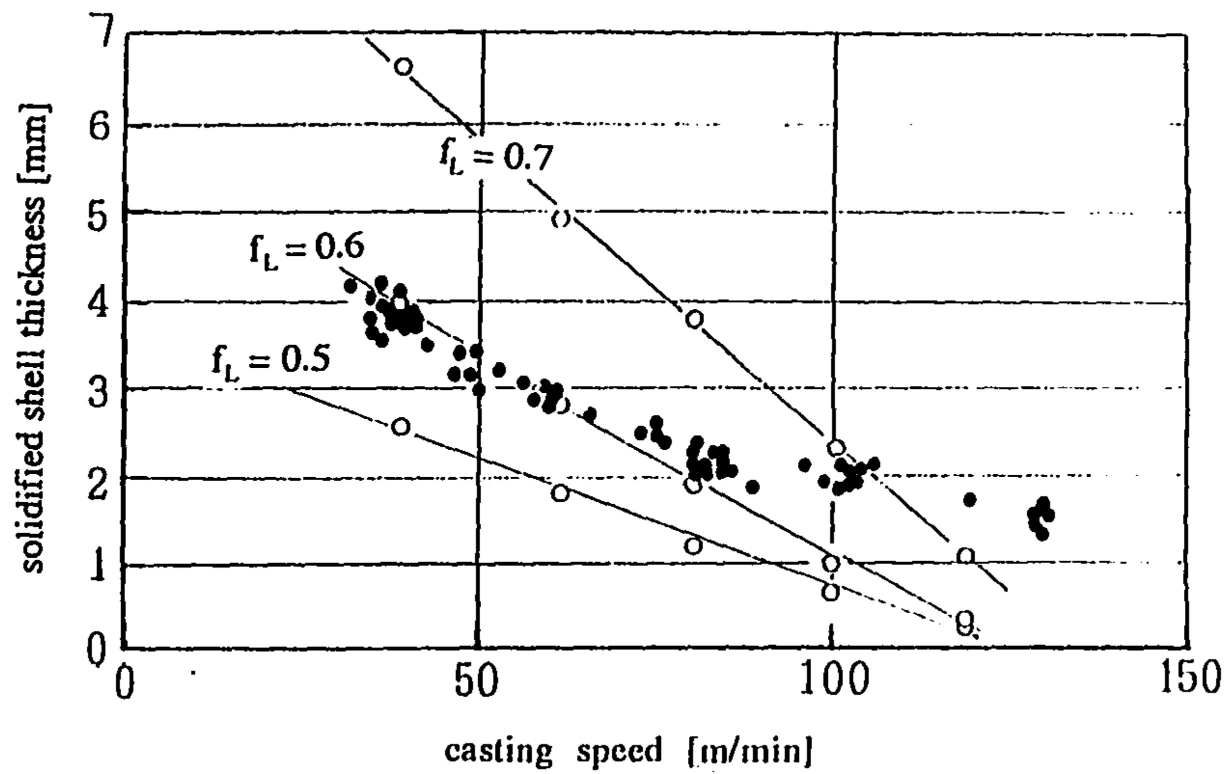

Figure 7.14 Relation between casting speed and shell thickness (super-heat = 20 K, h_i = 8000 W/m^{2}K)

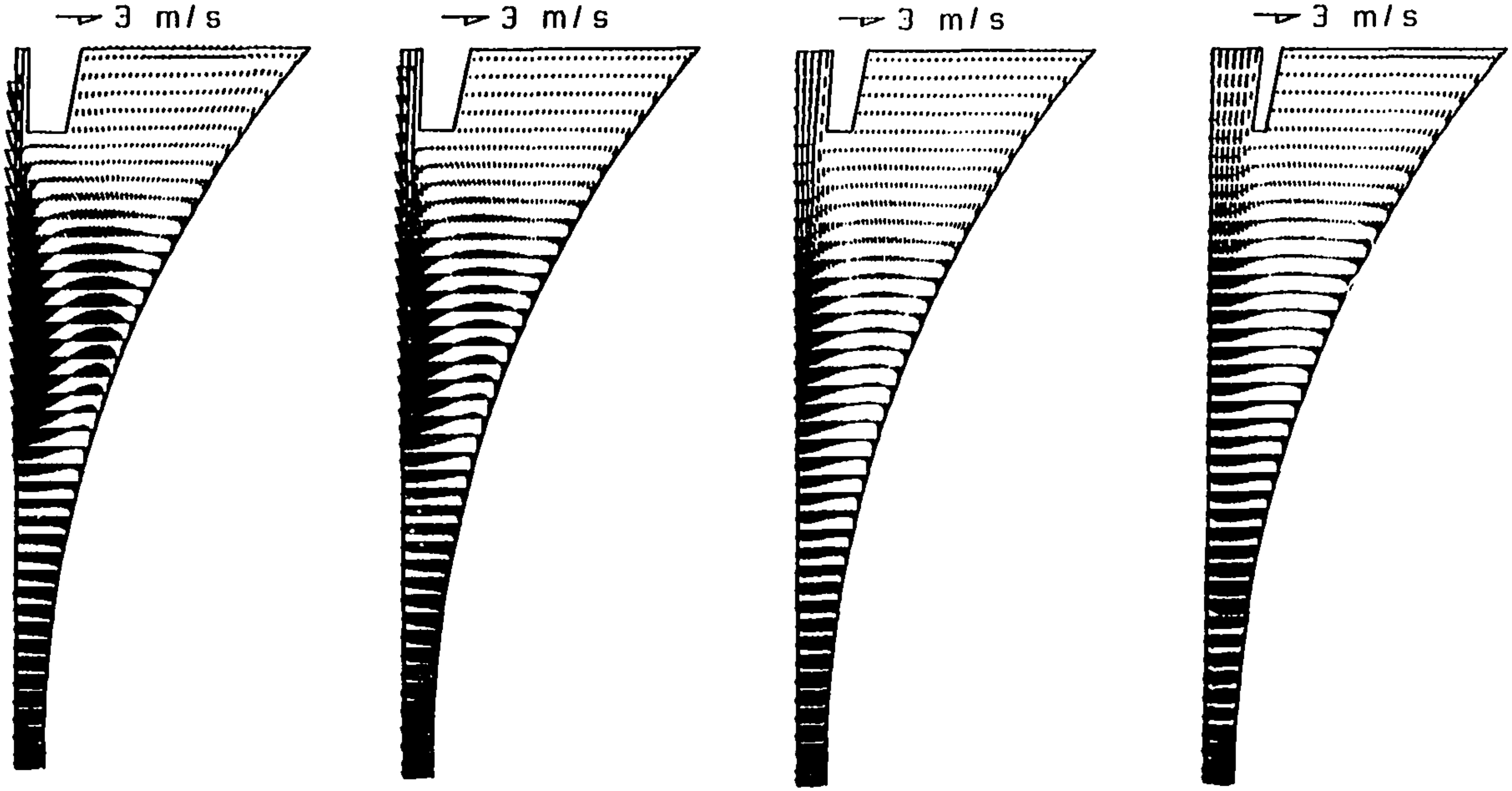

(a) inside thickness = 9 mm (b) 15 mm (c) 27 mm (d) 40 mm

Figure 7.15 Comparison of velocity profiles
Effect of inside gap of submerged nozzle
(casting speed = 60 m/min, super-heat = 20 K, h_l = 8000 W/m^2K)

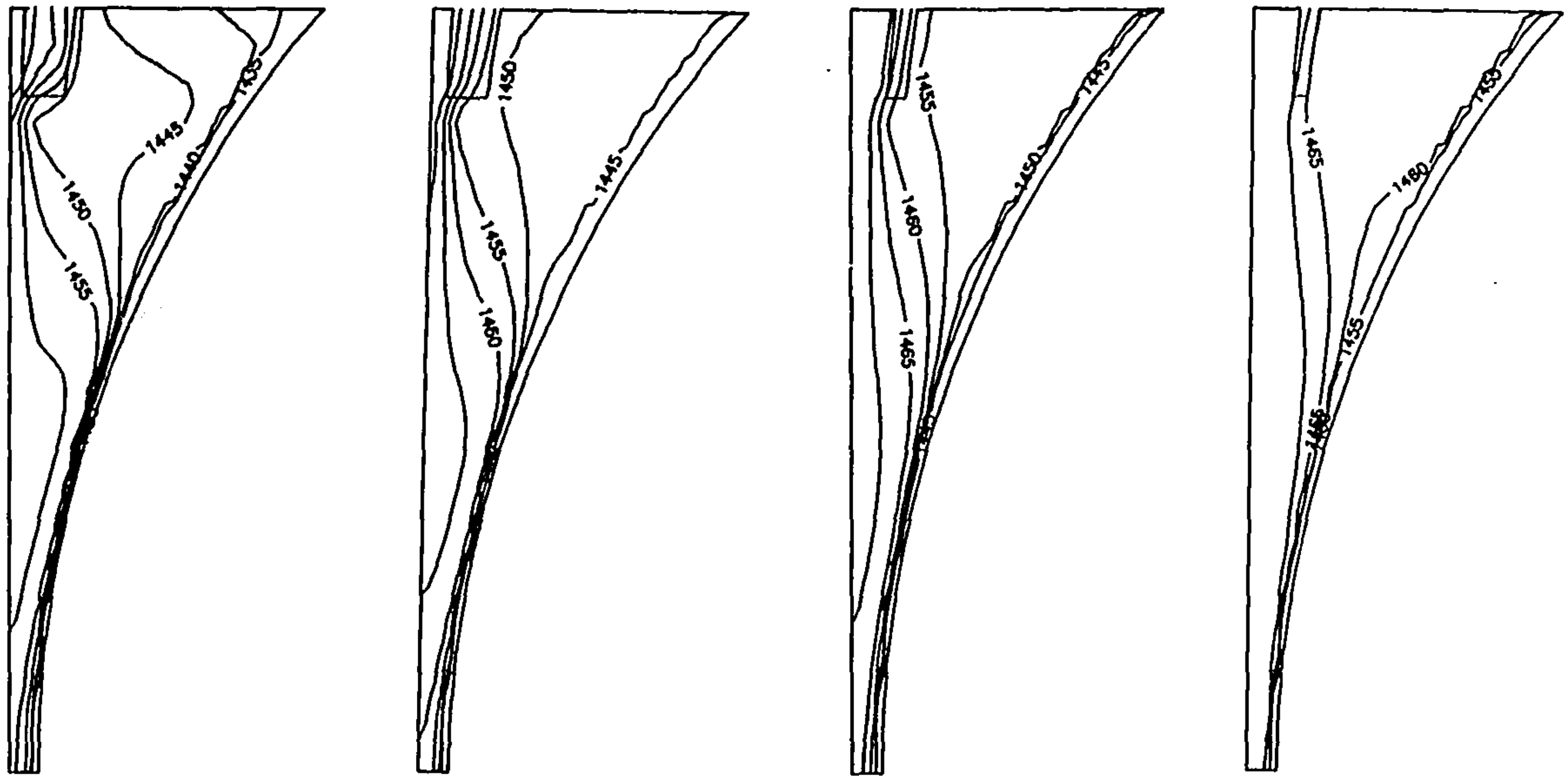

(a) inside thickness = 9 mm (b) 15 mm (c) 27 mm (d) 40 mm

Figure 7.16 Comparison of temperature profiles
Effect of inside thickness of submerged nozzle
(casting speed = 60 m/min, super-heat = 20 K, h_i = 8000 W/m^{2}K)

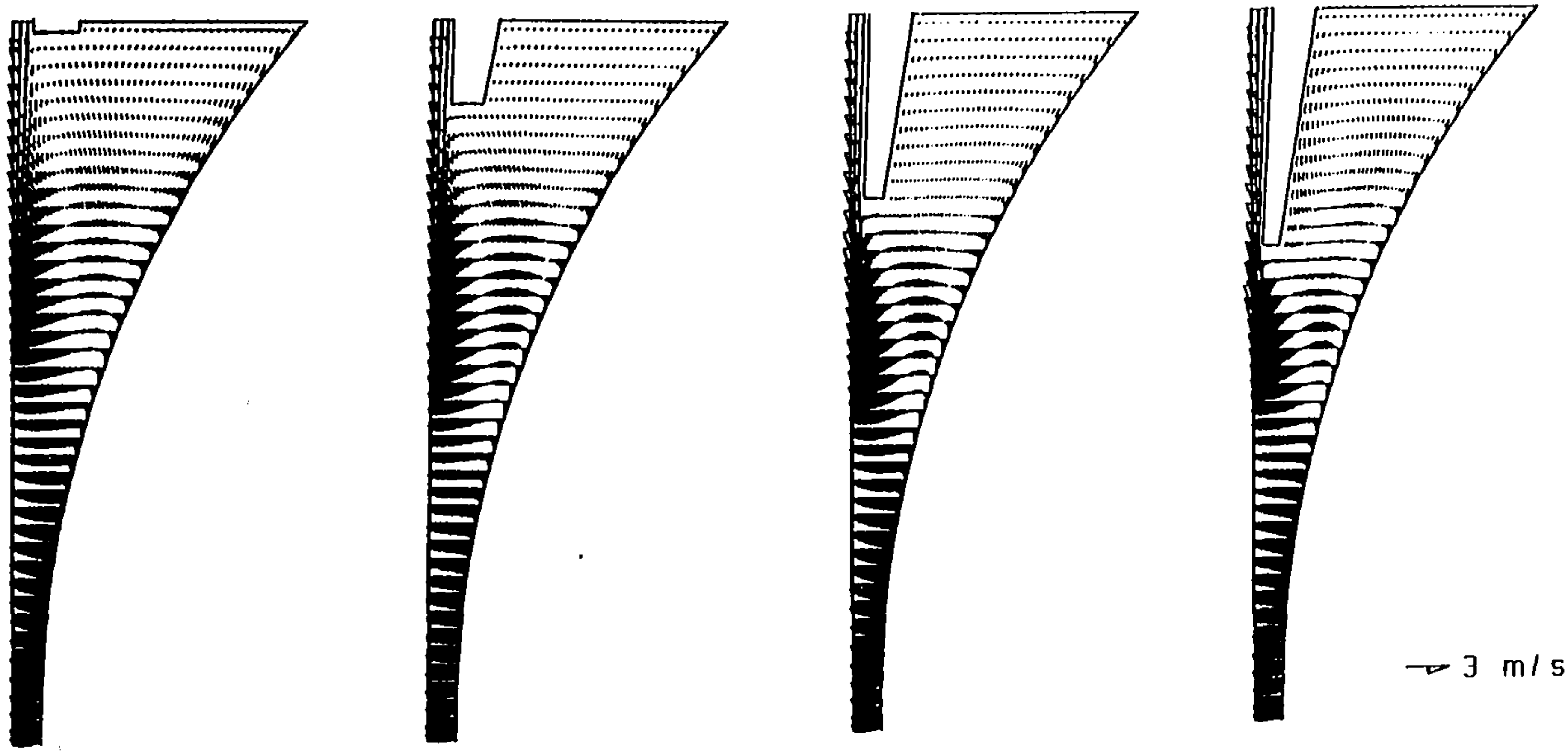

(a) depth = 5 mm (b) depth = 43 mm (c) depth = 101 mm (d) depth = 130 mm

Figure 7.17 Comparison of velocity profiles
Effect of depth of submerged nozzle
(casting speed = 60 m/min, super-heat = 20 K, h_l = 8000 W/m²K)

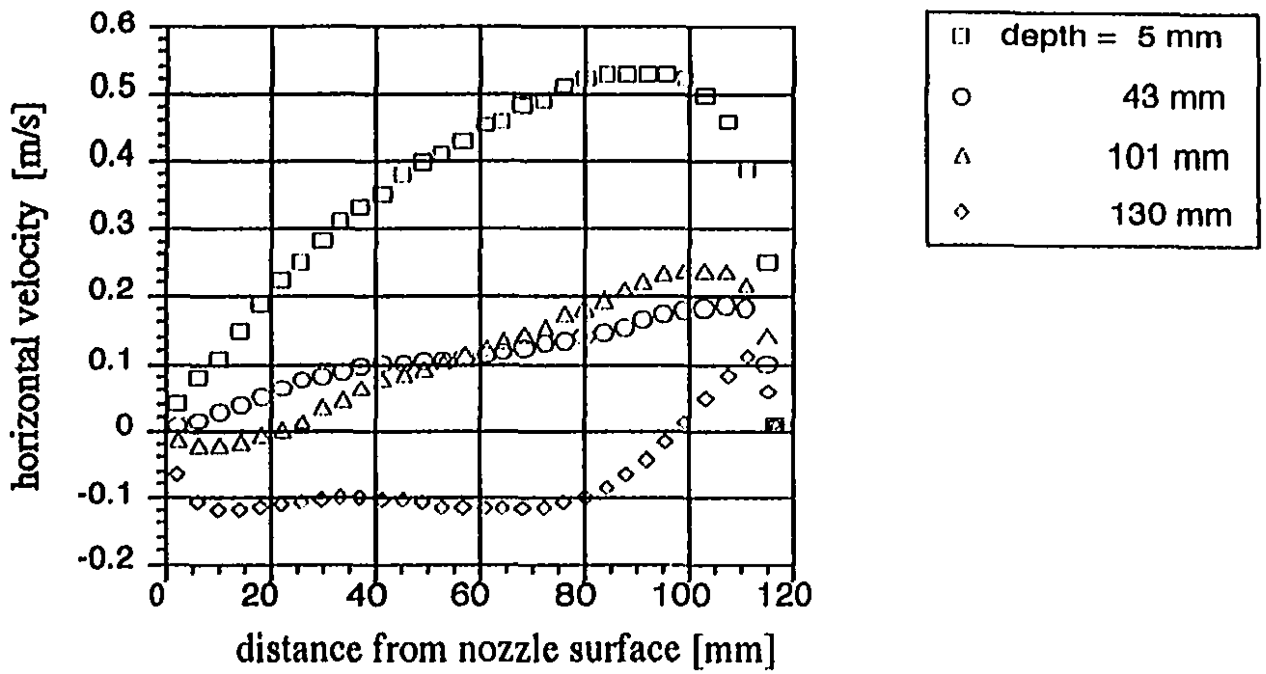

Figure 7.17 Horizontal velocity profile of meniscus surface
(casting speed = 60 m/min, SH = 20 K, h_i = 8000 W/m^{2}K)

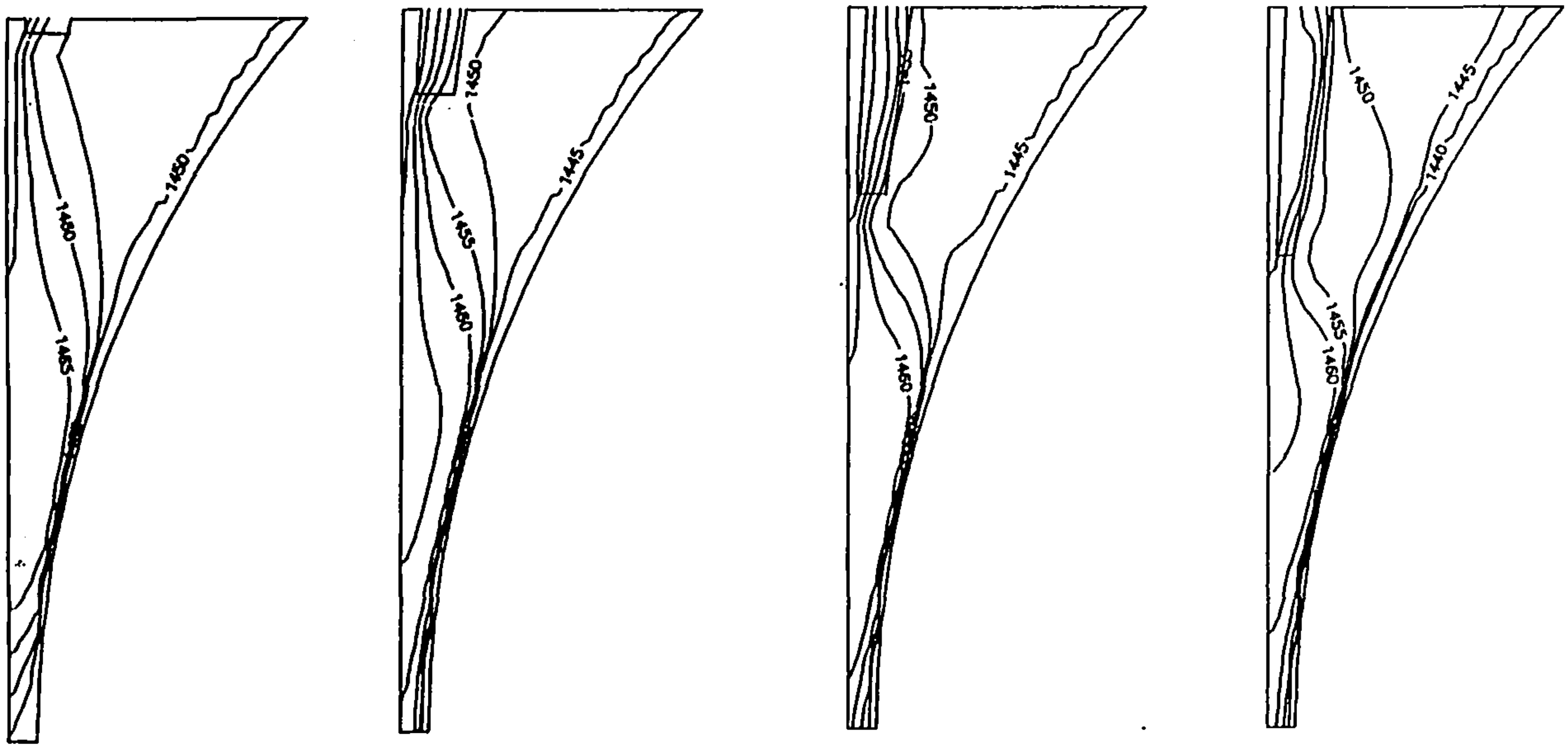

(a) depth = 5 mm **(b) depth = 43 mm** **(c) depth = 101 mm** **(d) depth = 130 mm**

Figure 7.19 Comparison of temperature profiles
Effect of depth of submerged nozzle
(casting speed = 60 m/min, super-heat = 20 K, h_l = 8000 W/m_2K)

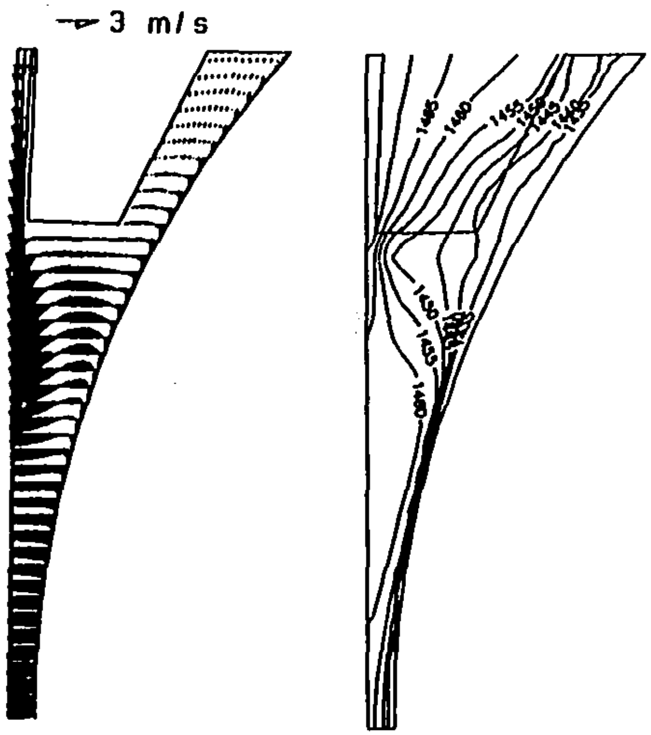

(a) velocity profile (b) isotherms

Figure 7.21 Fluid flow and temperature profile
outside thickness = 134 mm at the front - 221 mm at the meniscus
inside thickness = 15 mm, nozzle depth = 101 mm

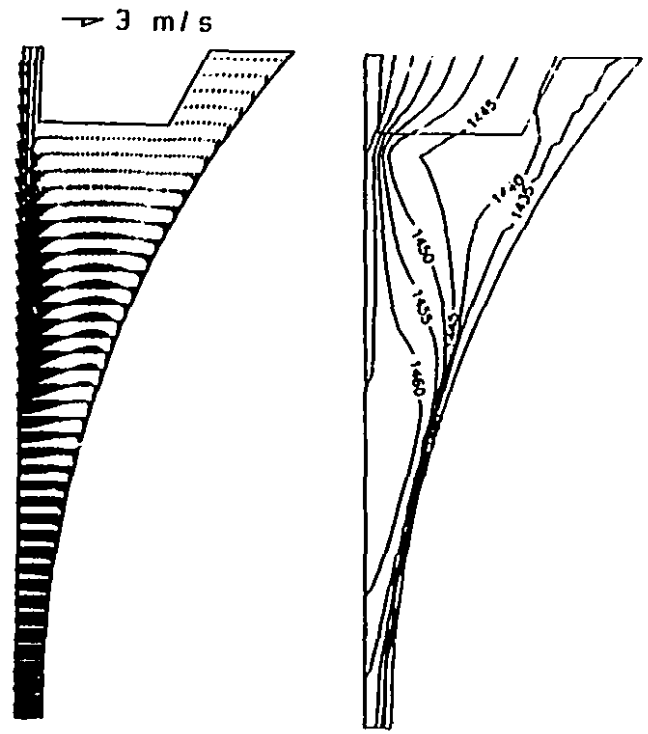

(a) velocity profile (b) isotherms

Figure 7.20 Fluid flow and temperature profile
outside thickness = 174 mm at the front - 221 mm at the meniscus
inside thickness = 15 mm, nozzle depth = 43 mm

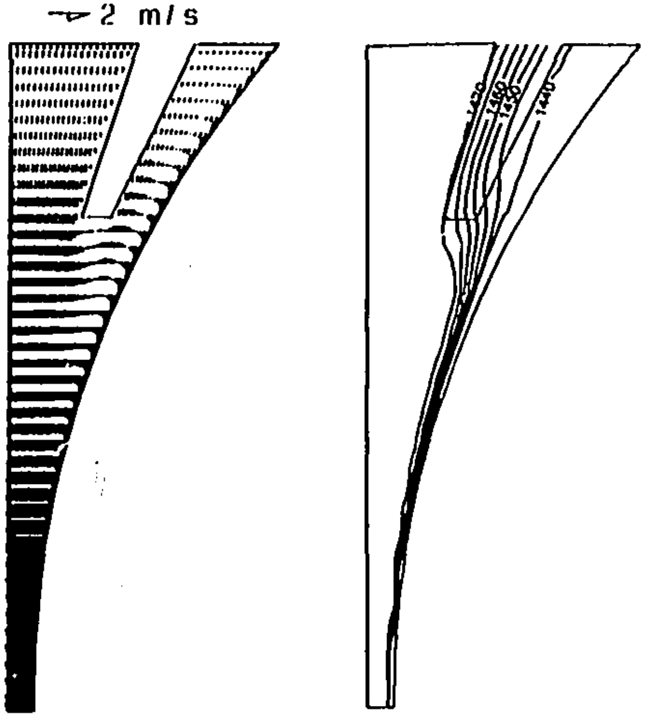

(a) velocity profile (b) isotherms

Figure 7.22 Fluid flow and temperature profile
outside thickness = 134 mm at the front - 221 mm at the meniscus
inside thickness = 80 mm, nozzle depth = 101 mm

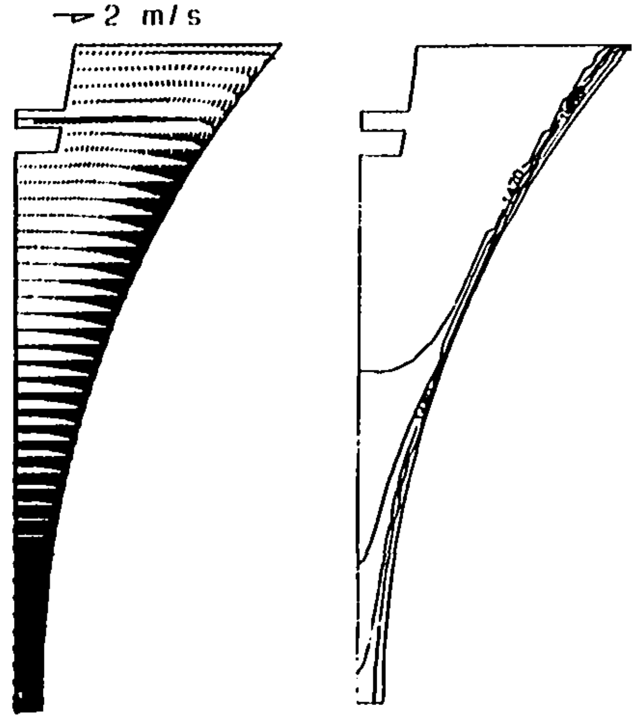

(a) velocity profile (b) isotherms

Figure 7.23 Fluid flow and temperature profile of horizontal impinging
outside thickness = 52 mm at the front - 74 mm at the meniscus
inside thickness = 10 mm, nozzle depth = 63 mm

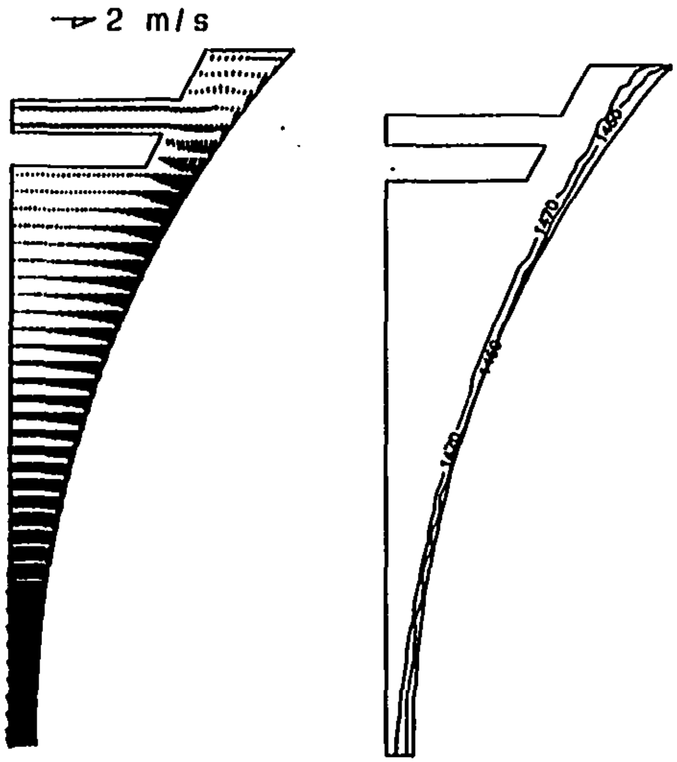

(a) velocity profile (b) isotherms

Figure 7.24 Fluid flow and temperature profile of horizontal impinging
outside thickness = 174 mm at the front - 221 mm at the meniscus
inside thickness = 19 mm, nozzle depth = 63 mm

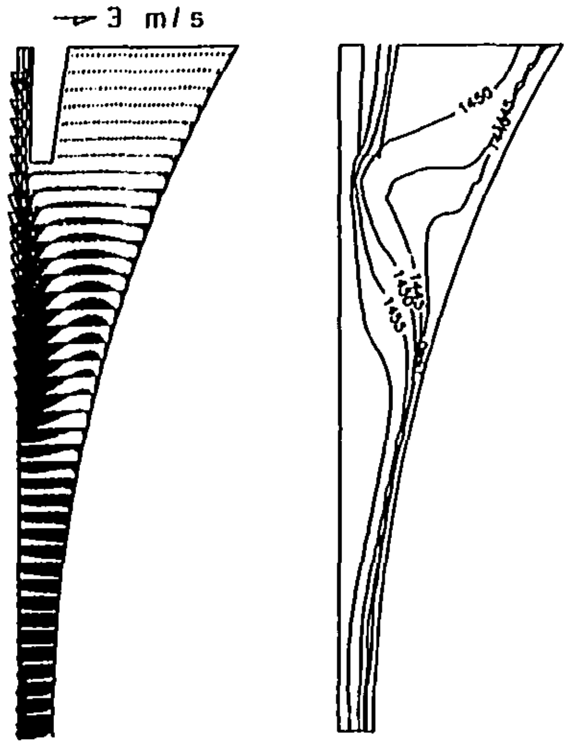

(a) velocity profile (b) isotherms

Figure 7.26 Fluid flow and temperature profile at a low pool mould
outside thickness = 32 mm at the front - 43 mm at the meniscus
inside thickness = 7 mm, nozzle depth = 49 mm

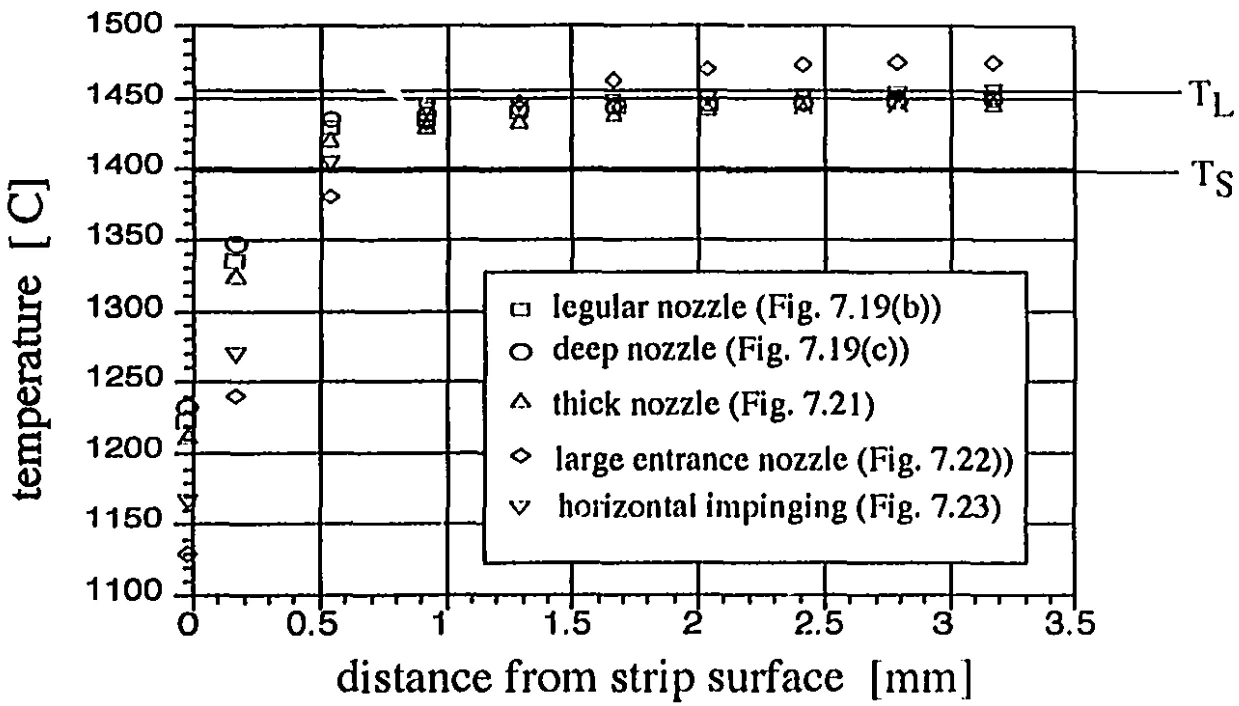

Figure 7.25 Temperature profile of the roll bite section
Effect of inlet system

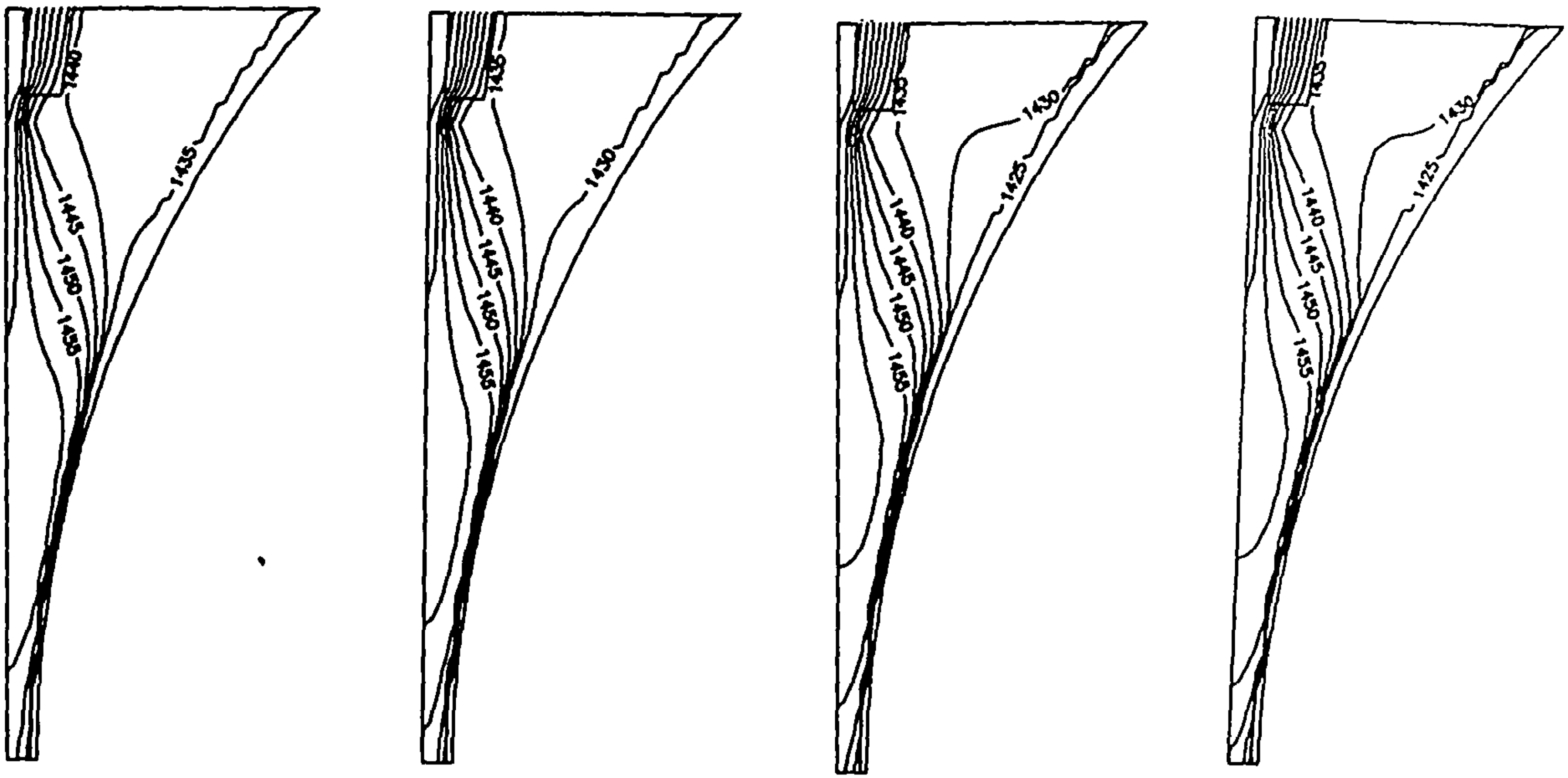

(a) h_l = 10000 W/m^{2}K (b) h_l = 12000 W/m^{2}K (c) h_l = 15000 W/m^{2}K (d) h_l = 18000 W/m^{2}K

Figure 7.27 Comparison of temperature profiles
Effect of cooling rate
(casting speed = 60 m/min, super-heat = 20 K)

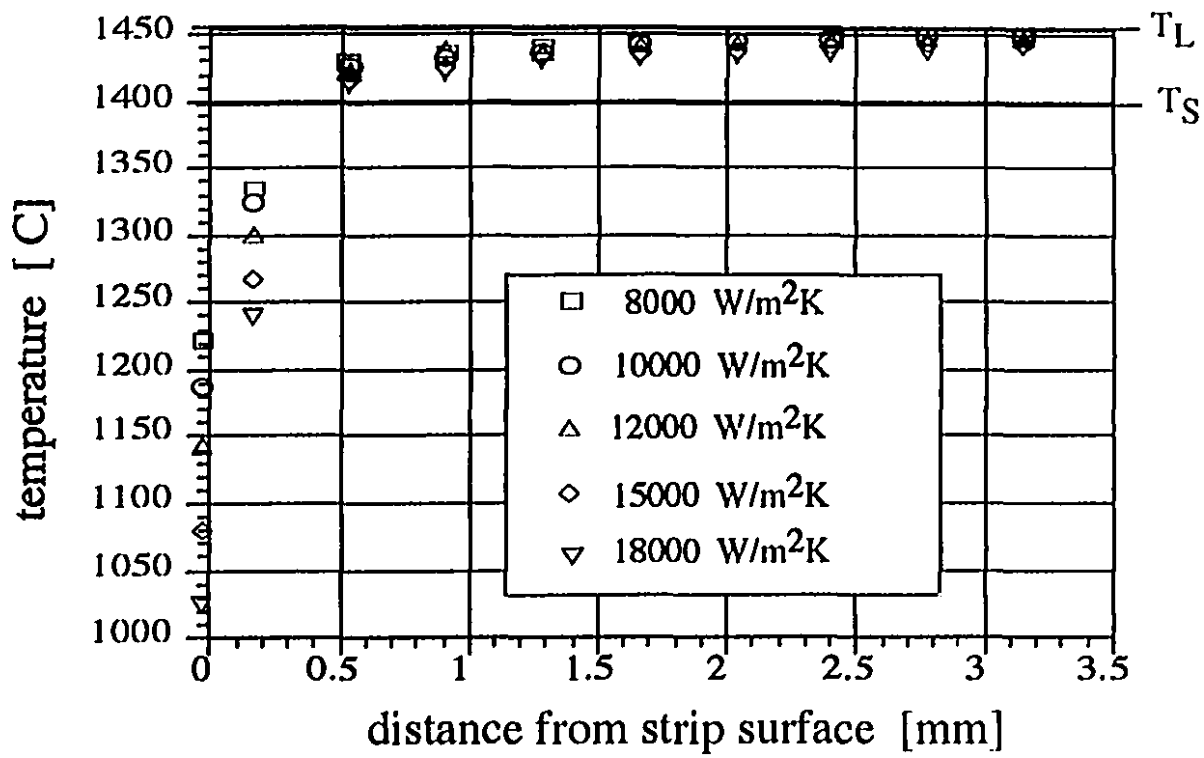

Figure 7.28 Temperature profile of the roll bite section
Effect of cooling rate

7.9 Summary

Computational studies for type 304 stainless steel were undertaken for various important parameters, based on the twin drum caster at N.S.C., using the model the author has developed. Much interesting information for the system has been obtained, as summarised below :

1. For the operating conditions being practised at N.S.C., neither the solid region nor the mushy region is large, and the energy field in the mould has little influence on the flow field.

2. The super-heat condition significantly affects the energy field, and its increase proportionally increases the bulk temperature within the pool.

3. Increase in casting speed increases the bulk temperature of the sump and proportionally decreases in the constant cooling rate and the fixed roll gap.

4. In the twin drum caster, the strip is not completely solid at the roll bite point, but the liquid fraction at the centre appears to be 0.5 and 0.7.

5. The smaller inside and outside nozzle causes hotter strip surface, and the small entrance, thick nozzle causes a thicker strip.

6. In usual conditions, the flow near the meniscus is towards the roll, and increase of the nozzle depth helps to reduce the velocity of the meniscus. Too deep a nozzle, however, gives rise to an oppositely directed flow, but the absolute value of the flow does not decrease so much.

7. The horizontal impinging nozzle causes the upper mould region to be hot and the lower mould region to be cold. Nevertheless, it leads to relatively thick shell

finally.

8. A doubling of the cooling rate, leads to approximately twice as thick strip, for the same conditions otherwise.

The parametric studies were carried out using personal computer (386 machine) in the 42 x 42 grid density and the roll gap is fixed 30 mm, for CPU condition.

CONCLUSIONS

A general mathematical model has been developed to study coupled turbulent flow and thermal transport in an arbitrary geometry and to predict the solidification heat transfer in the growing shell of a twin roll caster in alloy systems. The dendritic columnar solidification was modelled through implementation of the enthalpy–porosity technique selecting an appropriate value of the resistance constant for the porosity function. The transformed curvilinear mass, momentum and energy equations were suitably non–dimensionalized and solved with the physical variables and the contra–variant velocities, using a control–volume based finite difference method. The pressure–velocity coupling of the momentum equations were resolved through a modification of the SIMPLER algorithm. For the grid generation, Laplace equations were solved by SOR, and a simple uniform division approach was used. Computational studies were largely carried out with a personal computer (386 machine).
Carefully employing initial conditions and the step change approach help to obtain converged solutions.

The fluid flow model was validated by comparing its predictions with experimental data from a prototype water model at N.S.C. Regarding the solidification model, the numerical results for Sn–15%Pb alloy explain Hojo et al.'s experimental work quit well. Numerical predictions for 304 type stainless steel are also in agreement with facts that N.S.C. operators of the twin drum caster have found.

Many investigations for transport phenomena in the mould of the twin roll caster have been systematically performed, and interesting information obtained.

In the small laboratory type twin roll caster of the Sn–Pb system, most of the mould was occupied by solid and mushy regions. The flow field, therefore, was largely influenced by the energy field. Heat and momentum transport in the mould were strongly related to inlet conditions. The phenomenon of a remelting shell by the effects of flow, which no researcher has reported quantitatively, was described well by the model.

In the pilot scale twin roll caster, both solid and mushy regions are too thin to affect the flow field. The study suggested difficulty in the scale-up of information obtained from laboratory scale equipment, and the capability of a water model to predict flow fields within the mould.

The predictions by various parametric studies demonstrate a relationship exists between operational factors and fluid and energy conditions within the mould. In particular, concerning the inlet system (submerged nozzle), very important information was obtained, although no report has been appeared until today. (See chapter 7 for a full account of the point)

Contributions to knowledge

The following items represent the original contribution of this thesis to new knowledge:

1. 2-dimensional mathematical model of coupled turbulent fluid flow, heat transfer and solidification in the wedged-shape geometry, and the computational code for a personal computer (PC 386 or above/work station (ex.SUN)).

2. Validation of the model and suitable selection of numerical parameters. The model contains several techniques to obtain solutions in the twin roll caster.

3. Computational predictions for the twin roll caster. Detailed studies concerning the design of the submerged nozzle are the first attempt, and the results also have originality.

Recommendations for future work

Investigation of different metal and alloy systems should be carried out to understand the twin roll casting process. This author has already started.

In the author's experience, grid density and grid formation significantly affect the accuracy and stability of the solutions. During the research, the rate of the computer has become more than twice, therefore, more detail investigation using finer grid, particularly near the roll surface, is recommended. This should allow a more detailed shell profile to be computed.

A 3–dimensional version is expected in engineering stages because the flow in the mould has 3–dimensional features and information about the flow in the width direction is necessary for designing the nozzle precisely and optimally.

Experimental measurements in pilot plant scale equipment is strongly recommended, although it is difficult in practice. In particular, the relation between the strip quality and the physical conditions need to be understood using both experiments and calculations.

NOMENCLATURE

a_e : coefficient of east face (ref. eq(4·75)~(4·79))
d_s : strip thickness
dd : distance from the first contact point
f : function
f_1, f_2 : coefficient in a low Reynolds turbulent model
f_μ : dumping function in turbulent viscosity
g : gravity
h_T : overall heat transfer coefficient
h_i : local heat transfer coefficient
h : sensitive enthalpy
k : turbulent kinetic energy
l : length scale
l_m : mixing length in turbulence
n : normal unit
p : pressure
q : heat flux
t : time
u : velocity in x-direction
u^* : friction velocity
v : velocity in y-direction
x,y : direction in rectangular coordinate
y^+ : non-dimensional distance from the roll surface
y_i : distance from the meniscus in a mould
A : porosity function
A(| |): function for discretization of the convective terms
B_1, B_2 : constant value in Virtual Adjunct Method
C^* : resistance constant of the porosity function
C_1, C_2, C_D, C_μ : constant value in a turbulent model
C_p : heat capacity
D : representative length
E : constant of wall function (=9.79)
F : external force
F_S : solid fraction
H : total enthalpy
ΔH : elemental latent heat contribution
J : Jacobian
K : permeability
P : non-dimensional pressure
Pr : Prandtl number
Q : external heat
R' : constant of wall function (=0.41)
Ra : Raleigh number

Re : Reynolds number
Sc : Schmidt number
S() : source term
T : temperature
T_c : wall temperature
T_h : temperature of molten steel at the entrance
T_L : liquidus temperature
T_S : solidus temperature
U,V : contra-variant velocity
U_r : representative velocity = casting speed
α,β,γ : coefficient of the transformation
β_0 : coefficient of thermal expansion
δ : thickness of boundary layer
ϵ : dissipation rate of turbulent energy
θ : non-dimensional temperature
η,ξ : coordinate in a transformed plane
κ : heat conductivity
λ : latent heat of solidification
μ : viscosity
ν : kinematic viscosity
ρ : density
$\sigma_T,\sigma_k,\sigma_\epsilon$: coefficient in the turbulent model
τ : shear stress
Γ : coefficient in the governing equations
Θ : angle
Φ : heat generation by viscous dissipation

< subscript >
in : inlet
L : liquid region
M : mould
n : submerged nozzle
out : outlet
r : roll
ref : reference
roll : roll surface
S : solid region
t : turbulent
η,ξ : partial differential
∞ :ambient

< superscript >
' : component of fluctuation
- : non-dimensional
* : true value

BIBLIOGRAPHY

Bagshaw M.J., Hunt J.D., and Jordan R.M. "A Steady State Model for Roll Casting" Proc. Modeling and Control of Casting and Welding Processes Engineering Foundation Conferences. Santa Barbara, (1986) Jan. 12-17, pp135-147

Bagshaw M.J., Hunt J.D., and Jordan R.M. "A Theoretical and Experimental Study of Heat Line Formation in a Roll Caster" Cast Metals, 1 No1 (1988) pp16-22

Barfield W.D. "Numerical Method for Generating Orthogonal Curvilinear Meshes" J. Comp. Phys. 5 (1970) pp23-33

Bessemer H. "Ueber die Herstellung von Endlosem Blech aus schmiedbarem Eisen und Stahl direct aus dem flüssigen Metall" Stahl und Eisen, 11, (1891) pp921-926

Birat J.P. "Continuous casting for tomorrow : Near Net Shape Casting" La Revue de Métallurgie, CIT. (1988) Apr. pp317-334

*Boussinesq J. "Théorie de l'écoulement tourbillant" Mem. Pre. par. div. Sav. 23, (1877)

Braaten M. and Shyy W. "A Study of Recirculating Flow Computation Using Body-Fitted Coordinates: Consistency Aspects and Mesh Skewness" Numerical Heat Transfer, 9, (1986) pp559-574

Brent A.D., Voller V.R. and Reid K.J. "Enthalpy-Porosity Technique for Modelling Convection-Diffusion Phase Change: Application to Melting of a Pure Metal" Numr. Heat Transfer, 13, (1988) pp297-318

Burgo J.A., Conarty T.J. and Hlinka J.W. "Thermal design and Analysis of a Twin Roll Caster" Iron & Steel Engineer, (1990) July pp51-55

Carman P.C. "Fluid Flow Through Granular Beds" Trans. Inst. Chem. Eng., 15, (1937) pp150-166

Chien K-Y. "Predictions of Channel and Boundary-Layer Flows with a Low-Reynolds-Number Turbulence Model" AIAA 20 No1 (1982) pp33-38

**Courant R., Isaacson F. and Rees M. "On the Solution of Non-Linear Hyperbolic Differential Equations by Finite Difference" Comm. Pure Appl. Math., 5 (1952) pp243

Deardorff J.W. "A Numerical Study of Three-Dimensional Turbulent Channel Flow at Large Reynolds Number" J. Fluid Mech. 41, part2, (1970) pp453-480

Dubke M., Tacke K-H., Spiter K-H. and Schwerdtfeger K. "Flow Fields in Electromagnetic Stirring of Rectangular Strands with Linear Inductors: Part I. Theory and Experiments with Cold Models" Met. Trans. 19b, (1988) pp581-593

Farouk B., Kim Y.G. and Apelian D. "Numerical Study on the Solidification Process in a Twin-Belt Caster" Numerical Heat Transfer, part A, 20, (1991) pp375-393

Hadjisophocleous G.V., Sousa A.C.M. and Vernart J.E.S. "Prediction of Transient Natural Convection in Enclosures of Arbitrary Geometry Using a Non-orthogonal Numerical Model" Numerical Heat Transfer (1988) pp373-392

Henkes R.A.W.M. and Hoogendoorn C.J. "Comparison of Turbulence Models for the Natural Convection Boundary Layer Along a Heat Vertical Plate" Int. J. Heat Mass Transfer, 32, NO1 pp157-169

Hlinka J.W., Burgo J.A. and Conarty T.J. "Modelling and Design of Twin Roll Caster" 'Casting of Near Net Shape Products' Proc.Int.Symp. (1988) pp115-132

Hlinka J.W., Burgo J.A. and Conarty T.J. "Results of Twin-Roll Casting Trials" Proc. ISS Conference, AIME (1989) pp133-143

Hojo H., Kang C., Kato K., Tamakawa K. and Yaguchi H. "A Study on Twin-roll type Continuous Casting (1st Report, Solidification Characteristics and Casting Conditions)" Trans. JSME 53, (1987) pp2452-2458

Iwanami S. and Hirayama N. "Fluid Dynamics -Fundamental Practice-" (1983) Jitsukyo-Shuppan pp252-302

Jimbo I., Stepanek J. and Cramb A.W. "Laboratory Scale Strip Casting" PTD Conference Proceedings 10, (1992) pp335-341

Jones W.P.and Launder B.E. "The Prediction of Laminarization with a Two-Equation Model of Turbulence" Int. J. Heat Mass Transfer, 15, (1972) pp301-314

Jones W.P. and Launder B.E. "The Calculation of Low Reynolds Number Phenomena with a two-equation Model of Turbulence" Int. J. Heat Mass Transfer,16, (1973) pp1119-1129

Karki K.C. and Patankar S.V. "Calculation Procedure for Viscous Incompressible Flows in Complex Geometries" Numerical Heat Transfer 14, (1988) pp295-307 *von Karman T.H. "Mechaniche Ahnlichkeit und Turbulenz" Proc. 3rd Int. Congress Appl. Mech., Stockholm (1930) pp1-85

Karki K.C. and Patankar S.V. "Solution of Some Two-Dimensional Incompressible Flow Problems Using a Curvilinear Coordinate System Based Calculation Procedure" Numerical Heat Transfer, 14, (1988) pp309-321

Kasama A., Mizoguchi S., Miyazawa K., Ito M. and Sugai T. "A Consideration on the Rapid Solidification of Steels" ISIJ 26, (1986) pp139-140

Kasama A., Mizoguchi S., Miyazawa K., Ito M. and Sugai T. "A Consideration on the Rapid Solidification of Steels" ISS Publication 'Near Net Shape Casting' (1987) pp59-63

Kasama A., Tanaka S., Itoh Y., Kajioka H., Yanagi K. and Sasaki K. "Twin Drum Casting Process for Stainless Steel Strip" Proc.SRNC-90 (1990) pp643-652

Kawakami K., Inagaki J., Nishioka S., Sato H. and Ohtsuki M. "Research on Twin-Roll Casting Process" ISS Publication 'Near Net Shape Casting' (1987) pp71-80

Kays W.M. and Crawford M.E. 'Convective Heat and Mass Transfer.(2nd ed.)' McGraw-Hill (1980) pp243

*Kolmogorov A.N. "Equation of Turbulent Motion of an Incompressible Turbulent Fluid" Izv. Akad. Naak. USSR, Sev. Phys. 1, No1-2, (1942) pp56

Kraus H.G. 'Finite Element Model and Feasibility Study of Thin Strip Continuous Casting of Steel.' Numerical Heat Transfer 10, (1986) pp63-77

Kusakawa R. Tetsu to Hagane (1985) A200-A203

Lam C.G.K. and Bremhorst K. "A Modified Form of the k-ϵ Model for Predicting Wall Turbulence" Trans. ASME 103 (1981) pp456-460

Launder B.E. "Numerical Computation of Convective Heat Transfer in Complex Turbulent Flows; Time to Abandon Wall Functions?" Int. J. Heat Mass Transfer, 27, No9, (1984) pp1485-1491

Launder B.E. and Sharma B.I. "Application of the Energy Dissipation Model of Turbulence to the Calculation of Flow Near a Spinning Disc" Letters in Heat and Mass Transfer, 1, (1974) pp131-138

Launder B.E. and Spalding D.B. "Mathematical Models of Turbulence" Academic Press

London and New York. (1972)

Masounave J., Blain J., Essadiqi E. and Caron E. "The Design and Implementation of the IMRI Strip Caster." Proc. Int. Symp. "Casting of Near Net Shape Products" Sahai et al. Ed. (1988) pp473-492

Mazumdar D. and Guthrie R.I.L. "Hydrodynamic Modelling of Some Gas Injection Procedures in Ladle Metallurgy Operations" Met. Trans. 16B, (1985) pp83-90

McWhorter J.C. and Sadd M.M. "Numerical Unisotropic Heat Conduction Solutions Using Boundary-Fitted Coordinate Systems" Trans. ASME, 102, (1980) pp308-311

Miyazaki M., Suichi I., Tanaka S.and Takauchi H. "Heat Transfer Modelling for Solidification in Twin Drum Caster" CAMP-ISIJ 3, No1 (1990) p998

Miyazawa K., Ohashi T., Kasama A. and Kajioka H. "Theoretical Analysis of Twin Roll Rapid Solidification Process with Taking Account of Supercooling Phenomena of Metal" Trans. ISIJ, 26 (1986) B258

Miyazawa K., Mizoguchi T., Nakamura N. and Ohashi T. "The Formation of Thin Steel Strip in a Laboratory Scale Twin Roll Casting" "Casting of Near Net Shape Products" Sahai et al. Ed. Proc. Int. Symp. in Honolulu, Hawaii. (1988) pp629-643

Miyazawa K. and Szekely J. "A Mathematical Model of the Splat Cooling Process Using the Twin-Roll Technique" Met. Trans. 12A, (1981) pp1047-1057

Moin P. and Kim J. "Numerical Integration of Turbulent Channel Flow" J.Fluid Mech., 118, (1982) pp341-377

Murakami H., Hasan M. and Guthrie R.I.L. "A Mathematical Model for A Vertical Twin-Roll Caster" 10th PTD Conf. Proc. /ISS/AIME, Toronto (1992) pp347-354

Murakami S., Kato S., Suyama Y. and Nakagawa H. "Study on Air-Velocity Distribution in Conventional Flow Clear Row" SEISAN KENKYUU 40, No1 (1988) pp16-24

Patankar S.V. "Natural Heat Transfer and Fluid Flow" MacGraw Hill, (1980)

Patel V.C., Rodi W. and Scheaer G. "Turbulence Models for Near-Wall and Low Reynolds Number Flow : A Review" AIAA J., 23, NO9 (1984) pp1308-1319

Pope S.B. "The Calculation of Turbulent Recirculating Flows in General Orthogonal Coordinate" J. Comp. Phys. 26, (1978) pp197-217

*Prandtl L. "Bericht über Untersuchngen zur aus-gebildeten Turbulenz" ZAMM,5, (1925) pp136-

Rhie C.M. and Chow W.L. "Numerical Study of the Turbulent Flow Past an Airfoil with Trailing Edge Separation" AIAA J. 21, No11 (1983) pp1525-1532

Sahai Y., Battles J.E., Carbonara R.S. and Mobley C.E. Ed., "Casting of Near Net Shape Products" Proc. Int. Symp. Honolulu, Hawaii. Nov.13-17 (1988)

Saitoh T., Hojo H., Yaguchi H. and Kang C.G. "Two-Dimensional Method for Twin-Roll Continuous Casting" Met. Trans. 23B, (1989) pp381-390

Sanari H. and Inoue T. "Simulation of Strip Casting Process by Twin Roll Method (1st Report, Analysis of Solidification and Temperature, and the Experimental Verification)" Trans. JSME 56, (1989) pp984-989

Sanghoon J. "Modelling Metallurgical Phenomena in Ladle and Tundish Steel Processing Operations. Ph D Thesis, McGill Univ. (1989)

Shinde T., Ohsako T., Nakada M. and Komatsu M. "Strip Casting of Stainless Steel by Twin-Roll Process with A New Pouring System" ISS Conf. Proc. Toronto, (1992)

Shyy W. and Chen M.-H. "Steady-state natural convection with phase change" Int. J. Heat Mass Transfer, 33, No11 (1990) pp2545-2563

Shyy W., Pang Y., Hunter G.b., Wei D.Y. and Chen M.-H. "Modelling of Turbulent Transport and Solidification During Continuous Ingot Casting" Int. J. Heat Mass Transfer, 35, No5 (1992) pp1229-1245

Shyy W., Tong S.S. and Correa S.M. "Numerical Recirculating Flow Calculation Using a Body-Fitted Coordinate System" Numer. Heat Transfer 8, (1985) pp99-113

Sparrow E.M., Patankar S.V. and Ramadhyan S. "Analysis of Melting in The Presence of Natural Convection in the Melt Region" Trans. ASME, 99, (1977) pp520-526

**Spalding D.R. "A Novel Finite-Difference Formation for Differential Expressions Involving Both First & Second Derivatives" Int. J. Num. Methods Eng. 4, (1972) p551

Suichi I., Tanaka S., Kazama A., Takeuchi H., Sasaki K. and Hirai E. "Fluid Flow Molten Steel in Twin Drum Casting Process" CAMP-ISIJ 3, No1 (1990) p999

Szekely J. and Jassal A.S. "An Experimental and Analytical Study of the Solidification of a Binary Dendritic System" Met. Trans. 9B, (1978) pp389-398

Takuda H., Hatta N., Teramura M. and Kokudo J. "Simple Model for Thermal Calculation in Twin Roll Strip Casting Process" Steel Research, 61, NO7, (1990) pp312-317

Tanaka S., Suichi I., Ogawa S., Furuya T., Sasaki K. and Yanagi K. "Solidification Characteristics and Modelling Solidification Phenomena in Twin Drum Caster" Proc. ISS Conf. in Washington, Washington D.C., (1991) Apr.

Thomas B.G. and Najjar F.M. "Finite-Element Modelling of Turbulent Fluid Flow and Heat Transfer in Continuous Casting" App. Math. Modelling, January,1990

Thomas B.G., Mike L.I. and Najjar F.M. "Simulation of Fluid Flow inside a Continuous Slab-Casting Machine" Met. Trans. 21B, (1990) pp387-399

Thompson J.F., Warsi Z.U.A. and Hastin C.W. "Numerical Grid Generation. Foundations and Applications" North-Holland, Amsterdam (1985)

Thompson J.F., Thames F.C. and Mastin C.W. "Automatic Numerical Generation of Body-Fitted Curvilinear Coordinate System for Field Containing Any Number of Arbitrary Two-Dimensional Body" J. Comp. Phys. 15, (1974) pp299-319

Toyama N., Abo H., Arai H. and Yoshimura H. Testu to Hagane (1985) A245-A248

Voller V.R. and Prakash C. "A Fixed Grid Numerical modeling methodology for convection-diffusion mushy region phase-change problems" Int.J.Heat Mass Transfer, 30, (1987) pp1709-1719

Voller V.R., Swaminathan R. and Thomas B.G. "Fixed Grid Techniques for Phase Change Problems: A Review" Int. J. Numer. Methods Eng., 30, (1990) pp875-898

Yamada M., Nakashima H., Takeuchi H., Tanaka S., Yamakami Y., Yanagi K., Yamamoto K.and Sasaki K. "Development of Twin Drum Strip Casting Process for Stainless Steel" N.S.C. report

Yamane H., Yukumoto M., Miyake S. and Ozawa M. "Mathematical Analysis Rapid Solidification by Twin Roll Casting" PTD Conf. Proc. 10, (1992) pp343-346

Yoshida C., Taniguchi K., Nakagawa T., Sudo M. and Nozaki T. " Characteristics of Rapidly Solidified Cast Iron and High Carbon Steel" Trans. ISIJ 26, (1986) ppB145-146

Yoshimura Y., Arai T., Shimomura K., Nakashima H., Takeuchi M., Yamagami Y., Yanagi Y. and Sasaki K. "Casting Technologies with Twin-Drum Caster" CAMP-ISIJ 4, (1991) pp993

Wang Y-H. and Saucedo I.G. "The Feeding of Steel in Twin Roll Casters" Iron & Steelmaker , (1990) Jan. pp14-21

* : referenced in "Mathematical Models of Turbulence"
**: referenced in "Natural Heat Transfer and Fluid Flow"